

UNCLASSIFIED

NSWCCR/RDTR-03/12



A Comparison of Gyroscope Digital Models for an Electro-Optical/Infrared Guided Missile Simulation

February 2003

Prepared By: Crane Division
Naval Surface Warfare Center
Ordnance Engineering Directorate
Pyrotechnics Development Department
Missile Effectiveness Branch
Brent A. Waggoner (Code 4072)
300 Highway 361
Crane, IN 47522-5001

***Approved for Public Release,
Distribution Unlimited***



UNCLASSIFIED

REPORT DOCUMENTATION PAGE

Form Approved
OMB No. 0704-0188

Public reporting burden for this collection of information is estimated to average 1 hour per response, including the time for reviewing instructions, searching existing data sources, gathering and maintaining the data needed, and completing and reviewing the collection of information. Send comments regarding this burden estimate or any other aspect of this collection of information, including suggestions for reducing this burden, to Washington Headquarters Services, Directorate for Information Operations and Reports, 1215 Jefferson Davis Highway, Suite 1204, Arlington, VA 22202-4302, and to the office of Management and Budget, Paperwork Reduction Project (0704-0188), Washington, DC 20503

| | | | |
|--|---|--|---|
| 1. AGENCY USE ONLY (Leave Blank) | 2. REPORT DATE February 2003 | 3. REPORT TYPE AND DATES COVERED Final FEB 03 | |
| 4. TITLE AND SUBTITLE A Comparison of Gyroscope Digital Models for an Electro-Optical/Infrared Guided Missile Simulation | | 5. FUNDING NUMBERS ----- | |
| 6. AUTHOR(S) Waggoner, Brent | | 8. PERFORMING ORGANIZATION REPORT NUMBER NSWCCR/RDTR-03/12 | |
| 7. PERFORMING ORGANIZATION NAME(S) AND ADDRESS(ES) Naval Surface Warfare Center Code 4072, Bldg 3291 300 HWY 361 Crane, IN 47522-5001 | | 10. SPONSORING/MONITORING AGENCY REPORT NUMBER | |
| 9. SPONSORING/MONITORING AGENCY NAME(S) AND ADDRESS(ES) | | 11. SUPPLEMENTARY NOTES ----- | |
| 12a. DISTRIBUTION/AVAILABILITY STATEMENT Approved for public release, distribution is unlimited. | | 12b. DISTRIBUTION CODE ---- | |
| 13. ABSTRACT (Maximum 200 words) This report was prepared by the author as a Master's thesis which partially fulfilled the requirements for a Master of Science degree in Electrical Engineering from Rose Hulman Institute of Technology, Terre Haute IN. Equations of motion and digital models of a gyroscope were developed for use in electro-optical/infrared missile simulations. Three different models were developed, of varying complexity. Results from these models were compared to actual gyro test data to evaluate the fidelity of the various gyroscope models. | | | |
| 14. SUBJECT TERMS Infrared Missile Electro-optical Missile Gyroscope | | 15. NUMBER OF PAGES 211 | 16. PRICE CODE ---- |
| 17. SECURITY CLASSIFICATION OF REPORT UNCLASSIFIED | 18. SECURITY CLASSIFICATION OF THIS PAGE UNCLASSIFIED | 19. SECURITY CLASSIFICATION OF ABSTRACT UNCLASSIFIED | 20. LIMITATION OF ABSTRACT Approved for public release, distribution is unlimited |

A Comparison of Gyroscope Digital Models for an Electro-Optical/Infrared Guided Missile Simulation

A Thesis

Submitted to the Faculty of
Rose-Hulman Institute of Technology

by

Brent Alan Waggoner

In Partial Fulfillment of the
Requirements for the Degree of
Master of Science in Electrical Engineering

February 2003

Rose-Hulman Institute of Technology

FINAL EXAMINATION REPORT

Name Brent Waggoner Discipline(s) Electrical Engineering

Thesis Thesis Topic: A Comparison of Gyroscope Digital Models for an Electro-Optical/Infrared Guided Missile Simulation

Non thesis Topic of Relevant Experience: _____

I. EXAMINATION COMMITTEE:

| PROFESSOR | DEPT. |
|------------------------------------|-------|
| Chairperson: Dr. David J. Purdy | ME |
| Dr. Frank E. Acker | ECE |
| Dr. Edward R. Doering | ECE |
| | |
| | |
| | |

Requested by: David J. Purdy
Chairperson

Approved by: David Berger
Department Head

II. FINAL EXAMINATION REPORT:

Date of Exam: February 12, 2003

Passed
 Failed

Advisory Committee Signatures of Approval:

David J. Purdy Chairperson
Frank E. Acker
Edward R. Doering



When the report is complete, the Advisory Committee Chairperson will send this form to Graduate Studies. Copies will be sent to each committee member, the department head, and the student.

ABSTRACT

Waggoner, Brent Alan. M.S., Rose-Hulman Institute of Technology, February 2003. Comparison of Gyroscope Digital Models for an Electro-Optical/Infrared Guided Missile Simulation. Major Professor: Dr. David J. Purdy.

Increasingly, modeling and simulation are being used in the analysis and development of modern weapon systems, in particular electro-optical and infrared (EO/IR) guided missiles. Most EO/IR missiles use Cassegrain optical systems mounted on a gyroscope which provides a stable platform for the EO/IR sensor. Current missile simulations use digital gyroscope models of varying degrees of complexity. This thesis compares the performance of three digital gyroscope models of varying complexity. The fidelity of each model is evaluated based on comparison to actual gyroscope test data.

The three gyroscope models being compared are: (1) Ideal gyro, (2) Brown/Dougherty/Williams/Lamm (BDWL), and (3) Gallaspy. The Ideal gyro model precesses perfectly as commanded with no nonlinearities, no nutation effects, no spin torque / precession torque cross-coupling, and perfect instantaneous spin-up and spin-down.

The BDWL model uses gyro equations of motion derived from classic Newtonian dynamics, with gyro nutation and nutation damping, precession torque, spin torque, precession / spin cross coupling, as well as degradation of precession and spin efficiencies with off-boresight angle. The Gallaspy model

uses gyro equations of motion derived with the Lagrange method. It does not include nutation effects, off-boresight torque degradation, or precession / spin coupling, but it does have a rudimentary spin torque model.

Comparisons were made to actual gyro data in four areas: twice spin frequency nutation oscillations, open-loop nutation damping precession misalignment, rate table spin-up and spin-down, and signal phase comparison.

The BDWL model showed excellent agreement with the actual gyro data for the twice spin frequency nutation oscillations and the open-loop nutation damping. The Ideal and Gallaspy models did not match the actual gyro data in these cases (neither of these models includes any nutation effects).

The BDWL model had excellent correlation with the rate table spin-up and spin-down tests. The Gallaspy model showed good correlation in some cases and fair correlation in other cases. The Ideal model did not show good correlation to the rate table tests.

All three models gave similar results, and showed good correlation to the actual gyro data in the signal phase angle tests.

Thus, the BDWL model showed the best correlation to real gyro data but was the most computationally intensive. The Ideal gyro model had the worst correlation to actual gyro data, but was the least computationally intensive. The Gallaspy model gave performance somewhere between the BDWL and Ideal gyro models in both fidelity and computational requirements.

The performance of the Gallaspy model was controlled by the assumptions made during its development. The use of the Lagrange method to

derive the equations of motion showed no benefits or disadvantages in comparison to the Newtonian equation of motion derivation.

The results of this thesis give the EO/IR missile simulation developer a good set of criteria for choosing features of a gyro model and balancing gyro model fidelity with model execution speed.

DISCLAIMER

This thesis is being submitted as partial fulfillment of the requirements of Rose-Hulman Institute of Technology needed to obtain a Master of Science in Electrical Engineering degree.

The conclusions and opinions expressed in this thesis are those of the author and do not necessarily represent the position of Rose-Hulman Institute of Technology or the United States Government, or any of its directors, officers, agents, or employees about the matters discussed.

DEDICATION

This thesis is dedicated to my wife Susan and my children David, Kayla, Kara, and Noah for their support and sacrifice during this endeavor.

ACKNOWLEDGMENTS

I would like to thank Dr. David Purdy, chairman of my thesis committee for all his time and support on this project. I also thank Dr. Frank Acker and Dr. Edward Doering for serving on my thesis committee.

Several individuals provided me with invaluable information and previous research, without which, this thesis would not have been possible. These individuals include Mr. David Williams (Dynerics, Huntsville AL), Dr. Darrell Lamm (Georgia Tech Research Institute, Atlanta GA), Mr. James Brown (Naval Surface Warfare Center, Crane IN), Mr. Terry Dougherty (Naval Air Warfare Center, China Lake CA), Mr. Jason Gallaspy (Dynerics, Huntsville AL), and Mr. Bill Hecker (Redstone Arsenal, AL).

Many thanks are also owed to my co-workers at the Naval Surface Warfare Center, in Crane IN for review of my thesis, assistance in research, and help in taking actual gyro data. These include Mr. John Bennett, Mr. Tim Bradley, Mr. Ed Franklin, Mr. James Sweeten, Mr. Scot Brown, Mr. Michael Walls, Mr. Brad Strobel, Dr. Eric Hillenbrand, and Dr. Bernard Douda.

Finally, I would like to thank the management of the Naval Surface Warfare Center, Crane IN for providing me the opportunity to pursue this research and Master's degree. As well as the upper-management of NSWC

Crane, these individuals include Mr. Ted Smock, Mr. Steve Norris, Mr. Carl Lohkamp, and Mr. David Schulte.

TABLE OF CONTENTS

| | |
|--|-------|
| LIST OF FIGURES | ix |
| LIST OF TABLES | xvii |
| LIST OF ABBREVIATIONS | xviii |
| LIST OF SYMBOLS | xix |
| 1.0 Background on Electro-Optical/Infrared Guided Missiles | 1 |
| 2.0 Coordinate System Definition | 9 |
| 2.1 Direction Cosine Coordinate Transformation Matrix Definition | 12 |
| 3.0 Derivation of Brown/Dougherty/Williams/Lamm Gyro Model | 18 |
| 3.1 Equations of Motion / Gyro Dynamics Derivation | 19 |
| 3.2 Gyro Euler Angle Missile Dynamics Compensation | 27 |
| 3.3 Cage Coil Sensor Models | 44 |
| 3.3.1 Complete Cage Coil Model | 44 |
| 3.3.2 Cage Coil Small Angle Approximation | 46 |
| 3.4 Precession Coil | 48 |
| 3.5 Spin Coil | 51 |
| 3.6 BDWL Gyro Model Assumptions and Limitations | 57 |

| | |
|--|-----|
| 4.0 Derivation of Ideal Gyro Model | 58 |
| 4.1 Precession Coil | 59 |
| 4.2 Equations of Motion / Gyro Dynamics | 62 |
| 4.3 Ideal Gyro Model Assumptions and Limitations | 63 |
| 5.0 Derivation of Gallaspy Gyro Model | 65 |
| 5.1 Equation of Motion / Gyro Dynamics Derivation | 66 |
| 5.2 Rotation Dynamics | 76 |
| 5.3 Rotation Kinematics | 76 |
| 5.4 Sensor Coils (General) | 83 |
| 5.5 Lambda (Cage) Coil | 87 |
| 5.6 Reference Coils | 88 |
| 5.7 Spin Coils | 92 |
| 5.8 Caging Coil | 93 |
| 5.9 Precession Coil | 94 |
| 5.10 Gallaspy Model Limitations and Assumptions | 96 |
| 6.0 Model Comparisons to Gyro Test Data | 97 |
| 6.1 Twice Spin Frequency Nutation Oscillations | 97 |
| 6.2 Nutation Damping Misalignment | 105 |
| 6.3 Gyro Rate Table Spin-Up and Spin-Down Tests | 107 |
| 6.3.1 BDWL Track Loop Model and Implementation | 110 |
| 6.3.2 Ideal Track Loop Model and Implementation | 117 |
| 6.3.3 Gallaspy Track Loop Model and Implementation | 123 |

| | |
|---|-----|
| 6.3.4 Rate Table Test Comparison | 128 |
| 6.4 Gyro Signal Phase Comparison | 146 |
| 7.0 Summary | 180 |
| 8.0 Conclusions | 183 |
| 9.0 Recommendations for Further Study | 184 |
| LIST OF REFERENCES | 186 |

LIST OF FIGURES

| | |
|--|----|
| Figure 1 - Surface-to-air missile launch | 1 |
| Figure 2 - Typical EO/IR missile system components | 1 |
| Figure 3 - Air-to-ground EO/IR missile launch | 1 |
| Figure 4 - Missile and target geometry for guidance law derivation | 2 |
| Figure 5 - Cassegrain telescope layout | 3 |
| Figure 6 - More detailed Cassegrain telescope configuration for typical EO/IR missile system | 3 |
| Figure 7 - Reticule tracking system theory of operation | 4 |
| Figure 8 - Gyro magnetic field configuration | 5 |
| Figure 9 - Gyro coil diagram | 6 |
| Figure 10 - Missile body-fixed coordinate system | 10 |
| Figure 11 - Gyro body-fixed coordinate system | 10 |
| Figure 12 - Yaw rotation | 11 |
| Figure 13 - Pitch rotation | 11 |
| Figure 14 - Roll rotation | 11 |
| Figure 15 - Yaw rotation | 13 |
| Figure 16 - Pitch rotation | 14 |
| Figure 17 - Gyro spin rotation | 15 |
| Figure 18 - Top level of BDWL gyro model | 18 |

| | |
|---|----|
| Figure 19 - BDWL model gyro angular velocity block | 23 |
| Figure 20 - BDWL model gyro dynamics block | 24 |
| Figure 21 - BDWL model gyro angular position block | 27 |
| Figure 22 - BDWL gyro Euler angle missile dynamics compensation block . . | 28 |
| Figure 23 - Rate table missile position/orientation block | 29 |
| Figure 24 - BDWL gyro Euler angles with respect to missile body (GM) block | 32 |
| Figure 27 - BDWL calculate gyro Euler rates with respect to missile block . . . | 42 |
| Figure 28 - BDWL body angular rates from Euler angles and Euler rates block | 43 |
| Figure 29 - BDWL cage coil (full angle equations) block | 46 |
| Figure 30 - BDWL cage coil (small angle approximation) block | 47 |
| Figure 32 - Spin coil angle definitions | 51 |
| Figure 33 - BDWL gyro spin coil model | 55 |
| Figure 34 - BDWL spin coil commanded spin rate | 56 |
| Figure 35 - Top level of Ideal gyro model | 59 |
| Figure 36 - Ideal gyro model precession coil block | 62 |
| Figure 37 - Ideal gyro model gyro dynamics block | 63 |
| Figure 38 - Spin control block | 63 |
| Figure 39 - Top level of open-loop Gallaspy gyro model | 65 |
| Figure 40 - Missile and gyro geometry | 66 |
| Figure 41 - Gallaspy rotation dynamics block | 75 |
| Figure 42 - Gallaspy gyro dynamics block | 75 |
| Figure 43 - Gallaspy calculate gyro rate matrix inverse block | 76 |

| | |
|---|-----|
| Figure 44 - Gallaspy rotation kinematics block | 77 |
| Figure 45 - Gallaspy X rotation block | 78 |
| Figure 46 - Gallaspy Y rotation block | 78 |
| Figure 47 - Gallaspy Z rotation block | 79 |
| Figure 48 - Gallaspy calculate gyro-to-missile Euler angles block | 81 |
| Figure 49 - Gallaspy calculate nonrolling missile-to-earth transformation block | 82 |
| Figure 50 - Gallaspy calculate gyro-to-nonrolling missile Euler angles block | 83 |
| Figure 51 - Gallaspy form angular velocity matrix block | 86 |
| Figure 52 - Gallaspy lambda coil (cage coil) block | 87 |
| Figure 53 - Gallaspy reference coil block | 88 |
| Figure 54 - Gallaspy sensor coils block | 89 |
| Figure 55 - Gallaspy calculate gyro-to-missile roll rate block | 91 |
| Figure 56 - Gallaspy Spin Coils block | 92 |
| Figure 57 - Gallaspy caging coil block | 94 |
| Figure 58 - Gallaspy precession coil block | 95 |
| Figure 59 - Gyro nutation illustration | 97 |
| Figure 60 - FFT frequency components of actual gyro cage coil signal | 102 |
| Figure 61 - Zoom of gyro cage coil frequency components | 102 |
| Figure 62 - Gyro damping comparison | 103 |
| Figure 63 - Close-up of gyro damping comparison | 103 |
| Figure 64 - Gyro 200 Hz wobble from Dave Williams paper | 104 |

| | |
|--|-----|
| Figure 65 - Close-up of BDWL gyro model precession | 104 |
| Figure 66 - Close-up of Ideal1 gyro model precession | 104 |
| Figure 67 - Close-up of Gallaspy3 gyro model precession | 104 |
| Figure 68 - Gyro nutation damping misalignment comparison | 105 |
| Figure 69 - Rate table | 107 |
| Figure 70 - Rate table diagram | 107 |
| Figure 71 - Rate table | 107 |
| Figure 72 - BDWL gyro model with track loop implementation | 110 |
| Figure 73 - Missile, gyro, and target geometry and vectors | 112 |
| Figure 74 - BDWL track loop model | 113 |
| Figure 75 - Rate table target position geometry | 114 |
| Figure 76 - BDWL track loop target motion block | 115 |
| Figure 77 - BDWL space-to-body coordinate transform block | 116 |
| Figure 78 - BDWL track loop normalize vector block | 116 |
| Figure 79 - Ideal gyro model with track loop implementation | 117 |
| Figure 80 - Ideal gyro track direction and magnitude | 118 |
| Figure 81 - Ideal gyro model track loop block | 119 |
| Figure 82 - Ideal track loop space-to-nonrolling body coordinate transform block | 120 |
| Figure 83 - Ideal space-to-body Euler angles X block | 121 |
| Figure 84 - Ideal space-to-body Euler angles Y block | 121 |
| Figure 85 - Ideal space-to-body Euler angles Z block | 121 |
| Figure 86 - Ideal gyro tracker precession coil block | 122 |

| | |
|---|-----|
| Figure 87 - Gallaspy gyro model with track loop implementation | 123 |
| Figure 88 - Gallaspy track loop missile dynamics block | 124 |
| Figure 89 - Gallaspy track loop block | 125 |
| Figure 90 - Gallaspy track loop body-to-non-rolling body coordinate transform block | 126 |
| Figure 91 - Gallaspy gyro tracking error in the NRGI coordinate system | 127 |
| Figure 92 - Gallaspy track loop precession coil block | 127 |
| Figure 93 - Williams gyro data and model data for rate table test 1 | 130 |
| Figure 94 - BDWL response from rate table test 1 | 130 |
| Figure 95 - Ideal response for rate table test 1 | 131 |
| Figure 96 - Gallaspy response for rate table test 1 | 131 |
| Figure 97 - Williams gyro data and model data for rate table test 2 | 132 |
| Figure 98 - BDWL response for rate table test 2 | 132 |
| Figure 99 - Ideal response for rate table test 2 | 133 |
| Figure 100 - Gallaspy response for rate table test 2 | 133 |
| Figure 101 - Williams gyro data and model data for rate table test 3 | 134 |
| Figure 102 - BDWL response for rate table test 3 | 134 |
| Figure 103 - Ideal response for rate table test 3 | 135 |
| Figure 104 - Gallaspy response for rate table test 3 | 135 |
| Figure 105 - Williams gyro data and model data for rate table test 4 | 136 |
| Figure 106 - BDWL response for rate table test 4 | 136 |
| Figure 107 - Ideal response for rate table test 4 | 137 |
| Figure 108 - Gallaspy response for rate table test 4 | 137 |

| | |
|--|-----|
| Figure 109 - Williams gyro data and model data for rate table test 5 | 138 |
| Figure 110 - BDWL response for rate table test 5 | 138 |
| Figure 111 - Ideal response for rate table test 5 | 139 |
| Figure 112 - Gallaspy response for rate table test 5 | 139 |
| Figure 113 - Williams gyro data and model data for rate table test 6 | 140 |
| Figure 114 - BDWL response for rate table test 6 | 140 |
| Figure 115 - Ideal response for rate table test 6 | 142 |
| Figure 116 - Gallaspy response for rate table test 6 | 142 |
| Figure 117 - Williams gyro data and model data for rate table test 7 | 143 |
| Figure 118 - BDWL response for rate table test 7 | 143 |
| Figure 119 - Ideal response for rate table test 7 | 144 |
| Figure 120 - Gallaspy response for rate table test 7 | 144 |
| Figure 121 - Overall lab test gyro signals for horizontal right target motion . . | 152 |
| Figure 122 - BDWL overall signals for horizontal right target motion | 153 |
| Figure 123 - Ideal overall signals for horizontal right target motion | 154 |
| Figure 124 - Gallaspy overall signals for horizontal right target motion | 155 |
| Figure 125 - BDWL comparison to lab test data for horizontal right target motion | 156 |
| Figure 126 - Ideal gyro model comparison to lab test data for horizontal right target motion | 157 |
| Figure 127 - Gallaspy comparison to lab test data for horizontal right target motion | 158 |
| Figure 128 - Overall lab test signals for horizontal left target motion | 159 |
| Figure 129 - BDWL overall signals for horizontal left target motion | 160 |

| | |
|--|-----|
| Figure 130 - Ideal overall signals for horizontal left target motion | 161 |
| Figure 131 - Gallaspy overall signals for horizontal left target motion | 162 |
| Figure 132 - BDWL comparison to lab test data for horizontal left target motion | 163 |
| Figure 133 - Ideal gyro model comparison to lab test data for horizontal left target motion | 164 |
| Figure 134 - Gallaspy comparison to lab test data for horizontal left target motion | 165 |
| Figure 135 - Overall lab test signals for vertical up target motion | 166 |
| Figure 136 - BDWL overall signals for vertical up target motion | 167 |
| Figure 137 - Ideal overall signals for vertical up target motion | 168 |
| Figure 138 - Gallaspy overall signals for vertical up target motion | 169 |
| Figure 139 - BDWL comparison to lab test data for vertical up target motion | 170 |
| Figure 140 - Ideal gyro model comparison to lab test data for vertical up target motion | 171 |
| Figure 141 - Gallaspy comparison to lab test data for vertical up target motion | 172 |
| Figure 142 - Overall signals for lab test vertical down target motion | 173 |
| Figure 143 - BDWL overall signals for vertical down target motion | 174 |
| Figure 144 - Ideal overall signals for vertical down target motion | 175 |
| Figure 145 - Gallaspy overall signals for vertical down target motion | 176 |
| Figure 146 - BDWL comparison to lab test data for vertical down target motion | 177 |

Figure 147 - Ideal gyro model comparison to lab test data for vertical down target motion 178

Figure 148 - Gallaspy comparison to lab test data for vertical down target motion 179

LIST OF TABLES

| | |
|--|-----|
| Table 1 - Gyro lab test signals relative phase angle data | 147 |
| Table 2 - Gyro model signals relative phase angle data | 148 |
| Table 3 - Signal comparison figure numbers | 148 |
| Table 4 - Model feature comparison | 181 |

LIST OF ABBREVIATIONS

| | |
|---------|---|
| cg | Center of gravity |
| Conscan | Conical Scan |
| EO | Electro-Optical |
| Gyro | Gyroscope |
| Hz | Hertz (cycles per second) |
| IR | Infrared |
| kg | Kilogram |
| LOS | Line-of-sight |
| m | Meter |
| MANPADS | Man-portable air defense missile system |
| N | Newton |

LIST OF SYMBOLS

\vec{V} - Vector quantities are denoted by arrows, or

$\{V\}_s$ - Vector quantities can also be denoted by brackets and a subscript for the reference frame, which is “s” in this case

{G} - Coordinate systems are denoted by a letter in brackets, which is the gyro coordinate system in this case

$\hat{i}, \hat{j}, \hat{k}$ - Unit vectors are vectors one unit in length

${}^sD^0$ - Direction cosine coordinate transformation matrix from the 0 coordinate system to the s coordinate system

${}^sD_{1,2}^0$ - Element from the first row, second column of the direction cosine transformation matrix from the 0 coordinate system to the s coordinate system

$s_q - \sin(\mathbf{q})$

$c_q - \cos(\mathbf{q})$

$t_q - \tan(\mathbf{q})$

$\frac{{}^l d}{dt}$ - Time derivative taken with respect to the l reference frame

\otimes - Vector cross product

\cdot - Vector dot product

$|\vec{R}|$ - Magnitude of vector R

$O[(x)^n]$ - A term not quantified, with magnitude on the order of x to the n power

1.0 Background on Electro-Optical/Infrared Guided Missiles

In recent years, there has been a great proliferation in small electro-optical/infrared (EO/IR) guided missile systems. These include air and ground launched anti-tank missiles, as well as anti-aircraft missiles.

This proliferation is attributed to the low cost, ease of use, and excellent combat record of these systems. Figures 1 through 3 depict examples of EO/IR missile systems.

Most EO/IR missile systems use some form of proportional navigation for



Figure 1 - Surface-to-air missile launch (19).

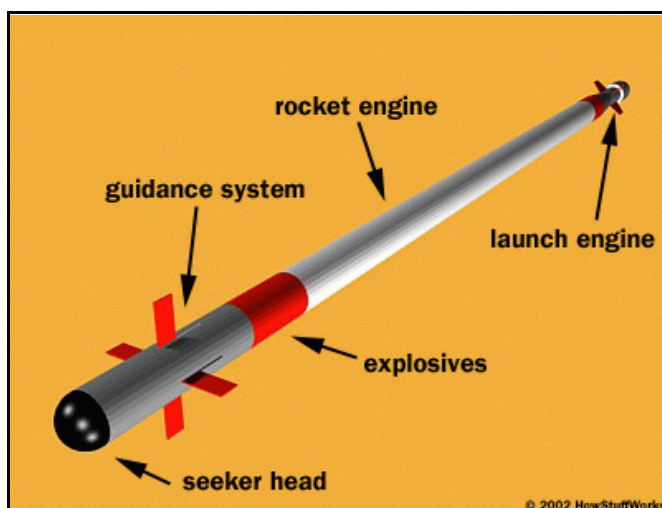


Figure 2 - Typical EO/IR missile system components (19).



Figure 3 - Air-to-ground EO/IR missile launch (20).

guidance (17). The proportional navigation guidance law is related to the constant bearing guidance law. This law states that two objects are on a collision course if the line-of-sight (LOS) angle between them (measured with respect to an inertial reference frame) remains constant.

Figure 4 shows missile and target geometry. For the constant bearing guidance law, the missile strives to keep \dot{g}_m constant. Proportional navigation guidance law is a modification of the constant bearing guidance law, stating that the missile inertial heading angular rate be proportional to the LOS inertial angular rate (17). Equation 1-1 illustrates the proportional navigation guidance law:

$$\dot{g}_m = N \cdot \dot{\gamma} \quad (1-1)$$

where \dot{g}_m = Inertial angular rate of the missile velocity vector

N = Proportional navigation constant, usually an integer

$\dot{\gamma}$ = Inertial angular rate of the missile-to-target line-of-sight vector.

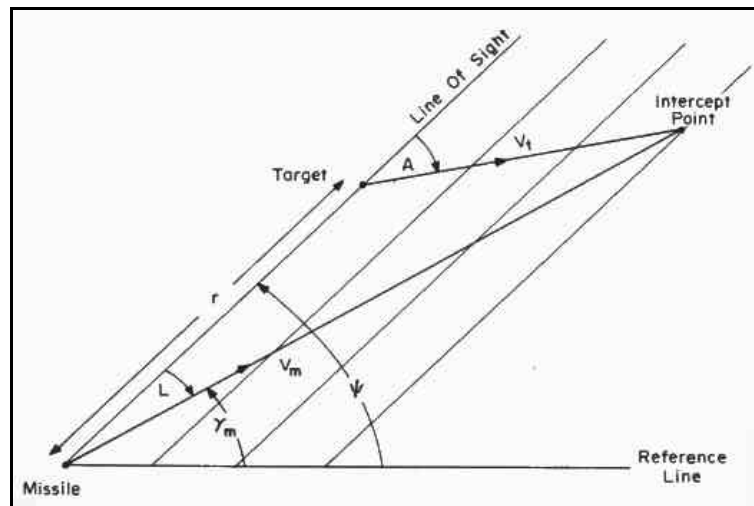


Figure 4 - Missile and target geometry for guidance law derivation (17).

In order to make an inertial LOS angle measurement, most EO/IR missiles incorporate a gyroscope (gyro) with their sensor and optics systems. The gyroscope provides this inertial reference. Also, the gyroscope is stabilized with respect to the missile body and is, thus, not affected by missile body motions, such as those from aerodynamic buffeting.

Without an inertial stabilization, the gimbaled EO/IR sensor would easily be pulled off of the target as a result of missile body motions.

These EO/IR missile seekers typically use a Cassegrain optical telescope (see Figures 5 and 6). For conical scan (conscan) seekers, one of the Cassegrain mirrors is canted with respect to

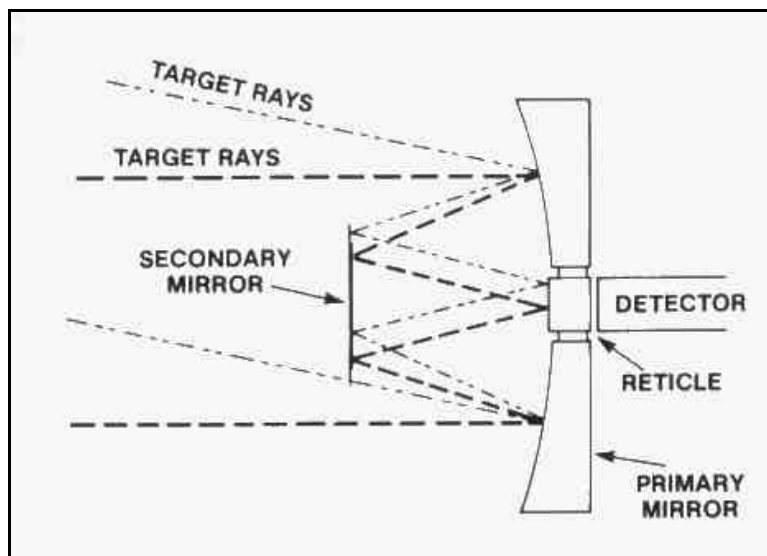


Figure 5 - Cassegrain telescope layout (15).

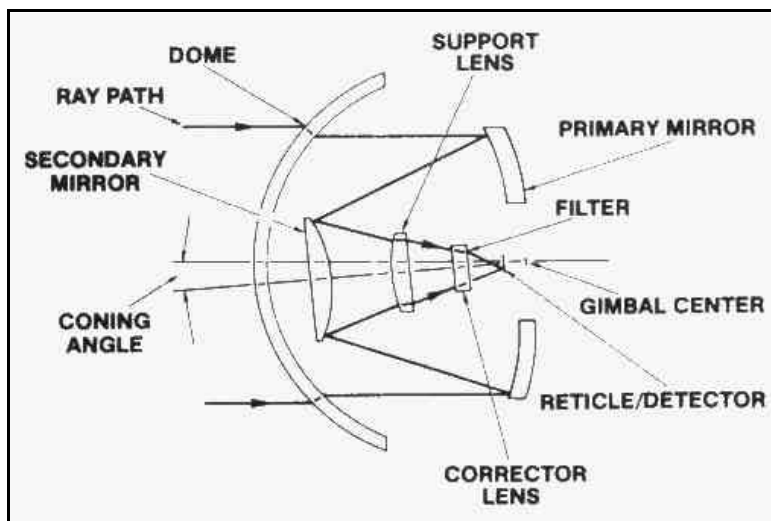


Figure 6 - More detailed Cassegrain telescope configuration for typical EO/IR missile system (15).

the other. This works with the seeker detector reticle mask to modulate the incoming EO/IR energy (see Figure 7).

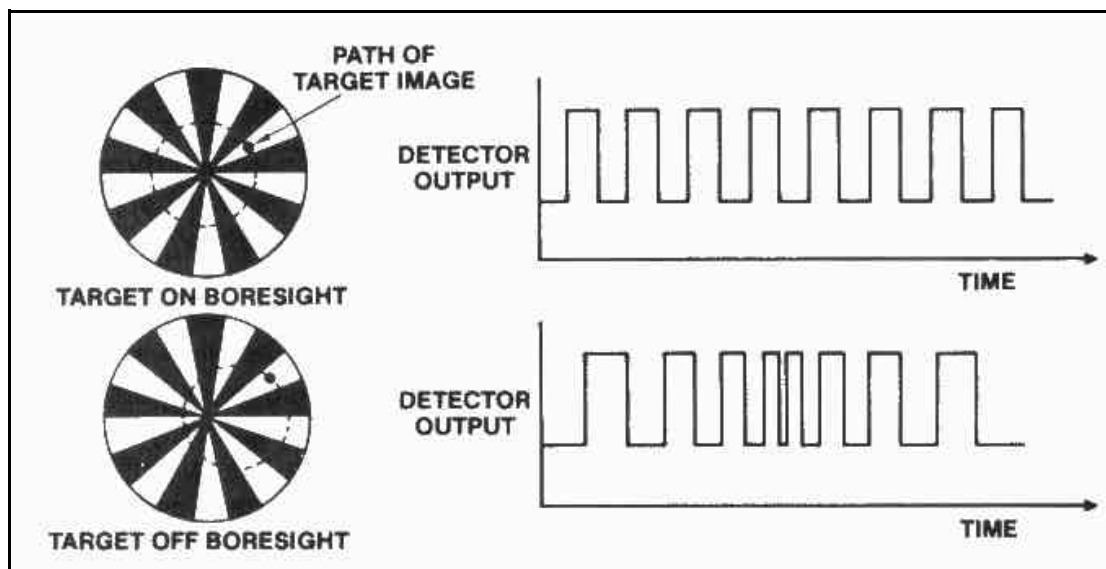


Figure 7 - Reticle tracking system theory of operation (15).

If a conscan seeker gyro is aimed directly at a point-sized EO/IR radiation source, the combination of gyro spin and the cant of one of the Cassegrain mirrors will cause the point source to trace a circle on the seeker reticle. The radius of the circle is proportional to the amount of angular misalignment of the Cassegrain mirrors. If there is a small error such that the gyro is not pointed directly at the point source, the circle will not be centered on the reticle. The magnitude of the difference between the reticle center and the point source center of rotation is proportional to the amount of angular error between the gyro look angle and the true LOS to the point source target.

In these systems, the gyro body itself is a permanent magnet. This is done so that wire coils embedded in the missile body can be used to control the

gyro and sense its angular position. The magnetic field of the spinning gyro cuts the sensor coils, inducing an electric current which is read to determine gyro position. A current is applied to the gyro precession (torque) coils which induces a magnetic field. This magnetic field interacts with the magnetic field of the gyro body to induce control torques on the gyro. Figure 8 shows the orientation of the gyro magnetic field; the gyro north pole is aligned with the gyro body-fixed Z_G axis.

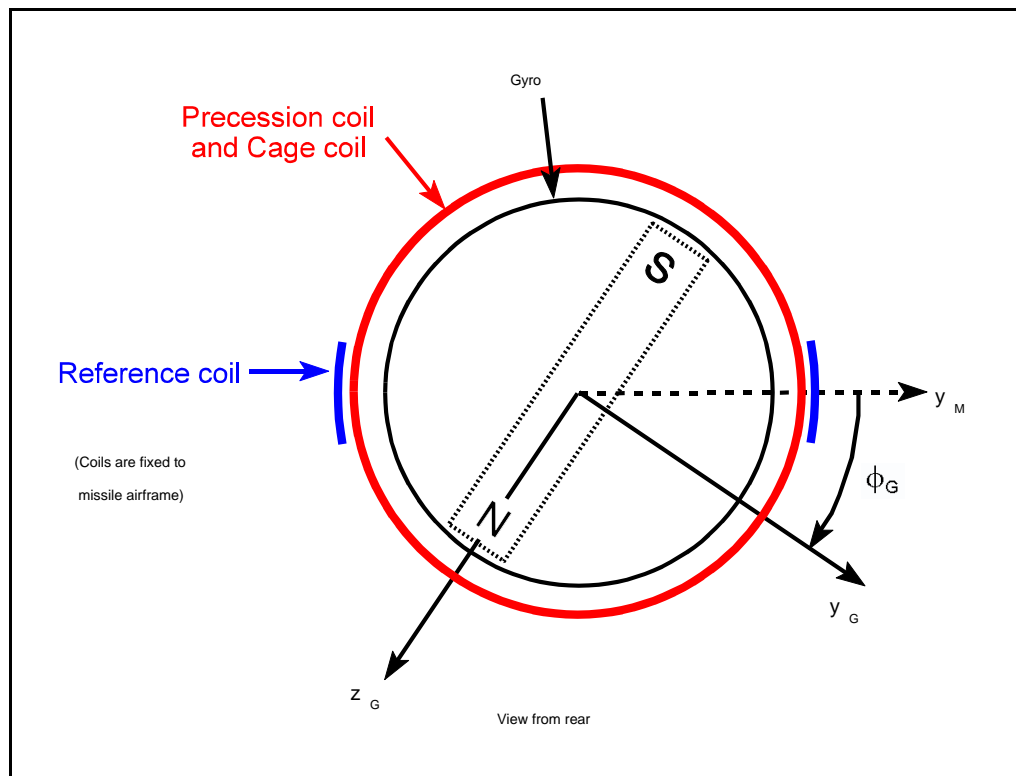


Figure 8 - Gyro magnetic field configuration.

Figure 9 depicts a gyro with Cassegrain optics attached and shows the configuration of the sensor and precession (control) coils. The reference coils are two “pancake” type coils placed on opposite sides of the missile body. As the gyro spins, the magnetic field of the gyro cuts these coils regardless of gyro

orientation. The resulting signal induced on the reference coils is a sinusoid at the relative gyro-to-missile body spin frequency.

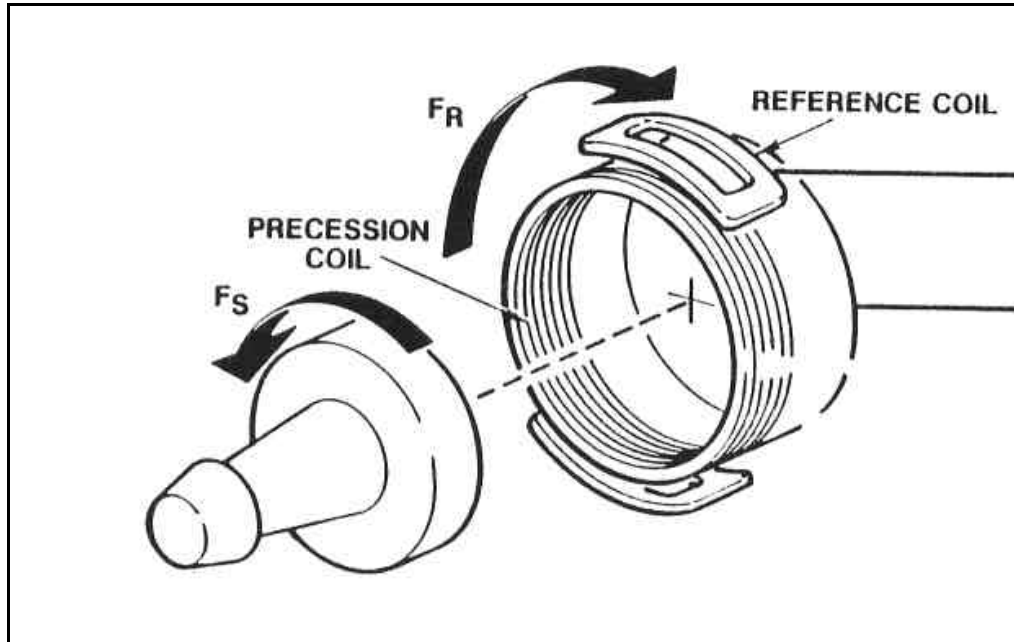


Figure 9 - Gyro coil diagram (14).

The cage coil sensor coils are wound circumferentially around the missile body, like the precession coils shown in Figure 9. If the gyro is angularly aligned with the missile body (boresighted), then no current is induced in the cage coil. As the gyro precesses off of missile boresight, the gyro magnetic field cuts the cage coils and induces a sinusoidal signal in the cage coils. The magnitude of this sinusoid is proportional to the gyro off-boresight angle (usually called lambda). The direction of gyro precession can be determined by comparing the relative phase difference between the reference coil signal and cage coil signal. Thus the missile seeker can determine the gyro angular position using the reference and cage coil signals.

The precession coils are used to control the gyro by magnetically inducing torques on the gyro. A current placed on the precession coils creates a magnetic field which is aligned with the missile body longitudinal axis (out the nose of the missile, also known as the missile body X_M axis). This magnetic field has either its north or its south pole pointing out the missile nose, depending on the direction of current flow in the precession coils. This induced magnetic field will induce a torque on the gyro by its interaction with the magnetic flux field of the spinning gyro.

Assuming that the gyro north pole is aligned with the gyro body-fixed $+Z_G$ axis (as shown in Figure 8), then the precession coil magnetic field will induce a torque on the gyro about the gyro body-fixed Y_G axis. The efficiency of the precession coils drops off as the gyro off-boresight angle increases. As the gyro precesses off of missile boresight, the induced precession torque has a component about the gyro body Y_G axis and a component about the gyro body X_G (spin) axis. The X_G component of this torque can affect the gyro spin rate, particularly at large off-boresight angles.

Some missiles spin up the gyroscope prior to missile launch, then let the gyro freely spin down during missile flight. This is acceptable, since the typical flight time for small EO/IR missiles is very short and the gyro will not spin down significantly in this short time. However, some missiles employ an on-board gyro spin drive. These spin drives use pancake type coils similar to the reference coils. A sinusoidal current is placed on the spin coils, which induces a magnetic field perpendicular to the missile body X_M axis. If this current is injected at the

gyro spin frequency, and is phased properly, it will create a torque about the gyro body X_G axis, which will control spin. As with the precession coils, the spin coils will also induce a precession torque on the gyro as the gyro moves off of missile boresight.

The gyro is an inertial device, due to its two-axis gimbal and the spinning mass of its rotor. The gyro rotor remains pointing in the same inertial direction, even if its outer gimbals are in motion. External torques applied to the gyro cause gyro angular motion (precession). The direction of this motion can be found by taking the cross product of the gyro spin vector and the torque vector (7, 25), using the right-hand rule. This motion can be thought of as the gyro trying to align its spin vector with the torque vector.

2.0 Coordinate System Definition

Before deriving gyro equations of motion, coordinate systems must be specified. The {I} coordinate system (x_I, y_I, z_I) is a right-handed coordinate system fixed in inertial space, with z_I positive down. It does not rotate with the gyro. The {M} coordinate system (x_M, y_M, z_M) is a right-handed coordinate system fixed in the missile body. The {G} coordinate system (x_G, y_G, z_G) is right-handed and fixed in the gyro.

There exists a set of Euler angles which describe the orientation of the gyro {G} coordinate system with respect to the inertial {I} coordinate system, $(\mathbf{y}_G, \mathbf{q}_G, \mathbf{f}_G)$. If these gyro Euler angles are all zero, the {G} coordinate system is aligned with the {I} coordinate system.

Similarly, there exists a set of Euler angles which describe the orientation of the missile body {M} coordinate system with respect to the inertial coordinate system, $(\mathbf{y}_M, \mathbf{q}_M, \mathbf{f}_M)$. If these missile Euler angles are all zero, the {M} coordinate system will be aligned with the {I} coordinate system. Similarly, there also exists a set of Euler angles which describe the orientation of the gyro {G} with respect to the missile {M}. These are the “gyro-with-respect-to-the-missile” Euler angles, $(\mathbf{y}_{GM}, \mathbf{q}_{GM}, \mathbf{f}_{GM})$.

The x_M axis points out the nose of the missile; the y_M axis points out the right side of the missile (see Figure 10). The {G} coordinate system is fixed in the gyro and spins with it. The x_G axis is aligned with the gyro pointing direction, the z_G axis is fixed in the direction of the gyro north pole (see Figure 11).

All Euler angles are defined as “3-2-1” body-based coordinate system rotations to get from a “space” coordinate system (like the missile body-fixed $\{M\}$ coordinate system or the inertial $\{I\}$ coordinate system) to a “body” coordinate system (like the gyro body fixed $\{G\}$ coordinate system).

A body 3-2-1 coordinate transformation defines the series of angular rotations that transform one coordinate system to another. The first angular rotation is done about the third space based axis (Z). Next the second rotation is done about the second axis (Y) of the coordinate system resulting from the first rotation. The final angular rotation is done about the first axis (X) of the coordinate system resulting from the first two rotations. This is the standard definition of Euler angles.

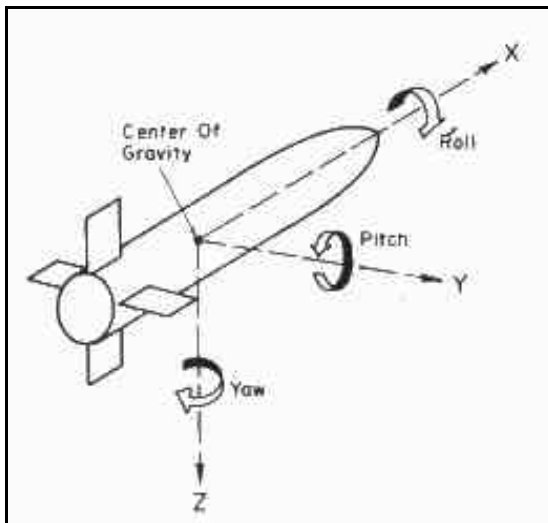


Figure 10 - Missile body-fixed coordinate system (16).

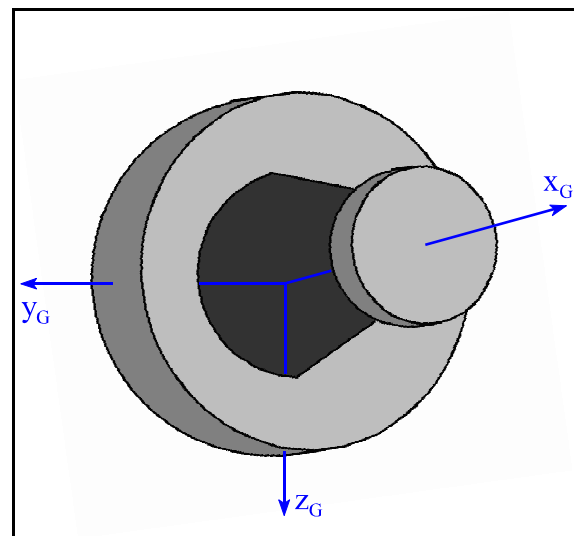


Figure 11 - Gyro body-fixed coordinate system.

Figures 12 through 14 depict the body 3-2-1 Euler angle rotations. In these figures, the initial coordinate system is labeled as $\{0\}$. This could

represent either the inertial $\{I\}$ or missile $\{M\}$ coordinate system. The $\{1\}$ coordinate system results after the yaw rotation about the z_0 axis. The gyro yaw angle is ψ , which represents a positive rotation about the z_0 axis. The z_1 axis is, therefore, identical to the z_0 axis.

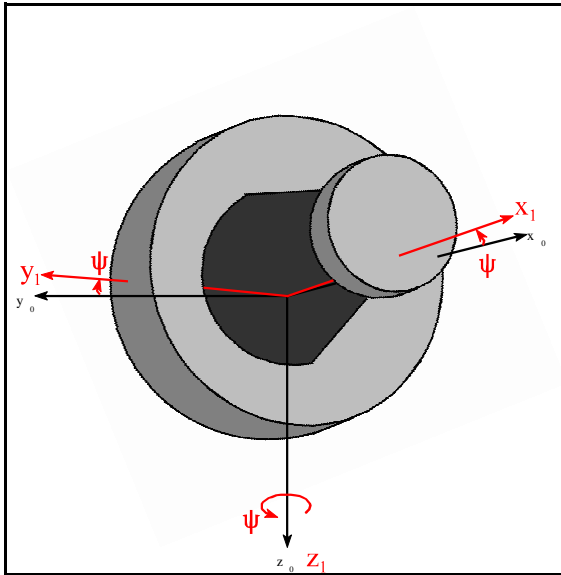


Figure 12 - Yaw rotation.

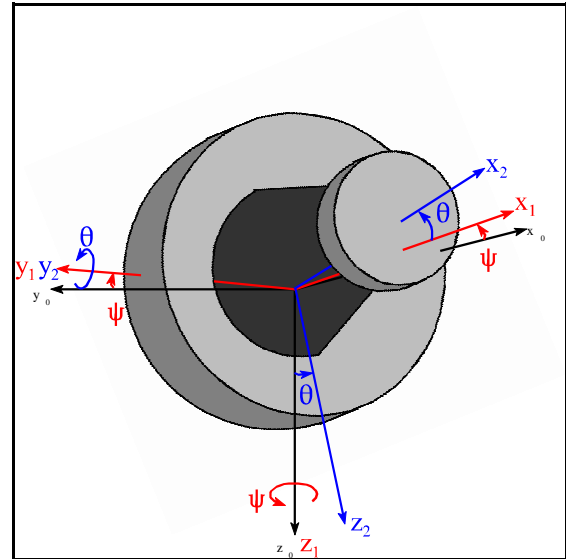


Figure 13 - Pitch rotation.

Next is a pitch rotation about the y_1 axis which produces the $\{2\}$ coordinate system. The pitch angle is θ , which represents a positive rotation about the y_1 axis. Thus, the y_1 and y_2 axes are identical. The $\{G\}$ coordinate system results after rotation of the $\{2\}$ coordinate system through the gyro spin angle of ϕ ; ϕ is a positive

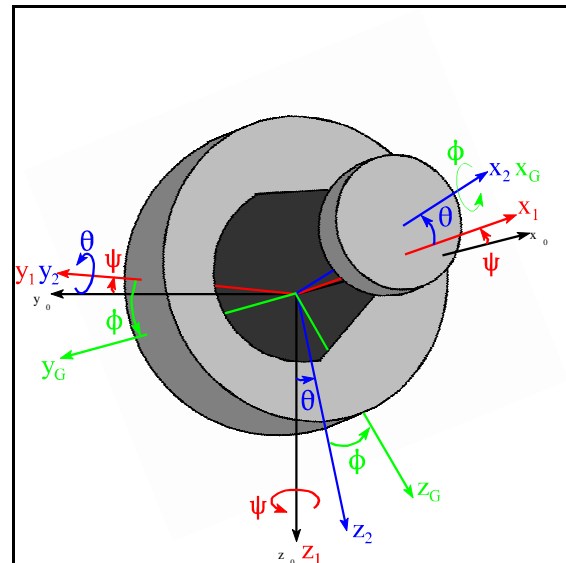


Figure 14 - Roll rotation.

rotation about the x_2 axis. If the gyro spin rate is constant, then the angle f is equal to the gyro spin rate times time ($\boldsymbol{w}_s \cdot t$).

2.1 Direction Cosine Coordinate Transformation Matrix Definition

Next, these coordinate system rotations were used to derive the direction cosine coordinate transformation matrices from the {0} to the {G} coordinate system. Recall that the {0} coordinate system represents a starting coordinate system, and could be either the inertial {I} or the missile {M} coordinate system. Also note that these coordinate system transformations can also be used with the inertial {I} to the missile body {M} Euler angles.

By definition, the determinate of a direction cosine matrix is equal to one. Thus, the inverse of a direction cosine matrix is merely its transposition (18). This makes it very easy to find direction cosine matrices both to and from two coordinate systems. For example, if one knows the {I} to {G} direction cosine, the {G} to {I} direction cosine is merely its inverse, which is its transpose.

Figures 15 through 17 and Equations 2-1 through 2-21 show the derivation of the individual yaw, pitch, and roll direction cosine coordinate transformation matrices.

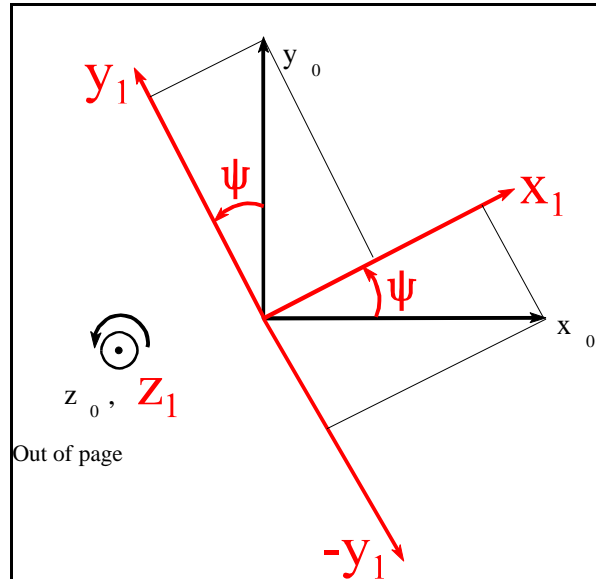


Figure 15 - Yaw rotation.

$$x_0 = \cos(\mathbf{y}) \cdot x_1 - \sin(\mathbf{y}) \cdot y_1 \quad (2-1)$$

$$y_0 = \sin(\mathbf{y}) \cdot x_1 + \cos(\mathbf{y}) \cdot y_1 \quad (2-2)$$

$$z_0 = z_1 \quad (2-3)$$

$$\begin{Bmatrix} x_0 \\ y_0 \\ z_0 \end{Bmatrix} = \begin{bmatrix} \cos(\mathbf{y}) & -\sin(\mathbf{y}) & 0 \\ \sin(\mathbf{y}) & \cos(\mathbf{y}) & 0 \\ 0 & 0 & 1 \end{bmatrix} \begin{Bmatrix} x_1 \\ y_1 \\ z_1 \end{Bmatrix} \quad (2-4)$$

$$\{p\}_0 = {}^0D^1 \cdot \{p\}_1 \quad (2-5)$$

Taking the inverse of this direction cosine (merely its transpose) yields:

$$\begin{Bmatrix} x_1 \\ y_1 \\ z_1 \end{Bmatrix} = \begin{bmatrix} \cos(\mathbf{y}) & \sin(\mathbf{y}) & 0 \\ -\sin(\mathbf{y}) & \cos(\mathbf{y}) & 0 \\ 0 & 0 & 1 \end{bmatrix} \begin{Bmatrix} x_0 \\ y_0 \\ z_0 \end{Bmatrix} \quad (2-6)$$

$$\{p\}_1 = {}^1D^0 \cdot \{p\}_0 = [{}^1D^0]^{-1} \cdot \{p\}_0 \quad (2-7)$$

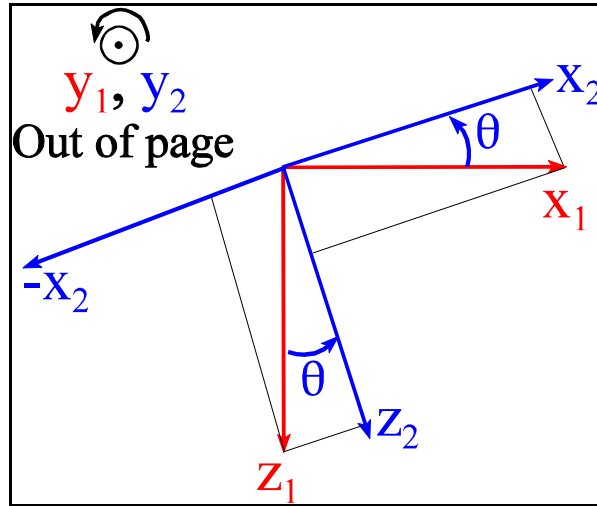


Figure 16 - Pitch rotation.

$$x_1 = \cos(\mathbf{q}) \cdot x_2 + \sin(\mathbf{q}) \cdot z_2 \quad (2-8)$$

$$y_1 = y_2 \quad (2-9)$$

$$z_1 = -\sin(\mathbf{q}) \cdot x_2 + \cos(\mathbf{q}) \cdot z_2 \quad (2-10)$$

$$\begin{Bmatrix} x_1 \\ y_1 \\ z_1 \end{Bmatrix} = \begin{bmatrix} \cos(\mathbf{q}) & 0 & \sin(\mathbf{q}) \\ 0 & 1 & 0 \\ -\sin(\mathbf{q}) & 0 & \cos(\mathbf{q}) \end{bmatrix} \begin{Bmatrix} x_2 \\ y_2 \\ z_2 \end{Bmatrix} \quad (2-11)$$

$$\{p\}_1 = {}^1D^2 \cdot \{p\}_2 \quad (2-12)$$

As before, taking the inverse of this direction cosine yields:

$$\begin{Bmatrix} x_2 \\ y_2 \\ z_2 \end{Bmatrix} = \begin{bmatrix} \cos(\mathbf{q}) & 0 & -\sin(\mathbf{q}) \\ 0 & 1 & 0 \\ \sin(\mathbf{q}) & 0 & \cos(\mathbf{q}) \end{bmatrix} \begin{Bmatrix} x_1 \\ y_1 \\ z_1 \end{Bmatrix} \quad (2-13)$$

$$\{p\}_2 = {}^2D^1 \cdot \{p\}_1 = [{}^2D^1]^{-1} \cdot \{p\}_1 \quad (2-14)$$

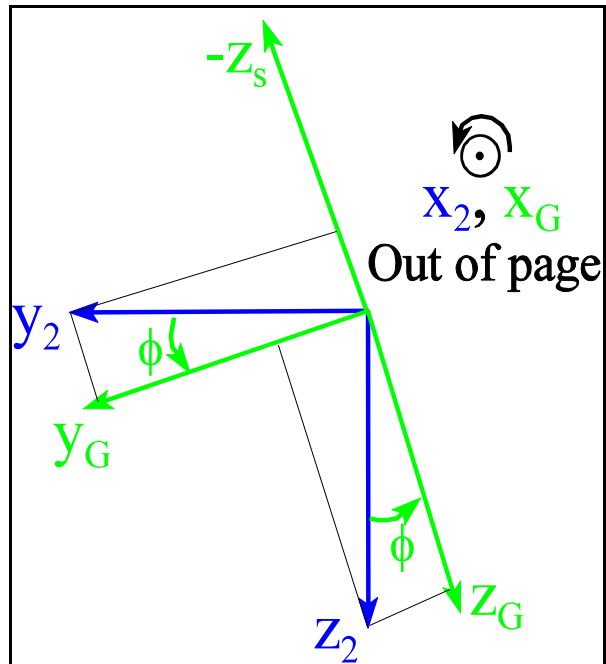


Figure 17 - Gyro spin rotation.

$$x_2 = x_G \quad (2-15)$$

$$y_2 = \cos(\mathbf{f}) \cdot y_G - \sin(\mathbf{f}) \cdot z_G \quad (2-16)$$

$$z_2 = \sin(\mathbf{f}) \cdot y_G + \cos(\mathbf{f}) \cdot z_G \quad (2-17)$$

$$\begin{Bmatrix} x_2 \\ y_2 \\ z_2 \end{Bmatrix} = \begin{bmatrix} 1 & 0 & 0 \\ 0 & \cos(\mathbf{f}) & -\sin(\mathbf{f}) \\ 0 & \sin(\mathbf{f}) & \cos(\mathbf{f}) \end{bmatrix} \begin{Bmatrix} x_G \\ y_G \\ z_G \end{Bmatrix} \quad (2-18)$$

$$\{p\}_2 = {}^2D^G \cdot \{p\}_G \quad (2-19)$$

Again, the corresponding direction cosine can be found by taking the inverse:

$$\begin{Bmatrix} x_G \\ y_G \\ z_G \end{Bmatrix} = \begin{bmatrix} 1 & 0 & 0 \\ 0 & \cos(\mathbf{f}) & \sin(\mathbf{f}) \\ 0 & -\sin(\mathbf{f}) & \cos(\mathbf{f}) \end{bmatrix} \begin{Bmatrix} x_2 \\ y_2 \\ z_2 \end{Bmatrix} \quad (2-20)$$

$$\{p\}_G = {}^G D^2 \cdot \{p\}_2 = [{}^G D^2]^{-1} \cdot \{p\}_2 \quad (2-21)$$

Direction cosine matrices can be multiplied together to get conglomerate direction cosine matrices. For example, the non-rolling gyro to missile direction cosine would be:

$${}^M D^2 = {}^M D^{1,1} \cdot D^2 \quad (2-22)$$

Note that when multiplying direction cosine matrices, the inner superscripts must match, then they cancel. Multiplying these matrices,

$${}^M D^2 = \begin{bmatrix} \cos(\mathbf{y}_{GM}) & -\sin(\mathbf{y}_{GM}) & 0 \\ \sin(\mathbf{y}_{GM}) & \cos(\mathbf{y}_{GM}) & 0 \\ 0 & 0 & 1 \end{bmatrix} \cdot \begin{bmatrix} \cos(\mathbf{q}_{GM}) & 0 & \sin(\mathbf{q}_{GM}) \\ 0 & 1 & 0 \\ -\sin(\mathbf{q}_{GM}) & 0 & \cos(\mathbf{q}_{GM}) \end{bmatrix} \quad (2-23)$$

$${}^M D^2 = \begin{bmatrix} \cos(\mathbf{y}_{GM})\cos(\mathbf{q}_{GM}) & -\sin(\mathbf{y}_{GM}) & \cos(\mathbf{y}_{GM})\sin(\mathbf{q}_{GM}) \\ \sin(\mathbf{y}_{GM})\cos(\mathbf{q}_{GM}) & \cos(\mathbf{y}_{GM}) & \sin(\mathbf{y}_{GM})\sin(\mathbf{q}_{GM}) \\ -\sin(\mathbf{q}_{GM}) & 0 & \cos(\mathbf{q}_{GM}) \end{bmatrix} \quad (2-24)$$

In order to calculate the direction cosine matrix from the gyro-fixed {G} coordinate system to the missile {M} coordinate system, one must multiply three individual direction cosines. These type of matrices can get very large, so a short-hand was used to denote the trigonometric functions. Sin, cos, and tan will be denoted by their first letter (s, c, t) with a subscript to represent the angle variable. The full gyro-to-missile direction cosine is calculated as follows:

$${}^M D^G = {}^M D^{1,1} \cdot D^{2,2} \cdot D^G \quad (2-25)$$

$${}^M D^G = \begin{bmatrix} c_{y_{GM}} & s_{y_{GM}} & 0 \\ s_{y_{GM}} & c_{y_{GM}} & 0 \\ 0 & 0 & 1 \end{bmatrix} \cdot \begin{bmatrix} c_{q_{GM}} & 0 & s_{q_{GM}} \\ 0 & 1 & 0 \\ -s_{q_{GM}} & 0 & c_{q_{GM}} \end{bmatrix} \cdot \begin{bmatrix} 1 & 0 & 0 \\ 0 & c_{f_{GM}} & -s_{f_{GM}} \\ 0 & s_{f_{GM}} & c_{f_{GM}} \end{bmatrix} \quad (2-26)$$

$${}^M D^G = \begin{bmatrix} c_{y_{GM}} c_{q_{GM}} & -s_{y_{GM}} c_{f_{GM}} + c_{y_{GM}} s_{q_{GM}} s_{f_{GM}} & s_{y_{GM}} s_{f_{GM}} + c_{y_{GM}} s_{q_{GM}} c_{f_{GM}} \\ s_{y_{GM}} c_{q_{GM}} & c_{y_{GM}} c_{f_{GM}} + s_{y_{GM}} s_{q_{GM}} s_{f_{GM}} & -c_{y_{GM}} s_{f_{GM}} + s_{y_{GM}} s_{q_{GM}} c_{f_{GM}} \\ -s_{q_{GM}} & c_{q_{GM}} s_{f_{GM}} & c_{q_{GM}} c_{f_{GM}} \end{bmatrix} \quad (2-27)$$

Note that the determinate of a direction cosine is equal to one by definition.

Therefore, the inverse of a direction cosine is merely its transpose. This makes it very easy to find the direction cosine from the missile {M} coordinate system to the gyro {G} coordinate system, which is merely the transpose of gyro-to-missile direction cosine matrix. The gyro-to-missile direction cosine matrix was verified with Kane, Likins, and Levinson (5).

3.0 Derivation of Brown/Dougherty/Williams/Lamm Gyro Model

The gyro model presented in this section is based on previous work by four individuals: James Brown (3), Terry Dougherty (1), David Williams (9, 10, and 11), and Darrell Lamm (13 and 19). This gyro model will be referred to as the “BDWL” gyro model, since it is based on work by Brown, Dougherty,

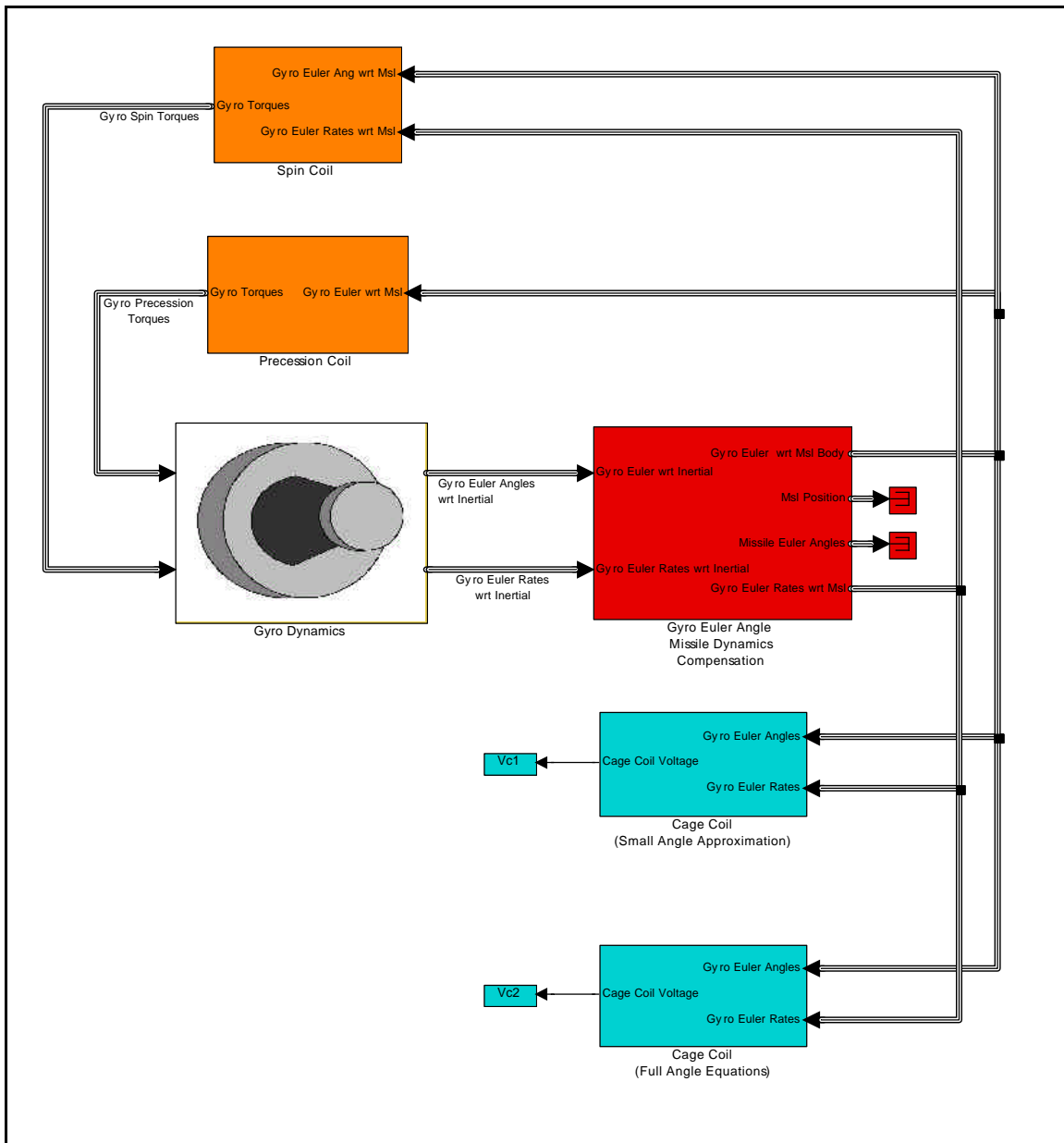


Figure 18 - Top level of BDWL gyro model.

Williams, and Lamm. The work of Wu (4) and White (8) form the historical basis for this model. Figure 18 shows the top level of the BDWL gyro model. The derivation of each block in Figure 18 will be discussed in the following sections.

3.1 Equations of Motion / Gyro Dynamics Derivation

The rotational kinematic equations of motion for this gyroscope model start with the rotational version of Newton's 2nd Law, which states that the summation of the torques on a rigid body is equal to the time derivative of the angular momentum in the inertial frame:

$$\sum \vec{\tau} = \frac{d\vec{H}}{dt} \quad (3-1)$$

$$\vec{H} = I\vec{\omega} \quad (3-2)$$

where,

$$\vec{\tau} = \text{Torques} \quad (3-3)$$

$$\vec{H} = \text{Angular momentum about gyro center of gravity}, \quad (3-4)$$

$$I = \begin{bmatrix} I_{xx} & I_{xy} & I_{xz} \\ I_{yx} & I_{yy} & I_{yz} \\ I_{zx} & I_{zy} & I_{zz} \end{bmatrix} = \text{Moment of inertia matrix}, \quad (3-5)$$

and $\vec{\omega} = \text{Gyro angular velocity} \quad (3-6)$

It is convenient to write the moment of inertia matrix with respect to a gyro body-fixed coordinate system. If this is not done, the moments of inertia can change with time and make the calculation of the angular momentum derivative

much more complex. Further, if one picks a gyro body-fixed coordinate system that is aligned with the body symmetry of the gyro, the products of inertia (I_{xy} , I_{yz} , I_{zx} , ...) equal zero. This is the rationale for choosing the gyro body fixed {G} coordinate system previously described, with the x_G axis out the face of the gyro. The z_G axis is aligned with the gyro magnetic north pole, and y_G is perpendicular to x_G and z_G such that $x_G \otimes y_G = z_G$ (see Figure 11). Finally, the gyro body-fixed coordinate system should be centered at the gyro center of gravity, which is its center of rotation and the center of its gimbal axes. Thus,

$$I = \begin{bmatrix} I_{xx} & 0 & 0 \\ 0 & I_{yy} & 0 \\ 0 & 0 & I_{zz} \end{bmatrix} \quad (3-7)$$

$$I_{xx} = I_s = \text{Gyro Spin Axis Inertia} \quad (3-8)$$

$$I_{yy} = I_{zz} = I_t = \text{Gyro Transverse Axis Inertia} \quad (3-9)$$

$$\vec{w} = w_x \hat{i}_G + w_y \hat{j}_G + w_z \hat{k}_G \quad (3-10)$$

$$\vec{H} = \begin{bmatrix} I_s & 0 & 0 \\ 0 & I_t & 0 \\ 0 & 0 & I_t \end{bmatrix} \begin{Bmatrix} w_x \\ w_y \\ w_z \end{Bmatrix}_G \quad (3-11)$$

$$\vec{H} = I_s w_x \hat{i}_G + I_t w_y \hat{j}_G + I_t w_z \hat{k}_G \quad (3-12)$$

Note that here \vec{w} represents the gyro angular rate measured with respect to the inertial coordinate system, but expressed in the gyro body-fixed {G} coordinate system. This is quite different than the gyro angular rate measured in the gyro

body-fixed coordinate system. If one measures the gyro angular rates in the {G} coordinate system, it would be zero since the gyro body-fixed coordinate system always moves with the gyro. The {G} coordinate system is moving and, thus, is non-inertial. Also, note that since the {G} coordinate system is fixed in the gyro, $\vec{\omega}$ is also the angular rate of the {G} coordinate system with respect to the inertial system. Thus, from Greenwood (2):

$$\frac{{}^I d\vec{H}}{dt} = \frac{{}^G d\vec{H}}{dt} + \vec{\omega} \otimes \vec{H} \quad (3-13)$$

$$\frac{{}^G d\vec{H}}{dt} = I_s \dot{\omega}_x \hat{i}_G + I_t \dot{\omega}_y \hat{j}_G + I_t \dot{\omega}_z \hat{k}_G \quad (3-14)$$

$$\vec{\omega} \otimes \vec{H} = \begin{vmatrix} \hat{i}_G & \hat{j}_G & \hat{k}_G \\ \mathbf{w}_x & \mathbf{w}_y & \mathbf{w}_z \\ I_s \mathbf{w}_x & I_t \mathbf{w}_y & I_t \mathbf{w}_z \end{vmatrix} \quad (3-15)$$

$$\vec{\omega} \otimes \vec{H} = (I_s - I_t) \mathbf{w}_x \mathbf{w}_z \hat{j}_G - (I_s - I_t) \mathbf{w}_x \mathbf{w}_y \hat{k}_G \quad (3-16)$$

Combining Equations 3-1, 3-13, 3-14, and 3-16:

$$\begin{Bmatrix} \mathbf{t}_x \\ \mathbf{t}_y \\ \mathbf{t}_z \end{Bmatrix}_G = \begin{Bmatrix} I_s \dot{\omega}_x \\ I_t \dot{\omega}_y + (I_s - I_t) \mathbf{w}_x \mathbf{w}_z \\ I_t \dot{\omega}_z - (I_s - I_t) \mathbf{w}_x \mathbf{w}_y \end{Bmatrix}_G \quad (3-17)$$

Note that the gyro torques are expressed with respect to the gyro body-fixed coordinate system. Thus, \mathbf{t}_x points in the x_G direction; \mathbf{t}_z points in the direction of the gyro magnetic north pole. Magnetic precession torques can only be

induced about the y_G axis. Thus, \mathbf{t}_z is zero by definition. Magnetic spin torques are induced about the x_G axis.

Most EO/IR missile seeker gyroscopes incorporate some type of nutation damping. Nutation consists of undesirable gyro motions perpendicular to desired direction of motion (precession). Nutation is explained in more detail in Section 6. In some systems, the nutation damper is a sealed radial groove inside the gyro, which is filled with liquid mercury. The liquid mercury provides the damping. Other systems use electronic nutation damping. The damping torque opposes the precession torque and is approximately proportional to the angular velocity in the y_G and z_G axes as follows:

$$\mathbf{t}_{yD} = -K_D \mathbf{w}_y \quad (3-18)$$

$$\mathbf{t}_{zD} = -K_D \mathbf{w}_z \quad (3-19)$$

where K_D is a constant damping coefficient. Incorporating these terms into equation 3-17 yields:

$$\begin{Bmatrix} \mathbf{t}_x \\ \mathbf{t}_y - K_D \mathbf{w}_y \\ \mathbf{t}_z - K_D \mathbf{w}_z \end{Bmatrix}_G = \begin{Bmatrix} I_s \dot{\mathbf{w}}_x \\ I_t \dot{\mathbf{w}}_y + (I_s - I_t) \mathbf{w}_x \mathbf{w}_z \\ I_t \dot{\mathbf{w}}_z - (I_s - I_t) \mathbf{w}_x \mathbf{w}_y \end{Bmatrix}_G \quad (3-20)$$

Solving each term for the derivative of angular velocity yields:

$$\begin{Bmatrix} \dot{\mathbf{w}}_x \\ \dot{\mathbf{w}}_y \\ \dot{\mathbf{w}}_z \end{Bmatrix}_G = \begin{Bmatrix} \mathbf{t}_x / I_s \\ \left[\mathbf{t}_y - K_D \mathbf{w}_y + (I_t - I_s) \mathbf{w}_x \mathbf{w}_z \right] / I_t \\ \left[\mathbf{t}_z - K_D \mathbf{w}_z - (I_t - I_s) \mathbf{w}_x \mathbf{w}_y \right] / I_t \end{Bmatrix}_G \quad (3-21)$$

These equations are implemented in the BDWL model in the “gyro angular velocities” block shown in Figure 19.

Note from Figure 19 that the gyro spin can be switched between a perfect spin frequency and an actual spin torque controller. The gyro angular velocity block is contained in the gyro dynamics block, which is shown in Figure 20.

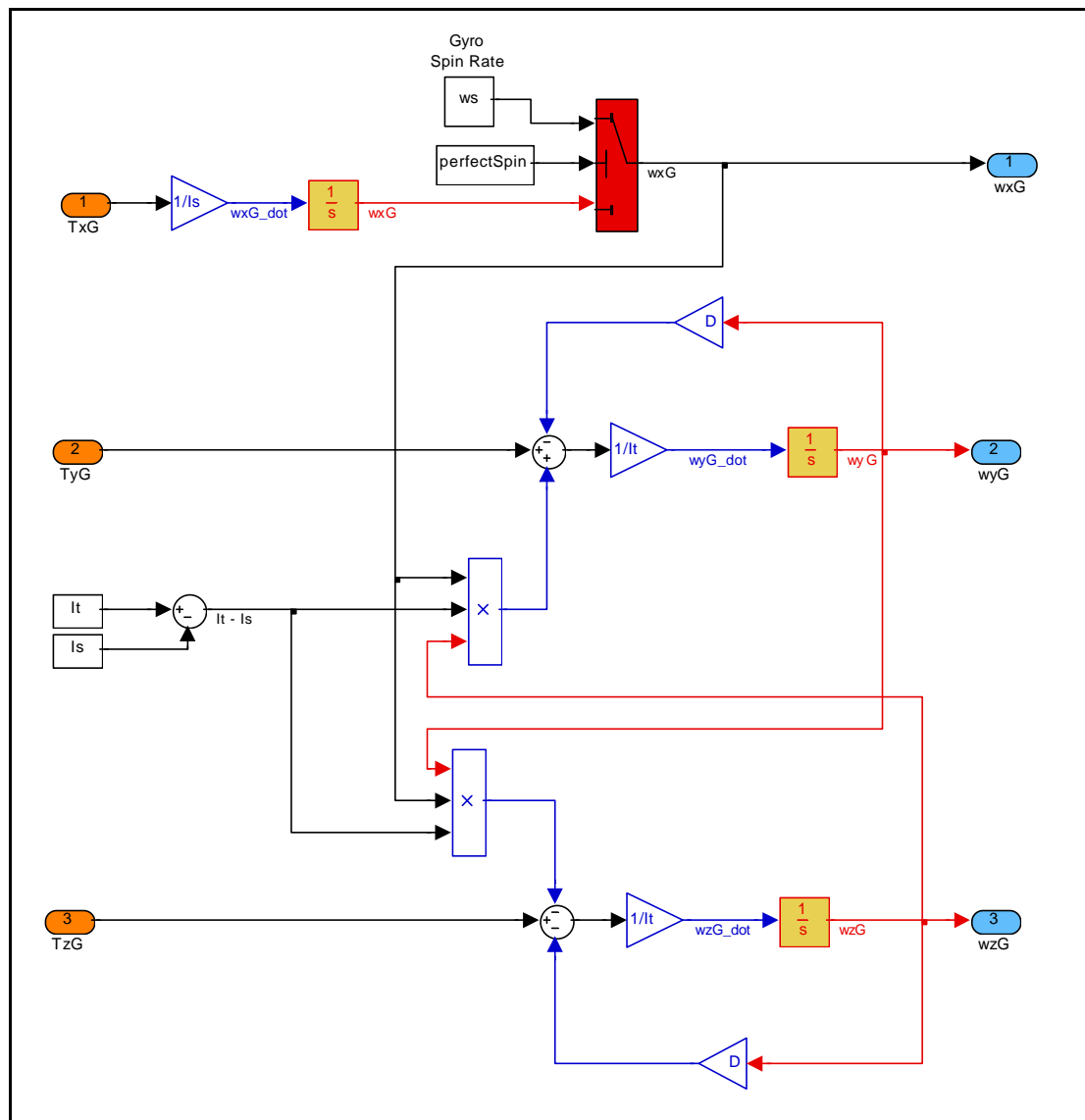


Figure 19 - BDWL model gyro angular velocity block.

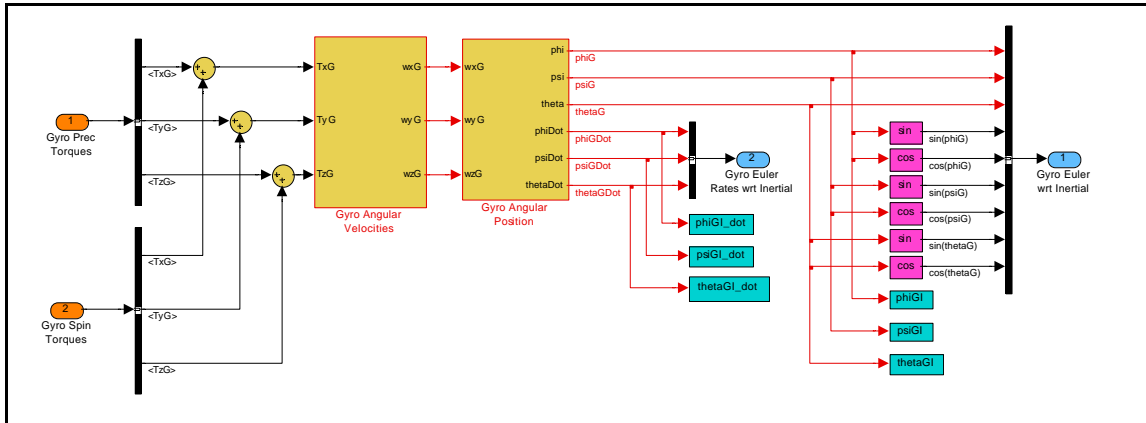


Figure 20 - BDWL model gyro dynamics block.

The gyro angular position block takes the gyro angular velocities and calculates the gyro position, expressed in Euler angles. Note that the gyro Euler angles and their sines and cosines are put on the “gyro Euler with-respect-to inertial” bus. The sines and cosines are included as a means of making the model execute faster. Previously, only the gyro Euler angles were passed between Simulink subsystems. It was discovered that the sines and cosines of these angles were being calculated at multiple locations in the model. Calculating them once and sending them on the Euler angle bus increases execution speed.

The gyro Euler angles are calculated from the angular velocities based on equations from Lamm (13). The relationship between the Euler angle rates and gyro angular velocity can be derived as follows: First, define the gyro angular velocity vector as:

$$\vec{W} = \begin{Bmatrix} W_x \\ W_y \\ W_z \end{Bmatrix}_G \quad (3-22)$$

Note that this vector is expressed in the gyro body-fixed coordinate system. This is where the gyro angular velocities are calculated. Next, it is assumed that the gyro angular velocity can totally be described by the Euler angular rates:

$$\vec{w} = [\dot{\mathbf{y}}] + [\dot{\mathbf{q}}] + [\dot{\mathbf{f}}] \quad (3-23)$$

From the definition of Euler angles (body 3-2-1 rotation), it is found that:

$$\vec{y} = \dot{\mathbf{y}} \cdot \hat{z}_1 = \begin{Bmatrix} 0 \\ 0 \\ \dot{\mathbf{y}} \end{Bmatrix}_1 \quad (3-24)$$

$$\vec{q} = \dot{\mathbf{q}} \cdot \hat{y}_2 = \begin{Bmatrix} 0 \\ \dot{\mathbf{q}} \\ 0 \end{Bmatrix}_2 \quad (3-25)$$

$$\vec{f} = \dot{\mathbf{f}} \cdot \hat{x}_G = \begin{Bmatrix} \dot{\mathbf{f}} \\ 0 \\ 0 \end{Bmatrix}_G \quad (3-26)$$

Each of these Euler angular rates must be transformed into the gyro body-fixed {G} coordinate system. The direction cosine matrices derived earlier in section 2 will be used here:

$$\left\{ \vec{y} \right\}_G = {}^G D^2 \cdot {}^2 D^1 \cdot \left\{ \vec{y} \right\}_1 = \begin{bmatrix} 1 & 0 & 0 \\ 0 & c_f & s_f \\ 0 & -s_f & c_f \end{bmatrix} \cdot \begin{bmatrix} c_q & 0 & -s_q \\ 0 & 1 & 0 \\ s_q & 0 & c_q \end{bmatrix} \cdot \begin{Bmatrix} 0 \\ 0 \\ \dot{\mathbf{y}} \end{Bmatrix}_1 = \begin{Bmatrix} -s_q \dot{\mathbf{y}} \\ c_q s_f \dot{\mathbf{y}} \\ c_q c_f \dot{\mathbf{y}} \end{Bmatrix}_G \quad (3-27)$$

$$\left\{ \vec{q} \right\}_G = {}^G D^2 \cdot \left\{ \vec{q} \right\}_2 = \begin{bmatrix} 1 & 0 & 0 \\ 0 & c_f & s_f \\ 0 & -s_f & c_f \end{bmatrix} \cdot \begin{Bmatrix} 0 \\ \dot{\mathbf{q}} \\ 0 \end{Bmatrix}_2 = \begin{Bmatrix} 0 \\ c_f \dot{\mathbf{q}} \\ -s_f \dot{\mathbf{q}} \end{Bmatrix}_G \quad (3-28)$$

$$\left\{ \vec{\dot{\mathbf{f}}} \right\}_G = \begin{Bmatrix} \dot{\mathbf{f}} \\ 0 \\ 0 \end{Bmatrix}_G \quad (3-29)$$

Summing,

$$\left\{ \vec{\mathbf{w}} \right\}_G = \left\{ \vec{\mathbf{y}} \right\}_G + \left\{ \vec{\mathbf{q}} \right\}_G + \left\{ \vec{\dot{\mathbf{f}}} \right\}_G = \begin{Bmatrix} \dot{\mathbf{f}} - s_q \dot{\mathbf{y}} \\ c_q s_f \dot{\mathbf{y}} + c_f \dot{\mathbf{q}} \\ c_q c_f \dot{\mathbf{y}} - s_f \dot{\mathbf{q}} \end{Bmatrix}_G = \begin{Bmatrix} \mathbf{w}_x \\ \mathbf{w}_y \\ \mathbf{w}_z \end{Bmatrix}_G \quad (3-30)$$

Solving for the Euler angular rates,

$$\dot{\mathbf{y}} = (\mathbf{w}_y \sin(\mathbf{f}_G) + \mathbf{w}_z \cos(\mathbf{f}_G)) / \cos(\mathbf{q}_G) \quad (3-31)$$

$$\dot{\mathbf{q}} = \mathbf{w}_y \cos(\mathbf{f}_G) - \mathbf{w}_z \sin(\mathbf{f}_G) \quad (3-32)$$

$$\mathbf{j} = \mathbf{w}_x + (\mathbf{w}_y \sin(\mathbf{f}_G) + \mathbf{w}_z \cos(\mathbf{f}_G)) \tan(\mathbf{q}) \quad (3-33)$$

Figure 21 shows the Simulink implementation of these Euler angle equations.

Note that these angular velocities and Euler angles are with respect to the inertial coordinate system.

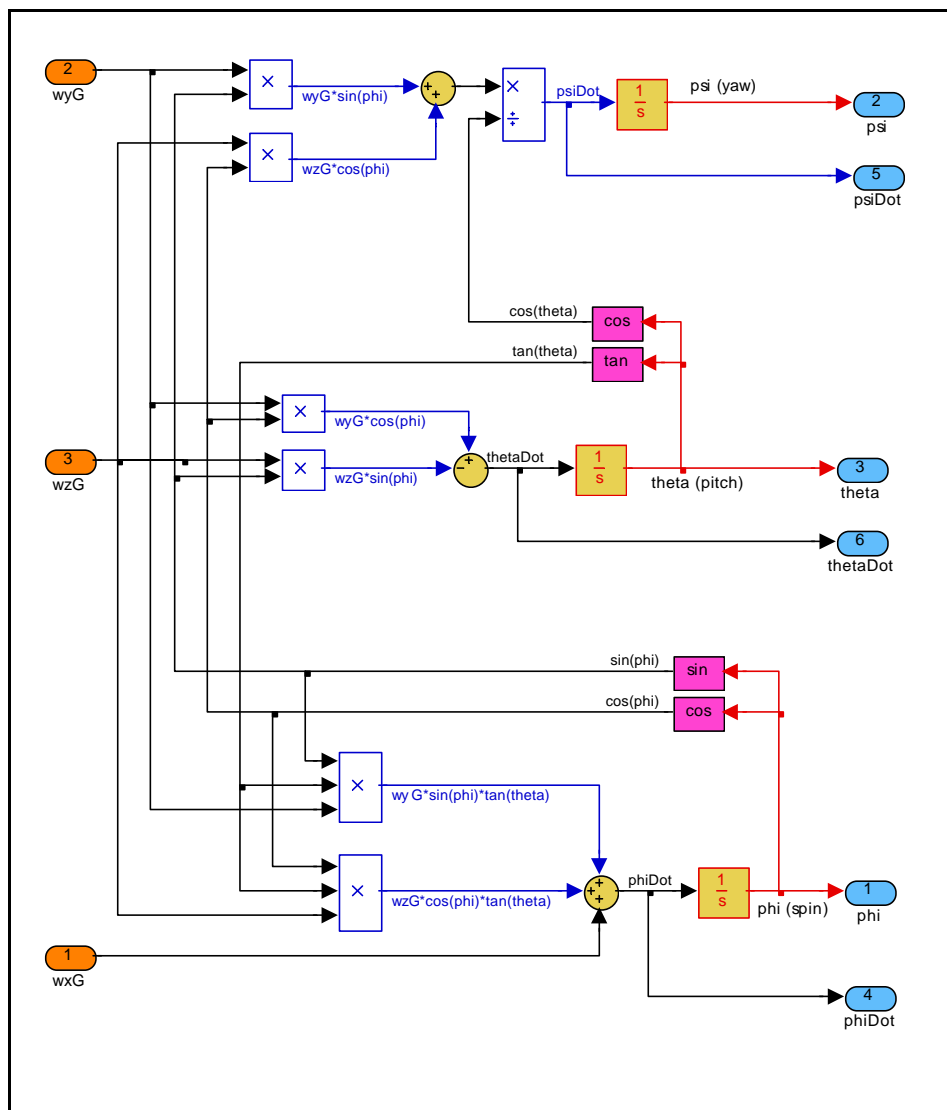


Figure 21 - BDWL model gyro angular position block.

3.2 Gyro Euler Angle Missile Dynamics Compensation

The “gyro dynamics” block outputs gyro Euler angles and Euler angle rates with respect to the inertial coordinate system. If the gyro is used as part of an EO/IR missile simulation, the gyro Euler angles (and their rates) with respect to the missile body-fixed coordinates are needed. The cage coil, precession coil, spin coil, and track loop models depend on the gyro Euler angles with

respect to the missile body. For example, the cage coil voltage is proportional to the gyro off-boresight angle with respect to the missile body, not with respect to the inertial reference frame.

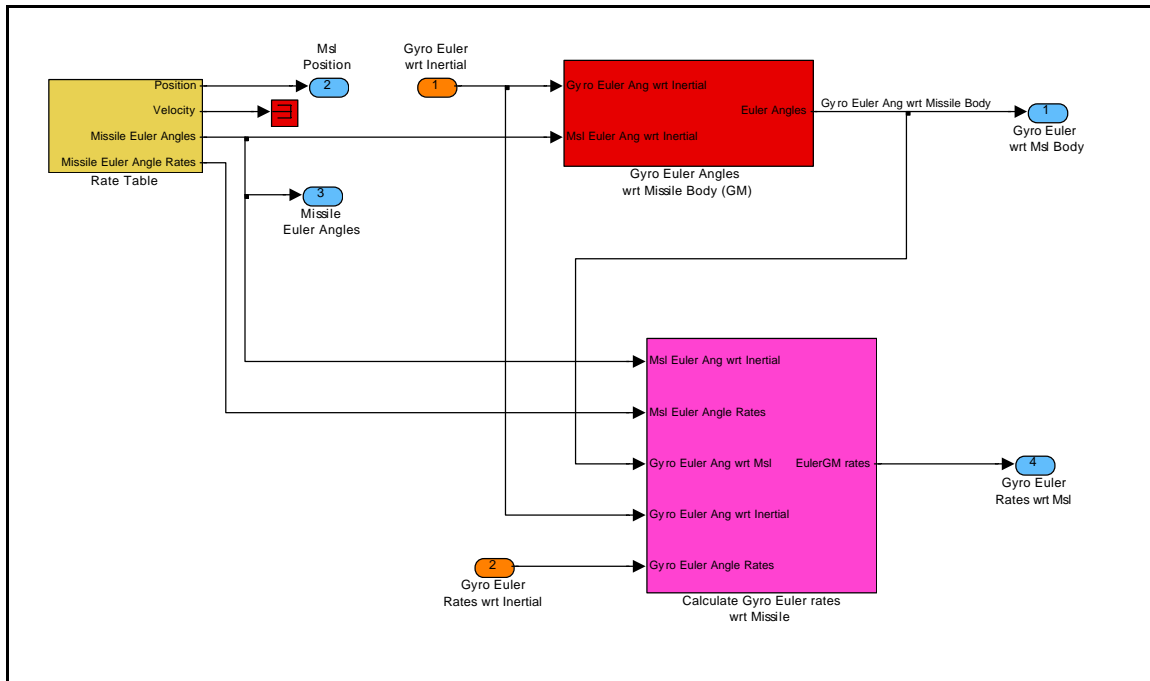


Figure 22 - BDWL gyro Euler angle missile dynamics compensation block.

Figure 22 shows the top level of the BDWL “gyro Euler angle missile dynamics compensation” block. Note that the calculation of the missile-to-gyro Euler angles and Euler angle rates are relatively simple if the missile is stationary, but if the missile is moving, this calculation can be challenging.

From Figure 22, note that the calculation of the gyro Euler angles and rates with respect to the missile body is divided into three functional blocks. The rate table block calculates the missile’s position, velocity, inertial Euler angles, and inertial Euler angle rates. This is used for modeling rate table missile seeker testing. A missile airframe model would be used in place of the rate table

block if a missile fly-out simulation was being used. Separate blocks are used to calculate the gyro Euler angles and the gyro Euler angle rates with respect to the missile body.

Note that the inputs to the gyro Euler angle missile dynamics compensation block are the gyro inertial Euler angles and inertial Euler angle rates. The missile position and angular information could also be considered to be inputs to this block, but for this model the rate table block is included inside the gyro Euler angle missile dynamics compensation block.

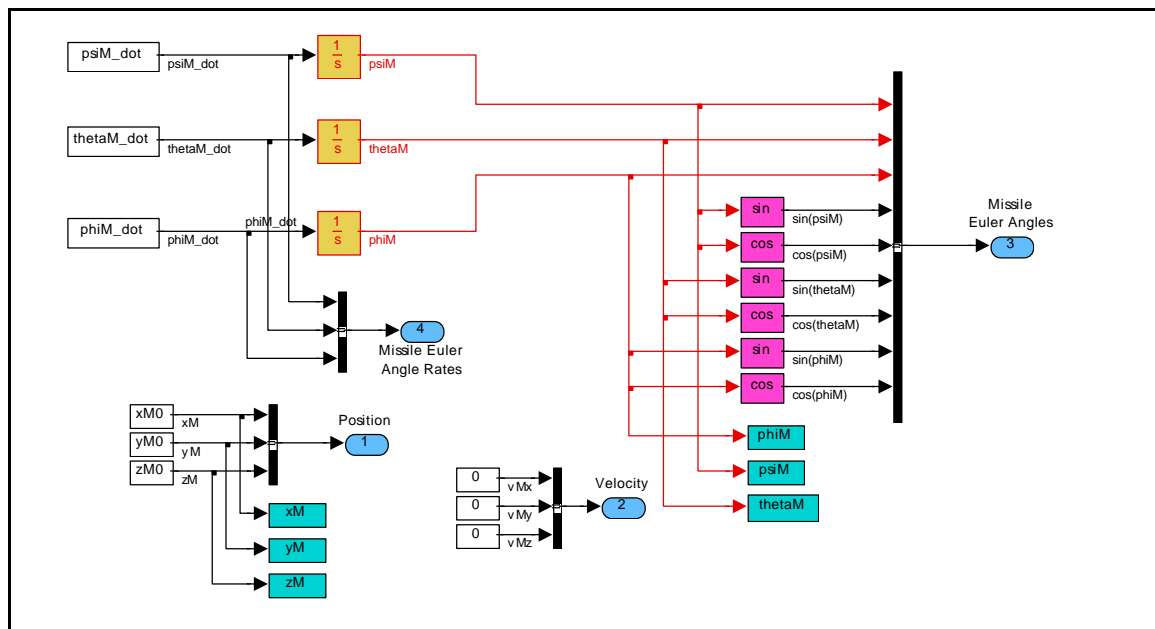


Figure 23 - Rate table missile position/orientation block.

Figure 23 shows the rate table block. This block supplies missile dynamic and angular information. Missile inertial Euler angles are found by integrating the inertial missile Euler angle rates (these are constant for a rate table test, and are set in the MATLAB script which runs this Simulink simulation). The missile

inertial Euler angles are placed on a signal bus along with their sines and cosines, as is done for other Euler angles. For a rate table test, the missile inertial position vector is constant (also set in the MATLAB run script), and the missile inertial velocity is zero.

The gyro Euler angles with respect to the missile can be calculated from the gyro-to-missile direction cosine matrix, given the definition of a direction cosine matrix. The gyro-to-missile direction cosine matrix can be calculated from the gyro-to-inertial direction cosine matrix and the inertial to missile direction cosine matrix. This technique comes from Lamm (13).

Equation 3-34 is the gyro-to-missile (body-to-space) Euler angle direction cosine matrix, developed in section 2.1, equation 2-27:

$${}^M D^G = \begin{bmatrix} c_{y_{GM}} c_{q_{GM}} & -s_{y_{GM}} c_{f_{GM}} + c_{y_{GM}} s_{q_{GM}} s_{f_{GM}} & s_{y_{GM}} s_{f_{GM}} + c_{y_{GM}} s_{q_{GM}} c_{f_{GM}} \\ s_{y_{GM}} c_{q_{GM}} & c_{y_{GM}} c_{f_{GM}} + s_{y_{GM}} s_{q_{GM}} s_{f_{GM}} & -c_{y_{GM}} s_{f_{GM}} + s_{y_{GM}} s_{q_{GM}} c_{f_{GM}} \\ -s_{q_{GM}} & c_{q_{GM}} s_{f_{GM}} & c_{q_{GM}} c_{f_{GM}} \end{bmatrix} \quad (3-34)$$

If the notation ${}^M D_{3,2}^G$ is used to refer to the element in the third row, second column of the gyro-to-missile direction cosine matrix, then it can be seen from equation 3-34 that

$${}^M D_{3,2}^G = -\sin(q_{GM}) \quad (3-35)$$

This can be used to calculate q_{GM} , the gyro pitch Euler angle with respect to the missile body,

$$\mathbf{q}_{GM} = -\sin^{-1}\left({}^M D_{3,1}^G\right) \quad (3-36)$$

which is valid for $-\mathbf{p}/2 \leq \mathbf{q}_{GM} \leq \mathbf{p}/2$.

Similarly, it can be seen that

$$\tan(\mathbf{y}_{GM}) = \frac{\sin(\mathbf{y}_{GM})}{\cos(\mathbf{y}_{GM})} = \frac{{}^M D_{2,1}^G}{{}^M D_{1,1}^G} \quad (3-37)$$

Thus,

$$\mathbf{y}_{GM} = \tan^{-1}\left(\frac{{}^M D_{2,1}^G}{{}^M D_{1,1}^G}\right) \quad (3-38)$$

which is valid for $0 \leq \mathbf{y}_{GM} \leq 2\mathbf{p}$.

Finally, the gyro roll angle with respect to the missile body can be found by using the appropriate gyro-to-missile direction cosine components in the same manner,

$$\mathbf{f}_{GM} = \tan^{-1}\left(\frac{{}^M D_{3,2}^G}{{}^M D_{3,3}^G}\right) \quad (3-39)$$

which is valid for $0 \leq \mathbf{f}_{GM} \leq 2\mathbf{p}$.

Next, note that the gyro-to-missile direction cosine matrix can be calculated by multiplying the gyro-to-inertial and the inertial-to-missile direction cosine matrices, as shown in section 2.1,

$${}^M D^G = {}^M D^I \cdot {}^I D^G \quad (3-40)$$

Since the gyro inertial Euler angles and the missile inertial Euler angles are both

known, the gyro-to-inertial and the inertial-to-missile direction cosine matrices can easily be calculated from the definition of a direction cosine matrix (see section 2.1). Figure 24 shows the block used to calculate the gyro Euler angles with respect to the missile body. This is based on equations 3-36, 3-38, 3-39, and 3-40. Figure 25 shows the “space-to-body direction cosine” block, used to calculate the inertial-to-missile direction cosine from the missile inertial Euler angles. Figure 26 shows the “body-to-space direction cosine” block, used to calculate the gyro-to-inertial direction cosine matrix from the gyro inertial Euler angles.

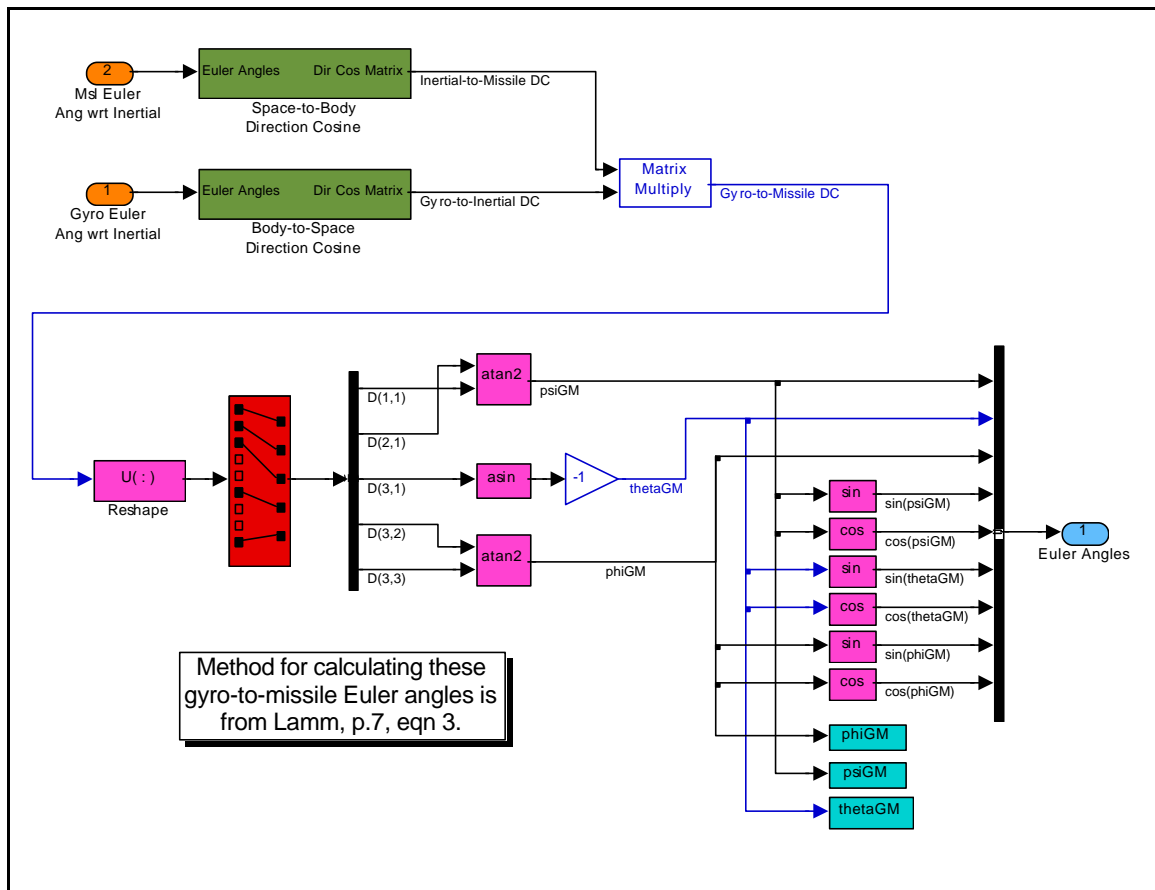


Figure 24 - BDWL gyro Euler angles with respect to missile body (GM) block.

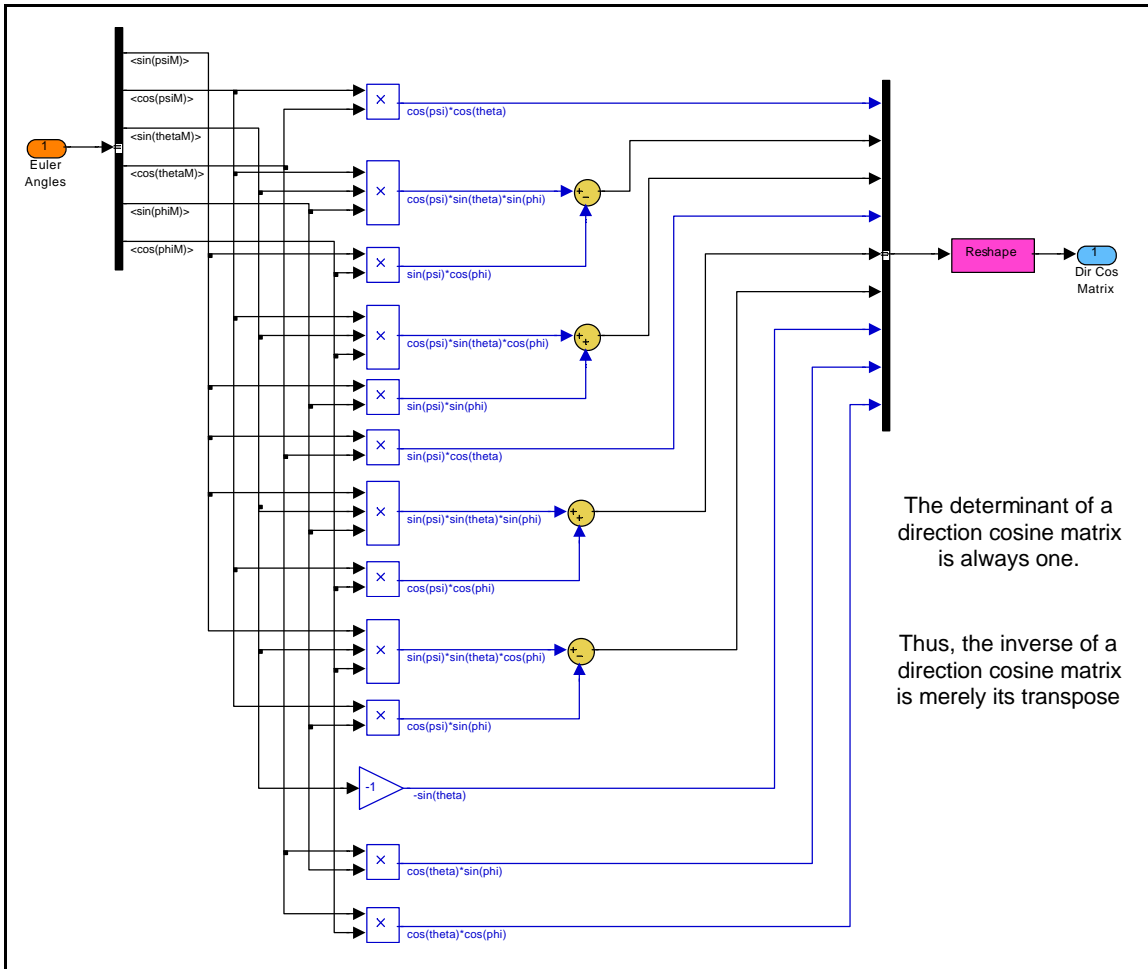


Figure 25 - BDWL space-to-body direction cosine block.

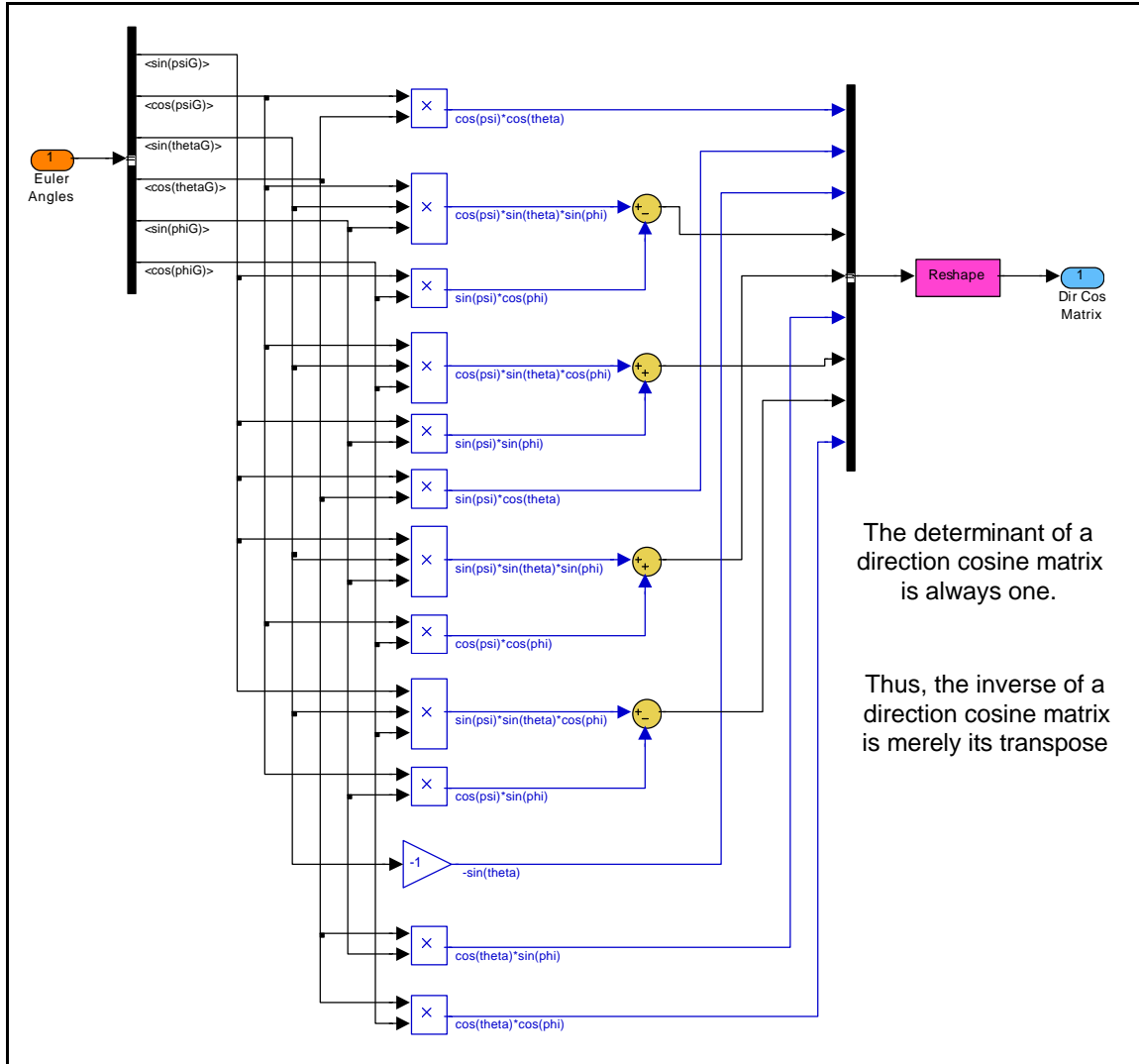


Figure 26 - BDWL body-to-space direction cosine block.

It is sometimes thought that the gyro with respect to missile Euler angular rates can be calculated by merely subtracting the gyro and missile inertial Euler angular rates. This is not correct, as pointed out by Lamm (13). Lamm provides the correct solution, which uses the time derivatives of the missile-to-gyro Euler angles. The expression for the gyro roll rate with respect to the missile body is given in equation 3-39. Taking the time derivative of this, the inverse tangent of a ratio, found in Larson and Hostettler (25),

$$\dot{\mathbf{f}}_{GM} = \frac{{}^M D_{3,3}^G \dot{{}^M D_{3,2}^G} - {}^M D_{3,2}^G \dot{{}^M D_{3,3}^G}}{({}^M D_{3,3}^G)^2 + ({}^M D_{3,2}^G)^2} \quad (3-41)$$

Next, Lamm (13) uses quaternions to derive an expression for the time derivative of a direction cosine matrix. Quaternions are an alternate way (as opposed to Euler angles) to describe the orientation of one coordinate system with respect to another coordinate system. Quaternions are based on the premise that when one coordinate system is rotated with respect to another, there exists a vector, \vec{n} , which has the same coordinates in both systems. Here, \vec{n} is a unit vector, whose components are the eigenvalues of the direction cosine matrices describing the rotation transformation between the two coordinate systems. Further, there exists an angle, Φ , which describes the rotation around \vec{n} that transforms from one coordinate system to the next. The vector \vec{n} and the rotation angle Φ form the basis for quaternions:

$$q_0 = \cos(\Phi / 2) \quad (3-42)$$

$$\vec{q} = \begin{Bmatrix} q_1 \\ q_2 \\ q_3 \end{Bmatrix} = \vec{n} \sin(\Phi / 2) \quad (3-43)$$

This defines the quaternion q , consisting of components q_0, q_1, q_2, q_3 .

From Lamm (13), a direction cosine vector between two coordinate systems can be described in terms of quaternions,

$${}^B D^A = \begin{bmatrix} q_0^2 + q_1^2 - q_2^2 - q_3^2 & 2(q_1 q_2 - q_0 q_3) & 2(q_1 q_3 + q_0 q_2) \\ 2(q_1 q_2 + q_0 q_3) & q_0^2 - q_1^2 + q_2^2 - q_3^2 & 2(q_2 q_3 - q_0 q_1) \\ 2(q_1 q_3 - q_0 q_2) & 2(q_2 q_3 + q_0 q_1) & q_0^2 - q_1^2 - q_2^2 + q_3^2 \end{bmatrix} \quad (3-44)$$

where A and B are two arbitrary coordinate systems, differing in orientation.

For a rotating coordinate system, consider its orientation from one time, t , to a short time later, $t + \Delta t$. The rotation of the coordinate system from time t to time $t + \Delta t$ can be described in terms of quaternions. If the coordinate system is rotating at an inertial rate $\vec{\omega}$, then a unit vector aligned with the $\vec{\omega}$ vector is actually the \vec{n} vector used in the quaternion definition. Further, if $\vec{\omega}$ is changing slowly in comparison to the time interval Δt , then the quaternion rotation angle Φ can be approximated by

$$\Phi \cong |\vec{\omega}| \Delta t + O[(\Delta t)^2] \quad (3-45)$$

Thus, using these expressions with the definitions of quaternions in equations 3-42 and 3-43, and applying a small angle approximation gives:

$$q_0(t + \Delta t) = \cos(\Phi(t + \Delta t) / 2) \quad (3-46)$$

$$q_0(t + \Delta t) = \cos\left(\frac{|\vec{\omega}| \Delta t}{2} + O[(\Delta t)^2]\right) \cong 1 \quad (3-47)$$

and,

$$q_i(t + \Delta t) = \hat{\omega}_i(t + \Delta t) \cdot \hat{x}_i \sin(\Phi(t + \Delta t) / 2) \quad (3-48)$$

where,

$$\hat{\mathbf{w}} = \text{A unit vector in the direction of } \vec{\mathbf{w}}$$

$$\hat{x}_i = \text{A unit vector in the direction of one of the three coordinate axes}$$

Thus,

$$q_i(t + \Delta t) = \begin{Bmatrix} \hat{\mathbf{w}}_x \\ \hat{\mathbf{w}}_y \\ \hat{\mathbf{w}}_z \end{Bmatrix} \sin\left(\frac{|\vec{\mathbf{w}}|\Delta t}{2} + O[(\Delta t)^2]\right) \quad (3-48)$$

Again using a small-angle approximation,

$$q_i(t + \Delta t) \cong \begin{Bmatrix} \hat{\mathbf{w}}_x \\ \hat{\mathbf{w}}_y \\ \hat{\mathbf{w}}_z \end{Bmatrix} \left\{ \frac{|\vec{\mathbf{w}}|\Delta t}{2} + O[(\Delta t)^2] \right\} = \begin{Bmatrix} \mathbf{w}_x \\ \mathbf{w}_y \\ \mathbf{w}_z \end{Bmatrix} \frac{\Delta t}{2} + O[(\Delta t)^2] \quad (3-49)$$

Substituting equations 3-49 and 3-47 into 3-44 gives,

$${}^{A(t+\Delta t)}D^{A(t)} = \begin{bmatrix} 1 & -\mathbf{w}_z\Delta t & \mathbf{w}_y\Delta t \\ \mathbf{w}_z\Delta t & 1 & -\mathbf{w}_x\Delta t \\ -\mathbf{w}_y\Delta t & \mathbf{w}_x\Delta t & 1 \end{bmatrix} + O[(\Delta t)^2] \quad (3-50)$$

If the $[\Omega]$ matrix and the identity matrix $[I]$ are defined as,

$$[\Omega] = \begin{bmatrix} 0 & -\mathbf{w}_z & \mathbf{w}_y \\ \mathbf{w}_z & 0 & -\mathbf{w}_x \\ -\mathbf{w}_y & \mathbf{w}_x & 0 \end{bmatrix} \quad (3-51)$$

$$[I] = \begin{bmatrix} 1 & 0 & 0 \\ 0 & 1 & 0 \\ 0 & 0 & 1 \end{bmatrix} \quad (3-52)$$

then,

$${}^{A(t+\Delta t)}D^{A(t)} = \left(I + [\Omega]\Delta t \right) + O\left[(\Delta t)^2 \right] \quad (3-53)$$

Conversely, a rotation in the opposite direction can be represented as

$${}^{A(t)}D^{A(t+\Delta t)} = \left(I - [\Omega]\Delta t \right) + O\left[(\Delta t)^2 \right] \quad (3-54)$$

From the definition of direction cosine matrices,

$${}^{B(t+\Delta t)}D^{A(t+\Delta t)} = {}^{B(t+\Delta t)}D^{B(t)} \cdot {}^{B(t)}D^{A(t)} \cdot {}^{A(t)}D^{A(t+\Delta t)} \quad (3-55)$$

Substituting equations 3-53 and 3-54 into 3-55,

$${}^{B(t+\Delta t)}D^{A(t+\Delta t)} = \left(I + [\Omega_B]\Delta t \right) {}^{B(t)}D^{A(t)} \left(I - [\Omega_A]\Delta t \right) + O\left[(\Delta t)^2 \right] \quad (3-56)$$

$${}^{B(t+\Delta t)}D^{A(t+\Delta t)} = {}^{B(t)}D^{A(t)} + \left({}^{B(t)}D^{A(t)} [\Omega_B] - [\Omega_A] {}^{B(t)}D^{A(t)} \right) \Delta t + O\left[(\Delta t)^2 \right] \quad (3-57)$$

Define

$$f(t) = {}^{B(t)}D^{A(t)} \quad (3-58)$$

$$f(t + \Delta t) = {}^{B(t+\Delta t)}D^{A(t+\Delta t)} \quad (3-59)$$

The definition of a derivative is:

$$\frac{d}{dt} f(t) = \lim_{\Delta t \rightarrow 0} \frac{f(t + \Delta t) - f(t)}{\Delta t} \quad (3-60)$$

Thus, combining equations 3-60, 3-59, 3-58, and 3-57 and ignoring higher order functions of Δt yields,

$${}^{B(t)}\dot{D}^{A(t)} = {}^{B(t)}D^{A(t)}[\Omega_B] - [\Omega_A]{}^{B(t)}D^{A(t)} \quad (3-61)$$

Using this expression to find time derivative of the direction cosine matrix from the gyro body-fixed coordinate system to the missile body-fixed coordinate system,

$${}^M\dot{D}^G = {}^M D^G \cdot \Omega_{GI} - \Omega_{MI} \cdot {}^M D^G \quad (3-62)$$

where,

$$\Omega_{GI} = \begin{bmatrix} 0 & -\mathbf{w}_{G_z} & \mathbf{w}_{G_y} \\ \mathbf{w}_{G_z} & 0 & -\mathbf{w}_{G_x} \\ -\mathbf{w}_{G_y} & \mathbf{w}_{G_x} & 0 \end{bmatrix} \quad (3-63)$$

and

$$\Omega_{MI} = \begin{bmatrix} 0 & -\mathbf{w}_{M_z} & \mathbf{w}_{M_y} \\ \mathbf{w}_{M_z} & 0 & -\mathbf{w}_{M_x} \\ -\mathbf{w}_{M_y} & \mathbf{w}_{M_x} & 0 \end{bmatrix} \quad (3-64)$$

Note that these gyro and missile angular velocities are the respective angular velocities with respect to inertial, expressed in gyro and missile body-fixed coordinates. Substituting equation 3-62 into equation 3-41 gives,

$$\begin{aligned} \dot{\mathbf{f}}_{GM} = & \left[{}^M D_{3,3}^G \cdot \left({}^M D^G \cdot \Omega_{GI} - \Omega_{MI} \cdot {}^M D^G \right)_{3,2} - \right. \\ & \left. {}^M D_{3,2}^G \cdot \left({}^M D^G \cdot \Omega_{GI} - \Omega_{MI} \cdot {}^M D^G \right)_{3,3} \right] / \\ & \left[\left({}^M D_{3,3}^G \right)^2 + \left({}^M D_{3,2}^G \right)^2 \right] \end{aligned} \quad (3-65)$$

Multiplying this out and combining terms yields,

$$\begin{aligned} \dot{\mathbf{f}}_{GM} = & \mathbf{w}_{G_x} + \mathbf{w}_{G_z} c_{f_{GM}} t_{q_{GM}} + \mathbf{w}_{G_y} s_{f_{GM}} t_{q_{GM}} \\ & - \mathbf{w}_{M_x} (c_{y_{GM}} / c_{q_{GM}}) - \mathbf{w}_{M_y} (s_{y_{GM}} / c_{q_{GM}}) \end{aligned} \quad (3-66)$$

Similarly, the equation for the time rate of change of the gyro pitch angular rate with respect to the missile can be found by starting with equation 3-36 and using the formula of the time derivative of an inverse sine angle from Larson and Hostettler (25):

$$\dot{\mathbf{q}}_{GM} = \frac{-{}^M \dot{D}_{3,1}^G}{\sqrt{1 - {}^M D_{3,1}^G}} \quad (3-67)$$

From equation 3-34,

$${}^M D_{3,1}^G = -\sin(\mathbf{q}_{GM}) \quad (3-68)$$

Substituting equations 3-68 and 3-62 into equation 3-67,

$$\dot{\mathbf{q}}_{GM} = \frac{-\left({}^M D^G \Omega_G - \Omega_M {}^M D^G\right)_{3,1}}{\sqrt{1 - s_{q_{GM}}^2}} \quad (3-69)$$

After substitution and simplification,

$$\dot{\mathbf{q}}_{GM} = \mathbf{w}_{G_y} c_{f_{GM}} - \mathbf{w}_{G_z} s_{f_{GM}} - \mathbf{w}_{M_y} c_{y_{GM}} + \mathbf{w}_{M_x} s_{y_{GM}} \quad (3-70)$$

Finally, the gyro yaw angular rate with respect to the missile is found in similar manner by using equation 3-38 along with the formula for the time derivative of an inverse tangent and the derivative “quotient rule”:

$$\dot{\mathbf{y}}_{GM} = \frac{{}^M D_{1,1}^G}{\left({}^M D_{1,1}^G\right)^2 + \left({}^M D_{2,1}^G\right)^2} \left(\frac{{}^M D_{1,1}^G \dot{{}^M D}_{2,1}^G - {}^M D_{2,1}^G \dot{{}^M D}_{1,1}^G}{\left({}^M D_{1,1}^G\right)^2} \right) \quad (3-71)$$

From equation 3-34,

$${}^M D_{1,1}^G = \cos(\mathbf{y}_{GM}) \cos(\mathbf{q}_{GM}) \quad (3-72)$$

$${}^M D_{2,1}^G = \sin(\mathbf{y}_{GM}) \cos(\mathbf{q}_{GM}) \quad (3-73)$$

Substituting equations 3-72, 3-73, and 3-62 into 3-71 yields,

$$\begin{aligned} \dot{\mathbf{y}}_{GM} = & \left[c_{y_{GM}} c_{q_{GM}} \left({}^M D^G \Omega_G - \Omega_M {}^M D^G \right)_{2,1} \right. \\ & \left. - s_{y_{GM}} c_{q_{GM}} \left({}^M D^G \Omega_G - \Omega_M {}^M D^G \right)_{1,1} \right] / \\ & \left(c_{y_{GM}}^2 c_{q_{GM}}^2 + s_{y_{GM}}^2 c_{q_{GM}}^2 \right) \end{aligned} \quad (3-74)$$

After substitution and simplification,

$$\dot{\mathbf{y}}_{GM} = \mathbf{w}_{G_y} \frac{s_{f_{GM}}}{c_{q_{GM}}} + \mathbf{w}_{G_z} \frac{c_{f_{GM}}}{c_{q_{GM}}} - \mathbf{w}_{M_x} c_{y_{GM}} t_{q_{GM}} - \mathbf{w}_{M_y} s_{y_{GM}} t_{q_{GM}} - \mathbf{w}_{M_z} \quad (3-75)$$

Equations 3-66, 3-70, and 3-75 are implemented in the “calculate gyro Euler rates with respect to missile” block, shown in Figure 27.

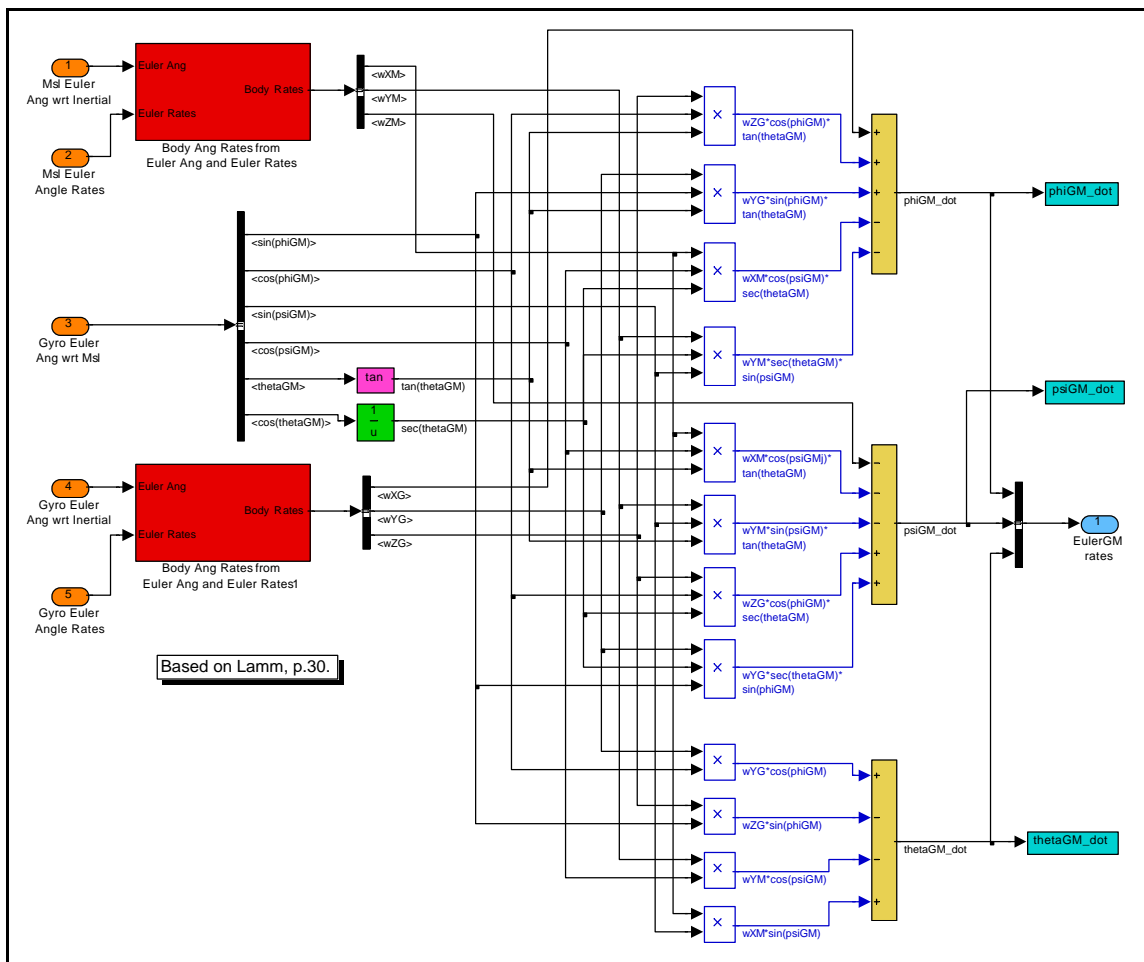


Figure 27 - BDWL calculate gyro Euler rates with respect to missile block.

Note that the calculation of the gyro Euler rates with respect to the missile are dependent upon knowing both the gyro and missile inertial angular velocities expressed respectively in the gyro and missile body-fixed coordinate systems. These angular velocities can be determined from the respective Euler angles and Euler angle rates. Equation 3-30 provides this relationship, which is implemented in the “body angular rates from Euler angles and Euler rates” block shown in Figure 28.

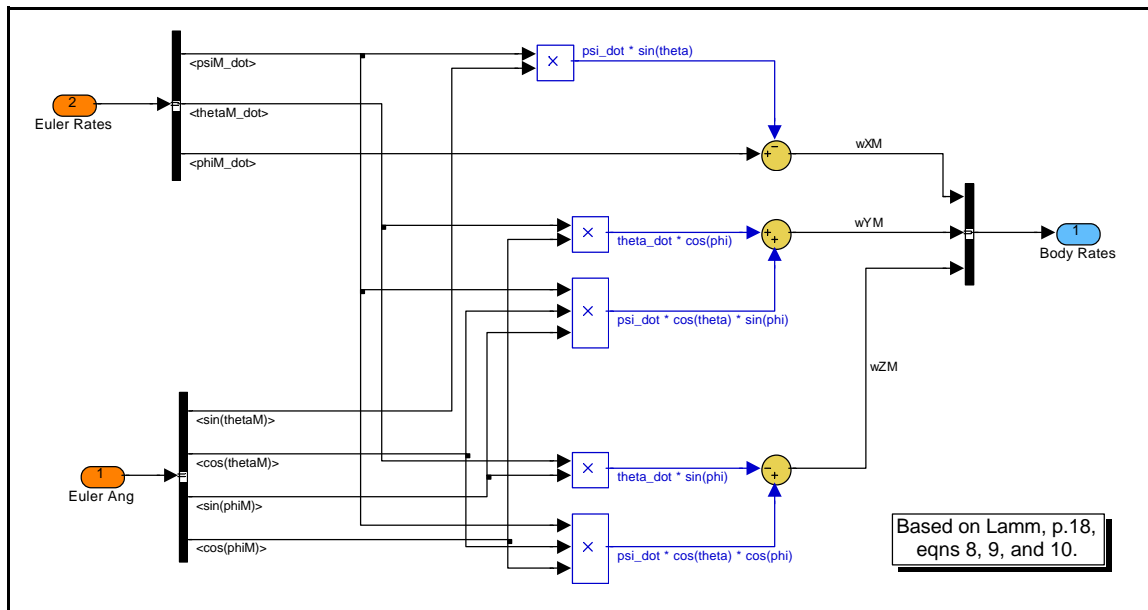


Figure 28 - BDWL body angular rates from Euler angles and Euler rates block.

3.3 Cage Coil Sensor Models

The cage coil sensor (described in Section 1.0) consists of a coil wound circumferentially around the missile body in the vicinity of the gyro, similar in configuration to the precession coil. If the gyro is not boresighted to the missile body, the gyro rotor magnetic field cuts the cage coil and induces a current in it proportional to the rate of change of the gyro flux cutting the cage coil. This current produces a voltage at the cage coil output, which is a sinusoid at the gyro spin frequency. The magnitude of this sinusoidal cage coil voltage is proportional to the gyro off-boresight angle (with respect to the missile body).

For the BDWL gyro model, two cage coil models were developed. The first represents the full cage coil equations. The second is an approximation of the cage coil signal based on the full cage coil equations, but simplified with a small-angle approximation. The full cage coil model is more accurate, but depending on the magnitude of the gyro off-boresight excursions, the small angle approximation cage coil model may provide adequate fidelity with enhanced execution speed.

3.3.1 Complete Cage Coil Model

The cage coil signal is defined as a voltage based on the rate of change of the gyro magnetic flux coupled onto the cage coil. The gyro magnetic north pole is aligned with the gyro body-fixed z_G axis. Using the right-hand rule, the cage coil vector is aligned with the missile body-fixed x_M axis. Thus, the cage

coil voltage is proportional to the time rate of change of the dot product of a unit vector aligned with the gyro z_G axis and a unit vector aligned with the missile x_M axis,

$$V_C = K_C \cdot \frac{d}{dt} (\hat{z}_G \cdot \hat{x}_M) \quad (3-76)$$

where K_C is a cage coil gain term incorporating the gyro magnetic flux density and cage coil gain, and V_C is the cage coil voltage signal. In order to take the unit vector dot product, the \hat{z}_G unit vector was transformed into the missile body-fixed coordinate system {M}:

$$\hat{z}_G = \begin{Bmatrix} 0 \\ 0 \\ 1 \end{Bmatrix}_G \quad (3-77)$$

$$\hat{z}_G = {}^M D^G \begin{Bmatrix} 0 \\ 0 \\ 1 \end{Bmatrix}_G = \begin{Bmatrix} c_{y_{GM}} s_{q_{GM}} c_{f_{GM}} + s_{y_{GM}} s_{f_{GM}} \\ s_{y_{GM}} s_{q_{GM}} c_{f_{GM}} - c_{y_{GM}} s_{f_{GM}} \\ c_{q_{GM}} c_{f_{GM}} \end{Bmatrix}_M \quad (3-78)$$

Therefore,

$$\hat{z}_G \cdot \hat{x}_M = c_{y_{GM}} s_{q_{GM}} c_{f_{GM}} + s_{y_{GM}} s_{f_{GM}} \quad (3-79)$$

Taking the time derivative and scaling by K_C gives,

$$V_C = K_C \left(-\dot{y}_{GM} s_{y_{GM}} s_{q_{GM}} c_{f_{GM}} + \dot{q}_{GM} c_{y_{GM}} c_{q_{GM}} c_{f_{GM}} - \dot{f}_{GM} c_{y_{GM}} s_{q_{GM}} s_{f_{GM}} + \dot{y}_{GM} c_{y_{GM}} s_{f_{GM}} + \dot{f}_{GM} s_{y_{GM}} c_{f_{GM}} \right) \quad (3-80)$$

Equation 3-80 represents the “full” cage coil equation. It is implemented in the BDWL model in the “cage coil (full angle equations)” block, shown in Figure 29.

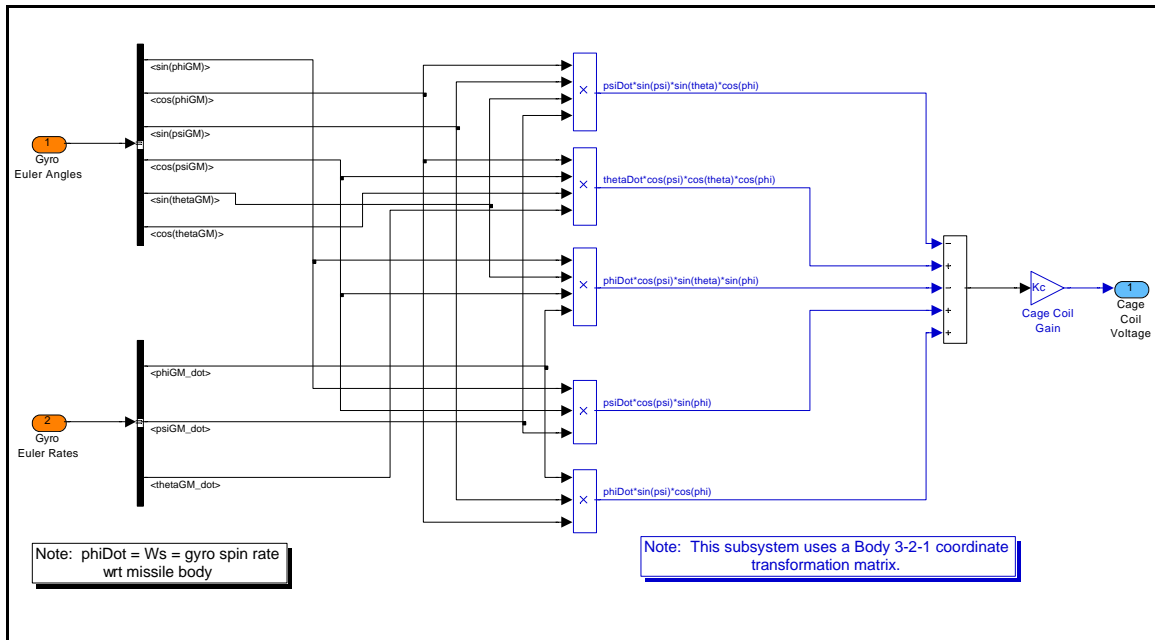


Figure 29 - BDWL cage coil (full angle equations) block.

3.3.2 Cage Coil Small Angle Approximation

The small angle approximation of the cage coil signal is based on the full cage coil voltage expression given in equation 3-80. For the small angle approximation, it is assumed that the gyro yaw and pitch angles (with respect to the missile body) are small. Since the gyro spins, its roll angle cannot be assumed to be small. For the small angle approximation, it is assumed that:

$$\sin(\mathbf{y}_{GM}) \cong \mathbf{y}_{GM} \quad (3-81)$$

$$\cos(\mathbf{y}_{GM}) \cong 1 \quad (3-82)$$

$$\sin(\mathbf{q}_{GM}) \cong \mathbf{q}_{GM} \quad (3-83)$$

$$\cos(\mathbf{q}_{GM}) \cong 1 \tag{3-84}$$

Substituting equations 3-81 through 3-84 into 3-80 yields the cage coil voltage small angle approximation,

$$V_C \cong K_C \left(-\dot{\mathbf{y}}_{GM} \mathbf{y}_{GM} \mathbf{q}_{GM} c_{f_{GM}} + \dot{\mathbf{q}}_{GM} c_{f_{GM}} - \dot{\mathbf{f}}_{GM} \mathbf{q}_{GM} s_{f_{GM}} + \dot{\mathbf{y}}_{GM} s_{f_{GM}} + \dot{\mathbf{f}}_{GM} \mathbf{y}_{GM} c_{f_{GM}} \right) \tag{3-85}$$

This expression is implemented in the BDWL gyro model in the “cage coil (small angle approximation)” block, shown in Figure 30.

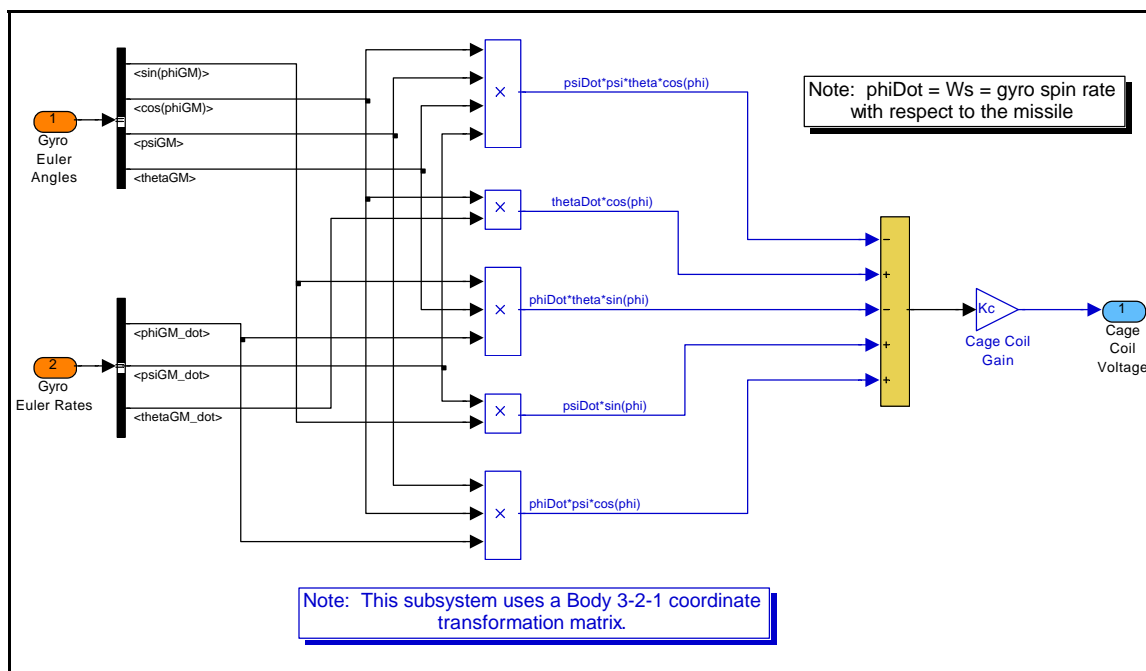


Figure 30 - BDWL cage coil (small angle approximation) block.

3.4 Precession Coil

The precession coil generates the precession torque values used by the gyro dynamics block to calculate gyro position. As discussed earlier, some of the precession torque can couple to the gyro spin axis if the gyro is off of missile boresight.

For convenience, the reference coil signal is generated in the precession coil block. As discussed earlier, the reference signal is generated from the current induced by the gyro magnetic field in flat, side mounted reference coils located adjacent to the gyro in the missile body. The reference signal is defined as,

$$ref = Kp \cdot \sin(\mathbf{f}_{GM}) \quad (3-86)$$

where Kp is determined experimentally from actual gyro signals. In this case Kp has been set to 4.465. Also, when tuning a gyro model to a specific gyro, it may be necessary to add a constant phase shift to the reference signal to compensate for the exact placement of the reference coils.

For the open-loop gyro model presented here, the precession command is generated by phase shifting the sine of the gyro roll angle with respect to the missile, and scaling it with a gain,

$$\vec{P}_{cmd} = T_y \sin(\mathbf{f}_{GM} + \mathbf{g}) \hat{x}_M \quad (3-87)$$

where the phase shift angle, gamma, represents the direction of precession, and the gain, T_y represents the precession rate.

This precession command represents the signal that is placed through the precession coils. It generates a magnetic field aligned with the missile x_M axis. The torque on the gyro results from the force produced by the attraction of this precession magnetic field and the magnetic field of the gyro. A positive precession command generates a precession magnetic field with its north pole aligned with the positive x_M axis, which attracts the gyro south pole. The resulting gyro torque can be found by taking the cross product of the gyro $-z_G$ axis (it is aligned with the south pole of the gyro magnetic field) and the precession command which is aligned with the missile x_M axis. In order to perform this cross product, the precession command magnetic force must be transformed from the missile body-fixed coordinate system to the gyro body-fixed coordinate system,

$$\left\{ \vec{P}_{cmd} \right\}_G = {}^G D^M \left\{ \begin{array}{c} T_y \sin(\mathbf{f}_{GM} + \mathbf{g}) \\ 0 \\ 0 \end{array} \right\}_M \quad (3-88)$$

$$\left\{ \vec{P}_{cmd} \right\}_G = T_y \sin(\mathbf{f}_{GM} + \mathbf{g}) \left\{ \begin{array}{c} c_{y_{GM}} c_{q_{GM}} \\ c_{y_{GM}} s_{q_{GM}} s_{f_{GM}} - s_{y_{GM}} c_{f_{GM}} \\ c_{y_{GM}} s_{q_{GM}} c_{f_{GM}} + s_{y_{GM}} s_{f_{GM}} \end{array} \right\}_G \quad (3-89)$$

Gyro precession torque (\vec{t}_p) is obtained by taking the cross product of the gyro

$-z_G$ axis and the precession command,

$$\vec{t}_p = (-\hat{z}_G) \otimes \vec{P}_{cmd} \quad (3-90)$$

This results in

$$\vec{\tau}_p = T_y \sin(\mathbf{f}_{GM} + \mathbf{g}) \begin{Bmatrix} c_{y_{GM}} s_{q_{GM}} s_{f_{GM}} - s_{y_{GM}} c_{f_{GM}} \\ c_{y_{GM}} c_{q_{GM}} \\ 0 \end{Bmatrix}_G \quad (3-91)$$

The gyro torque is expressed in the gyro body-fixed coordinate system, which is where it is needed for use as input to the gyro dynamics block.

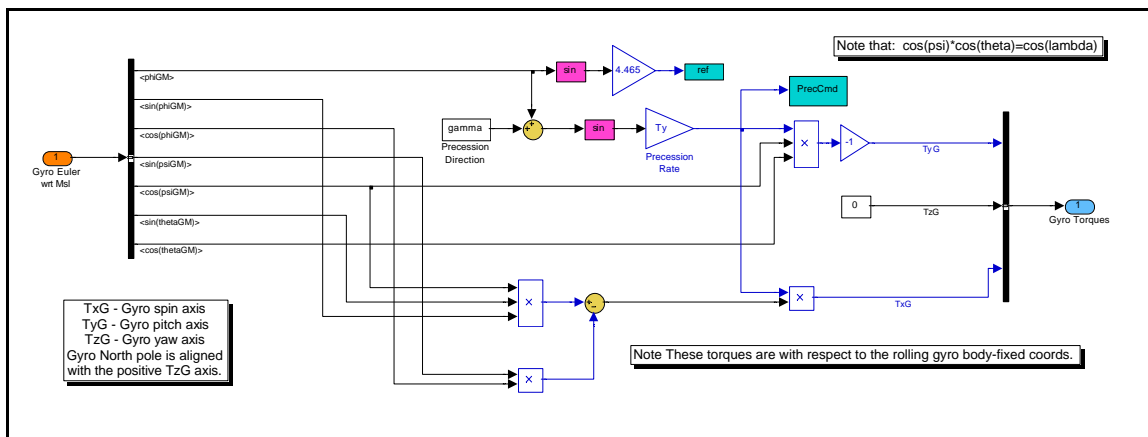


Figure 31 - BDWL precession coil block.

Figure 31 shows the BDWL model precession coil block. It is based on equations 3-86 and 3-91. Note that this precession coil block is for the BDWL open-loop gyro model. A slightly different version is used when a track loop block is included for missile gyro rate table test comparisons in section 6.3. For the tracker version, a precession command is generated in an additional track loop block and injected into the precession coil block where the PrecCmd output block is located in Figure 31.

3.5 Spin Coil

The spin coils generate a magnetic field which is used to keep the gyro spinning at the desired rate. The BDWL model is set up so that the user can choose either the spin coil model, or an idealized spin rate model where the gyro is kept at the desired spin rate perfectly. This section details the derivation of the non-ideal spin coil model, which was based on Williams (9). Figure 32 shows the spin coil geometry and angle definitions.

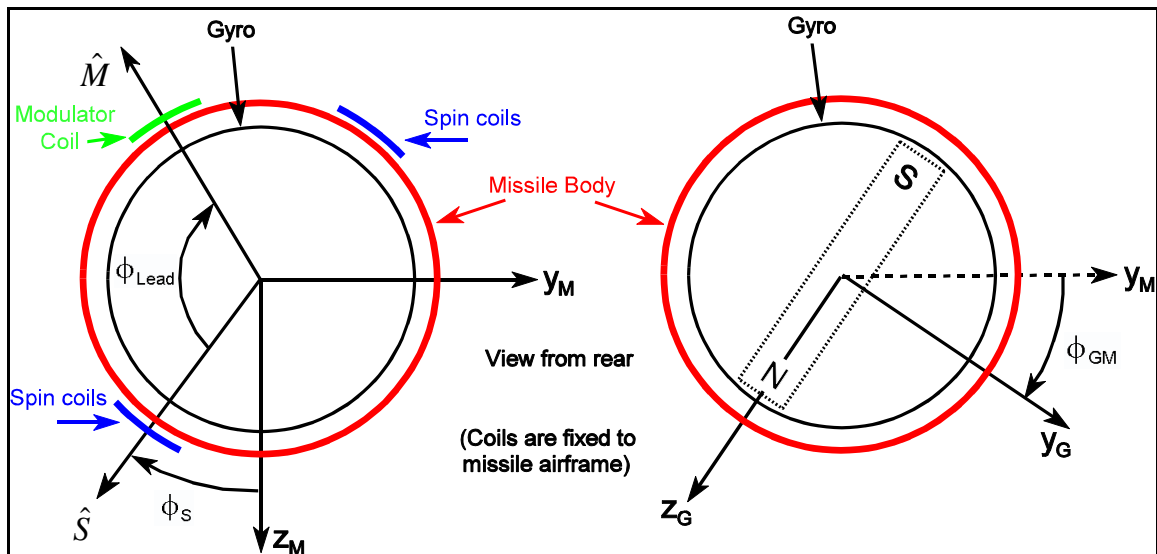


Figure 32 - Spin coil angle definitions.

This model assumes that a torque is applied to the gyro to control its spin rate via spin coils. These coils are “pancake” type coils much like the reference coils. Further, it is assumed that a modulator coil is used to sense the position of the gyro, which provides a reference sinusoid for input to the spin coils. A current in the spin coils produces a magnetic field aligned with the \hat{S} vector. The modulator sensor coil is aligned with the \hat{M} vector.

The spin coils are fixed in the missile body, thus, their magnetic field can induce precession torques if the gyro is not aligned (boresighted) with the missile body. It is assumed that a positive current in the spin coils will induce a magnetic field which will attract the gyro south pole toward the \hat{S} axis, thus, the spin torque can be expressed as

$$\vec{\tau}_s = K_s J_s (-\hat{z}_G \otimes \hat{S}) \quad (3-92)$$

where $K_s =$ Torque/current conversion factor

$J_s =$ Spin coil current

First, the magnitude of the spin torque (the $K_s J_s$ term) will be derived, then the spin torque direction will be calculated. From Williams (9) the magnitude of the spin torque is defined as

$$K_s J_s = \frac{2I_s}{\sin(\mathbf{f}_{Lead})} (\hat{M} \cdot \hat{z}_G) \dot{\mathbf{w}}_{X_G} \Big|_{Nom} \quad (3-93)$$

where $\dot{\mathbf{w}}_{X_G} \Big|_{Nom} =$ Nominal spin acceleration

Williams also approximates the nominal spin acceleration as

$$\dot{\mathbf{w}}_{X_G} \Big|_{Nom} = \frac{(\mathbf{w}_{X_G}^{Desired} - \mathbf{w}_{X_G})}{T_S} \quad (3-94)$$

where $\mathbf{w}_{X_G}^{Desired} =$ Commanded spin rate

\mathbf{w}_{x_G} = Actual spin rate

T_s = Time constant

The directional component of $K_s J_s$ is computed in the non-rolling gyro with respect to missile (NRGM) reference frame. First, the \hat{z}_G and the \hat{M} unit vectors are written in the NRGM coordinate system. For \hat{z}_G this can be done by inspection of Figure 32,

$$\hat{z}_G = \left\{ \begin{array}{c} 0 \\ -s_{f_{GM}} \\ c_{f_{GM}} \end{array} \right\}_{NRGM} \quad (3-95)$$

For the \hat{M} vector, start in the missile body-fixed coordinate system {M},

$$\hat{M} = \left\{ \begin{array}{c} 0 \\ -s_{(f_s + f_{Lead})} \\ c_{(f_s + f_{Lead})} \end{array} \right\}_M \quad (3-96)$$

This can be transformed into the NRGM coordinate system using the missile-to-non-rolling gyro with respect to the missile direction cosine matrix,

$$\hat{M} = {}^{NRGM}D^M \left\{ \hat{M} \right\}_M \quad (3-97)$$

$$\hat{M} = \begin{bmatrix} c_{y_{GM}} & c_{q_{GM}} & s_{y_{GM}} & c_{q_{GM}} & -s_{q_{GM}} \\ -s_{y_{GM}} & c_{y_{GM}} & c_{y_{GM}} & c_{q_{GM}} & 0 \\ c_{y_{GM}} & s_{q_{GM}} & s_{y_{GM}} & s_{q_{GM}} & c_{q_{GM}} \end{bmatrix} \left\{ \begin{array}{c} 0 \\ -s_{f_{S+L}} \\ c_{f_{S+L}} \end{array} \right\} \quad (3-98)$$

For convenience, let

$$\mathbf{f}_{S+L} = \mathbf{f}_S + \mathbf{f}_{Lead} \quad (3-99)$$

Thus,

$$\hat{\mathbf{M}} = \left\{ \begin{array}{l} -s_{f_{S+L}} s_{y_{GM}} c_{q_{GM}} - c_{f_{S+L}} s_{q_{GM}} \\ -s_{f_{S+L}} c_{y_{GM}} \\ -s_{f_{S+L}} s_{y_{GM}} s_{q_{GM}} + c_{f_{S+L}} c_{q_{GM}} \end{array} \right\}_{NRGM} \quad (3-100)$$

and

$$\hat{\mathbf{M}} \cdot \hat{\mathbf{z}}_G = s_{f_{S+L}} c_{y_{GM}} s_{f_{GM}} - c_{f_{GM}} (s_{f_{S+L}} s_{y_{GM}} s_{q_{GM}} - c_{f_{S+L}} c_{q_{GM}}) \quad (3-101)$$

Next, the spin torque direction will be calculated by evaluating the cross product term from equation 3-92. It is necessary to calculate spin torque in the gyro body-fixed coordinate system, as this is where the precession torque is calculated, and that is where the gyro dynamics equations of motion are solved. From the definition of a vector cross product, and the fact that the $-\hat{\mathbf{z}}_G$ vector does not have components in the gyro body $\hat{\mathbf{x}}_G$ or $\hat{\mathbf{y}}_G$ axes,

$$(-\hat{\mathbf{z}}_G \otimes \hat{\mathbf{S}}) = (\hat{\mathbf{S}} \cdot \hat{\mathbf{y}}_G) \hat{\mathbf{x}}_G - (\hat{\mathbf{S}} \cdot \hat{\mathbf{x}}_G) \hat{\mathbf{y}}_G \quad (3-102)$$

The $\hat{\mathbf{S}}$ vector must be transformed from the missile body-fixed coordinate system to the gyro body-fixed coordinate system

$$\hat{\mathbf{S}} = \left\{ \begin{array}{l} 0 \\ -s_{f_S} \\ c_{f_S} \end{array} \right\}_M \quad (3-103)$$

$$\hat{S} = {}^G D^M \left\{ \hat{S} \right\}_M \quad (3-104)$$

$$\hat{S} = \begin{bmatrix} \dots & s_{y_{GM}} c_{q_{GM}} & -s_{q_{GM}} \\ \dots & c_{y_{GM}} c_{f_{GM}} + s_{y_{GM}} s_{q_{GM}} s_{f_{GM}} & c_{q_{GM}} s_{f_{GM}} \\ \dots & -c_{y_{GM}} s_{f_{GM}} + s_{y_{GM}} s_{q_{GM}} c_{f_{GM}} & c_{q_{GM}} c_{f_{GM}} \end{bmatrix} \begin{Bmatrix} 0 \\ -s_{f_S} \\ c_{f_S} \end{Bmatrix}_M \quad (3-105)$$

(Note that values from the first column of the direction cosine matrix are omitted since they are not needed for this calculation.)

$$\hat{S} = \begin{Bmatrix} -s_{y_{GM}} c_{q_{GM}} s_{f_S} - s_{q_{GM}} c_{f_S} \\ -s_{f_S} (c_{y_{GM}} c_{f_{GM}} + s_{y_{GM}} s_{q_{GM}} s_{f_{GM}}) + c_{q_{GM}} s_{f_{GM}} c_{f_S} \\ -s_{f_S} (-c_{y_{GM}} s_{f_{GM}} + s_{y_{GM}} s_{q_{GM}} c_{f_{GM}}) + c_{q_{GM}} c_{f_{GM}} c_{f_S} \end{Bmatrix}_G \quad (3-106)$$

Substituting this into equation 3-102 yields

$$\left(-\hat{z}_G \otimes \hat{S} \right) = \begin{Bmatrix} -s_{f_S} (c_{y_{GM}} c_{f_{GM}} + s_{y_{GM}} s_{q_{GM}} s_{f_{GM}}) + c_{q_{GM}} s_{f_{GM}} c_{f_S} \\ s_{y_{GM}} c_{q_{GM}} s_{f_S} + s_{q_{GM}} c_{f_S} \\ 0 \end{Bmatrix}_G \quad (3-107)$$

Equations 3-92, 3-93, 3-94, 3-101, and 3-107 constitute the basis of the BDWL gyro spin coil model. These equations are shown as implemented in Simulink in Figures 33 and 34.

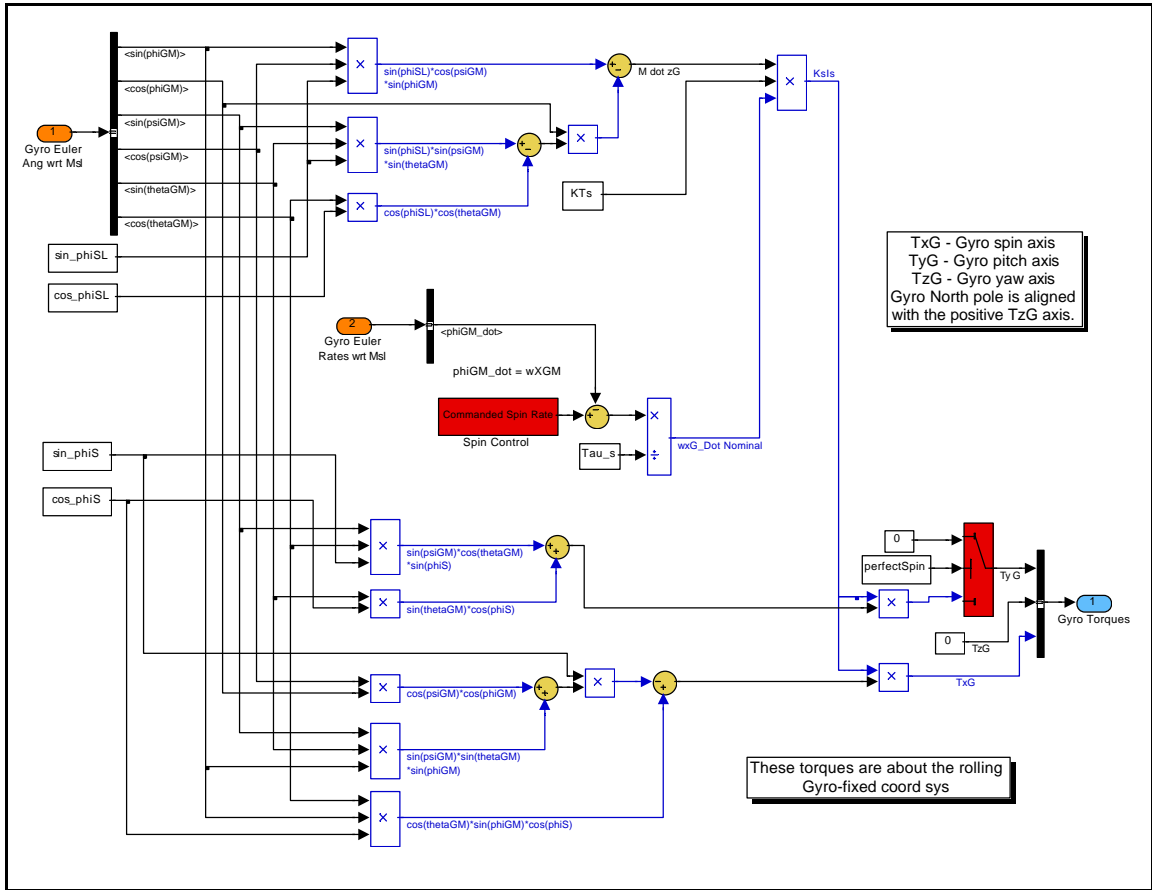


Figure 33 - BDWL gyro spin coil model.

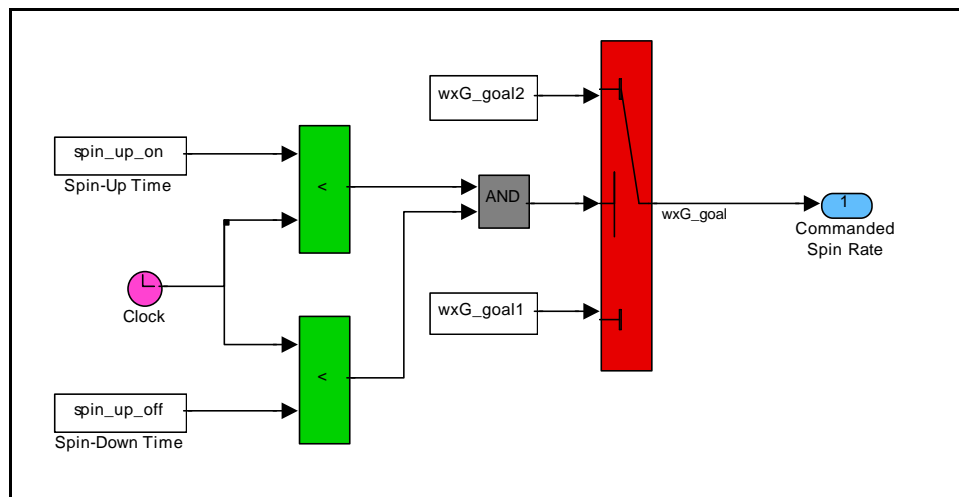


Figure 34 - BDWL spin coil commanded spin rate.

3.6 BDWL Gyro Model Assumptions and Limitations

The BDWL gyro model is the most detailed model of the three presented in this paper. It incorporates complex models of the gyro spin coil, precession coil and cage coil, as well as the effects of nutation damping. The BDWL model assumes that the gyro center of mass is perfectly aligned with its center of rotation. If this is not the case, then additional torques will be induced on the gyro from gravity effects and missile body motion. The BDWL model assumes that the gyro gimbal inertia is zero, or insignificant in comparison to the gyro inertia. Gyro spin friction drag is also not included in this model.

4.0 Derivation of Ideal Gyro Model

The ideal gyro model assumes that the gyro precesses in a perfectly linear fashion in the exact direction of commanded precession, at the exact commanded angular rate. The gyro spin control is also assumed to maintain the gyro spin rate at the exact commanded rate, with instantaneous spin-up and spin-down.

Many EO/IR missile models use ideal gyro models. Sometimes this is done to decrease computational complexity of the model, thus increasing execution speed. Proponents of this approach argue that an ideal gyro model is acceptable because the overall gyro performance is approximately ideal for a large portion of its region of operation.

Figure 35 shows the top level of the Ideal gyro model. It was based on the BDWL gyro model discussed in the previous section. The “gyro Euler angle missile dynamics compensation” block and the two cage coil blocks are identical to those used in the BDWL model and were explained in Chapter 3. The precession coil and gyro dynamics block are different than the BDWL model. Note that the Ideal model does not use a spin coil block.

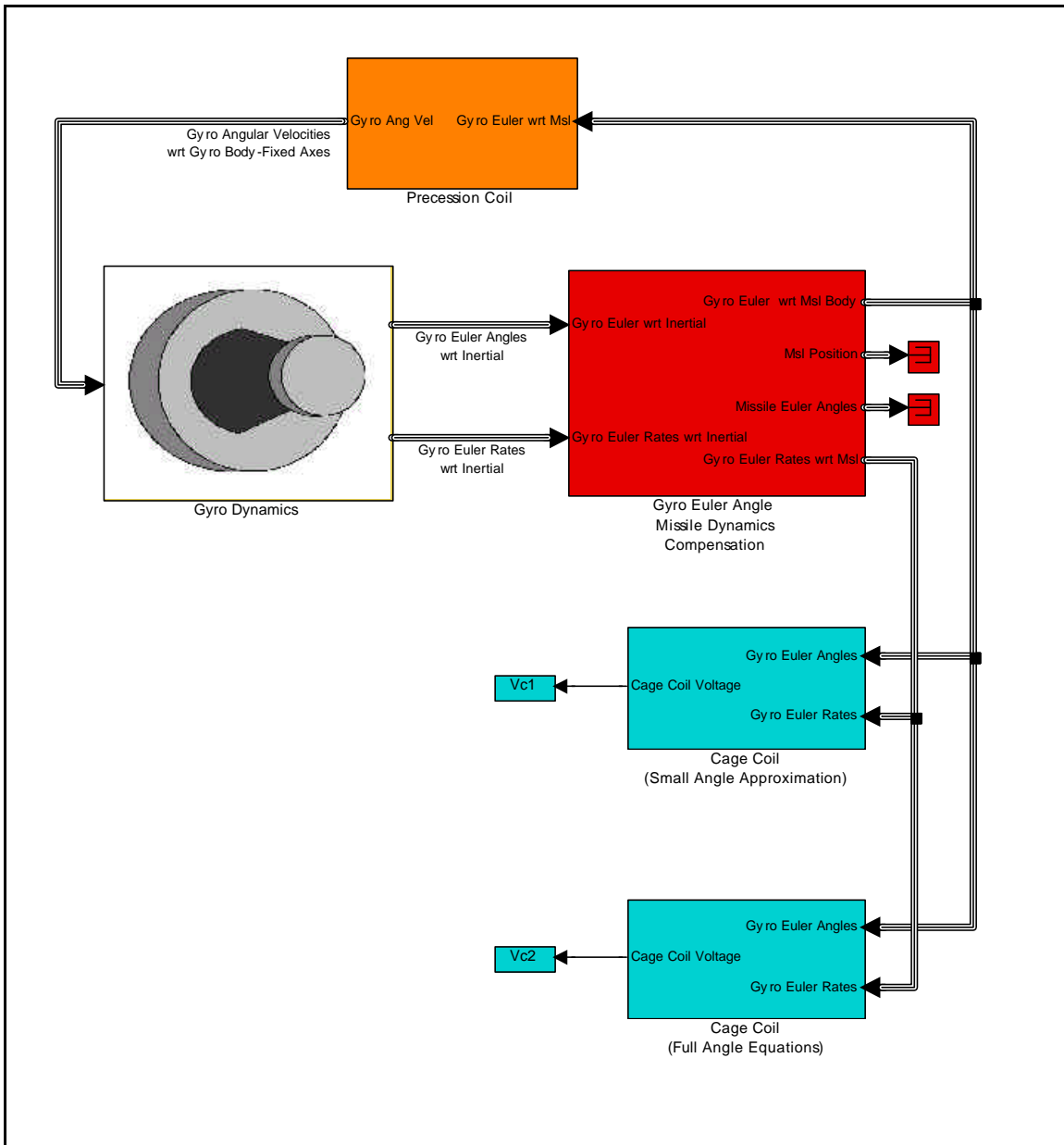


Figure 35 - Top level of Ideal gyro model.

4.1 Precession Coil

The Ideal gyro model executes the commanded precession in the precise direction and at the exact commanded angular rate. For this reason, it does not need inertia information for the gyro; thus, gyro torques are also not needed.

The only information necessary to compute gyro position is the commanded precession direction and rate. It was decided to use the commanded gyro precession direction and magnitude to find the gyro angular velocity in the precession coil block. The gyro dynamics block would then use this angular velocity to find the gyro inertial Euler angles.

For ease of use, it was decided to keep the control of the Ideal gyro model as close to the BDWL model as possible. Since the BDWL open loop model uses the angle \mathbf{g} to specify gyro precession direction and a variable called T_y to specify precession angular rate, it was decided to keep these variables the same. In the BDWL model, a \mathbf{g} of 0E produced a gyro pitch down precession. This equates to an angular rate in the $-y_{NRGM}$ (non-rolling gyro with respect to the missile) direction. Also, a \mathbf{g} of +90E produces a gyro yaw motion to the right (looking forward from the rear of the missile). This equates to an angular rate in the $+z_{NRGM}$ direction.

Thus, the gyro angular rate is measured by \mathbf{g} with $\mathbf{g} = 0^\circ$ being a rotation in the direction of the $-y_{NRGM}$ axis and \mathbf{g} increasing toward the $+z_{NRGM}$ axis. Also, noting that the angular rate is merely the value T_y , the expression for the gyro inertial angular rate in the non-rolling gyro with respect to missile coordinate system is,

$$\vec{\mathbf{w}}_{GI} = T_y \left[-\cos(\mathbf{g}) \hat{y}_{NRGM} + \sin(\mathbf{g}) \hat{z}_{NRGM} \right] \quad (4-1)$$

The gyro angular velocity must then be converted from the non-rolling gyro with respect to the missile coordinate system to the gyro body-fixed coordinate system,

$$\vec{\omega}_{GI} = {}^G D^{NRGM} \{ \vec{\omega}_{GI} \}_{NRGM} \quad (4-2)$$

$$\vec{\omega}_{GI} = \begin{bmatrix} 1 & 0 & 0 \\ 0 & \cos(\mathbf{f}_{GM}) & \sin(\mathbf{f}_{GM}) \\ 0 & -\sin(\mathbf{f}_{GM}) & \cos(\mathbf{f}_{GM}) \end{bmatrix} \begin{bmatrix} 0 \\ -T_y \cos(\mathbf{g}) \\ T_y \sin(\mathbf{g}) \end{bmatrix}_{NRGM} \quad (4-3)$$

$$\vec{\omega}_{GI} = T_y \begin{bmatrix} 0 \\ -c_g c_{\mathbf{f}_{GM}} + s_g s_{\mathbf{f}_{GM}} \\ c_g s_{\mathbf{f}_{GM}} + s_g c_{\mathbf{f}_{GM}} \end{bmatrix}_G \quad (4-4)$$

Equation 4-4 represents the generation of the gyro body-fixed angular velocity from the commanded precession rate and direction. This is shown in the Ideal gyro precession coil block in Figure 36. Note also that the reference coil signal is generated in the precession coil block in the same manner as the BDWL model.

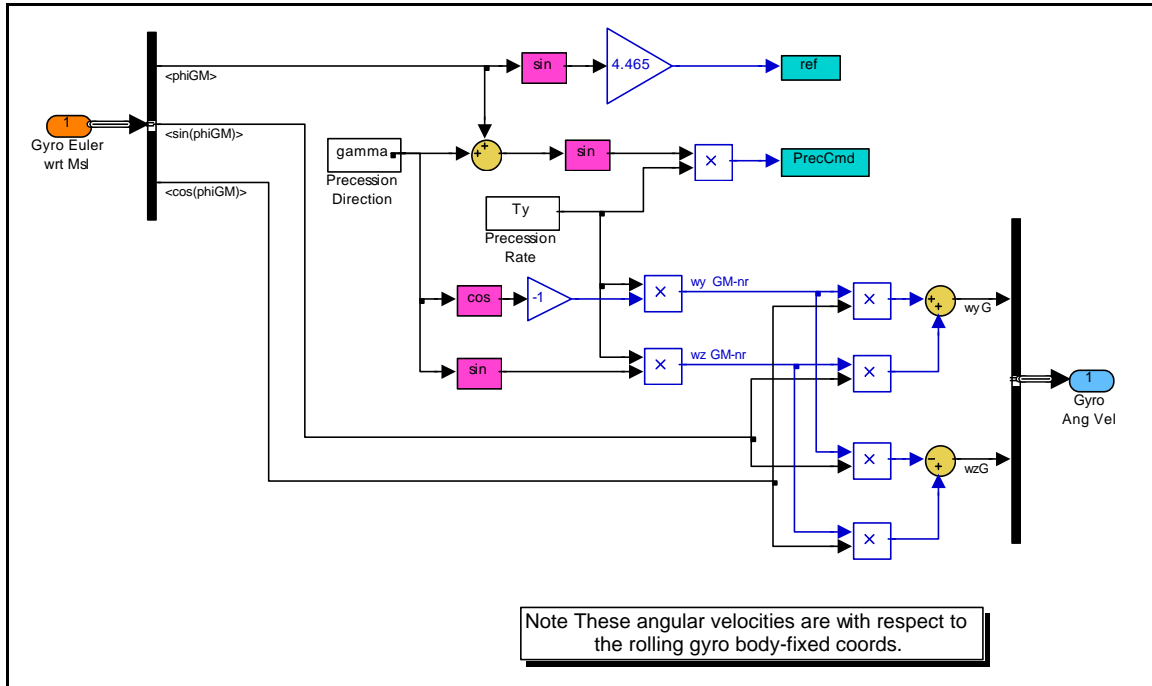


Figure 36 - Ideal gyro model precession coil block.

4.2 Equations of Motion / Gyro Dynamics

Figure 37 shows the Ideal gyro model “gyro dynamics” block. The gyro Euler angles are calculated from the gyro inertial angular rates (calculated in the precession coil block), which are expressed in the gyro body-fixed coordinate system. This is done with the “gyro angular position” block, which is identical to the “gyro angular position” block in the BDWL model. The y and z angular rates are input from the precession coil block, the x (spin) angular rate comes from a spin control block, shown in Figure 38. This block contains logic that causes the gyro spin rate to be the exact commanded rate.

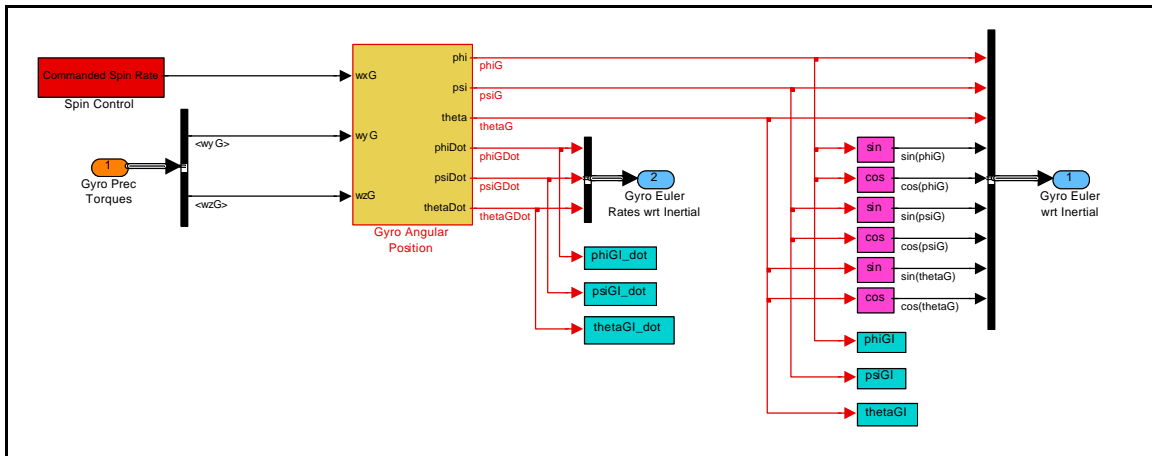


Figure 37 - Ideal gyro model gyro dynamics block.

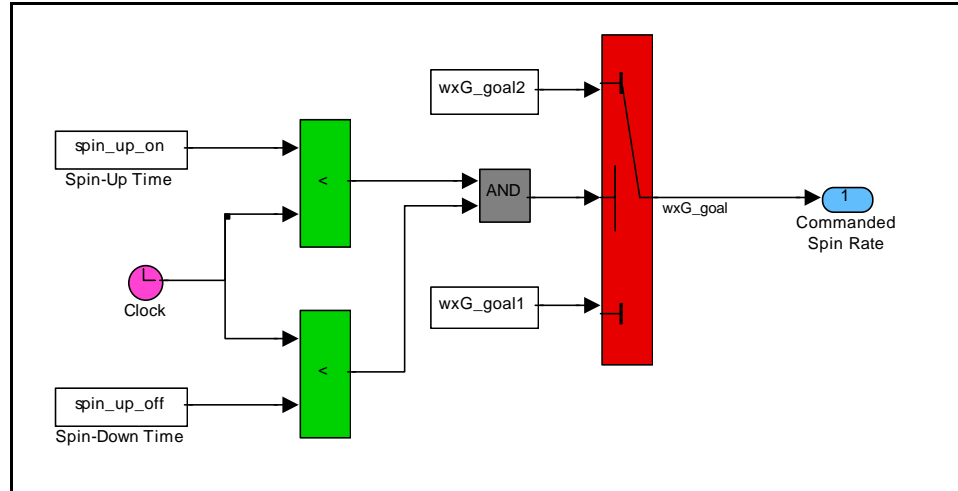


Figure 38 - Spin control block.

4.3 Ideal Gyro Model Assumptions and Limitations

The ideal gyro model assumes that the gyro executes the current precession command perfectly (both direction and angular rate), with no degradation regardless of the magnitude of the off boresight angle. Gyro torque is assumed to overcome gyro inertia perfectly. There is no nutation or nutation

damping, and spin control is perfect. The gyro executes the exact commanded spin rate with instantaneous spin-up and spin-down.

In addition to these assumptions, all the assumptions of the BDWL apply, such as gravity effects being ignored with the assumption that the gyro center of mass is perfectly aligned with its center of rotation.

5.0 Derivation of Gallaspy Gyro Model

This section details the derivation of the gyro model based on the work of Mr. Jason Gallaspy (12). In addition to being an independent gyro model derivation, Gallaspy derives his gyro equations of motion using the Lagrange method instead of classical Newtonian mechanics, which was used for the derivation of the Brown/Dougherty/Williams/Lamm gyro model. Figure 39 shows the top-level of the open loop Gallaspy gyro model containing the main gyro model function blocks, gyro dynamics and the torque and sensor coils (precession, cage, and spin coils).

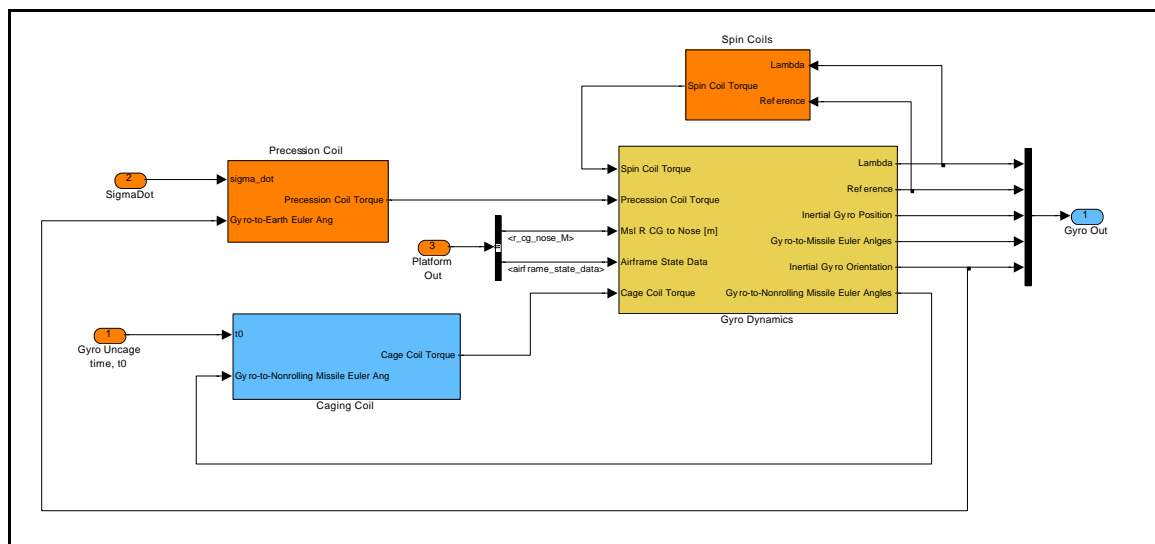


Figure 39 - Top level of open-loop Gallaspy gyro model.

As with the other models, Gallaspy assumes that the gyro center of rotation is at the gyro center of mass; this decouples the translational dynamics from the rotational dynamics. Also, it is assumed that the gyro rotational motion in inertial space is independent of missile motion and that the gyro motion is limited to spin and precession, with no nutation.

Gyro precession is defined as the motion of the gyro in the desired or commanded direction; gyro nutation is the unwanted motion of the gyro perpendicular to the desired direction of motion. (Nutation is seen as small “loops” on a plot of gyro motion.) Section 6.1 presents a more detailed discussion on the causes of gyro nutation. Gallaspy deems the omission of nutation effects in his gyro model acceptable, since most gyros use some form of nutation damping to minimize nutation effects.

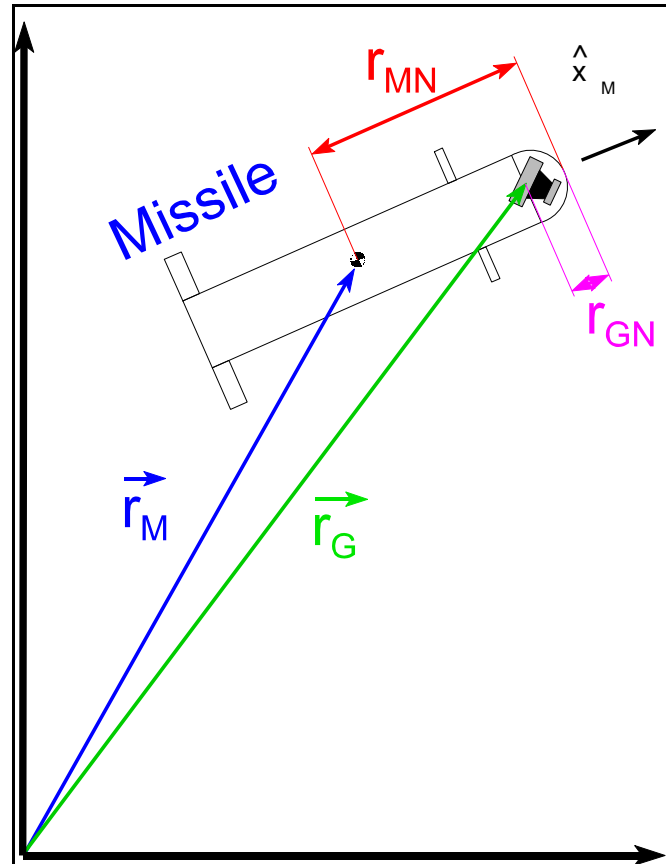


Figure 40 - Missile and gyro geometry.

5.1 Equation of Motion / Gyro Dynamics Derivation

The gyro position in inertial space is (see Figure 40):

$$\vec{r}_G = \vec{r}_M + (r_{MN} - r_{GN}) \cdot \hat{x}_M \quad (5-1)$$

where,

$$\vec{r}_G = \text{Gyro inertial position}$$

$$\vec{r}_M = \text{Missile inertial position}$$

r_{MN} = Distance of missile nose from missile cg

r_{GN} = Distance of gyro cg from missile nose

\hat{x}_M = Unit vector along missile longitudinal axis

The Lagrange method of deriving equations of motion comes from the idea that an external force acting on a system of rigid bodies will perform “work” on the system. Due to the conservation of energy, this work changes either the potential or the kinetic energy of the system. Lagrange’s method is expressed in the following equation (see Greenwood [2] for more detail on Lagrange’s method):

$$\frac{d}{dt} \left(\frac{\mathcal{T}}{\mathcal{I}\dot{q}_i} \right) - \frac{\mathcal{T}}{\mathcal{I}q_i} + \frac{\mathcal{V}}{\mathcal{I}q_i} = Q_i \quad (5-2)$$

where,

i = number of degrees of freedom

q_i = i th degree of freedom

Q_i = i th generalized force

T = system kinetic energy

V = system potential energy

For the Gallaspy gyro model,

$$i = 1,2,3 \quad (5-3)$$

$$\mathbf{q}_i = \{ \mathbf{y}_{GI} \quad \mathbf{q}_{GI} \quad \mathbf{f}_{GI} \} \quad (5-4)$$

$$\mathbf{Q}_i = \{ Q_{y_{GI}} \quad Q_{q_{GI}} \quad Q_{f_{GI}} \} \quad (5-5)$$

Here, \mathbf{y}_{GI} , \mathbf{q}_{GI} , and \mathbf{f}_{GI} are the gyro Euler angles with respect to the inertial reference frame, as previously defined.

Since the gyro center of rotation is at the gyro cg, gravity does not affect the rotation of the gyro. Also, Gallaspy assumes that the gyro has no means of storing energy (in gimbal structures, etc.), thus, the gyro potential energy is zero,

$$V = 0 \quad (5-6)$$

The gyro rotational kinetic energy is the vectorized rotational equivalent of the linear kinetic energy ($\frac{1}{2} mv^2$),

$$T = \frac{1}{2} \cdot \left\{ \mathbf{w}_{G_x} \quad \mathbf{w}_{G_y} \quad \mathbf{w}_{G_z} \right\} \cdot [I_G] \cdot \begin{Bmatrix} \mathbf{w}_{G_x} \\ \mathbf{w}_{G_y} \\ \mathbf{w}_{G_z} \end{Bmatrix} \quad (5-7)$$

where \mathbf{w}_{G_x} = Gyro angular velocity about gyro body X axis

\mathbf{w}_{G_y} = Gyro angular velocity about gyro body Y axis

\mathbf{w}_{G_z} = Gyro angular velocity about gyro body Z axis

$[I_G]$ = Gyro rotational inertia matrix

From the definition of Euler angles (body 3-2-1 rotation as defined in section 2.0), and using the inertial coordinate system, an expression for the gyro angular velocity vector can be found,

$$\begin{aligned} \bar{\mathbf{w}}_G = & \dot{\mathbf{y}}_{GI} \hat{\mathbf{z}}_I + \dot{\mathbf{q}}_{GI} (-\sin(\mathbf{y}_{GI}) \hat{\mathbf{x}}_I + \cos(\mathbf{y}_{GI}) \hat{\mathbf{y}}_I) \\ & + \dot{\mathbf{f}}_{GI} [\cos(\mathbf{q}_{GI}) (\cos(\mathbf{y}_{GI}) \hat{\mathbf{x}}_I + \sin(\mathbf{y}_{GI}) \hat{\mathbf{y}}_I) - \sin(\mathbf{q}_{GI}) \hat{\mathbf{z}}_I] \end{aligned} \quad (5-8)$$

Rearranging this and collecting terms yields:

$$\begin{aligned} \bar{\mathbf{w}}_G = & \left(-\dot{\mathbf{q}}_{GI} s_{y_{GI}} + \dot{\mathbf{f}}_{GI} c_{y_{GI}} c_{q_{GI}} \right) \hat{x}_I + \left(\dot{\mathbf{q}}_{GI} c_{y_{GI}} + \dot{\mathbf{f}}_{GI} s_{y_{GI}} c_{q_{GI}} \right) \hat{y}_I \\ & + \left(\dot{\mathbf{y}}_{GI} - \dot{\mathbf{f}}_{GI} s_{q_{GI}} \right) \hat{z}_I \end{aligned} \quad (5-9)$$

Finally, the inertial-to-gyro direction cosine coordinate transformation matrix is used to convert this to the gyro body-fixed coordinate system:

$$\begin{aligned} \bar{\mathbf{w}}_G = & \left(-\dot{\mathbf{y}}_{GI} s_{q_{GI}} + \dot{\mathbf{f}}_{GI} \right) \hat{x}_G + \left(\dot{\mathbf{y}}_{GI} c_{q_{GI}} s_{f_{GI}} + \dot{\mathbf{q}}_{GI} c_{f_{GI}} \right) \hat{y}_G \\ & + \left(\dot{\mathbf{y}}_{GI} c_{q_{GI}} c_{f_{GI}} - \dot{\mathbf{q}}_{GI} s_{f_{GI}} \right) \hat{z}_G \end{aligned} \quad (5-10)$$

Thus,

$$\bar{\mathbf{w}}_G = \begin{Bmatrix} -\dot{\mathbf{y}}_{GI} s_{q_{GI}} + \dot{\mathbf{f}}_{GI} \\ \dot{\mathbf{y}}_{GI} c_{q_{GI}} s_{f_{GI}} + \dot{\mathbf{q}}_{GI} c_{f_{GI}} \\ \dot{\mathbf{y}}_{GI} c_{q_{GI}} c_{f_{GI}} - \dot{\mathbf{q}}_{GI} s_{f_{GI}} \end{Bmatrix}_G \quad (5-11)$$

and,

$$\mathbf{w}_{G_x} = -\dot{\mathbf{y}}_{GI} s_{q_{GI}} + \dot{\mathbf{f}}_{GI} \quad (5-12)$$

$$\mathbf{w}_{G_y} = \dot{\mathbf{y}}_{GI} c_{q_{GI}} s_{f_{GI}} + \dot{\mathbf{q}}_{GI} c_{f_{GI}} \quad (5-13)$$

$$\mathbf{w}_{G_z} = \dot{\mathbf{y}}_{GI} c_{q_{GI}} c_{f_{GI}} - \dot{\mathbf{q}}_{GI} s_{f_{GI}} \quad (5-14)$$

The inertia matrix is the same as was shown in equations 3-7, 3-8, and 3-9:

$$I_G = \begin{bmatrix} I_s & 0 & 0 \\ 0 & I_t & 0 \\ 0 & 0 & I_t \end{bmatrix} \quad (5-15)$$

The gyro rotational kinetic energy, T , can now be calculated by substituting equations 5-12 through 5-15 into equation 5-7:

$$T = (I_s/2) \cdot (\dot{\mathbf{y}}_{GI}^2 s_{q_{GI}}^2 - 2\dot{\mathbf{y}}_{GI} \dot{\mathbf{f}}_{GI} s_{q_{GI}} + \dot{\mathbf{f}}_{GI}^2) + (I_t/2) \cdot (\dot{\mathbf{y}}_{GI}^2 c_{q_{GI}}^2 + \dot{\mathbf{q}}_{GI}^2) \quad (5-16)$$

Next, the partial derivatives and time derivatives of T must be calculated for inclusion into the Lagrange equation (5-2), start with the \mathbf{y} related terms:

$$\frac{\mathcal{I}T}{\mathcal{I}\dot{\mathbf{y}}} = I_s \dot{\mathbf{y}}_{GI} s_{q_{GI}}^2 - I_s \dot{\mathbf{f}}_{GI} s_{q_{GI}} + I_t \dot{\mathbf{y}}_{GI} c_{q_{GI}}^2 \quad (5-17)$$

$$\begin{aligned} \frac{d}{dt} \left(\frac{\mathcal{I}T}{\mathcal{I}\dot{\mathbf{y}}} \right) &= I_s \ddot{\mathbf{y}}_{GI} s_{q_{GI}}^2 + 2I_s \dot{\mathbf{y}}_{GI} \dot{\mathbf{q}}_{GI} s_{q_{GI}} c_{q_{GI}} - I_s \ddot{\mathbf{f}}_{GI} s_{q_{GI}} - I_s \dot{\mathbf{q}}_{GI} \dot{\mathbf{f}}_{GI} c_{q_{GI}} \\ &+ I_t \ddot{\mathbf{y}}_{GI} c_{q_{GI}}^2 - 2I_t \dot{\mathbf{y}}_{GI} \dot{\mathbf{q}}_{GI} s_{q_{GI}} c_{q_{GI}} \end{aligned} \quad (5-18)$$

$$-\frac{\mathcal{I}T}{\mathcal{I}\mathbf{y}} = 0 \quad (5-19)$$

Substituting equations 5-18 and 5-19 into equation 5-2 produces the first term of the Lagrange equations:

$$\begin{aligned} &- I_s \ddot{\mathbf{f}}_{GI} s_{q_{GI}} - I_s \dot{\mathbf{f}}_{GI} \dot{\mathbf{q}}_{GI} c_{q_{GI}} + (I_s s_{q_{GI}}^2 + I_t c_{q_{GI}}^2) \ddot{\mathbf{y}}_{GI} \\ &+ 2(I_s - I_t) \dot{\mathbf{y}}_{GI} \dot{\mathbf{q}}_{GI} s_{q_{GI}} c_{q_{GI}} = Q_{y_{GI}} \end{aligned} \quad (5-20)$$

Next, evaluate the \mathbf{q} terms:

$$\frac{\mathcal{I}T}{\mathcal{I}\dot{\mathbf{q}}} = I_t \dot{\mathbf{q}}_{GI} \quad (5-21)$$

$$\frac{d}{dt} \left(\frac{\mathcal{I}T}{\mathcal{I}\dot{\mathbf{q}}} \right) = I_t \ddot{\mathbf{q}}_{GI} \quad (5-22)$$

$$-\frac{\mathcal{T}}{\mathcal{q}} = -I_s \dot{\mathbf{y}}_{GI}^2 s_{q_{GI}} c_{q_{GI}} + I_s \dot{\mathbf{y}}_{GI} \dot{\mathbf{f}}_{GI} c_{q_{GI}} + I_s \dot{\mathbf{y}}_{GI}^2 s_{q_{GI}} c_{q_{GI}} \quad (5-23)$$

The \mathbf{q} related term of the Lagrange equation is found by substituting equations 5-22 and 5-23 into equation 5-2:

$$I_t \ddot{\mathbf{q}}_{GI} + I_s \dot{\mathbf{f}}_{GI} \dot{\mathbf{y}}_{GI} c_{q_{GI}} - (I_s - I_t) \dot{\mathbf{y}}_{GI}^2 s_{q_{GI}} c_{q_{GI}} = Q_{q_{GI}} \quad (5-24)$$

Finally, the \mathbf{f} terms are calculated:

$$\frac{\mathcal{T}}{\mathcal{f}} = -I_s \dot{\mathbf{y}}_{GI} s_{q_{GI}} + I_s \dot{\mathbf{f}}_{GI} \quad (5-25)$$

$$\frac{d}{dt} \left(\frac{\mathcal{T}}{\mathcal{f}} \right) = -I_s \ddot{\mathbf{y}}_{GI} s_{q_{GI}} - I_s \dot{\mathbf{y}}_{GI} \dot{\mathbf{q}}_{GI} c_{q_{GI}} + I_s \ddot{\mathbf{f}}_{GI} \quad (5-26)$$

$$-\frac{\mathcal{T}}{\mathcal{f}} = 0 \quad (5-27)$$

The final Lagrange equation is found by substituting equations 5-26 and 5-27 into equation 5-2:

$$I_s \ddot{\mathbf{f}}_{GI} - I_s \ddot{\mathbf{y}}_{GI} s_{q_{GI}} - I_s \dot{\mathbf{y}}_{GI} \dot{\mathbf{q}}_{GI} c_{q_{GI}} = Q_{f_{GI}} \quad (5-28)$$

The complete system of Lagrange equations are made up of equations 5-20, 5-24, and 5-28. These equations are for the general case. Recall Gallaspy assumes that the gyro has an effective nutation damper which limits its motion to spin and precession. Thus, terms involving roll rate and roll acceleration are kept, while terms which are solely functions of pitch or yaw rates or accelerations are dropped, which leaves:

$$Q_{y_{GI}} = -I_s \ddot{\mathbf{f}}_{GI} s_{q_{GI}} - I_s \dot{\mathbf{f}}_{GI} \dot{\mathbf{q}}_{GI} c_{q_{GI}} \quad (5-29)$$

$$Q_{q_{GI}} = I_s \dot{\mathbf{f}}_{GI} \dot{\mathbf{y}}_{GI} c_{q_{GI}} \quad (5-30)$$

$$Q_{f_{GI}} = I_s \ddot{\mathbf{f}}_{GI} \quad (5-31)$$

In the case of applying the Lagrange method to the rotational dynamics of a gyro, the generalized forces (Q_i) are the torques acting on gyro. These torques cause incremental changes in the gyro degrees of freedom (q_i), which are the Euler angles. In order to calculate the gyro torques, Gallaspy starts with the total incremental work done on the system, which is also called virtual work:

$$dW = \sum_i Q_i dq_i \quad (5-32)$$

For an arbitrary torque $\vec{\tau}$, and an arbitrary Euler angle incremental change represented by $d\mathbf{g}$ (also called virtual displacement), the virtual work is

$$dW = \vec{\tau} d\mathbf{g} \quad (5-33)$$

The virtual displacement can be found by

$$d\mathbf{g} = \vec{\mathbf{w}}_G \Big|_{\dot{q}_i = dq_i} \quad (5-34)$$

Note that $\vec{\tau}$ and $\vec{\mathbf{w}}_G$ could be written in any coordinate system. Gallaspy chooses the non-rolling gyro (with respect to inertial) coordinate system, which simplifies the terms. The non-rolling gyro with respect to inertial coordinate system will be designated with the subscript "NRGI". The NRGI-to-inertial

direction cosine matrix can be calculated from the gyro-to-inertial direction cosine as follows:

$$\left[{}^I D^{NRGI} \right] = \left[{}^I D^G \right]_{\mathbf{f}_{GI}=0} \quad (5-35)$$

Transforming the gyro angular velocity to the NRGI coordinate system yields:

$$\bar{\mathbf{w}}_G = \left(-\dot{\mathbf{y}}_{GI} s_{q_{GI}} + \dot{\mathbf{f}}_{GI} \right) \hat{x}_{NRGI} + \left(\dot{\mathbf{q}}_{GI} \right) \hat{y}_{NRGI} + \left(\dot{\mathbf{y}}_{GI} c_{q_{GI}} \right) \hat{z}_{NRGI} \quad (5-36)$$

Using this expression for gyro angular velocity with the definition of virtual displacement, equation 5-34, gives:

$$\overrightarrow{d\mathbf{g}} = \left(-d\mathbf{y}_{GI} s_{q_{GI}} + d\mathbf{f}_{GI} \right) \hat{x}_{NRGI} + \left(d\mathbf{q}_{GI} \right) \hat{y}_{NRGI} + \left(d\mathbf{y}_{GI} c_{q_{GI}} \right) \hat{z}_{NRGI} \quad (5-37)$$

Substituting equation 5-37 into equation 5-33 gives the virtual work done by $\bar{\mathbf{f}}$,

$$dW = \left(-d\mathbf{y}_{GI} s_{q_{GI}} + d\mathbf{f}_{GI} \right) \mathbf{t}_{x_{NRGI}} + \left(d\mathbf{q}_{GI} \right) \mathbf{t}_{y_{NRGI}} + \left(d\mathbf{y}_{GI} c_{q_{GI}} \right) \mathbf{t}_{z_{NRGI}} \quad (5-38)$$

By definition, this virtual work is equal to

$$dW = Q_{y_{GI}} d\mathbf{y}_{GI} + Q_{q_{GI}} d\mathbf{q}_{GI} + Q_{f_{GI}} d\mathbf{f}_{GI} \quad (5-39)$$

Combining equations 5-38 and 5-39 and putting in vector form yields

$$\begin{Bmatrix} Q_{f_{GI}} \\ Q_{q_{GI}} \\ Q_{y_{GI}} \end{Bmatrix} = \begin{bmatrix} 1 & 0 & 0 \\ 0 & 1 & 0 \\ -s_{q_{GI}} & 0 & c_{q_{GI}} \end{bmatrix} \begin{Bmatrix} \mathbf{t}_{x_{NRGI}} \\ \mathbf{t}_{y_{NRGI}} \\ \mathbf{t}_{z_{NRGI}} \end{Bmatrix} \quad (5-40)$$

Solving this expression for the torques,

$$\begin{Bmatrix} \mathbf{t}_{x_{NRGI}} \\ \mathbf{t}_{y_{NRGI}} \\ \mathbf{t}_{z_{NRGI}} \end{Bmatrix} = \begin{bmatrix} 1 & 0 & 0 \\ 0 & 1 & 0 \\ t_{q_{GI}} & 0 & 1/c_{q_{GI}} \end{bmatrix} \begin{Bmatrix} Q_{j_{GI}} \\ Q_{q_{GI}} \\ Q_{y_{GI}} \end{Bmatrix} \quad (5-41)$$

Using equation 5-41 with equations 5-29, 5-30, and 5-31 gives the gyro rotational equations of motion:

$$\mathbf{t}_{x_{NRGI}} = I_s \ddot{\mathbf{f}}_{GI} \quad (5-42)$$

$$\mathbf{t}_{y_{NRGI}} = I_s \dot{\mathbf{f}}_{GI} \dot{\mathbf{y}}_{GI} c_{q_{GI}} \quad (5-43)$$

$$\mathbf{t}_{z_{NRGI}} = -I_s \dot{\mathbf{f}}_{GI} \dot{\mathbf{q}}_{GI} \quad (5-44)$$

In order to implement these equations of motion into a simulation, Gallaspy solves for the Euler angular rates:

$$\dot{\mathbf{f}}_{GI} = \frac{1}{I_s} \int_0^t \mathbf{t}_{x_{NRGI}} dt + \dot{\mathbf{f}}(0) \quad (5-45)$$

$$\dot{\mathbf{q}}_{GI} = -\frac{1}{I_s \dot{\mathbf{f}}_{GI}} \mathbf{t}_{z_{NRGI}} \quad (5-46)$$

$$\dot{\mathbf{y}}_{GI} = \frac{1}{I_s \dot{\mathbf{f}}_{GI} c_{q_{GI}}} \mathbf{t}_{y_{NRGI}} \quad (5-47)$$

The differential equations shown above in equations 5-45, 5-46, and 5-47 can be used to calculate the gyro Euler angles, given the input torques. Recall Figure 39 which shows the top-level of the Gallaspy gyro model. Figure 41 shows the gyro dynamics block. Inside the gyro dynamics block is the rotation dynamics block, shown in Figure 42. This block is where the gyro equations of motion, equations 5-45, 5-46, and 5-47 are implemented.

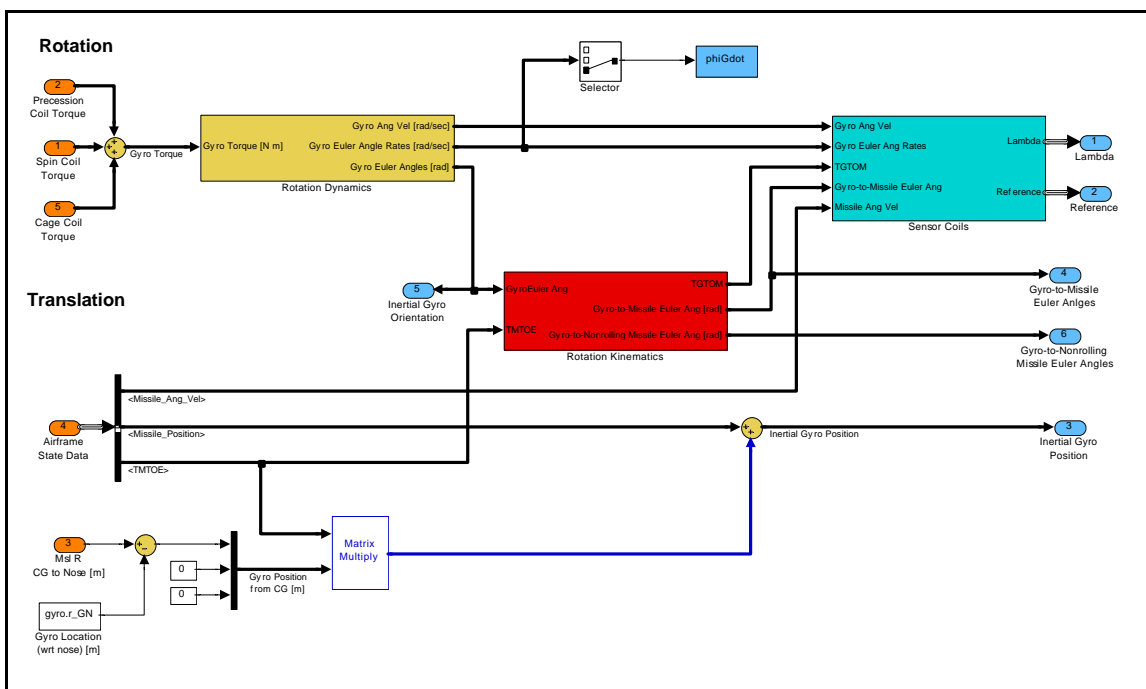


Figure 42 - Gallaspy gyro dynamics block.

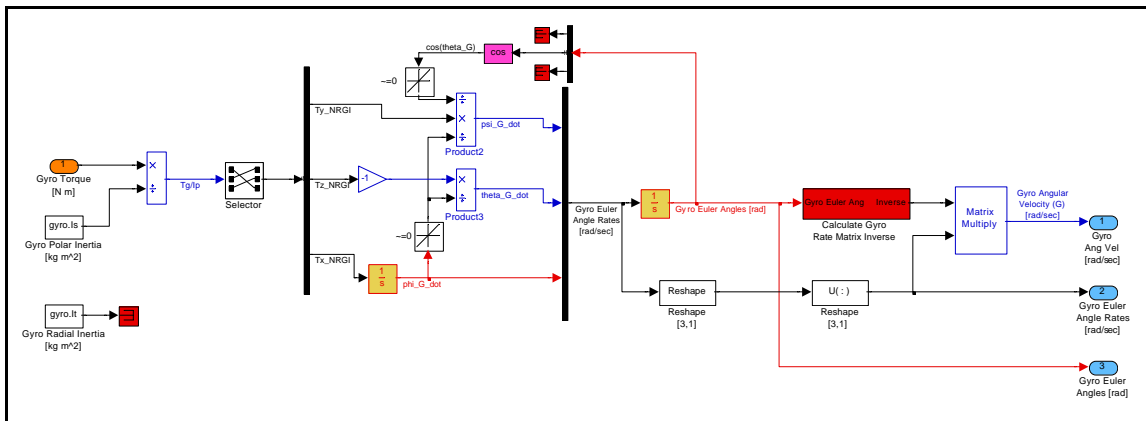


Figure 41 - Gallaspy rotation dynamics block.

5.2 Rotation Dynamics

Note from Figure 41 that the gyro angular velocity vector is also an output of the rotation dynamics block. The gyro angular velocity can be calculated from the gyro Euler angles and the Euler angle rates. This is derived from equation 5-11, which can be rewritten in matrix form

$$\begin{Bmatrix} \mathbf{w}_{G_xGI} \\ \mathbf{w}_{G_yGI} \\ \mathbf{w}_{G_zGI} \end{Bmatrix} = \begin{bmatrix} -s_{q_{GI}} & 0 & 1 \\ c_{q_{GI}} s_{f_{GI}} & c_{f_{GI}} & 0 \\ c_{q_{GI}} c_{f_{GI}} & -s_{f_{GI}} & 0 \end{bmatrix} \begin{Bmatrix} \dot{\mathbf{y}}_{GI} \\ \dot{\mathbf{q}}_{GI} \\ \dot{\mathbf{f}}_{GI} \end{Bmatrix} \quad (5-48)$$

Equation 5-48 is implemented in the rotation dynamics block, in a block called “calculate gyro rate matrix inverse”. This block is shown in Figure 43.

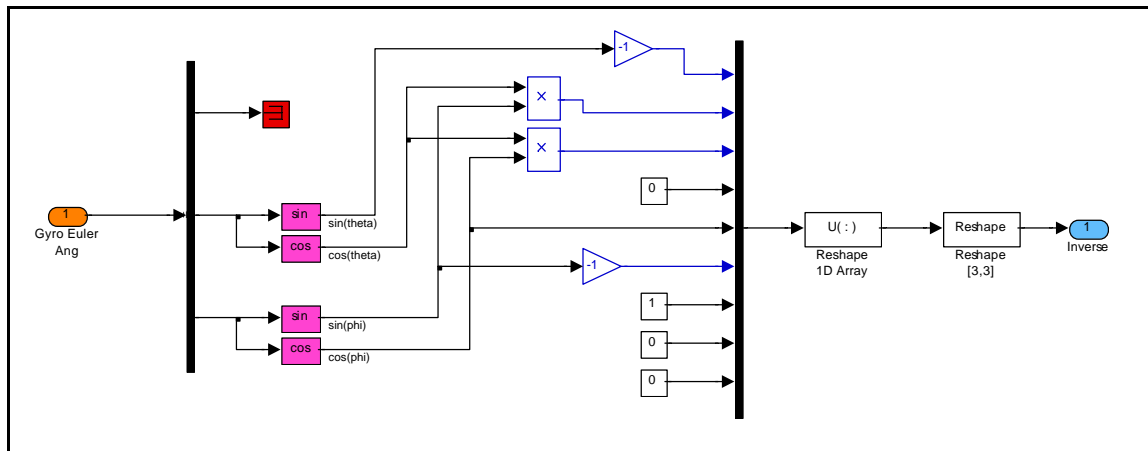


Figure 43 - Gallaspy calculate gyro rate matrix inverse block.

5.3 Rotation Kinematics

The next block in the Gallaspy Gyro Dynamics block is the rotation kinematics block. This block takes the gyro inertial Euler angles and the missile inertial Euler angles and combines them using linear algebra to obtain the gyro

Euler angles with respect to the missile. Figure 44 shows the rotation kinematics block.

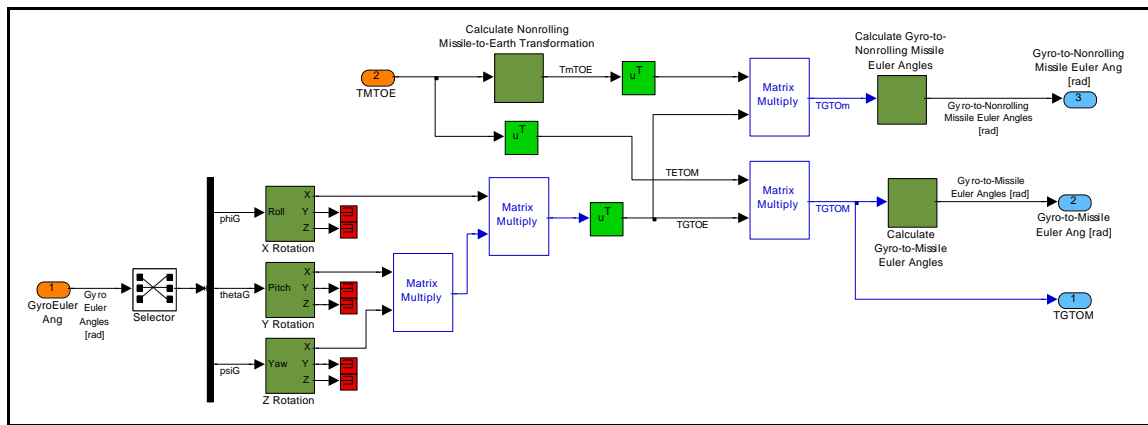


Figure 44 - Gallaspy rotation kinematics block.

Starting from the left, with input 1, the gyro-to-inertial direction transformation matrix is formed (labeled TGTOE in the rotation kinematics block). This is done by forming the individual Euler angle direction cosine matrices, then multiplying them together. The X rotation, Y rotation, and Z rotation blocks form each individual Euler angle direction cosine matrix (see Section 2.1 for a discussion on Euler angle rotations). Figures 45 - 47 show the X rotation, Y rotation, and Z rotation blocks.

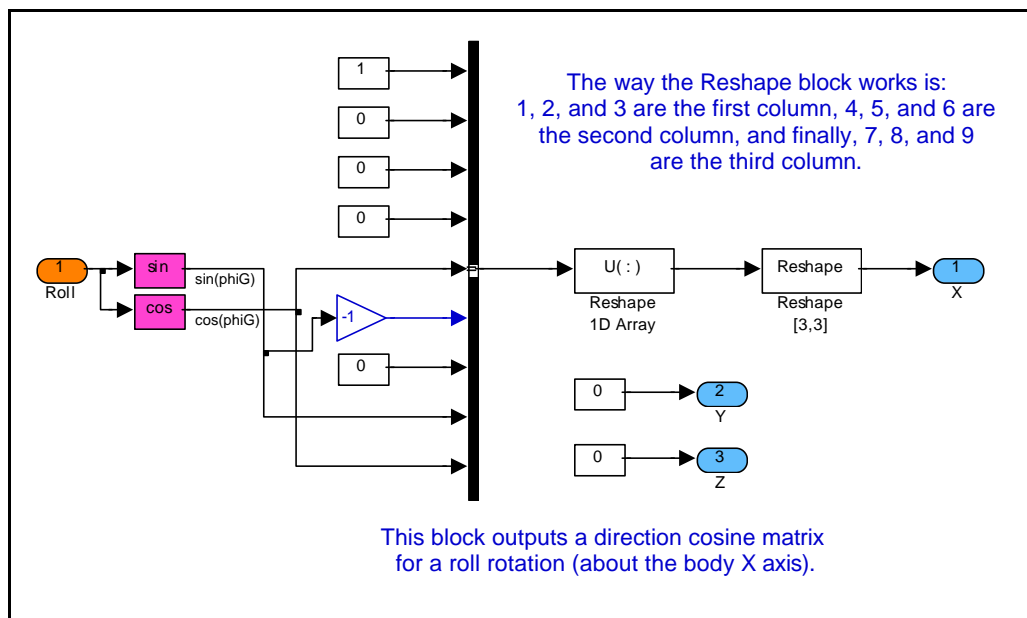


Figure 45 - Gallaspy X rotation block.

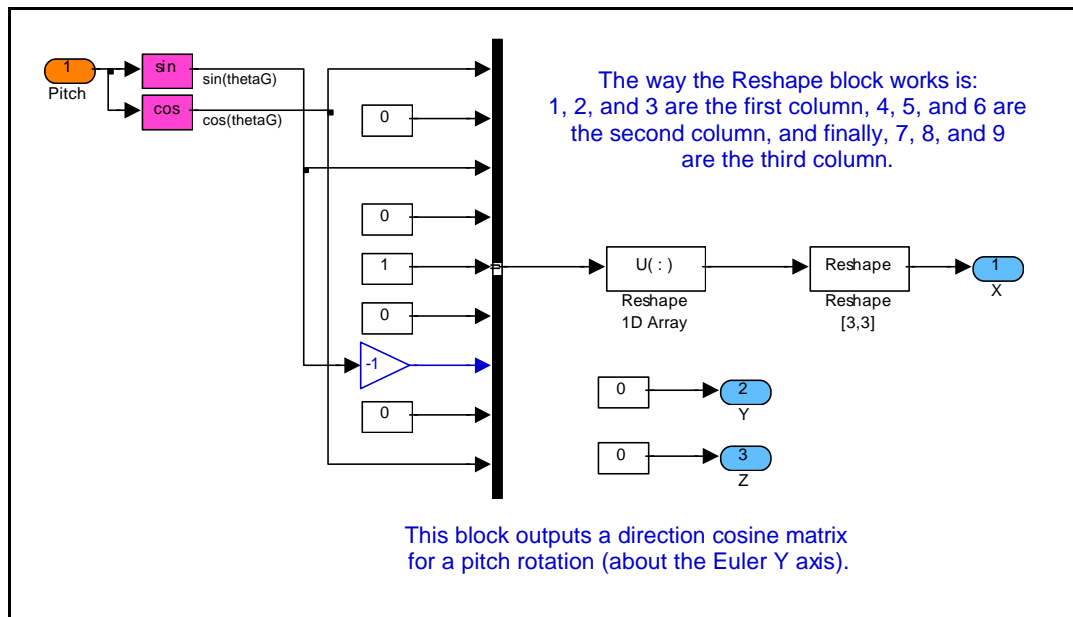


Figure 46 - Gallaspy Y rotation block.

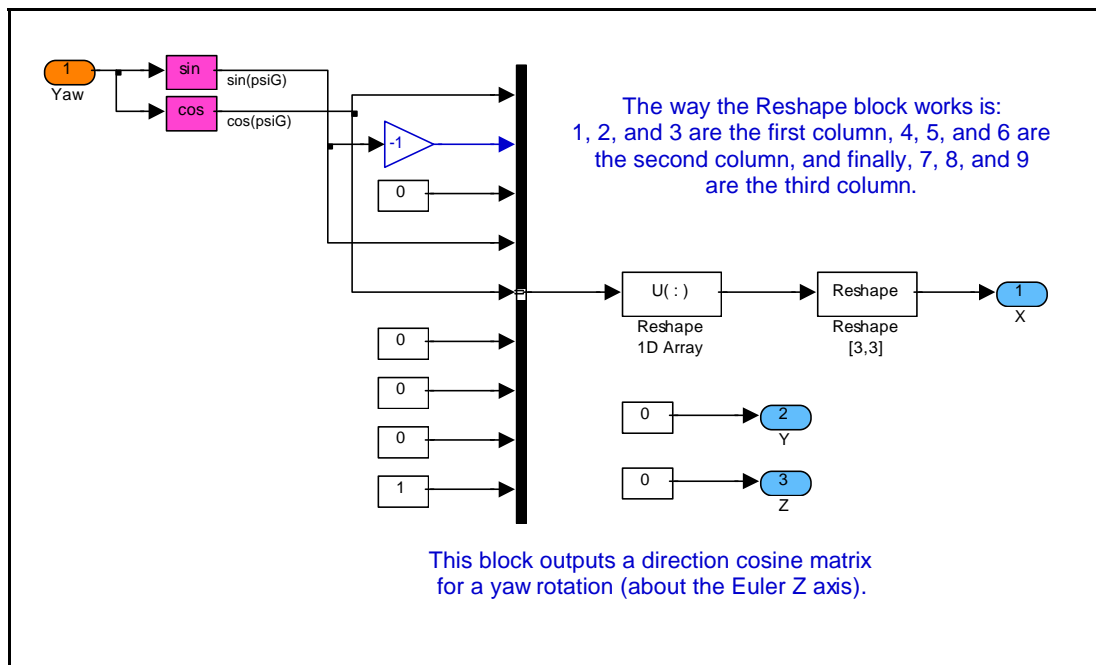


Figure 47 - Gallaspy Z rotation block.

Input 2 to the rotation kinematics block is the missile-to-inertial (TMTOE) coordinate transformation matrix. This is transposed to form the inertial-to-missile (TETOM) direction cosine matrix. The inertial-to-missile direction cosine matrix is multiplied with the gyro-to-inertial direction cosine matrix to form the gyro-to-missile transformation matrix. In equation form this can be expressed as

$${}^M D^G = {}^M D^I \cdot {}^I D^G \quad (5-49)$$

The gyro-to-missile Euler angles can be calculated by taking the inverse trigonometric functions of certain direction cosine elements. This follows from the definition of a direction cosine matrix in Gallaspy (12) and Lamm (13). These relationships are detailed in equations 5-50, 5-51, and 5-52. In these equations, the individual direction cosine elements are referred to by using subscripts. For example, the element in the second row, first column of the

gyro-to-missile direction cosine matrix is denoted by ${}^M D_{2,1}^G$.

$$\mathbf{y}_{GM} = \tan^{-1}\left({}^M D_{2,1}^G / {}^M D_{1,1}^G\right) \quad (5-50)$$

for $0 \leq \mathbf{y}_{GM} \leq 2\mathbf{p}$,

$$\mathbf{q}_{GM} = -\sin^{-1}\left({}^M D_{3,1}^G\right) \quad (5-51)$$

for $-\mathbf{p}/2 \leq \mathbf{q}_{GM} \leq \mathbf{p}/2$,

$$\mathbf{f}_{GM} = \tan^{-1}\left({}^M D_{3,2}^G / {}^M D_{3,3}^G\right) \quad (5-52)$$

for $0 \leq \mathbf{f}_{GM} \leq 2\mathbf{p}$.

These equations are implemented in the “calculate gyro-to-missile Euler angle” block, shown in Figure 48. The gyro-to-missile direction cosine and the gyro-to-missile Euler angles are outputs 1 and 2 for the rotation kinematics block. Input 2, the missile-to-inertial direction cosine matrix, goes through the “calculate nonrolling missile-to-earth transformation” block, shown in Figure 49. Here, Earth is used synonymously with “inertial”. This block calculates the missile roll angle with respect to inertial, then forms the roll direction cosine matrix and uses it with the missile-to-inertial direction cosine to remove the roll component rotation.

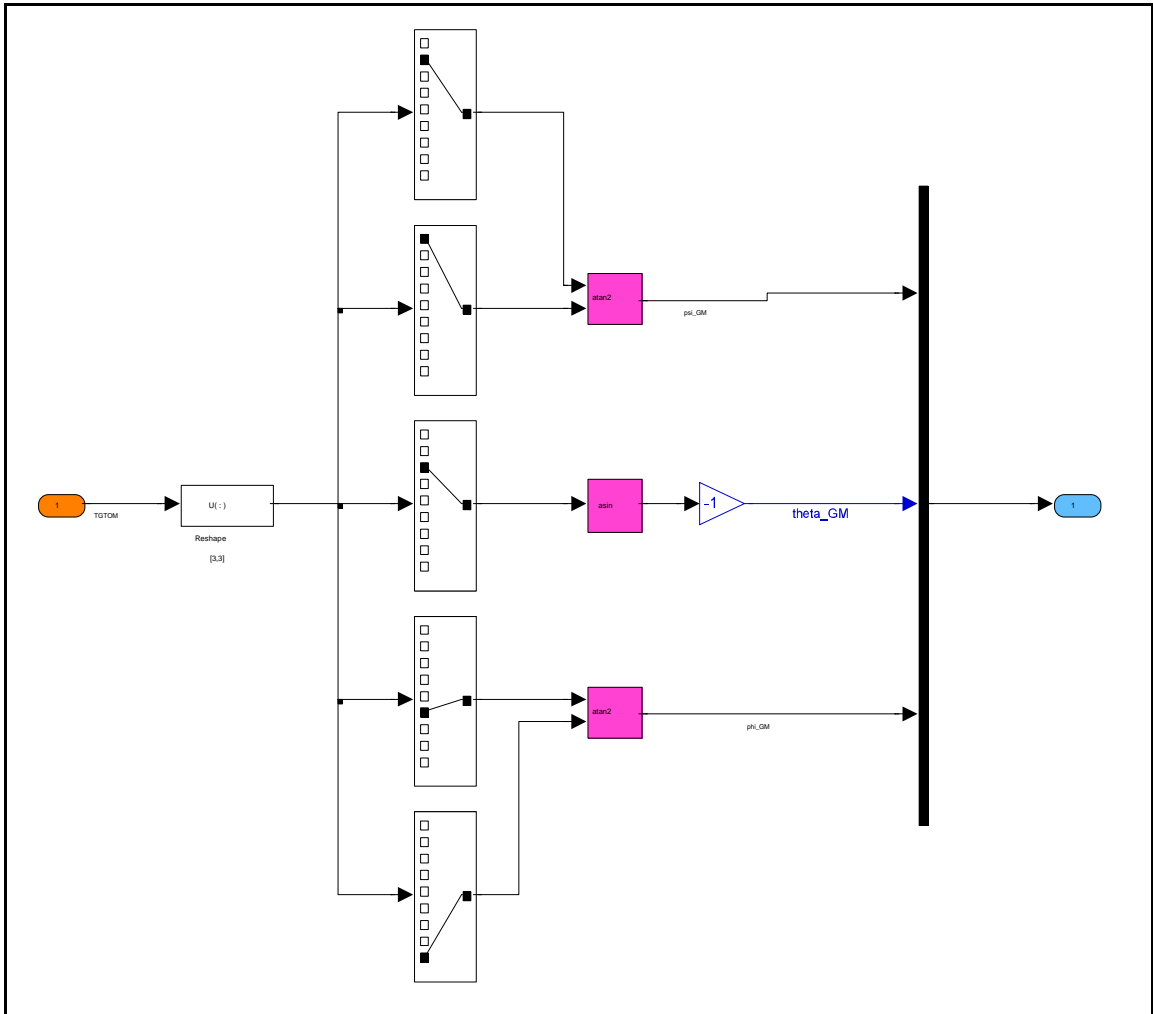


Figure 48 - Gallaspy calculate gyro-to-missile Euler angles block.

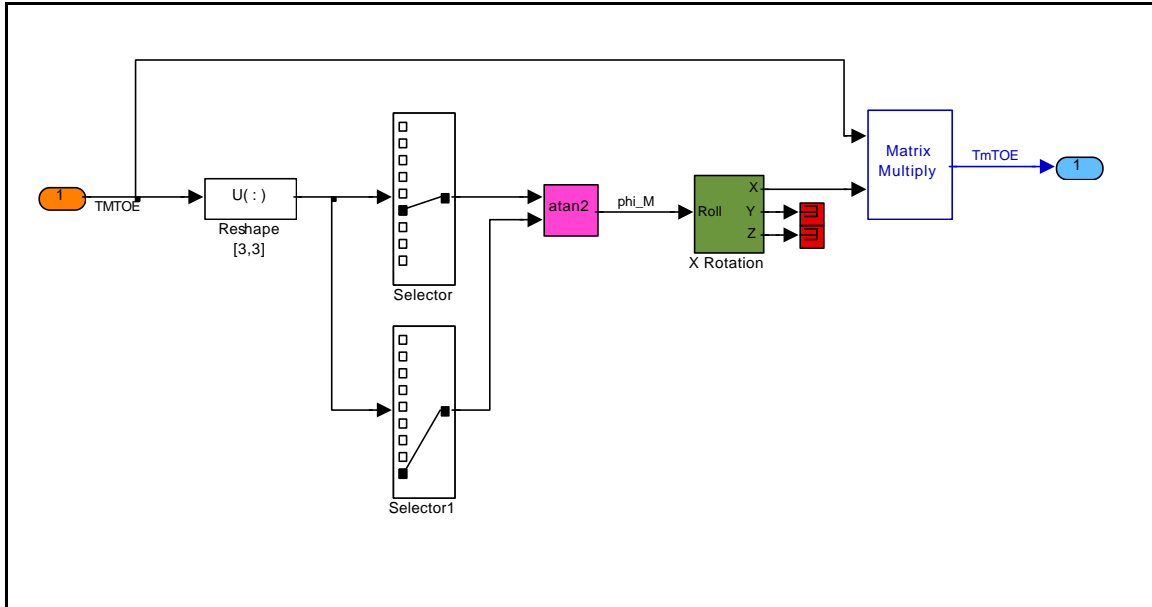


Figure 49 - Gallaspy calculate nonrolling missile-to-earth transformation block.

The rotation kinematics block transposes the nonrolling missile-to-inertial direction matrix to form the inertial-to-nonrolling missile direction cosine matrix. This is then multiplied with the gyro-to-inertial direction cosine matrix to form the gyro-to-nonrolling missile matrix. This operation can be expressed by

$${}^{NRMI}D^G = {}^{NRMI}D^I \cdot I D^G \quad (5-53)$$

Finally, the gyro-to-nonrolling missile Euler angles are calculated by the “calculate gyro-to-nonrolling missile Euler angles” block, shown in Figure 50. This block is similar to the “calculate gyro-to-missile Euler angles” block in Figure 48.

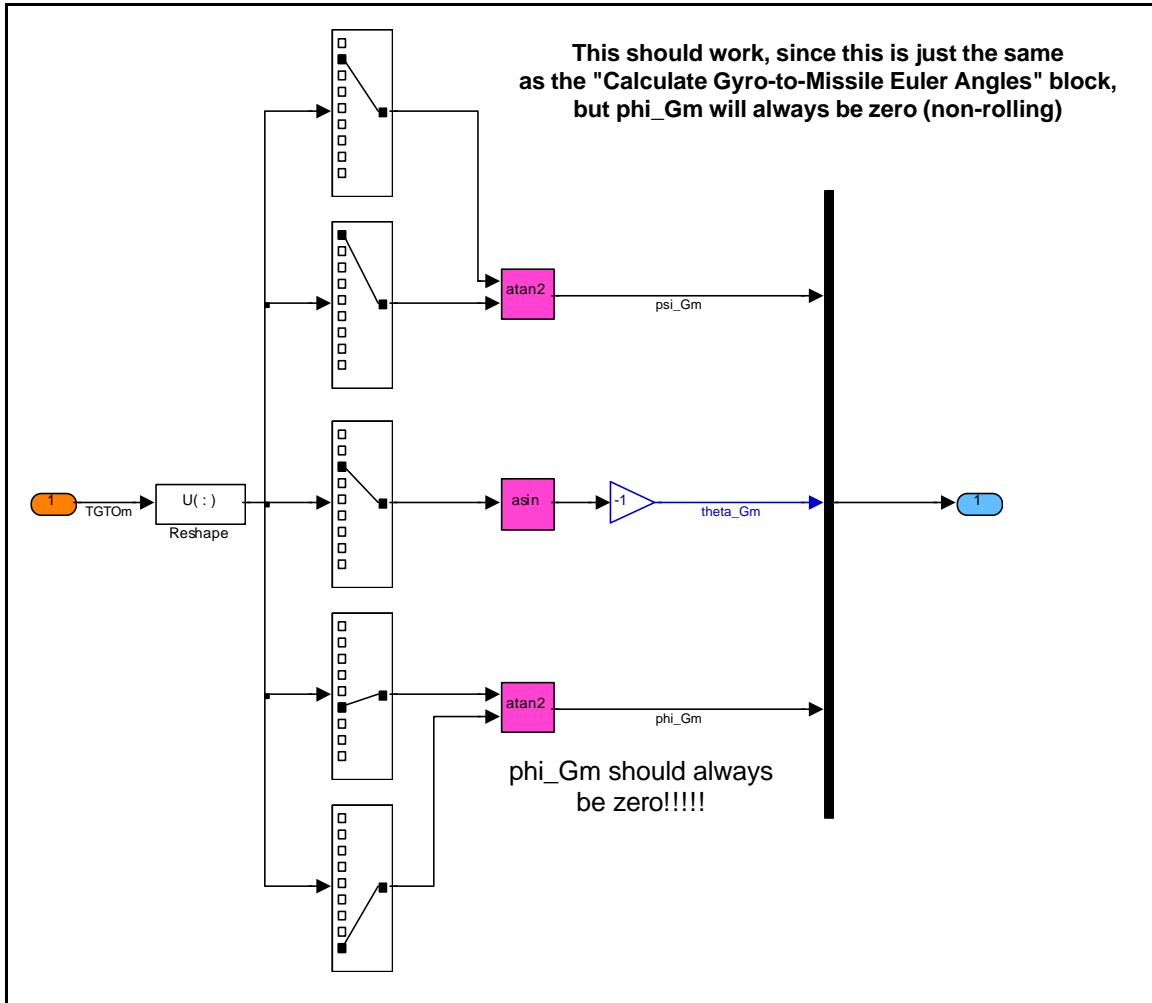


Figure 50 - Gallaspy calculate gyro-to-nonrolling missile Euler angles block.

5.4 Sensor Coils (General)

As discussed earlier, all EO/IR missile seekers use sensor coils to determine the position and state of the gyro. The gyro rotor is a permanent magnet and its motion induces currents/voltages in the sensor coils. There are typically two types of sensor coils, the lambda coil (also known as the cage coil), which is wound circumferentially around the missile body, and the reference coils which are "pancake" type coils (see Figure 9). Gallaspy gives the general

equation for calculating sensor coil voltage as:

$$v = -\frac{d}{dt} \int_S \vec{B} \cdot \vec{dS} \quad (5-54)$$

where \vec{B} = gyro magnetic flux density vector

\vec{dS} = differential surface element vector

S = Riemann integral of coil surface area

v = voltage induced in the coil

Gallaspy assumes that the gyro magnetic flux density does not vary significantly over the coil area during any given instant of time, thus

$$v = -\frac{d}{dt} \left(\vec{B} \cdot \int_S \vec{dS} \right) = -\frac{d\vec{B}}{dt} \cdot \int_S \vec{dS} - \vec{B} \cdot \frac{d}{dt} \int_S \vec{dS} \quad (5-55)$$

If the vectors are all written in the missile body-fixed reference frame, then the sensor coil surface area vectors are constant in time. This causes their time derivative to be zero, yielding

$$v = -\frac{d\vec{B}}{dt} \cdot \int_S \vec{dS} = -\frac{d\vec{B}}{dt} \cdot \vec{S} \quad (5-56)$$

Here, \vec{S} is a vector that points in a direction normal to the surface area of the sensor coil. The magnitude of \vec{S} is equal to the sensor coil area and the number of turns of the coil. Since \vec{B} is a function solely of the gyro magnetic

field strength and not of sensor coil characteristics, each sensor coil can be represented by its surface vector, \vec{S} . Thus, the voltage on any coil can be found by evaluating

$$v_{coil} = -\frac{d\vec{B}}{dt} \cdot \vec{S}_{coil} \quad (5-57)$$

The time derivative of the gyro magnetic flux density is found next. It is assumed that the gyro north pole is aligned with the $+\hat{z}_G$ vector, and the gyro magnetic field has a flux density of B, thus

$$\vec{B} = \begin{Bmatrix} B_{x_G} \\ B_{y_G} \\ B_{z_G} \end{Bmatrix} = B \begin{Bmatrix} 0 \\ 0 \\ 1 \end{Bmatrix} \quad (5-58)$$

Transforming this to the missile coordinate system,

$$\vec{B} = \begin{Bmatrix} B_{x_M} \\ B_{y_M} \\ B_{z_M} \end{Bmatrix} = B \cdot {}^M D^G \begin{Bmatrix} 0 \\ 0 \\ 1 \end{Bmatrix} \quad (5-59)$$

The gyro-to-missile direction cosine matrix is the only time-varying component of this equation, thus, the time derivative of the gyro flux density can be evaluated by evaluating the time derivative of the gyro-to-missile direction cosine matrix.

From Lamm (18), the time derivative of the gyro flux density is

$$\frac{d\vec{B}}{dt} = \begin{Bmatrix} \dot{B}_{x_M} \\ \dot{B}_{y_M} \\ \dot{B}_{z_M} \end{Bmatrix} = B \left({}^M D^G [\Omega_G] - [\Omega_M] {}^M D^G \right) \begin{Bmatrix} 0 \\ 0 \\ 1 \end{Bmatrix} \quad (5-60)$$

where,

$$[\Omega_G] = \begin{bmatrix} 0 & -w_{G_z} & w_{G_y} \\ w_{G_z} & 0 & -w_{G_x} \\ -w_{G_y} & w_{G_x} & 0 \end{bmatrix} \quad (5-61)$$

and $[\Omega_M]$ is defined similarly. A matrix in the form of equation 5-61 is referred to as the “angular velocity matrix”. A Simulink block was developed for use in forming this angular velocity matrix. The “form angular velocity matrix” block is shown in Figure 51, and is used later in the sensor coils Simulink blocks.

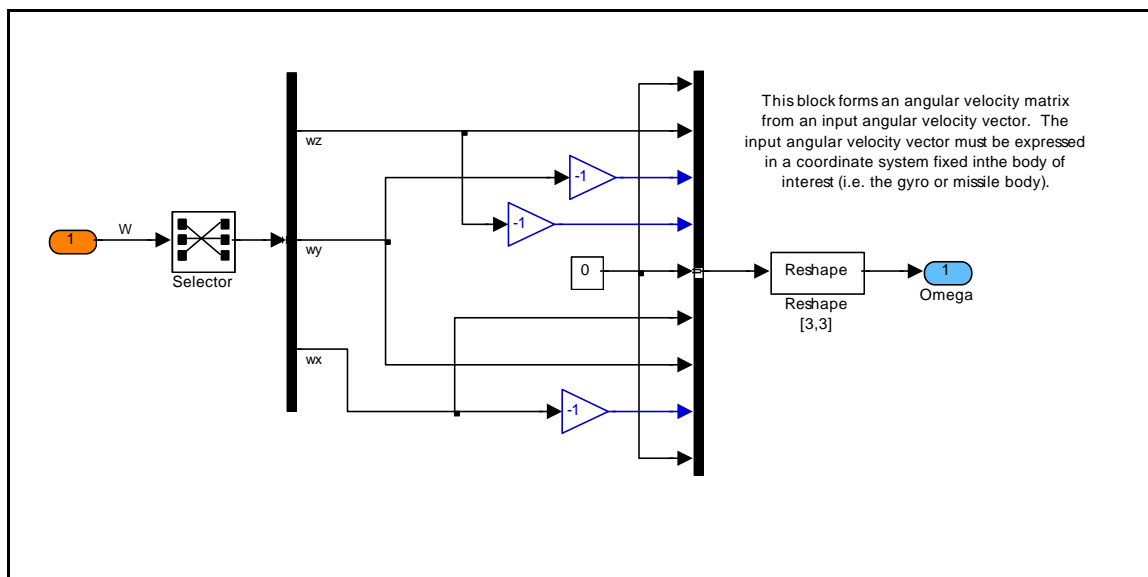


Figure 51 - Gallaspy form angular velocity matrix block.

5.5 Lambda (Cage) Coil

The cage coil (also known as the lambda coil), is wound longitudinally around the missile body. Thus, its surface area vector can be written as:

$$\vec{S}_I = A_I \hat{x}_M \quad (5-62)$$

Substituting this into Equation 5-57 gives:

$$v_I = -\frac{d\vec{B}}{dt} \cdot \vec{S} = -A_I \left(\frac{d\vec{B}}{dt} \right)_x \quad (5-63)$$

This equation is implemented in the “lambda coil” block, shown in Figure 52.

Note that the cage coil signal is by definition always at the gyro spin frequency.

Gallaspy outputs the cage coil (lambda) signal in his standard signal format.

Here, only frequency and signal are used. The amplitude and phase

components of this signal are not used in this model. Also, note that all cage

coil constants have been combined in the gyro.KI term.

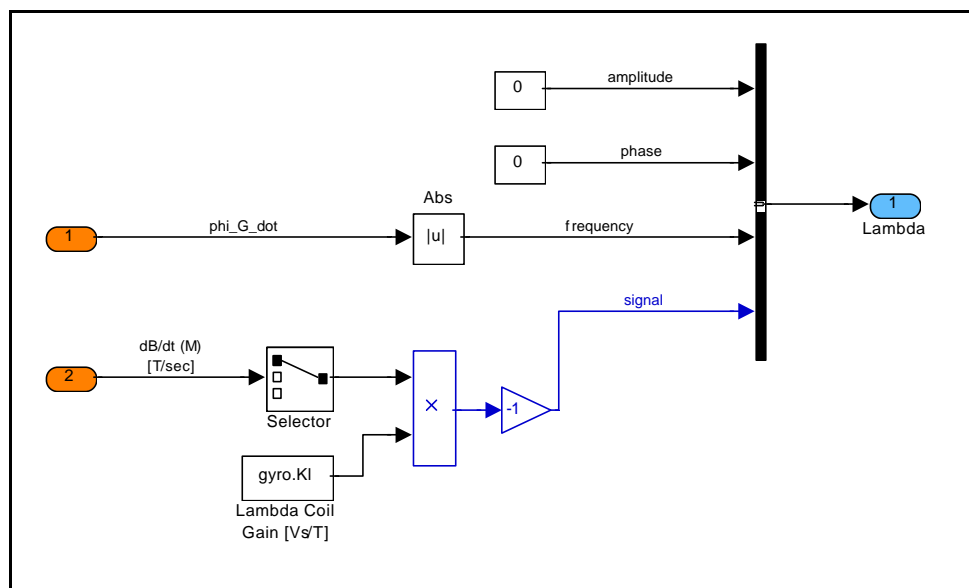


Figure 52 - Gallaspy lambda coil (cage coil) block.

5.6 Reference Coils

The reference coils are the “pancake” type coils discussed earlier. Gallaspy’s model features two sets of reference coils, physically separated by 90E on the missile body. One is aligned with the missile y axis, the other is aligned with the missile z axis. Their coil surface areas can be expressed as

$$\vec{S}_{r_1} = A_{r_1} \hat{y}_M \quad (5-64)$$

$$\vec{S}_{r_2} = A_{r_2} \hat{z}_M \quad (5-65)$$

The reference coil signals can be calculated by using Equations 5-64 and 5-65 with Equation 5-57, as was done with the lambda coil.

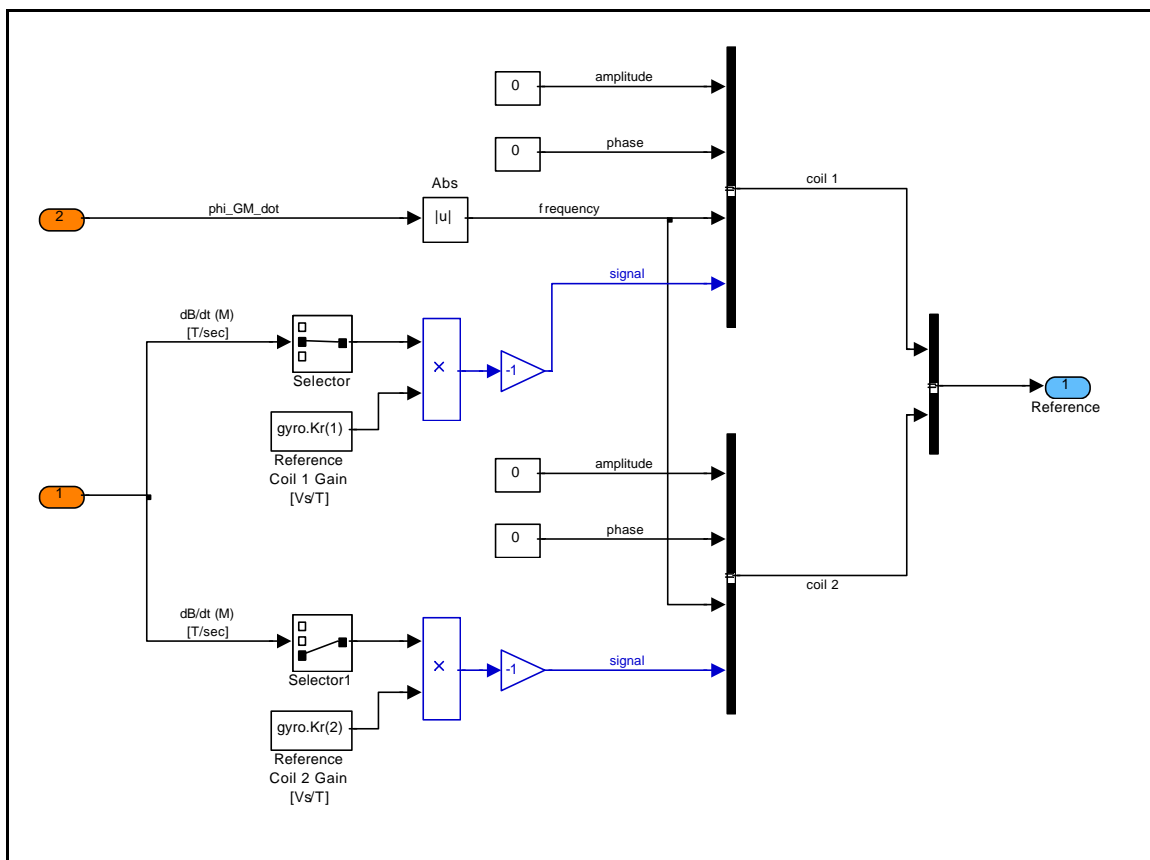


Figure 53 - Gallaspy reference coil block.

Also, note that the reference coil constants are combined into one term for each reference coil, as was done for the lambda coil. Also, it is assumed that the reference coil frequency is the relative gyro-to-missile roll rate. The reference coil block is shown in Figure 53.

The reference coil, lambda coil, and “form angular velocity matrix” blocks are implemented in the sensor coils block, which is inside the gyro dynamics block. The sensor coils block is shown in Figure 54.

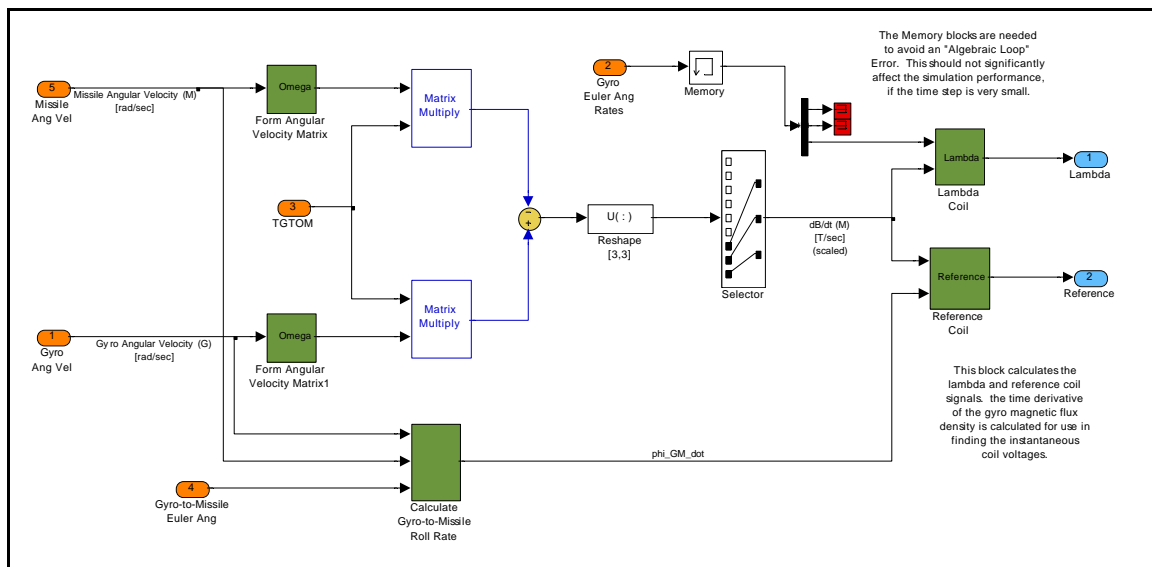


Figure 54 - Gallaspy sensor coils block.

The relative gyro-to-missile roll rate is needed for the reference coil calculations. The formula for calculating the relative gyro-to-missile roll rate is given by Lamm (13). Start with the expression for the relative gyro-to-missile roll angle, equation 5-52 (repeated here)

$$\mathbf{f}_{GM} = \tan^{-1} \left({}^M D_{3,2}^G / {}^M D_{3,3}^G \right) \quad (5-66)$$

From Larson and Hostettler (25) the derivative of an arctangent function is

$$\frac{d}{dt}[\text{Arc tan}(u)] = \frac{1}{1+u^2} \frac{du}{dt} \quad (5-67)$$

Substituting Equation 5-66 into equation 5-67 and rearranging yields

$$\dot{\mathbf{f}}_{GM} = \frac{{}^M D_{3,3}^G \dot{{}^M D_{3,2}^G} - {}^M D_{3,2}^G \dot{{}^M D_{3,3}^G}}{({}^M D_{3,3}^G)^2 + ({}^M D_{3,2}^G)^2} \quad (5-68)$$

Using the formula of the derivative of a direction cosine matrix from equations 5-60 and 5-61,

$$\dot{\mathbf{f}}_{GM} = \frac{{}^M D_{3,3}^G ({}^M D^G \boldsymbol{\Omega}_G - \boldsymbol{\Omega}_M {}^M D^G)_{3,2} - {}^M D_{3,2}^G ({}^M D^G \boldsymbol{\Omega}_G - \boldsymbol{\Omega}_M {}^M D^G)_{3,3}}{({}^M D_{3,3}^G)^2 + ({}^M D_{3,2}^G)^2} \quad (5-69)$$

Expanding this gives the final equation for the gyro roll rate with respect to the missile body:

$$\begin{aligned} \dot{\mathbf{f}}_{GM} = & \mathbf{w}_{G_x} + \mathbf{w}_{G_z} c_{f_{GM}} t_{q_{GM}} + \mathbf{w}_{G_y} s_{f_{GM}} t_{q_{GM}} \\ & - (\mathbf{w}_{M_x} c_{y_{GM}} / c_{q_{GM}}) - (\mathbf{w}_{M_y} s_{y_{GM}} / c_{q_{GM}}) \end{aligned} \quad (5-70)$$

This is the equation that is implemented in the “calculate gyro-to-missile roll rate” block shown in Figure 55. This completes the description of the Gallaspy gyro dynamics block.

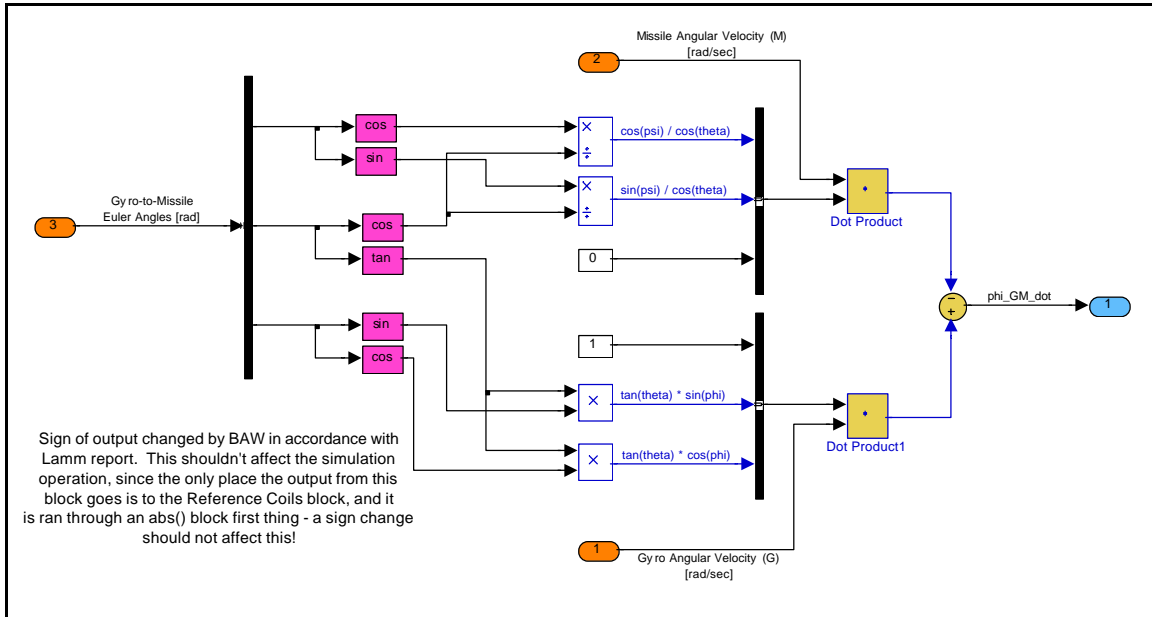


Figure 55 - Gallaspy calculate gyro-to-missile roll rate block.

5.7 Spin Coils

From Figure 39, it is seen that the lambda and reference coil outputs of the gyro dynamics block are the inputs to the spin coils block. The spin coils block calculates the spin torque that is needed to maintain the desired gyro spin speed. Gallaspy uses a simple spin coil torque model. The spin torque (torque about the \hat{x}_G axis) is proportional to the measured spin speed minus the desired spin speed. The spin speed can be measured from either the lambda coils or the reference coils. Gallaspy uses the lambda coils. This is of some concern, since the lambda signal goes to zero when the gyro is aligned with the missile body. The following equation represents Gallaspy's spin torque model:

$$\vec{t}_{Spin} = K_S (\mathbf{w}_{desired} - \mathbf{w}_{measured}) \hat{x}_G \quad (5-71)$$

Figure 56 shows the Simulink implementation of the gyro spin coils.

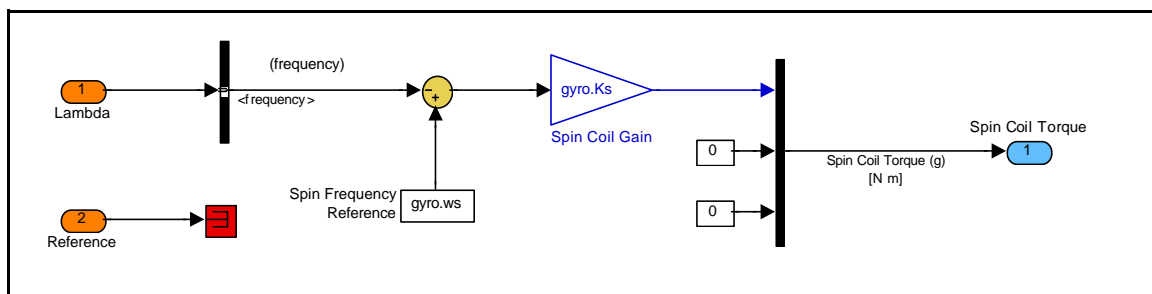


Figure 56 - Gallaspy Spin Coils block.

5.8 Caging Coil

There exists a slight terminology problem between the Gallaspy model and the gyro models discussed earlier. Previously in this paper, the radially wound sensing coils in the other gyro models were referred to as the “cage coil”. Gallaspy calls these sensing coils “lambda coils”. Gallaspy’s caging coil is wound the same as the lambda coils, but it is a torquing coil which exerts a torque on the gyro to cause it to align with the missile body (also known as “caging” the gyro).

Gallaspy’s caging coil model operates in the non-rolling gyro with respect to missile (NRGM) reference frame. Because of gyroscopic motion, a yaw error is corrected by a torque about the $-\hat{y}_{NRGM}$ axis; similarly, a pitch error is corrected by a torque about the $+\hat{z}_{NRGM}$ axis. The same gain, K_c , is used for both axes. Also, the caging coil is setup with a switch to cage and uncage the gyro at specified simulation times. The governing equations are

$$\bar{\mathbf{t}}_{cage} = \left\{ \begin{array}{ll} K_c(-\mathbf{y}_{GM} \hat{y}_{NRGM} + \mathbf{q}_{GM} \hat{z}_{NRGM}), & t_{C_{on}} \leq t < t_{C_{off}} \\ 0, & t < t_{C_{on}}, \quad t \geq t_{C_{off}} \end{array} \right\} \quad (5-72)$$

Figure 57 shows the Simulink caging coil model.

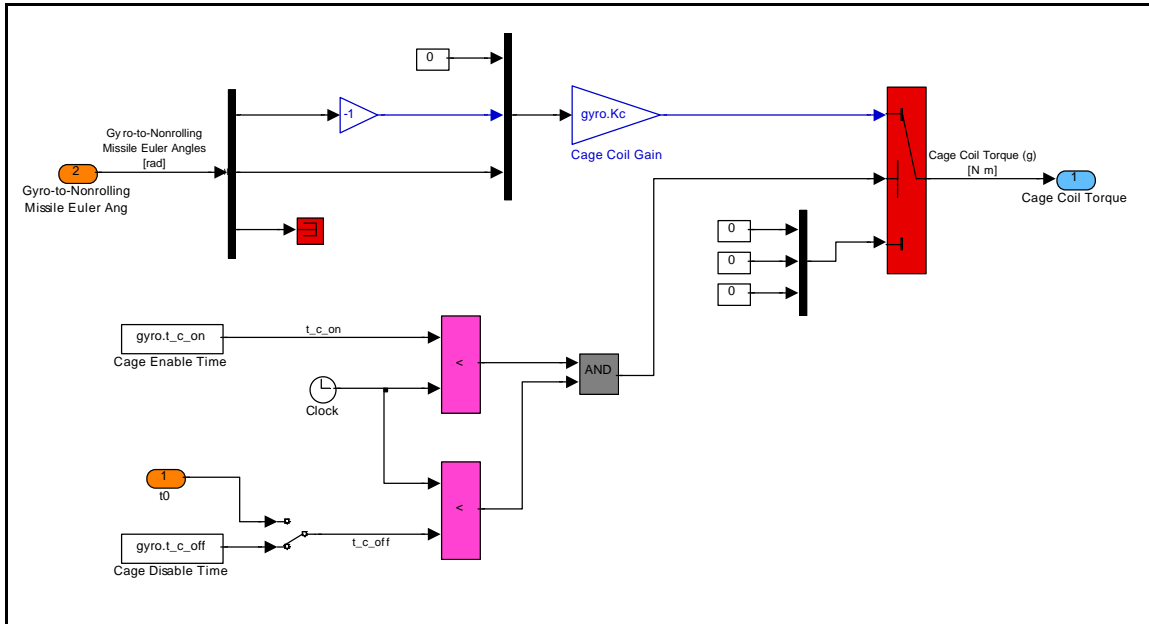


Figure 57 - Gallaspy caging coil block.

5.9 Precession Coil

The gyro precession coil creates a magnetic field along the missile longitudinal axis, causing a torque on the gyro. This precession torque is used to steer the gyro in the desired direction to track a target. The gyro tracking signal is referred to as sigma dot ($\dot{\mathbf{s}}$). The phase of sigma dot (in comparison to the reference signal) indicates the desired direction of precession. The magnitude of sigma dot indicates the desired tracking rate, which is proportional to the magnitude of the tracking error. Sigma dot can be represented as

$$\dot{\mathbf{s}} = A_{\dot{\mathbf{s}}} \cos(\mathbf{f}_{GM} - \mathbf{f}_{\dot{\mathbf{s}}}) \quad (5-73)$$

where $A_{\dot{\mathbf{s}}}$ is the amplitude, and $\mathbf{f}_{\dot{\mathbf{s}}}$ is the phase angle. Note that in the open

loop version of this model, sigma dot is not modeled, it is merely represented by an input variable.

As with the caging torque, the precession torque is applied in the nonrolling gyro with respect to missile coordinate system. This torque actually acts on the gyro magnetic field, which spins with the gyro. This is compensated for by using the sine and cosine of the gyro with respect to missile roll angle. The precession gain is represented by K_p . There is also a switch incorporated which activates gyro precession at a predetermined time. The precession torque is represented by

$$\vec{t}_{Prec} = \begin{cases} K_p \dot{\mathbf{s}} [\cos(\mathbf{f}_{GM}) \hat{y}_{NRGM} + \sin(\mathbf{f}_{GM}) \hat{z}_{NRGM}], & t \geq t_{P_{on}} \\ 0, & t < t_{P_{on}} \end{cases} \quad (5-74)$$

The Gallaspy Precession Coil Simulink model is shown in Figure 58.

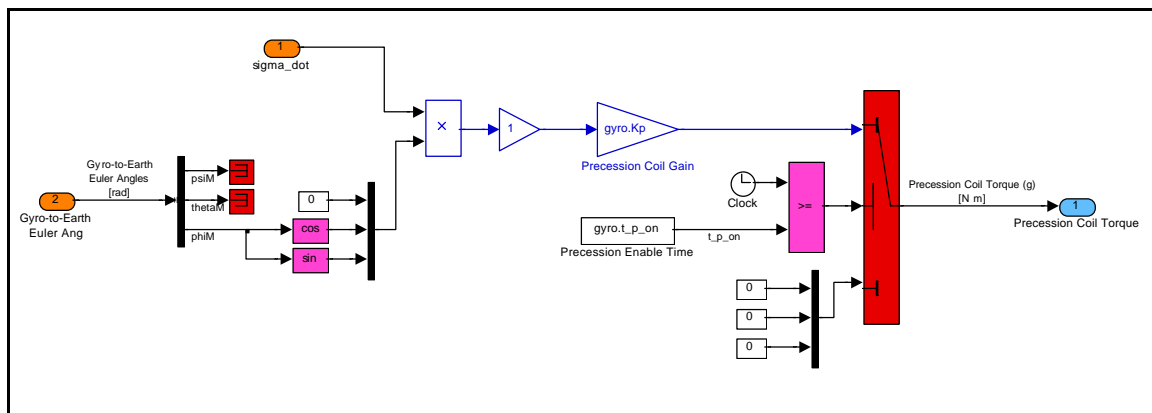


Figure 58 - Gallaspy precession coil block.

5.10 Gallaspy Model Limitations and Assumptions

This model was designed to capture the predominant gyro motion characteristics, namely spin and precession. Other effects (assumed to be less significant) which are not included in the model are gyro nutation and nutation damping, gimbal friction, aerodynamic friction, and gimbal inertia. Also, the gyro is modeled as a free body, which would not be true if the gyro encountered its physical gimbal limits, or if there is missile motion and the gyro center of mass is not located exactly at its center of rotation. Gravity would also induce additional drift torques on the gyro if its center of mass were not exactly co-located with its center of rotation.

Gallaspy notes that the gyro torquing coils are modeled as the ideal interactions necessary to produce a desired motion, not using the complex interaction of magnetic fields. This neglects effects such as precession coil loss of efficiency at large gyro off-boresight angles, precession torque coupling on the spin axis, and spin torque coupling to precession.

6.0 Model Comparisons to Gyro Test Data

In order to evaluate the fidelity differences between the three gyro models presented in this paper, comparisons to actual gyro test data were conducted. Gyro test data was difficult to find; however, data comparisons were done in four areas: twice spin frequency nutation oscillations, nutation damping misalignment, rate table spin-up and spin-down tests, and gyro signal phasing.

6.1 Twice Spin Frequency Nutation Oscillations

Due to the nature of sinusoidal magnetic precession torques on gyros, they exhibit motion oscillations at twice their spin frequency. These oscillations are also called gyro nutation effects. The nutation effects are seen as small “loops” on a plot of gyro position (seen while the gyro is precessing). These nutation “loops” oscillate at twice the gyro spin frequency.

Figure 59 will help to explain the cause of this twice spin frequency nutation oscillation. Note that

Figure 59 is a view of the gyro from the front (nose) of the missile. In this respect, both the positive x_M and positive x_G axes point out of the page. Also, note that a new angle has been defined, f_{ZG} . The f_{ZG} angle differs from the standard f_{GM} Euler roll angle in that f_{ZG} is the

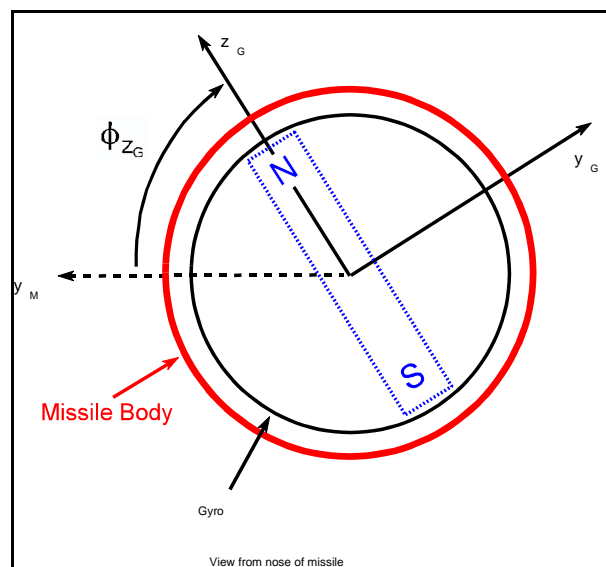


Figure 59 - Gyro nutation illustration.

angle between the missile body y_M axis and the gyro z_G axis. The traditional f_{GM} Euler roll angle is between the missile y_M axis and the gyro y_G axis (in this case, the gyro x_G axis is aligned, or boresighted with, the missile x_M axis).

In order to understand the cause of the nutation effects, consider an example, say that the missile is executing a gyro precession command which will cause the gyro to pitch up. Referring to Figure 59, this will cause the gyro as it is presently shown to move its north pole into the page and its south pole out of the page. This precession command is caused by passing a sinusoidal current (phased properly at the gyro spin frequency) through the precession coils (wound radially around the missile body).

This sinusoidal precession current induces a corresponding sinusoidal magnetic field which is aligned with the missile x_M axis. For a gyro pitch-up command, the precession command sinusoid must be phased such that the positive peak of the sinusoid occurs when the north pole of the gyro magnetic field is straight up ($f_{zG} = 90E$). The peak positive precession magnetic field (north pole aligned with the positive x_M axis, out of the page) attracts the south pole of the gyro magnet and repels the north pole of the gyro magnet. This produces a torque on the gyro which pitches it upward.

If the precession command sinusoidal signal is at the gyro spin rate, and it is at its maximum when the gyro north pole is straight up, then the precession command minimum happens when the gyro north pole is straight down. Thus, the precession command sinusoid is zero when the gyro poles are horizontal. A

pure gyro pitch motion would occur if it were possible to execute an infinitesimally short precession magnetic field at the exact instant when the gyro was vertical. Since this is not possible a sinusoidal precession command is used, which causes gyro nutation.

Imagine the same gyro scenario shown in Figure 59, starting from the z_G axis being aligned with the y_M axis ($f_{zG} = 0E$). Here, the precession command is zero for a pitch-up precession, since the gyro is horizontal. As the gyro north pole rotates toward a vertical position, the precession command sinusoid increases from zero, reaching its positive peak when the gyro north pole is vertical. As the precession coil magnetic field is increasing, it begins to attract the gyro south pole and repel the gyro north pole, while the gyro magnet is in the process of rotating from horizontal to vertical. This magnetic torque causes the gyro to pitch up, but it also causes a yaw to the left.

Similarly, as the gyro north pole rotates from its vertical position back to horizontal ($f_{zG} = 180E$), the precession command sinusoid gradually decreases from its maximum value to zero. This decreasing magnetic field attracts the gyro magnetic south pole and repels the gyro magnetic north pole as it rotates from vertical to horizontal. This causes the gyro to pitch-up but it also causes a yaw motion to the right. The left and right yaw motions cancel each other on average, but they cause the nutation, or looping oscillations. A similar yaw nutation happens during the second half of the gyro rotation when the north pole is on the bottom side of the missile.

Since one nutation cycle (yaw left, yaw right) is completed during half of the gyro spin rotation ($f_{z_G} = 0E$ to $f_{z_G} = 180E$), a single complete gyro rotation generates two complete nutation cycles. Thus, the nutation oscillation is at twice the gyro spin frequency.

Note: in reality, the above example of a gyro pitch-up maneuver would have a maximum precession command (positive or negative peak of the sinusoidal precession signal) when the gyro magnetic poles are aligned horizontally. This is due to the gyro law, which states that the gyro precesses in a direction that is the cross product of the gyro spin vector and the torque applied to the gyro (as discussed in Section 1.0).

Gyro nutation is undesirable, thus, most gyros employ nutation damping. In most cases, this is done either electronically, or mechanically with liquid mercury in an enclosed circular groove in the gyro y_G - z_G plane. Consequently, the nutation effects of actual gyros are very small and not readily detectable in testing. Model nutation results can be seen by examining the small details of a plot of gyro yaw angle versus pitch angle. A real gyro does not output pitch angle or yaw angle, it outputs a cage coil signal and a reference coil signal. These signals can be demodulated to determine gyro position, but due to noise and other phenomena, the gyro nutation effects are difficult to see from this type of gyro position data. It might be possible to see gyro nutation effects with a scanning laser system reflected off of the gyro during precession, but no data of this type is currently available.

Another way was found to verify the actual gyro nutation effects. The frequency content of gyro cage coil data was analyzed with a fast-fourier transform (FFT). The FFT should show the cage coil primary frequency content to be at the gyro spin frequency. If gyro nutation effects are present, a frequency component in the cage coil should be present at twice the gyro spin frequency.

Data from four gyro tests were analyzed with an FFT. For these tests, the gyro spin frequency was 100 Hz. All the data sets showed 200 Hz (twice spin frequency) components. Figure 60 shows the gyro cage coil FFT frequency content from the data set with the most prominent 200 Hz component. Note the predominant 100 Hz (spin frequency) component. No other frequency components are visible in this view. Figure 61 is a zoom of the same plot, showing a much smaller y axis scale. Here the 200 Hz frequency component can easily be seen. There are also smaller frequency components at 300 Hz, 400 Hz and 500 Hz. The cause of these additional frequency components is not known, it is possible that they may be FFT artifacts. This data does (indirectly) verify that nutation oscillations at twice spin frequency occur in actual gyros.

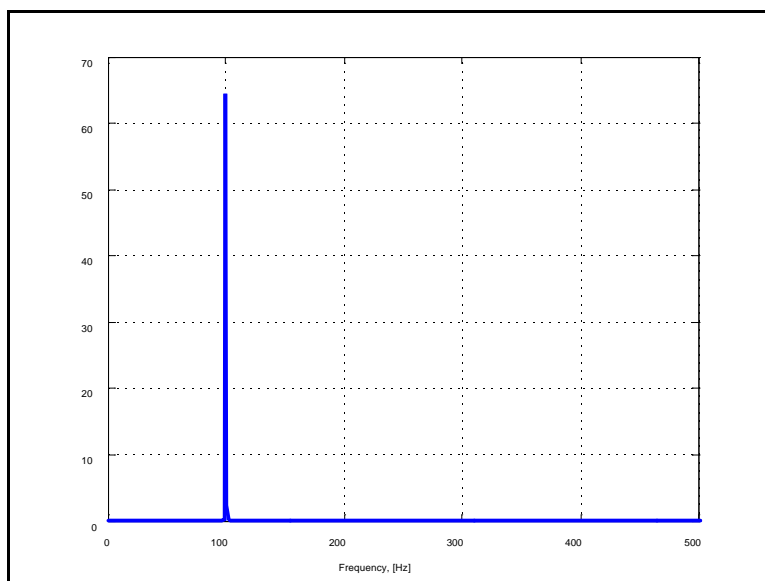


Figure 60 - FFT frequency components of actual gyro cage coil signal.

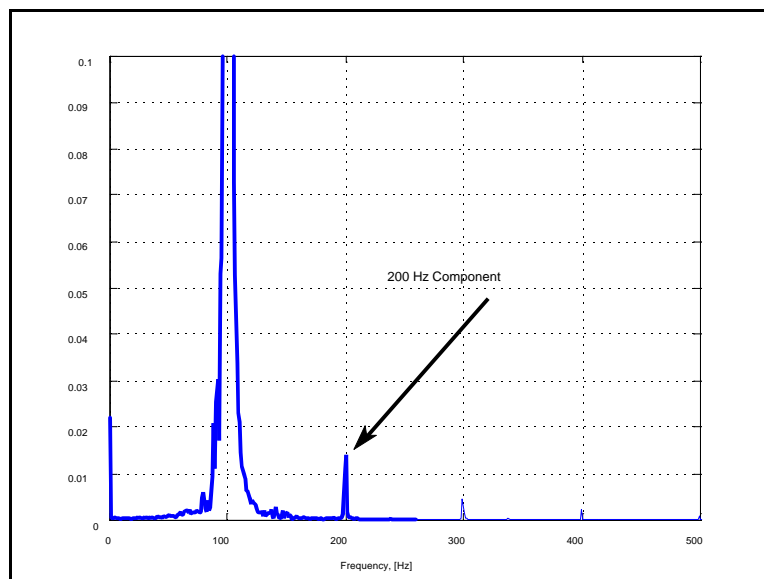


Figure 61 - Zoom of gyro cage coil frequency components.

The BDWL gyro model was run with nutation damping active and with nutation damping set to zero to illustrate the effects of nutation damping. Figures 62 and 63 show this data. Note from Figure 63 that the nutation damping definitely decreases the magnitude of the nutation “looping” oscillations. Also, note from both figures that the nutation damping causes a slight misalignment of precession direction. This effect will be discussed in the next section.

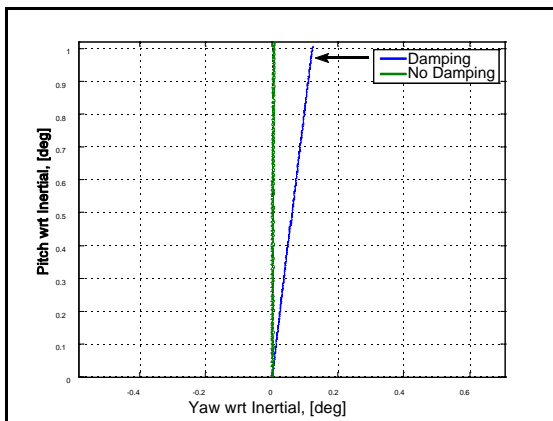


Figure 62 - Gyro damping comparison.

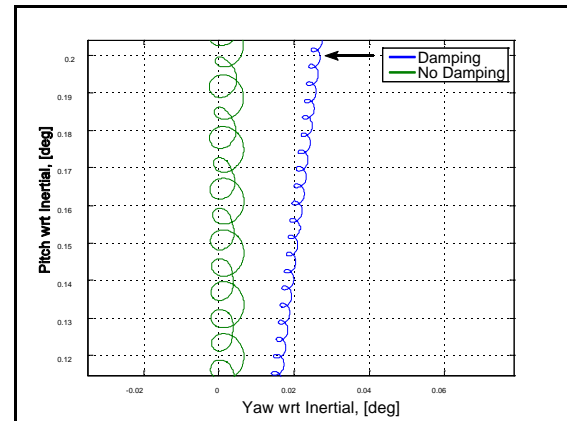


Figure 63 - Close-up of gyro damping comparison.

Figure 64 shows an example of the twice spin frequency nutation effects from the Dave Williams paper. This is model data, not actual gyro data. Actual gyro data is not available for the reasons stated above. Comparison runs were done with the three candidate models in this paper. These comparisons are shown in Figures 65 - 67. As expected, the BDWL model shows the nutation effects, while the Ideal and Gallaspy gyro models do not. The data in Figures 65 - 67 are from the nutation damping misalignment tests presented in the next section 6.2.

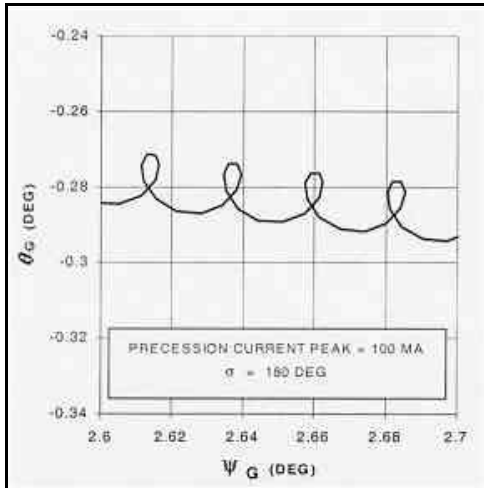


Figure 64 - Gyro 200 Hz wobble from Dave Williams paper.

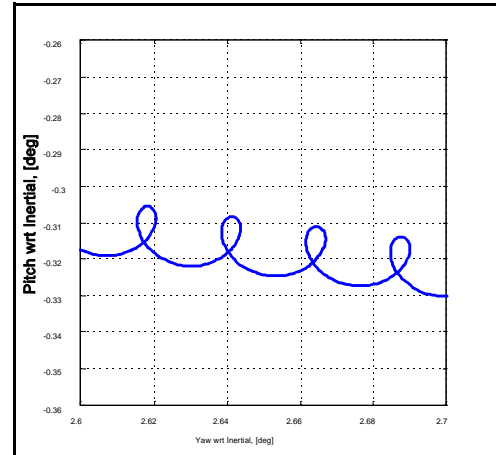


Figure 65 - Close-up of BDWL gyro model precession.

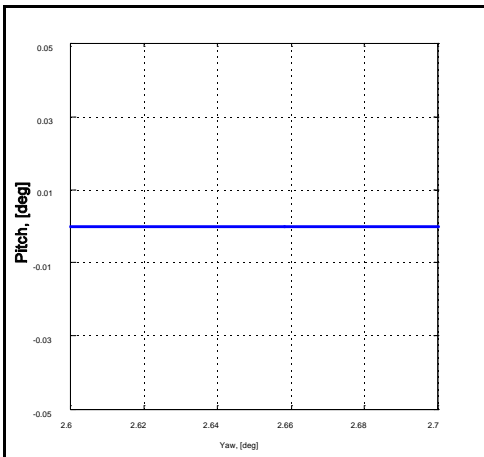


Figure 66 - Close-up of Ideal1 gyro model precession.

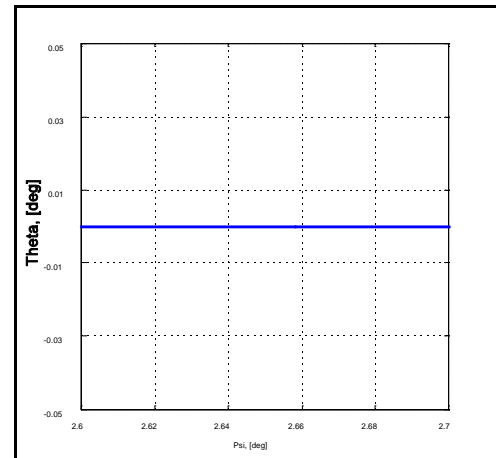


Figure 67 - Close-up of Gallaspy3 gyro model precession.

6.2 Nutation Damping Misalignment

The presence of nutation damping in a gyro, or gyro model, causes a slight misalignment in the precession direction when compared to open-loop precession responses with no damping present. Note that this is only seen in open-loop gyro tests, not in closed-loop tracking tests. In an actual EO/IR missile system, the misalignment is likely compensated for by adjusting the phase of the precession signal.

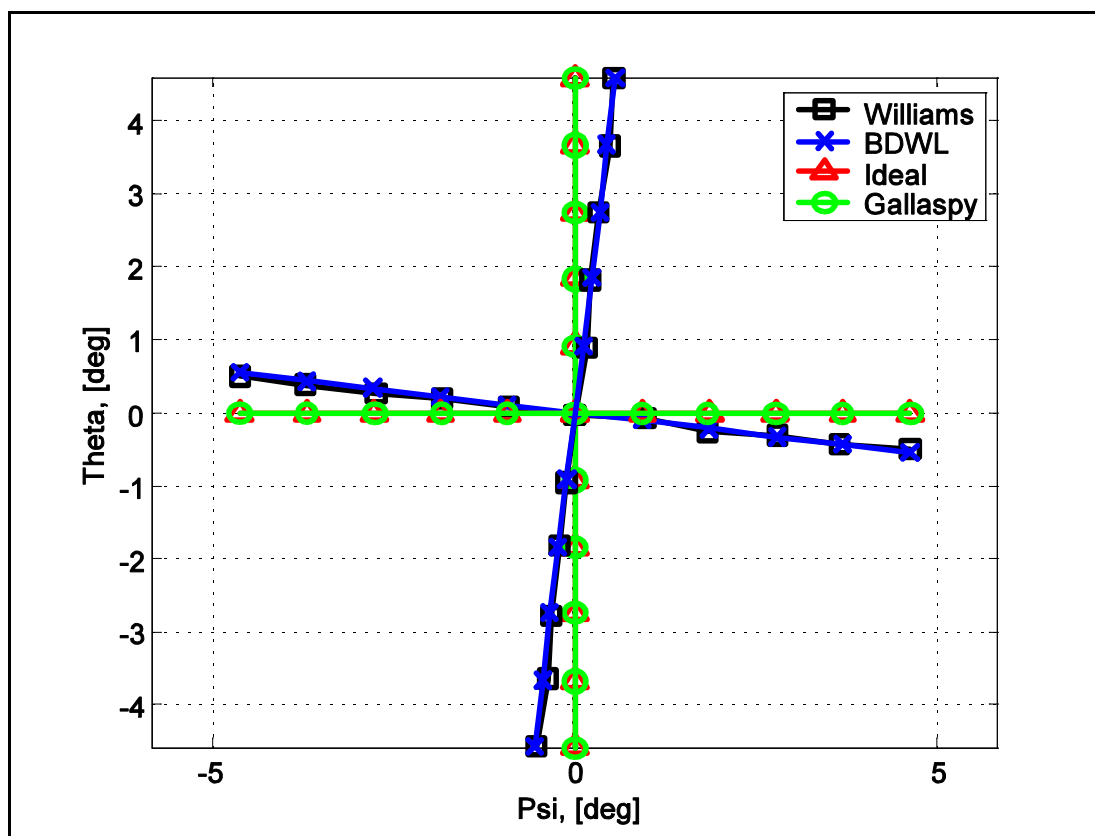


Figure 68 - Gyro nutation damping misalignment comparison.

Figure 68 shows the results of the nutation damping misalignment tests. The actual gyro data came from Williams (9). Note that the BDWL model was the only model to show a damping misalignment, which was expected, since it is

the only model to incorporate nutation effects. The BDWL model data match the Williams gyro data very well. In Figure 68, the Ideal and Gallaspy gyro models performed almost identically with constant precession rates along the axes.

Note that the precession command magnitude was tuned for all three models to get 4.59E vertical displacement and 4.62E horizontal displacement (in one second) to match the actual gyro data from the Dave Williams paper. The symbol markers in Figure 68 denote the gyro position at 0.2 sec intervals

It is postulated that the nutation damping misalignment occurs because of the non-symmetric nature of the damping compensation. For a gyro model with nutation effects but no damping (as shown in Figures 62 and 63), the off-axis nutation effects exactly cancel each other. This causes the “looping” behavior, but does not affect the overall direction of precession. Since the damping is proportional to angular velocity, it is not symmetric and has a slightly more pronounced effect in one off-axis direction than the other. It is believed that this causes the nutation damping misalignment.

6.3 Gyro Rate Table Spin-Up and Spin-Down Tests

The Williams paper (9) presents a set of rate table comparisons between actual gyro data and model data. This gyro data will be used here for comparison to the three gyro models presented herein. In these tests, the EO/IR missile seeker is placed on a rate table (see Figures 69, 70, and 71). A suitable EO/IR source is placed at the edge of the rate table, which the missile seeker tracks. The source is placed at some off-boresight angle (look angle) with respect to the missile body-fixed x_M axis. The missile and the target both rotate with the rate table at a constant angular rate, thus, the look angle between the missile body and the target stays constant.

During these tests, the gyro spin rate is set initially to 100 Hz. After two seconds, the gyro is commanded to spin-up to 115 Hz, and it is finally commanded to

spin back down to the initial value of 100 Hz at 6 seconds into the test. The missile-to-target look angle, the rate table angular rate, and the missile roll position are all varied between tests.

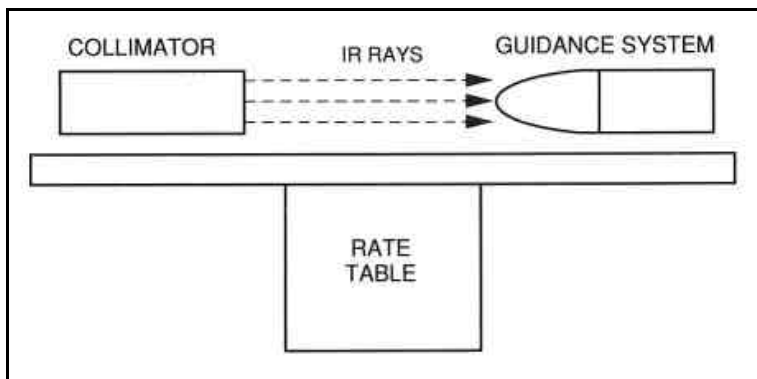


Figure 70 - Rate table diagram (21).



Figure 69 - Rate table (22).

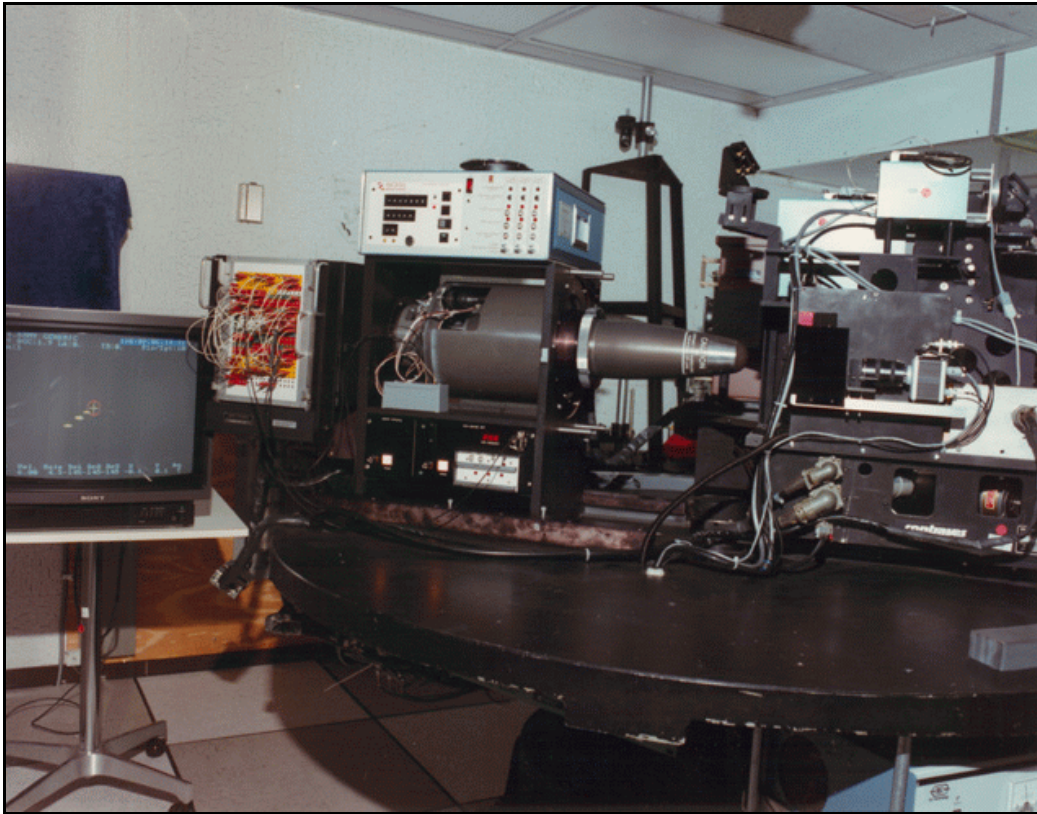


Figure 71 - Rate table (23).

The results of these rate table tests which are used for model comparison are the missile sigma dot signal and the actual gyro spin rate versus time. The missile sigma dot signal is closely related to the precession command. Since sigma dot is not represented in the models, model precession command is compared to the missile sigma dot signal. (The Gallaspy model actually has a signal it calls sigma dot, but this is similar to the precession command signal in the BDWL and Ideal gyro models.) For this reason, the absolute magnitudes of the sigma dot and precession command signals cannot be directly compared, but their overall shape and response should be similar.

As stated earlier, the missile body and target are both fixed to the rate table and rotate with it. Thus, the overall gyro look angle with respect to the

missile body should remain constant. Since the gyro is an inertial device, the missile must precess the gyro to remain tracking the target which is moving with respect to inertial space. If no precession command is given to the gyro, it will remain in the same inertial orientation as the missile body moves (thus changing the gyro-to-missile look angle).

As explained in the gyro model derivation sections, the precession coils lose efficiency as the gyro-to-missile look angle increases. Also, the coupling of the spin magnetic torque into gyro precession, and the precession torque coupling into gyro spin both increase in magnitude as the gyro-to-missile look angle increases. These effects are demonstrated in the rate table tests.

The gyro model derivations in Chapters 3, 4, and 5 only dealt with open-loop gyro models. In order to simulate these rate table tests, a track loop model was implemented in each gyro model. The track loop model was based on Williams (9), and is detailed in section 6.3.1, along with its implementation in each of the three candidate gyro models.

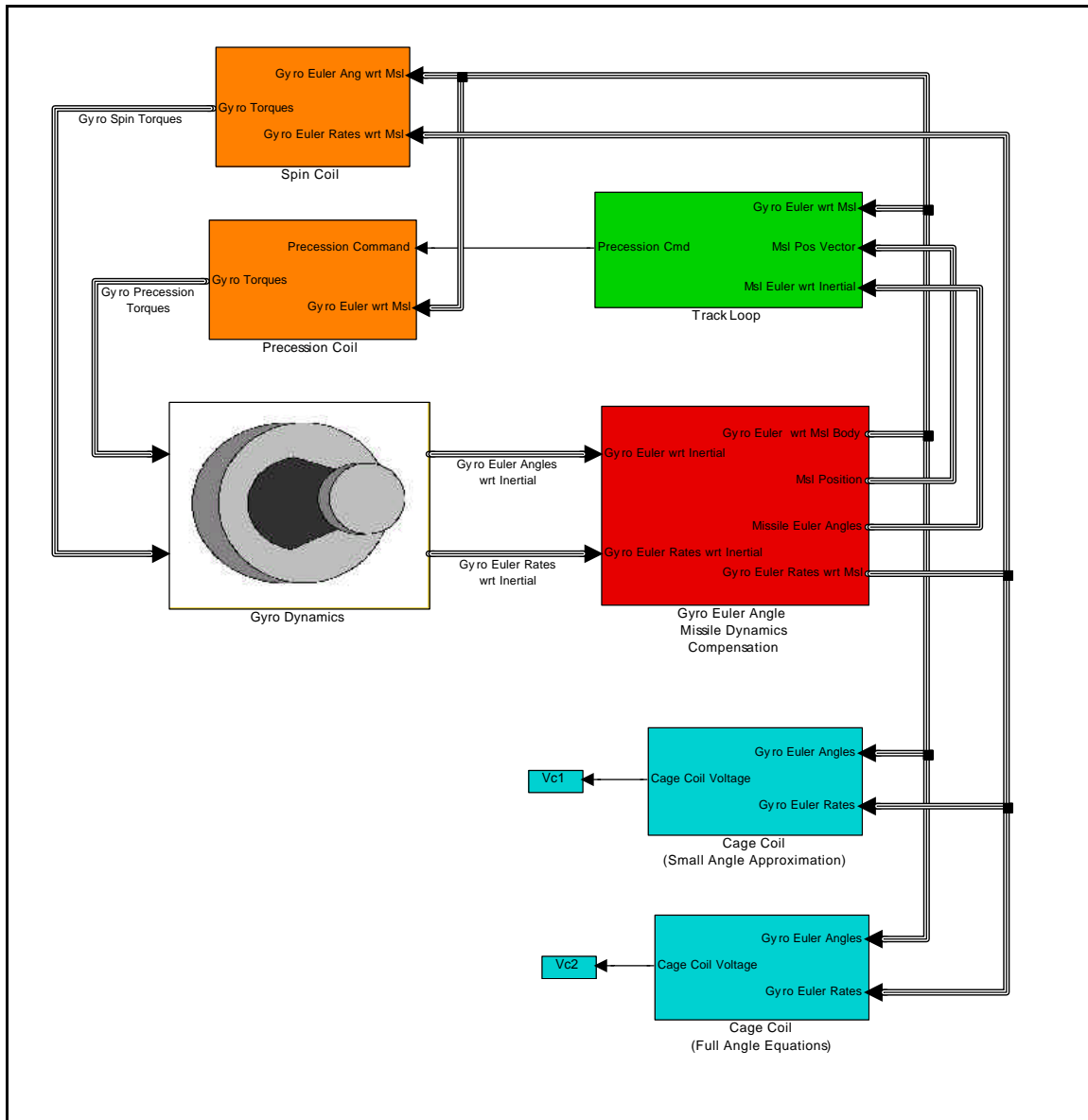


Figure 72 - BDWL gyro model with track loop implementation.

6.3.1 BDWL Track Loop Model and Implementation

Figure 72 shows the top-level of the BDWL gyro model with the track loop block included. The track block uses the gyro Euler angles with respect to the missile, the missile position, and the missile Euler angles with respect to inertial

to compute a gyro precession command. From Williams (9), the missile track loop can calculate the gyro precession command by

$$I_p(t) = P_{CurMax} \left(\hat{y}_G \cdot \hat{R}_{LOS} \right) \quad (6-1)$$

and

$$precCmd = R_{GC} \left(\frac{I_p(t) + I_p(t-1)}{2} \right) \quad (6-2)$$

where \hat{R}_{LOS} = Unit vector along Line-of-sight from gyro to target

P_{CurMax} = Precession current scale factor

I_p = Precession current

R_{GC} = Precession current to torque scale factor

$precCmd$ = Gyro precession command

Note that due to the spin of the gyro, the term $\hat{y}_G \cdot \hat{R}_{LOS}$ is zero if the gyro is pointing directly at the target. If there is a pointing error between the gyro and target, this term is a sinusoid at the gyro spin frequency whose amplitude is proportional to the gyro pointing error. Using \hat{y}_G for this term provides the proper phase for the precession command to precess the gyro toward the target, thus nulling out the error. Also, note that Williams uses a two value average (at t and t-1) of the precession current to calculate the precession command.

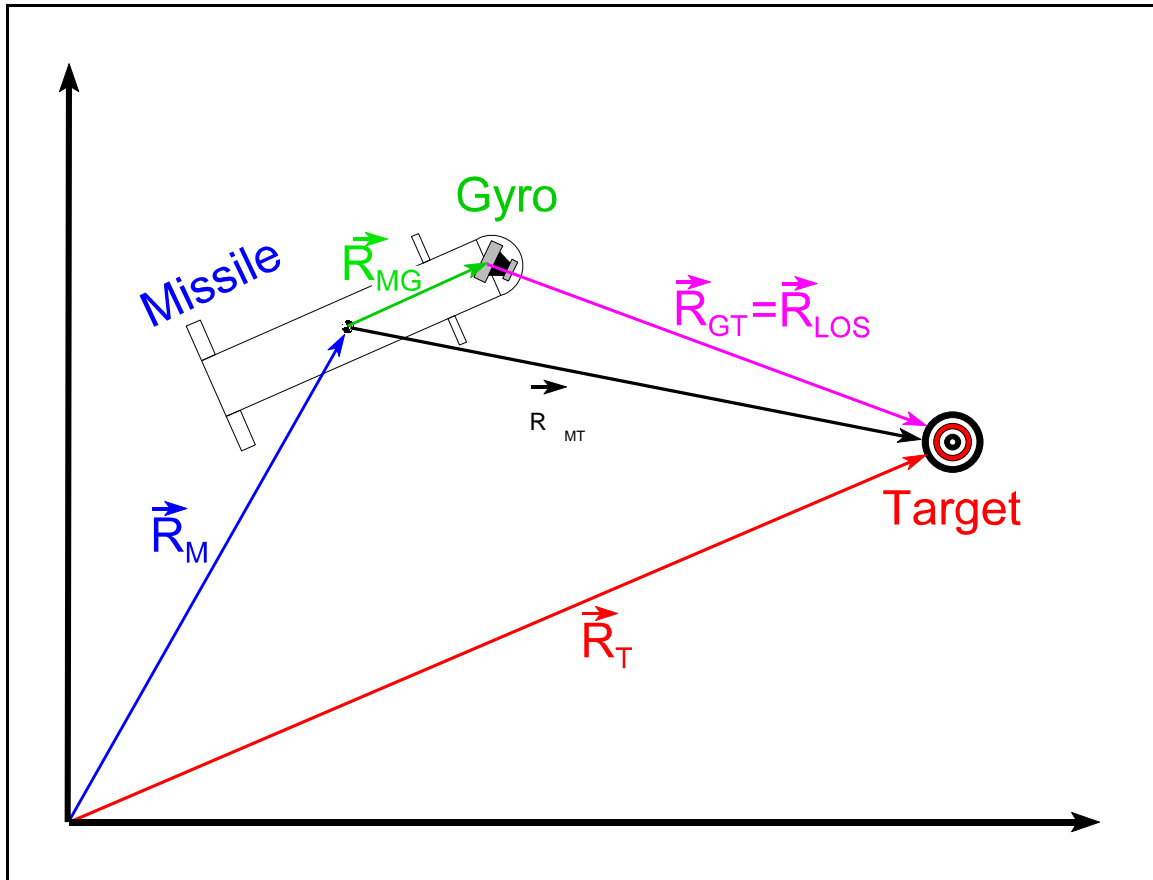


Figure 73 - Missile, gyro, and target geometry and vectors.

In order to calculate the $\hat{y}_G \cdot \hat{R}_{LOS}$ dot product, \hat{R}_{LOS} was calculated and transformed into the gyro body-fixed coordinate system. Referring to Figure 73,

$$\vec{R}_M = \text{Missile position vector}$$

$$\vec{R}_T = \text{Target position vector}$$

$$\vec{R}_{MG} = \text{Missile to gyro position vector}$$

$$\vec{R}_{MT} = \text{Missile to target position vector}$$

$$\vec{R}_{GT} = \vec{R}_{LOS} = \text{Gyro to target position vector}$$

From Figure 73, it can be seen that

$$\vec{R}_{MT} = \vec{R}_T - \vec{R}_M \tag{6-3}$$

$$\vec{R}_{LOS} = \vec{R}_{GT} = \vec{R}_{MT} - \vec{R}_{MG} \tag{6-4}$$

and

$$\hat{R}_{LOS} = \frac{\vec{R}_{LOS}}{|\vec{R}_{LOS}|} \tag{6-5}$$

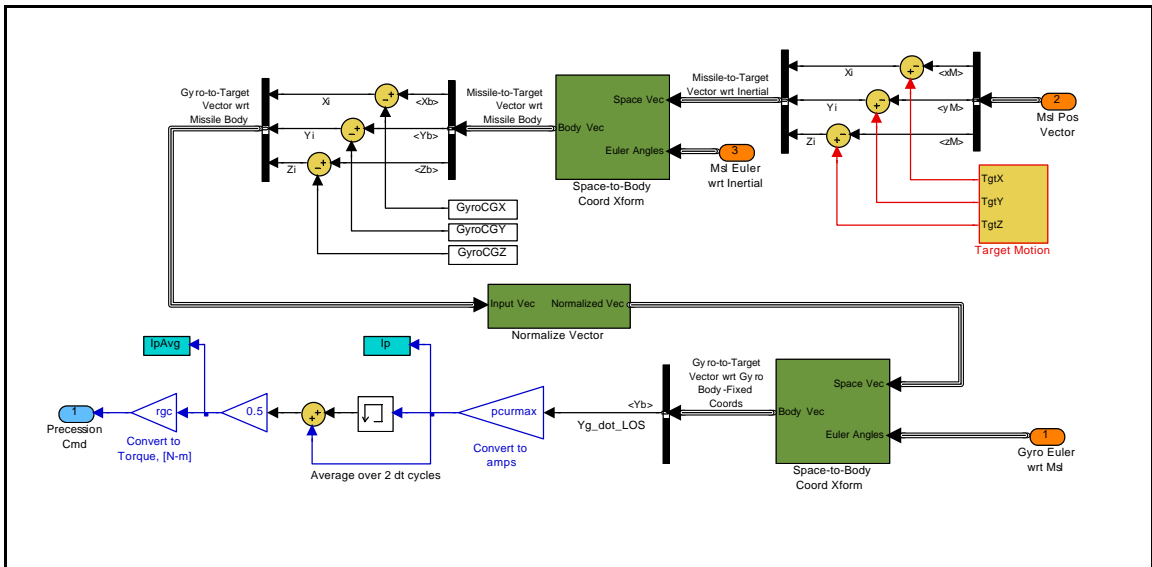


Figure 74 - BDWL track loop model.

Figure 74 shows the BDWL track loop block, which is based on Equations 6-1, 6-2, 6-3, 6-4, and 6-5. The inertial target position vector is needed for input to Equation 6-3. For a rate table test scenario, it is assumed that the missile is stationary in position (not rotation), the missile-to-target range is constant, and

the target inertial azimuth and elevation rates with respect to the missile are constant. Figure 75 shows the target geometry.

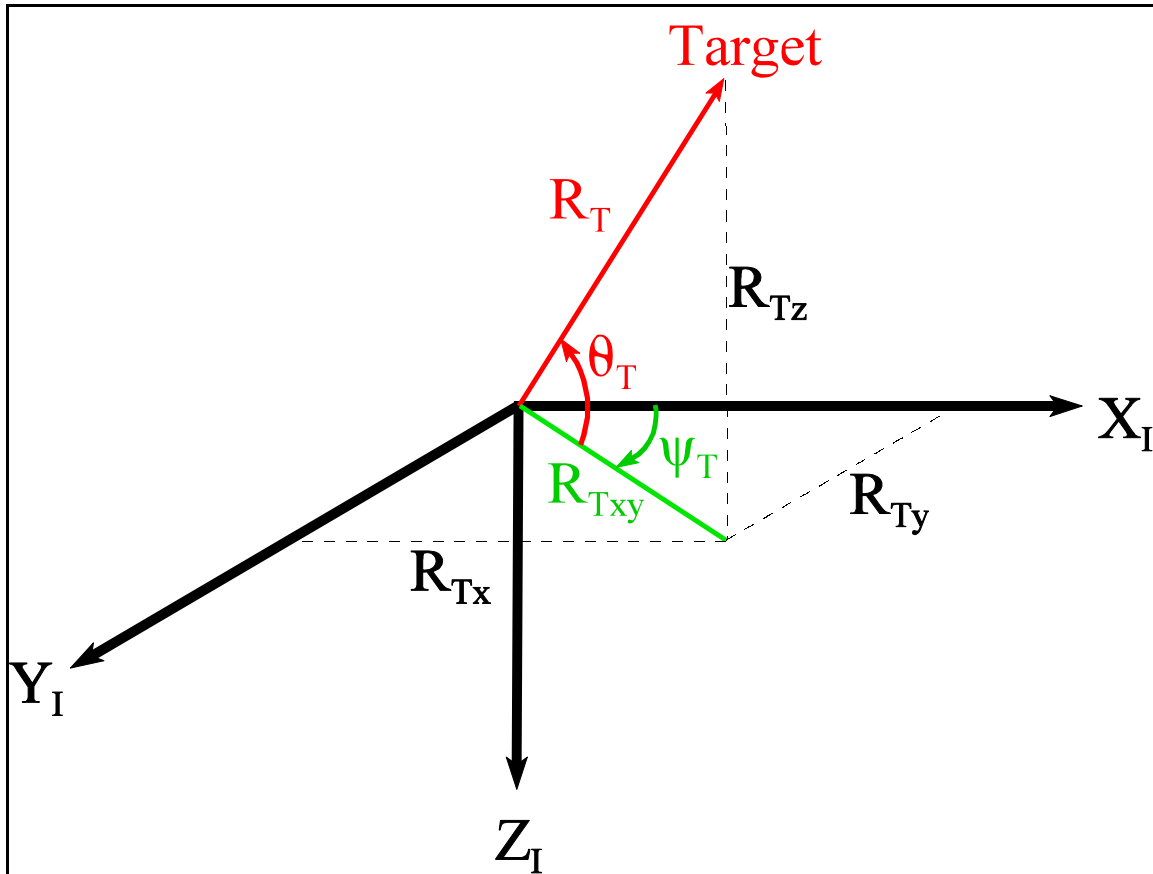


Figure 75 - Rate table target position geometry.

If the target inertial azimuth and elevation rates (\dot{y}_T and \dot{q}_T) are constant, then,

$$y_T = \int \dot{y}_T dt \quad (6-6)$$

$$q_T = \int \dot{q}_T dt \quad (6-7)$$

From Figure 75 it can be seen that

$$R_{Tz} = -R_T \sin(\mathbf{q}_T) \quad (6-8)$$

$$R_{Txy} = R_T \cos(\mathbf{q}_T) \quad (6-9)$$

$$R_{Tx} = R_{Txy} \cos(\mathbf{y}_T) = R_T \cos(\mathbf{q}_T) \cos(\mathbf{y}_T) \quad (6-10)$$

$$R_{Ty} = R_{Txy} \sin(\mathbf{y}_T) = R_T \cos(\mathbf{q}_T) \sin(\mathbf{y}_T) \quad (6-11)$$

Equations 6-6, 6-7, 6-8, 6-10, and 6-11 are used in the target motion block, shown in Figure 76.

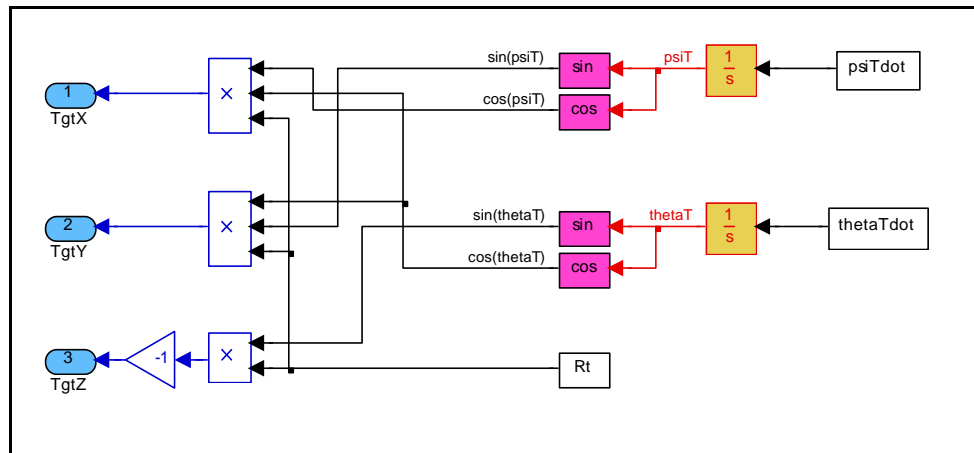


Figure 76 - BDWL track loop target motion block.

There are two identical subsystems in the BDWL track loop block called “space-to-body coordinate transform”. These blocks perform an Euler angle coordinate transformation which converts a vector from a space based coordinate system to a body-based coordinate system. This is done by implementing the appropriate direction cosine matrix. Figure 77 shows the space-to-body coordinate transform block. It uses the space-to-body direction cosine block previously described in Section 3.2.

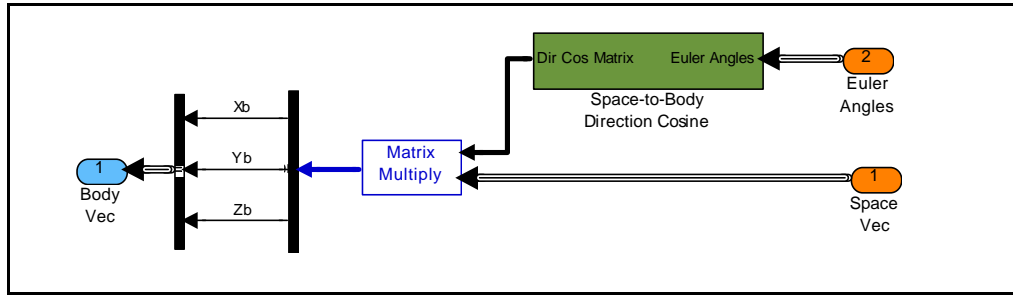


Figure 77 - BDWL space-to-body coordinate transform block.

In order to calculate the unit vector \hat{R}_{LOS} from the vector \vec{R}_{LOS} , a normalize vector block was developed. This block is shown in Figure 78, it calculates the length of the \vec{R}_{LOS} vector using the square root of the sum of the squares of its three vector components. Each vector component is then divided by the total vector length to produce a unit vector aligned with the original vector. There is also a block to prevent a “divide-by-zero” error in the case of a zero length vector.

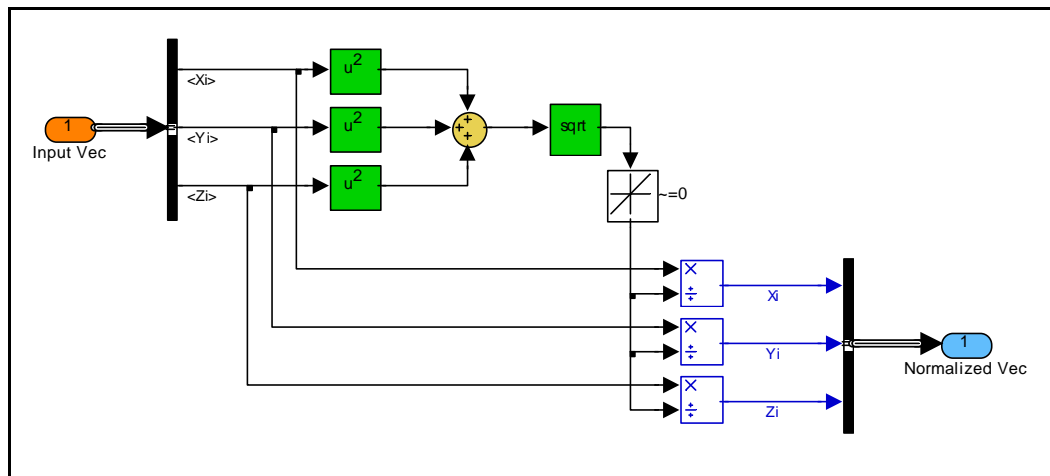


Figure 78 - BDWL track loop normalize vector block.

6.3.2 Ideal Track Loop Model and Implementation

Figure 79 shows the tracker implementation in the Ideal gyro model. The Ideal gyro model does not use a precession signal or gyro torques as the BDWL gyro model does. The Ideal gyro model merely uses gamma, the direction of gyro precession, and T_y , the magnitude (in radians / second) of the desired gyro

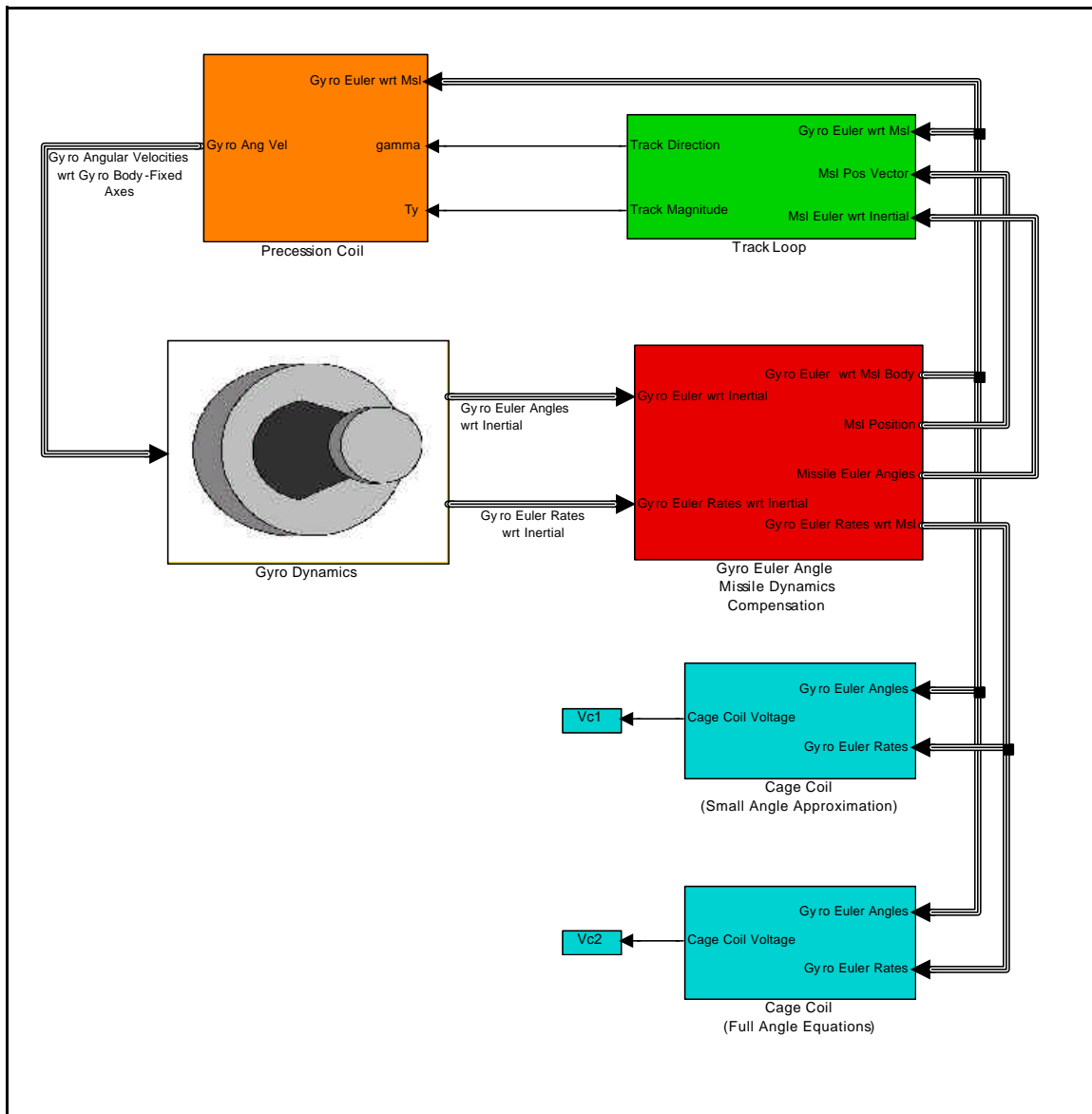


Figure 79 - Ideal gyro model with track loop implementation.

precession. A modified version of the BDWL track loop model was implemented in the Ideal gyro tracking model.

Figure 80 shows the geometry of the gyro-to-target line-of-sight vector in the non-rolling gyro with respect to missile coordinate system. From Figure 80, it can be seen that

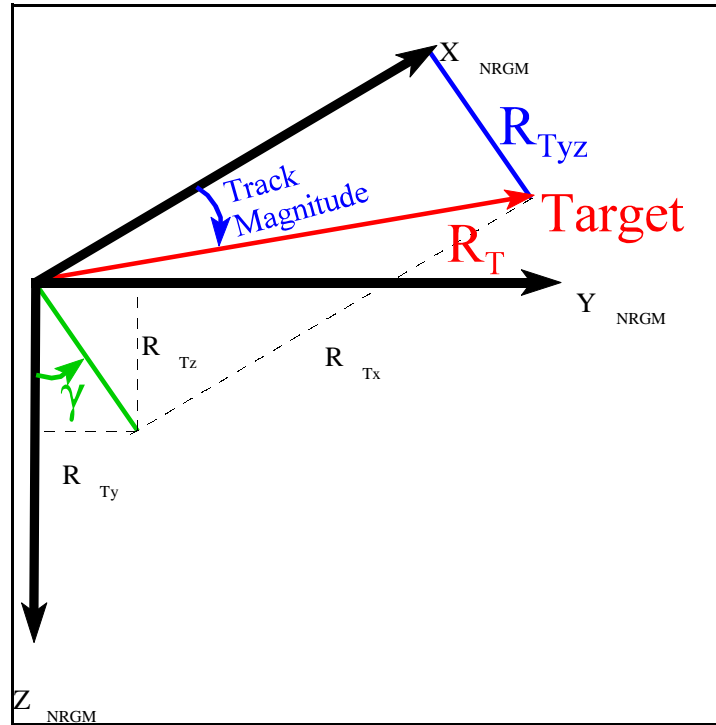


Figure 80 - Ideal gyro track direction and magnitude.

$$g = \tan^{-1}\left(\frac{R_{Ty}}{R_{Tz}}\right) \quad (6-12)$$

$$R_{Tyz} = \sqrt{R_{Ty}^2 + R_{Tz}^2} \quad (6-13)$$

$$\text{Track Magnitude} = \tan^{-1}\left(\frac{R_{Tyz}}{R_{Tx}}\right) \quad (6-14)$$

Figure 81 shows the Ideal gyro track loop block. It is very similar to the BDWL track loop block, with Equation 6-12, 6-13, and 6-14 implemented. A gain of 40 was added to the Track Magnitude channel, which was calculated experimentally

so that the second track loop test yielded a 0.25E steady state error, which is commensurate with the BDWL model.

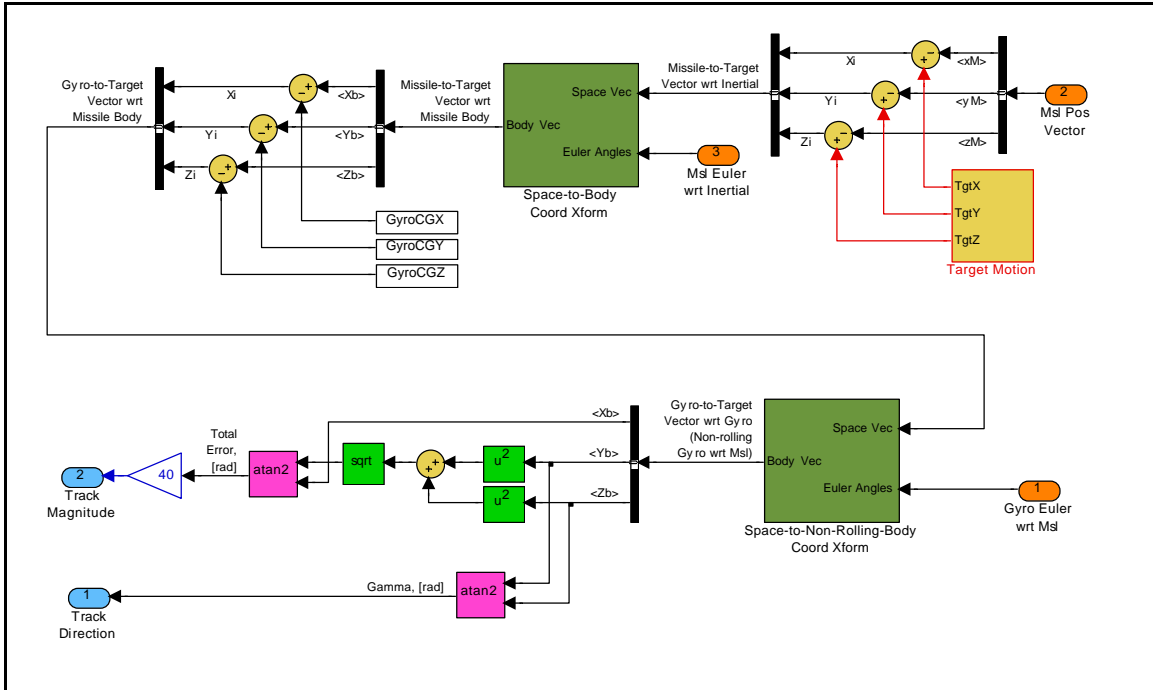


Figure 81 - Ideal gyro model track loop block.

The Ideal gyro model track loop block contains a “space-to-non-rolling-body coordinate transform” which is a modification of the space-to-body coordinate transform, using only the pitch and yaw Euler angles. This is essentially an implementation of the space-to-non-rolling-body direction cosine matrix

$${}^{NRGM}D^M = \begin{bmatrix} C_{y_{GM}} C_{q_{GM}} & S_{y_{GM}} C_{q_{GM}} & -S_{q_{GM}} \\ -S_{y_{GM}} & C_{y_{GM}} & 0 \\ C_{y_{GM}} S_{q_{GM}} & S_{y_{GM}} S_{q_{GM}} & C_{q_{GM}} \end{bmatrix} \quad (6-15)$$

The space-to-non-rolling-body coordinate transform block is shown in Figures 82 through 85.

The Ideal gyro model precession coil block was also modified to accept the track direction (γ), and track magnitude as external inputs. It is shown in Figure 86.

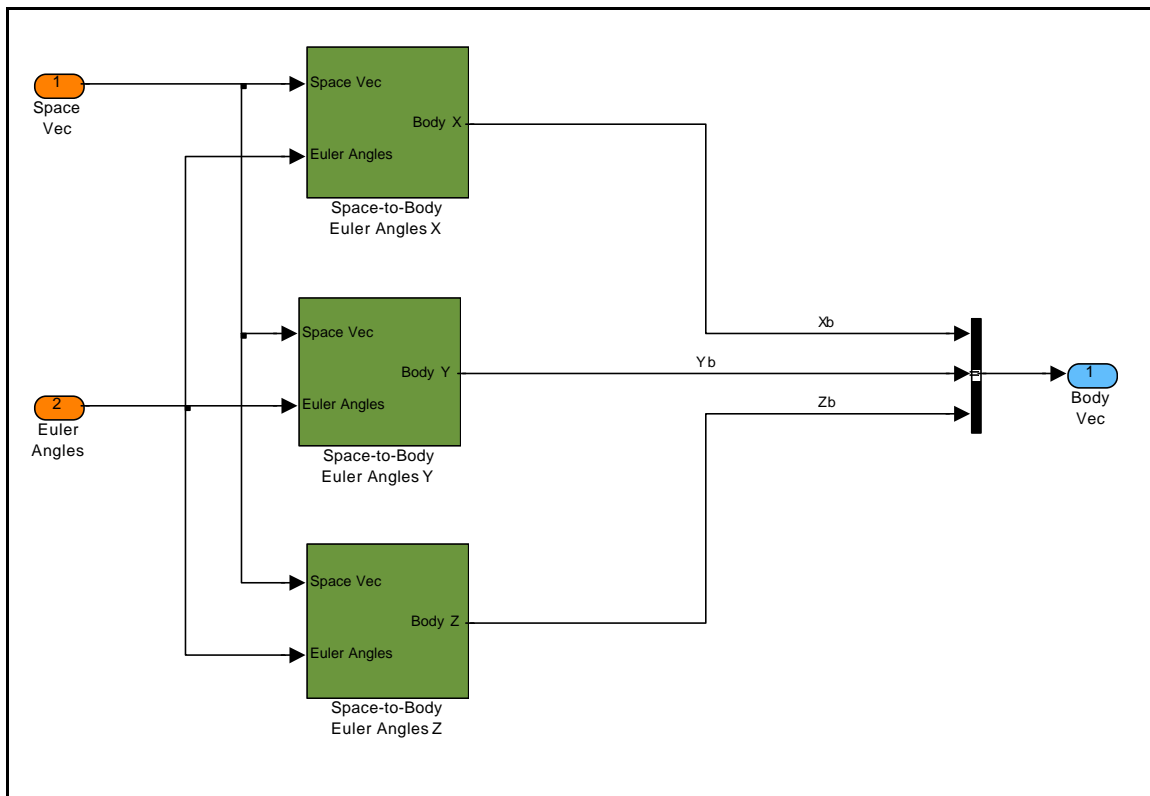


Figure 82 - Ideal track loop space-to-nonrolling body coordinate transform block.

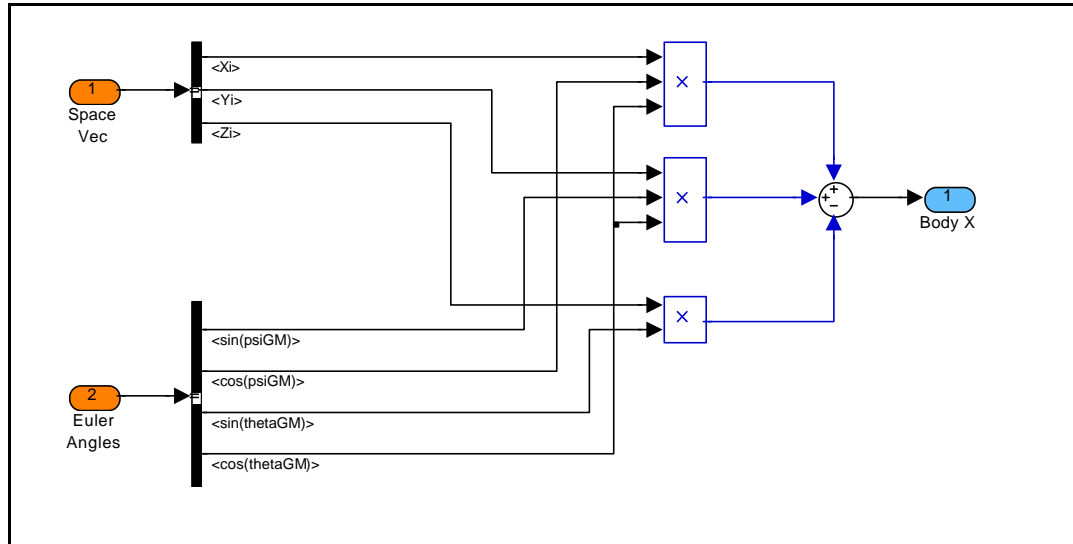


Figure 83 - Ideal space-to-body Euler angles X block.

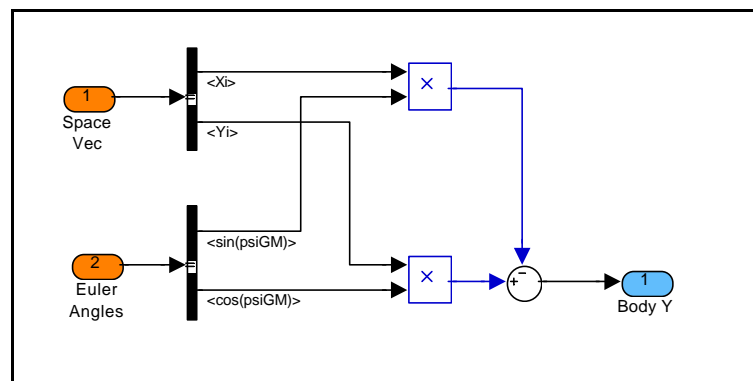


Figure 84 - Ideal space-to-body Euler angles Y block.

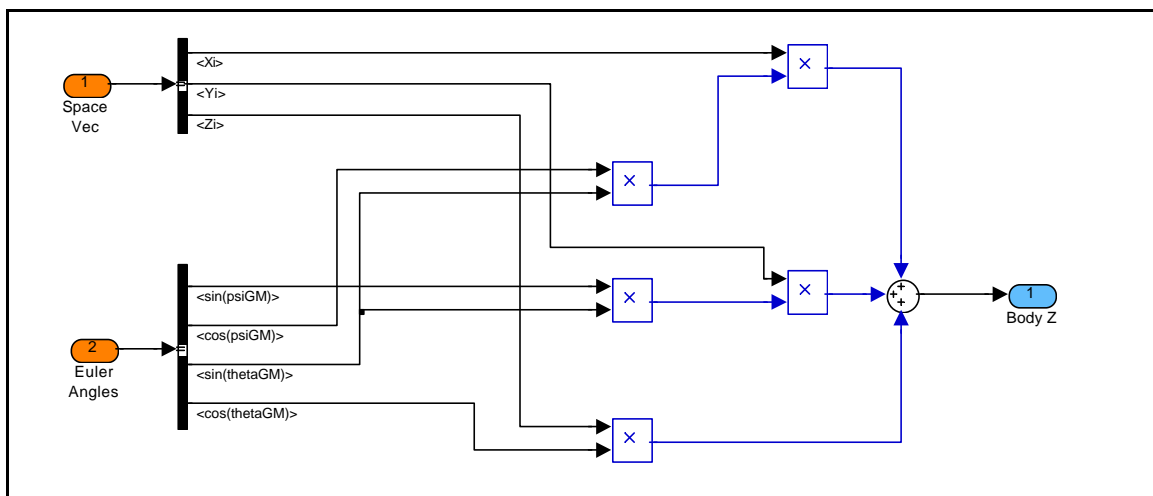


Figure 85 - Ideal space-to-body Euler angles Z block.

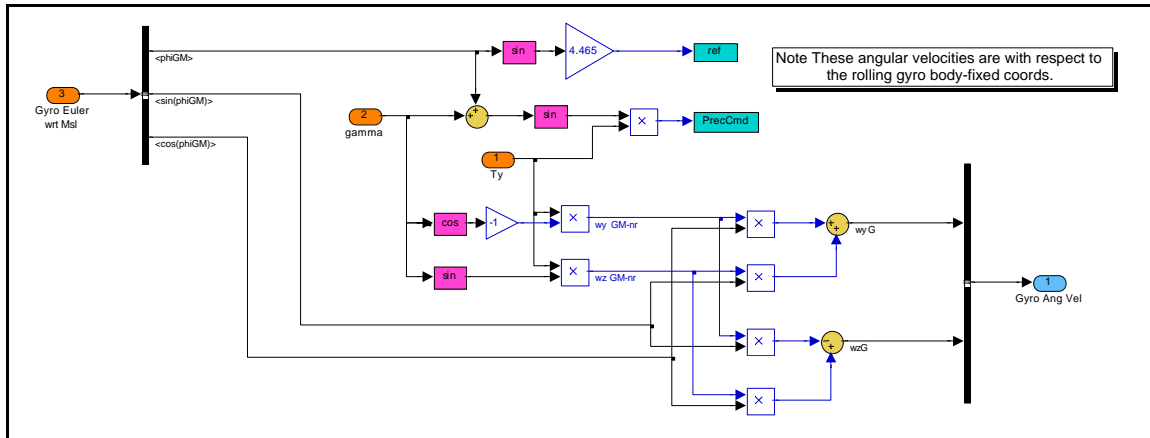


Figure 86 - Ideal gyro tracker precession coil block.

6.3.3 Gallaspy Track Loop Model and Implementation

The implementation of a track loop block in the Gallaspy gyro model is based on the track loop from the Ideal gyro model. Figure 87 shows the top level of the Gallaspy gyro model with track loop included. The Gallaspy equations of motion require gyro torque inputs based on a gyro commanded rate of change and direction in the non-rolling gyro with respect to inertial coordinate system.

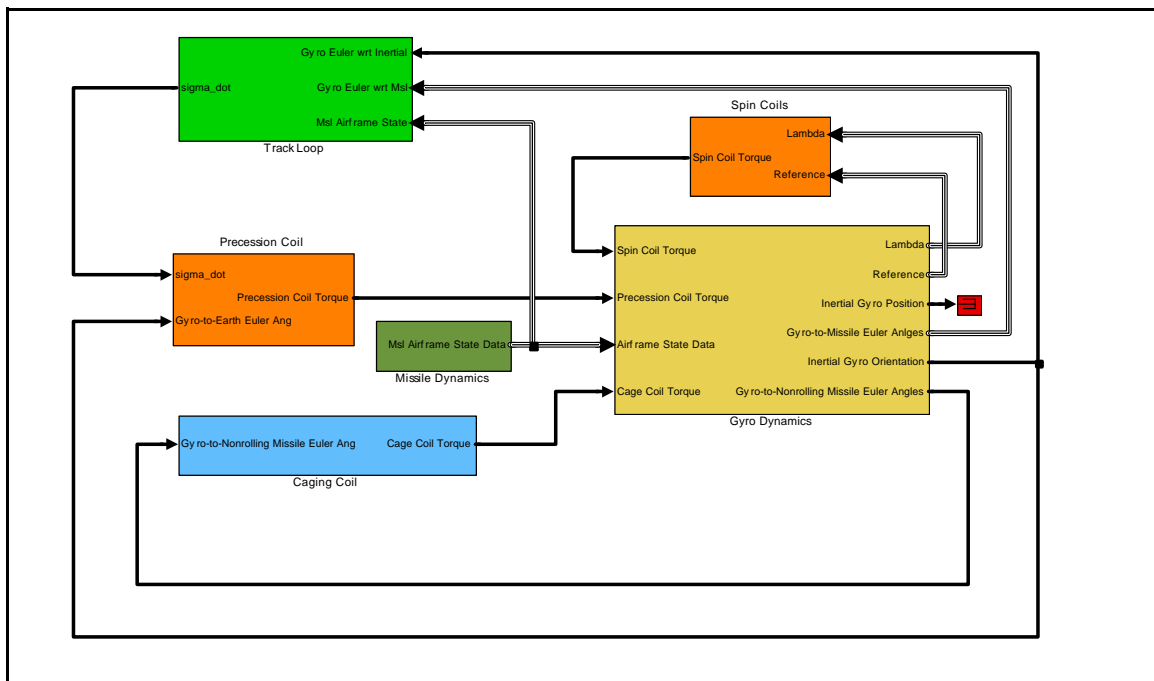


Figure 87 - Gallaspy gyro model with track loop implementation.

A missile dynamics block has been added to the Gallaspy gyro model. Figure 88 shows this block. This block provides missile state data consisting of the missile linear position, missile angular velocity, missile-to-inertial (earth) direction cosine matrix, and the missile Euler angles with respect to the inertial coordinate system. This is done with a combination of the rate table block and

the body-to-space direction cosine block, both previously derived in Section 3 for the BDWL gyro model.

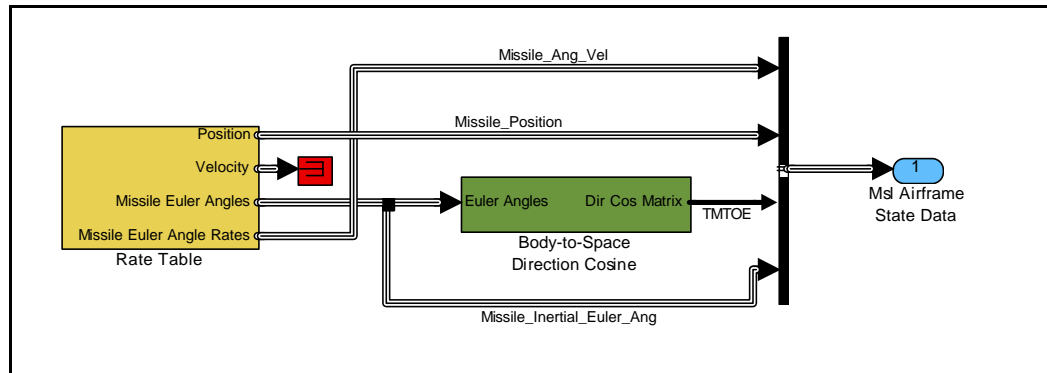


Figure 88 - Gallaspy track loop missile dynamics block.

The Gallaspy track loop block is shown in Figure 89. It is very similar to the Ideal gyro model track loop. First, the missile-to-target vector is formed in the inertial coordinate system. It is transformed to the missile body-fixed coordinate system. The relative gyro position with respect to the missile center of gravity is used to form the gyro-to-target vector in the missile body-fixed coordinate system. This vector is transformed to the gyro body-fixed coordinate system using the gyro with-respect-to-missile Euler angles.

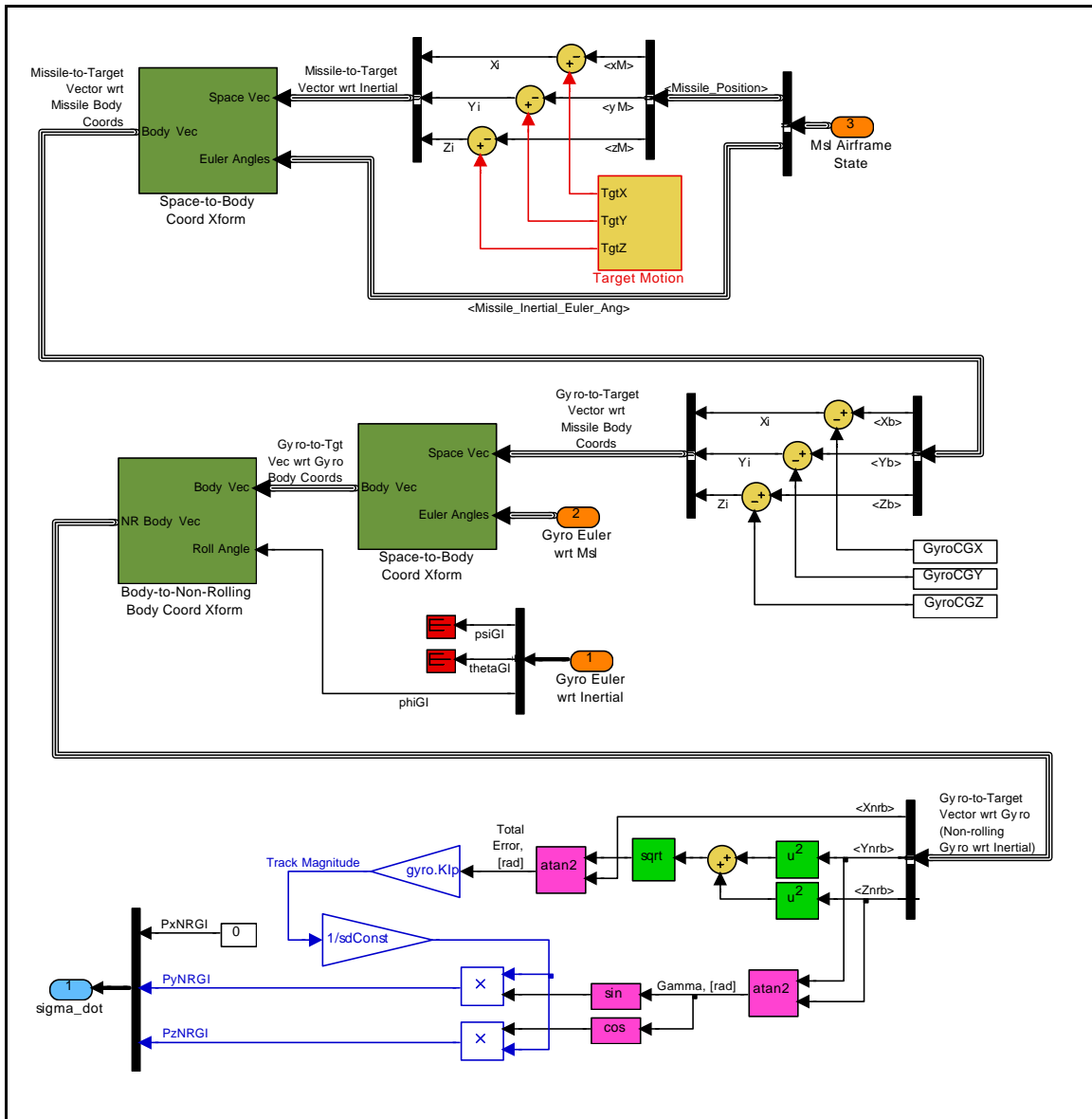


Figure 89 - Gallaspy track loop block.

The gyro-to-target vector is then transformed from the gyro body-fixed coordinate system to the non-rolling gyro with respect to inertial coordinate system. This is done with the body-to-non-rolling body coordinate transform block shown in Figure 90, which is based on the following direction cosine matrix:

$$\left\{ \vec{R}_{GT} \right\}_{NRGI} = {}^{NRGI}D^G \left\{ \vec{R}_{GT} \right\}_G \tag{6-16}$$

where \vec{R}_{GT} = Vector from gyro to target

and,

$${}^{NRGI}D^G = \begin{bmatrix} 1 & 0 & 0 \\ 0 & \cos(\mathbf{f}_{GI}) & -\sin(\mathbf{f}_{GI}) \\ 0 & \sin(\mathbf{f}_{GI}) & \cos(\mathbf{f}_{GI}) \end{bmatrix} \quad (6-17)$$

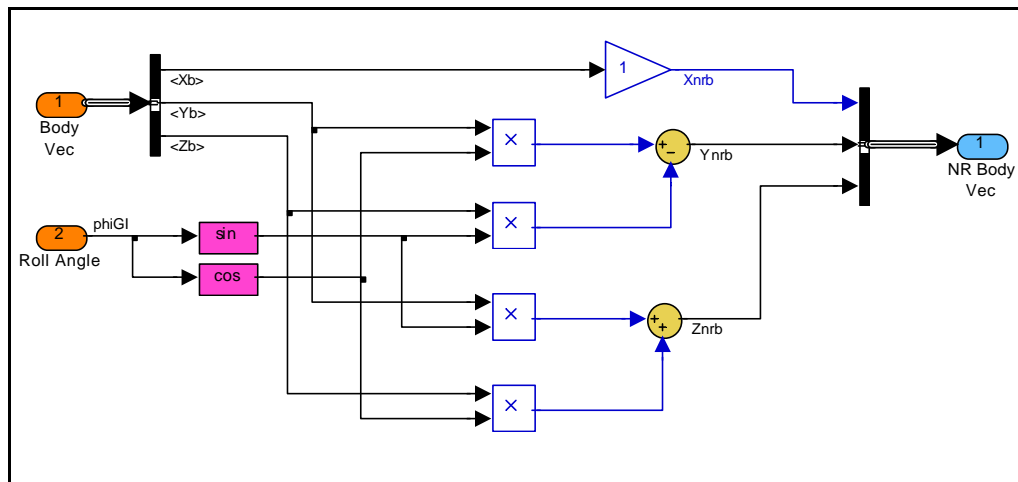


Figure 90 - Gallaspy track loop body-to-non-rolling body coordinate transform block.

The Gallaspy gyro track loop then calculates the total gyro pointing error and the direction of this error in the non-rolling gyro with respect to inertial coordinate system in a similar manner to the Ideal gyro track loop model. The sigma dot signal is then created by resolving the precession magnitude and direction into the non-rolling gyro with respect to inertial Y and Z axes. Figure 91 shows the basis for this transformation, given by

$$\{P_y\}_{NRGI} = \frac{KI p}{sdconst} \mathbf{e} \cdot \sin(\mathbf{g}) \quad (6-18)$$

where $\{P_y\}_{NRGI}$ = Precession command in the NRGI Y direction

KIp = Precession current conversion factor

$sdconst$ = Sigma dot constant

e = Magnitude of total gyro pointing error

and

$$\{P_z\}_{NRGI} = \frac{KIp}{sdconst} e \cdot \cos(\mathbf{g}) \quad (6-19)$$

where $\{P_z\}_{NRGI}$ = Precession command in NRGI Z direction

There is no precession command in the NRGI X direction because this would cause a spin torque. The precession coils and track loop only precess the gyro.

The spin coil model controls gyro spin rates and torques. Of course, in reality, a precession torque can cause spin

torques, but this effect is not included in the Gallaspy model.

The Gallaspy track loop gain (gyro.KIs) was tuned so that the gyro's steady state tracking error for the second Williams rate table test (15E look angle, 10E/sec track rate) was 0.25E, which matches the BDWL

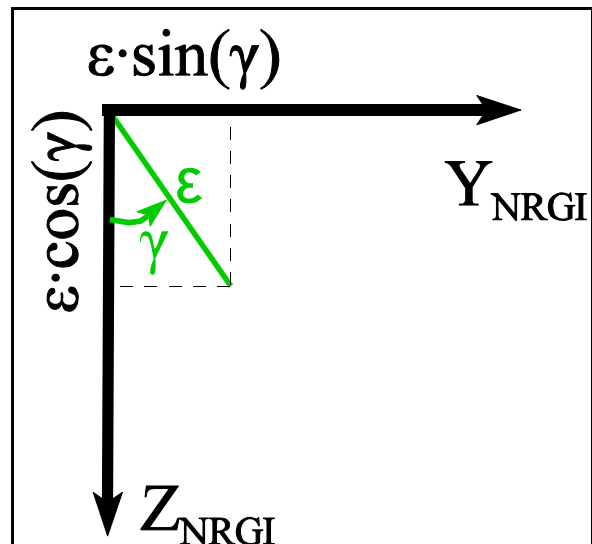


Figure 91 - Gallaspy gyro tracking error in the NRGI coordinate system.

gyro model. Also, the Gallaspy spin coil gain was adjusted so that the gyro spin-up profile matched the spin-up profile from the BDWL model for the first Williams gyro rate table test (15E look angle, 0E/sec track rate).

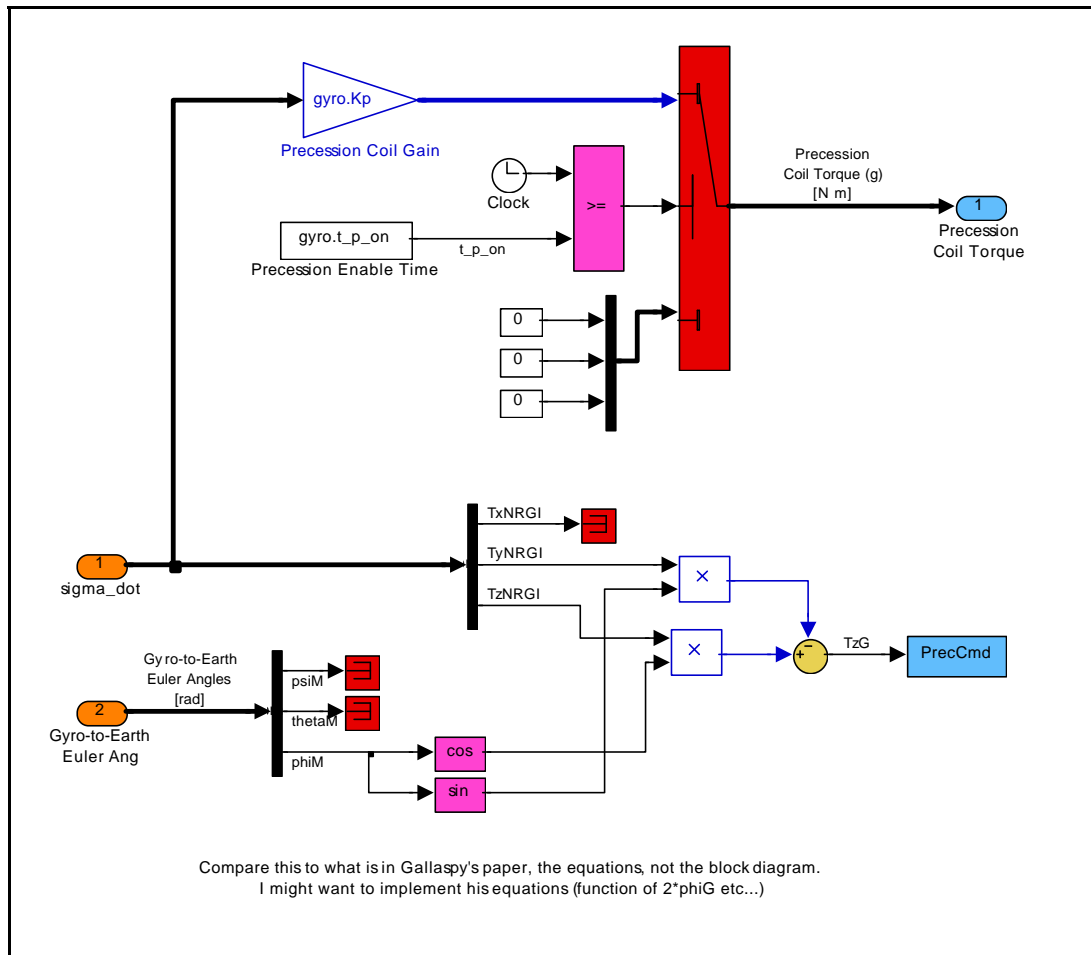


Figure 92 - Gallaspy track loop precession coil block.

The Gallaspy precession coil block, shown in Figure 92, was modified to accept a sigma dot precession command from the track loop block. This signal was also transformed back into the gyro body-fixed coordinate system to produce a gyro precession command comparable to the output for the Williams rate table tests. This was done using the standard direction cosine coordinate

transform matrix definition,

$$\{T\}_G = {}^G D^{NRGI} \{T\}_{NRGI} \quad (6-20)$$

where

$${}^G D^{NRGI} = \begin{bmatrix} 1 & 0 & 0 \\ 0 & \cos(\mathbf{f}_{GI}) & \sin(\mathbf{f}_{GI}) \\ 0 & -\sin(\mathbf{f}_{GI}) & \cos(\mathbf{f}_{GI}) \end{bmatrix} \quad (6-21)$$

A few other minor adjustments were made to the baseline Gallaspy gyro model to allow the rate table tests to work properly, such as modifications to the spin coils block to allow timed gyro spin up and spin down.

6.3.4 Rate Table Test Comparison

As stated at the beginning of Section 6.3, the rate table gyro tests from Williams (9) were done with the gyro look angle, missile rotation rate, and missile roll angle being varied from test to test. These parameters stayed constant during any individual test. During each of these tests, the gyro was started spinning at 100 Hz, then commanded to spin up to 115 Hz at 2 seconds into the run. At 6 seconds into the simulation run, the gyro was commanded to spin back down from 115 Hz to 100 Hz. The relative effects of look angle, missile body rate, and missile roll angle can be seen in the responses to these test runs. The output is compared using the missile sigma dot signal and gyro spin rate.

The missile sigma dot signal is directly related to the model precession command signals. Their relative magnitudes will be different, but their overall

shape and response should be similar. The gyro spin frequency is directly comparable between the actual gyro data and the model data. For each rate table test, the Williams actual gyro data is shown along with the Williams model data, next the results from the three candidate models (BDWL, Ideal, and Gallaspy) are shown.

Comments on the model rate table test results are provided with the data for each test. General comments which apply to all rate table tests include the fact that the Ideal gyro model has instantaneous spin-up and spin-down, which does not match the actual gyro data well. The Gallaspy model has a spin-up and spin-down response, but it was tuned to match the first rate table test, and it does not change for the other rate table tests. Also, the Ideal and Gallaspy models show zero precession command (even during gyro spin-up and spin-down) during the rate table tests when the rate table is stationary.

Rate Table Test 1, 15E look angle, 0E/sec rate, 0E roll position:

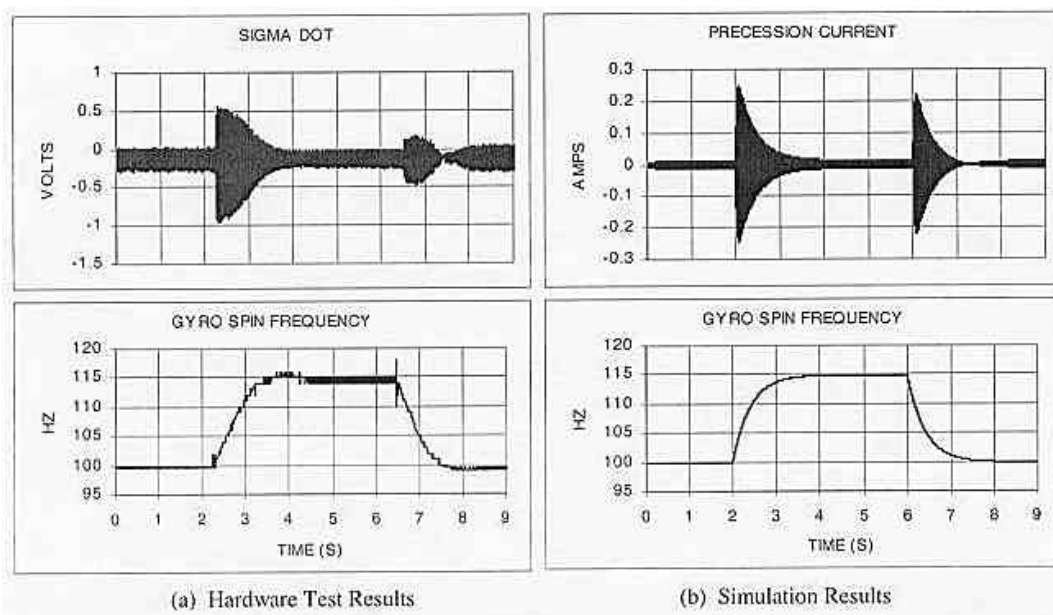


Figure 93 - Williams gyro data and model data for rate table test 1.

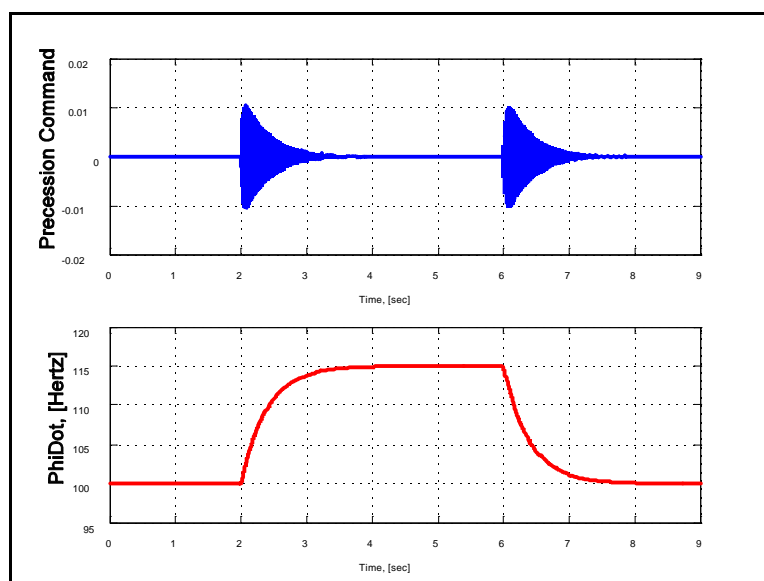


Figure 94 - BDWL response from rate table test 1.

The BDWL model matches the real gyro data well. The spin rate shows excellent correlation. The precession command matches sigma dot well, although the real gyro data shows less sigma dot magnitude on gyro spin-down.

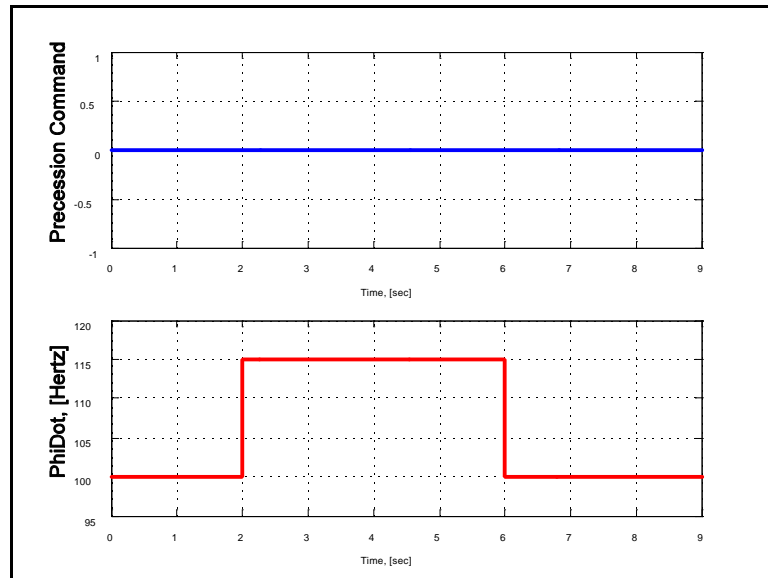


Figure 95 - Ideal response for rate table test 1.

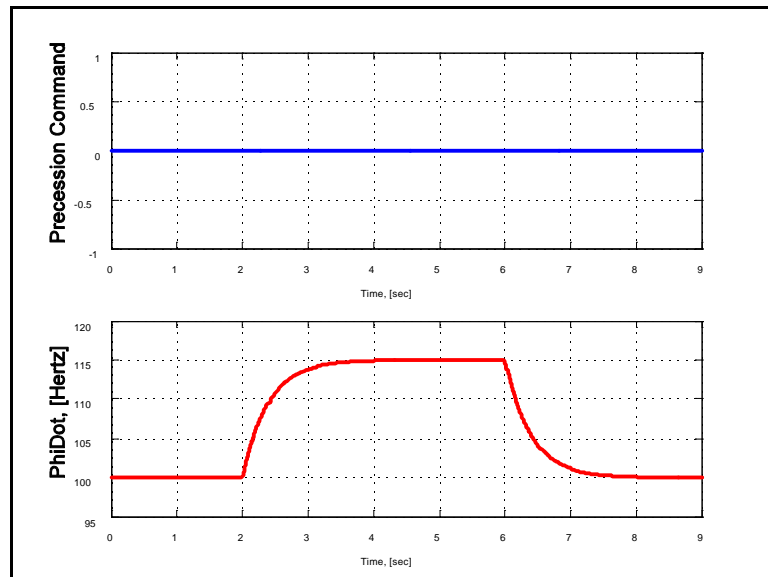


Figure 96 - Gallaspy response for rate table test 1.

As expected, the Ideal model shows the least correlation with actual gyro data. The Ideal model's precession command is zero, and its spin rate shows instantaneous spin-up and spin-down. The Gallaspy precession command is also flat, but the spin profile matches the real gyro data well.

Rate table test 2, 15E look angle, 10E/sec rate, 0E roll position:

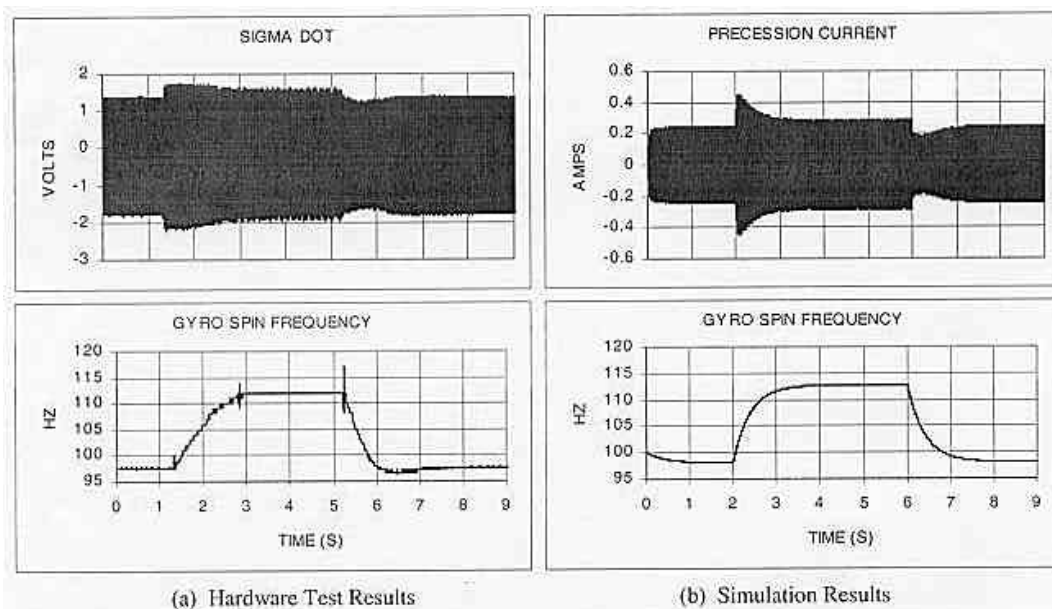


Figure 97 - Williams gyro data and model data for rate table test 2.

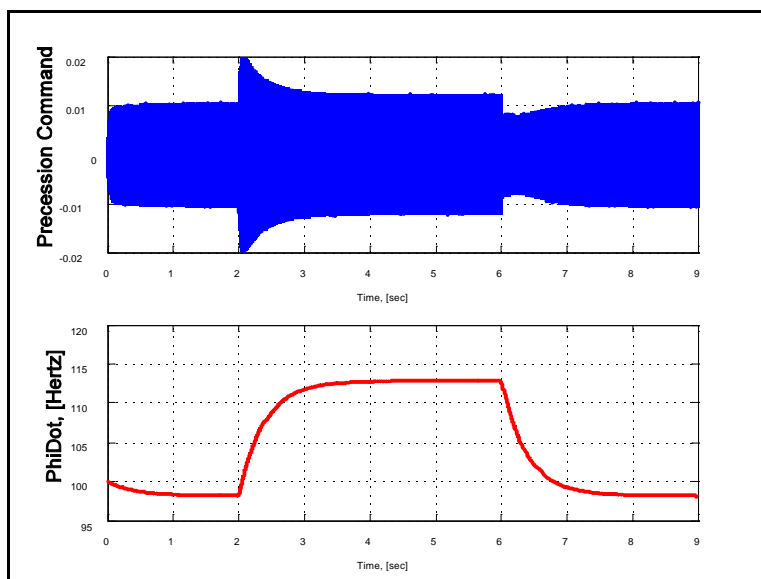


Figure 98 - BDWL response for rate table test 2.

The BDWL model matches the real gyro data well for this test. Note that the steady state spin rates are less than 100 Hz and less than 115 Hz. This is due to the inefficiencies in the spin coils at large off-boresight angles.

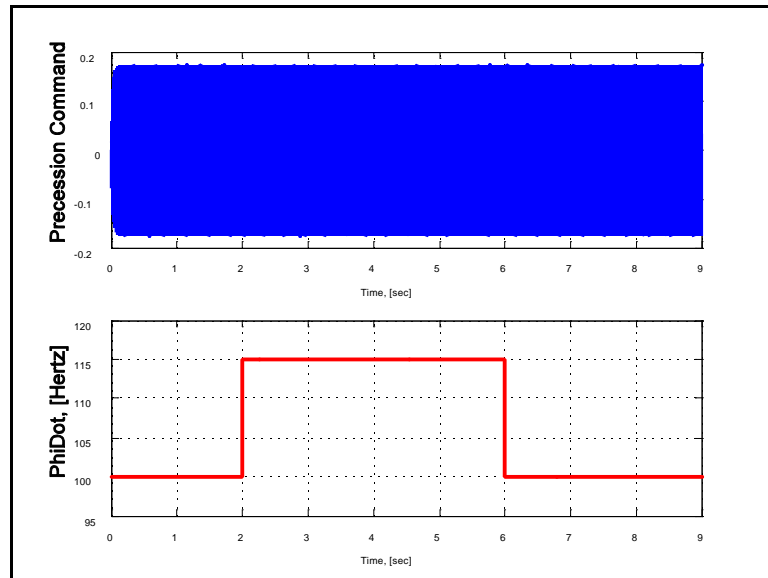


Figure 99 - Ideal response for rate table test 2.

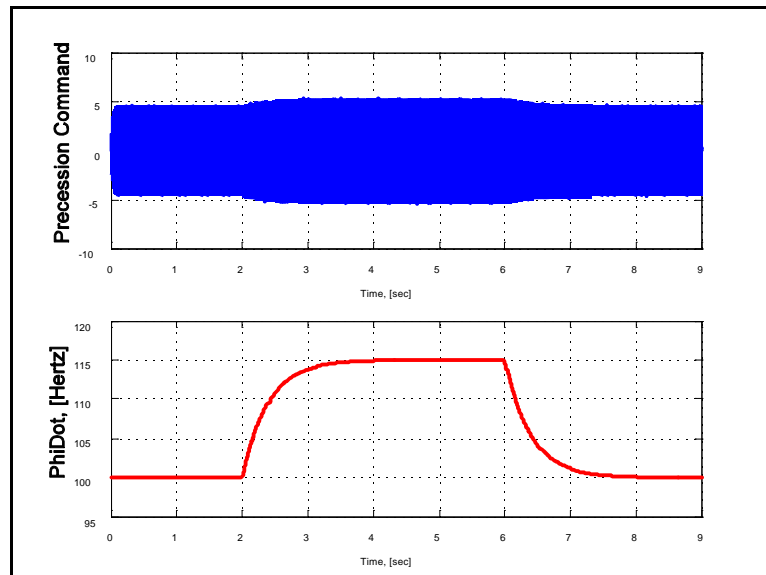


Figure 100 - Gallaspy response for rate table test 2.

The Ideal model shows instant gyro spin response and constant precession command and, thus, has the least fidelity. The Gallaspy model shows an increased precession command at the higher spin rate, but does not show the spin coil inefficiencies for large look angles.

Rate table test 3, 30E look angle, 0E/sec rate, 0E roll position:

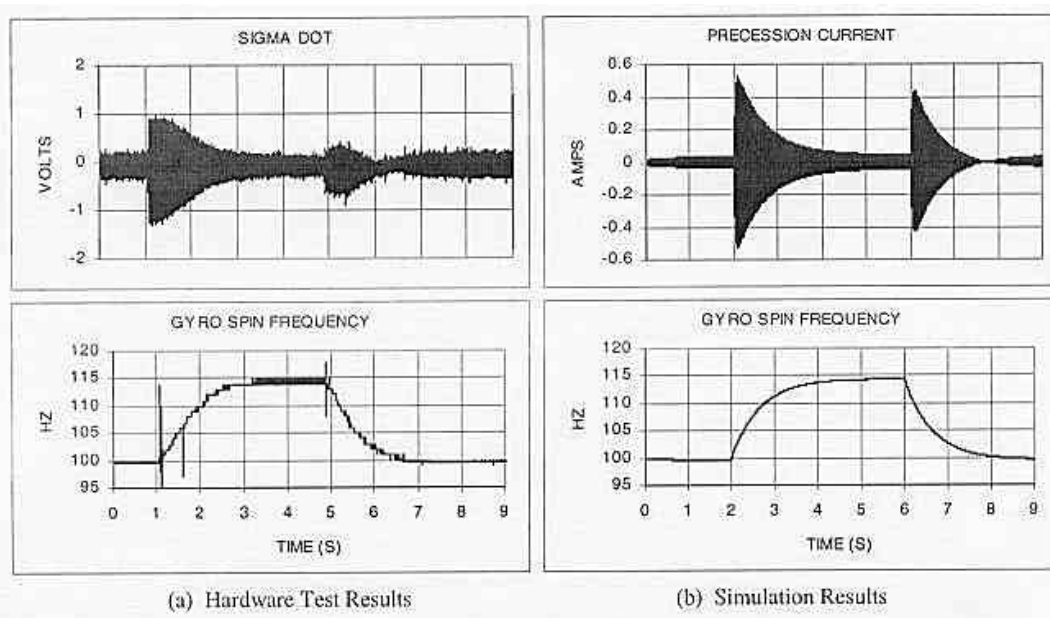


Figure 101 - Williams gyro data and model data for rate table test 3.

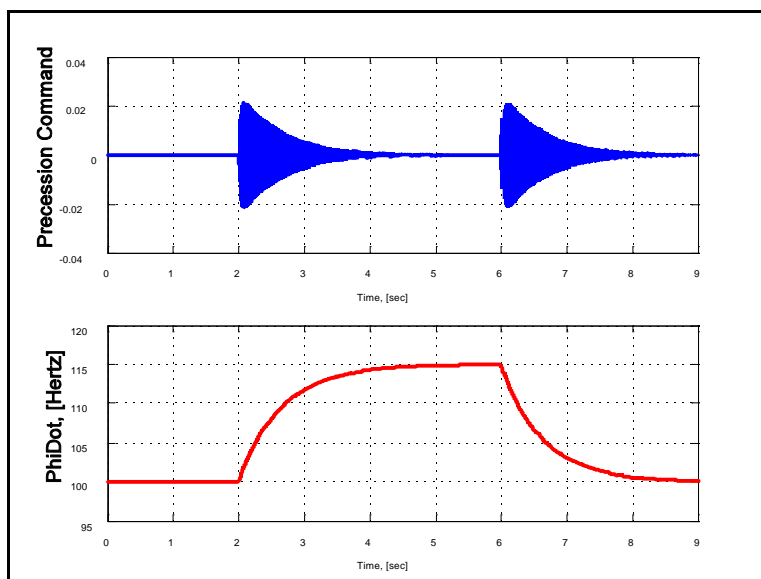


Figure 102 - BDWL response for rate table test 3.

The BDWL model matches the actual gyro well for this test. As in test 1, the actual data shows a decreased sigma dot magnitude on spin-down, which is not shown in the BDWL model. The spin rate profile matches well.

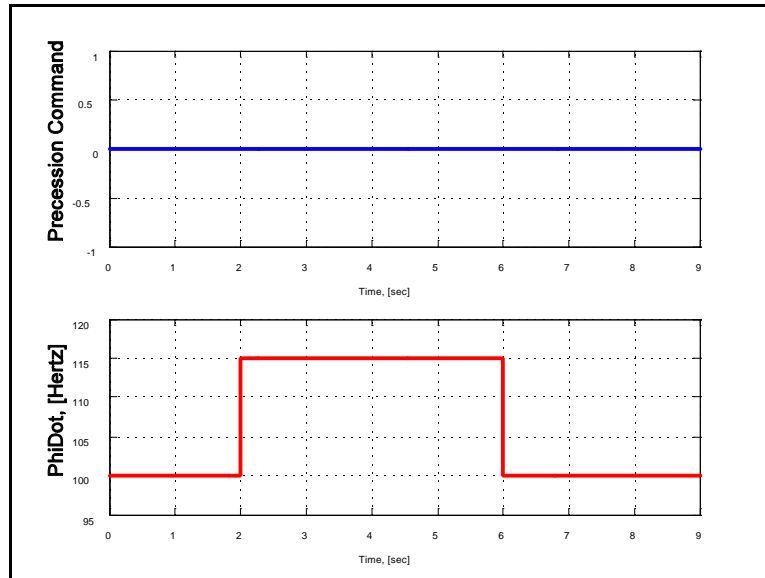


Figure 103 - Ideal response for rate table test 3.

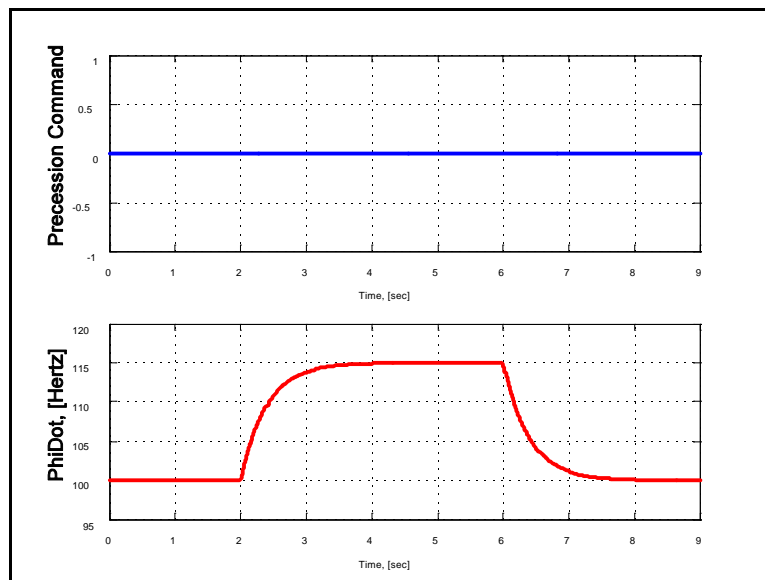


Figure 104 - Gallaspy response for rate table test 3.

The Ideal model and the Gallaspy model show no precession command since there is no rate table motion. The Gallaspy model spin rate profile does not match the actual gyro response, since it is not affected by precession command or look angle.

Rate table test 4, 30E look angle, 5E/sec rate, 0E roll position:

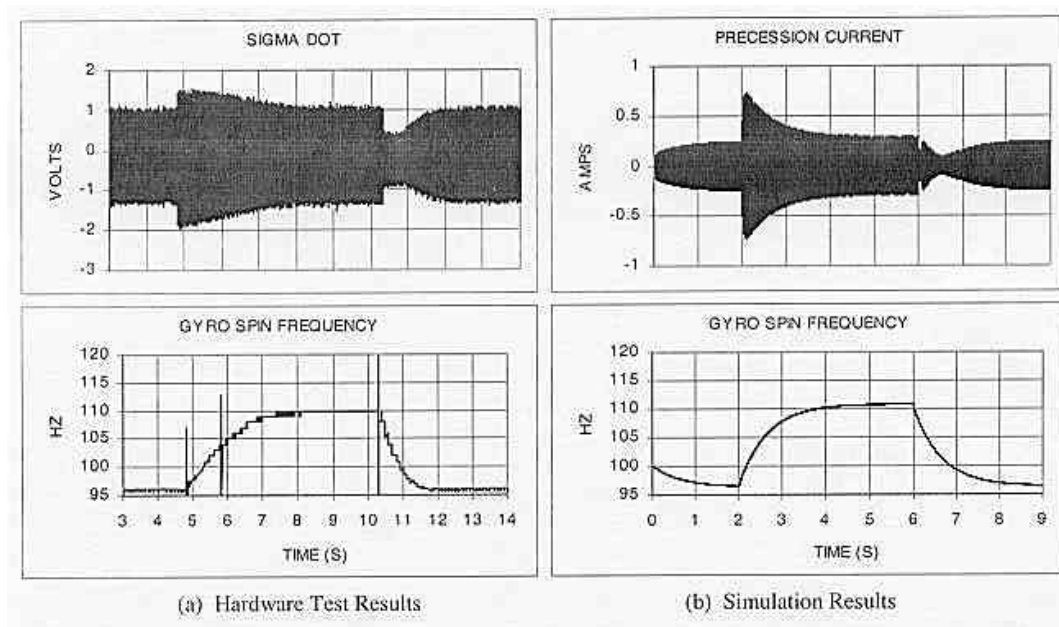


Figure 105 - Williams gyro data and model data for rate table test 4.

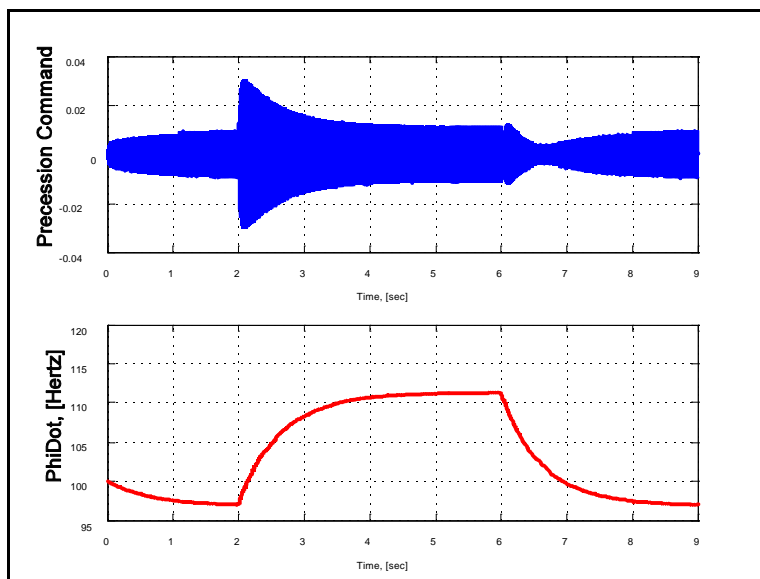


Figure 106 - BDWL response for rate table test 4.

The BDWL model matches the actual gyro data well. The spin rate profiles show that the spin coils cannot maintain steady state rates of 100 Hz or 115 Hz due to the large look angle.

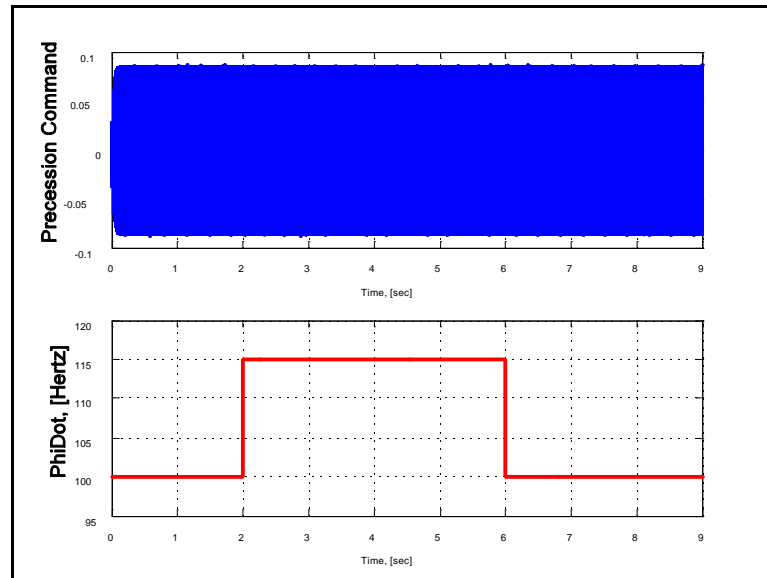


Figure 107 - Ideal response for rate table test 4.

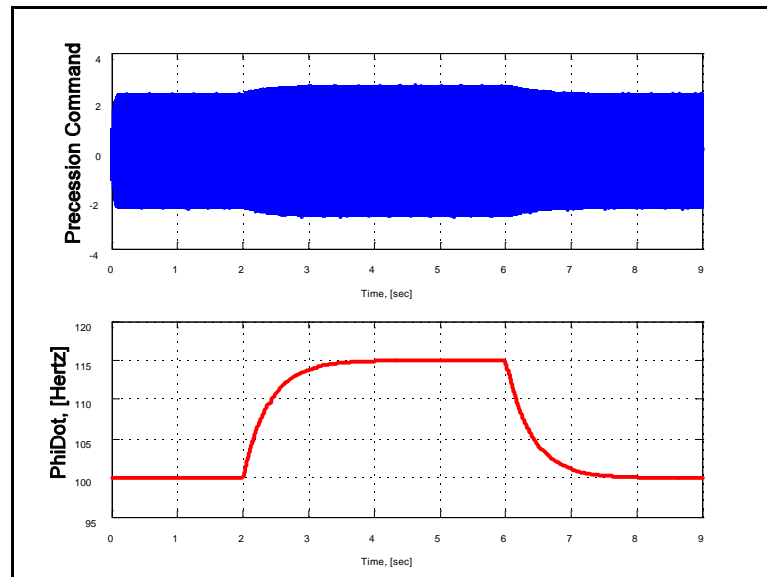


Figure 108 - Gallaspy response for rate table test 4.

The Ideal model has a constant magnitude precession command, with instantaneous spin-up and spin-down. The Gallaspy model shows increased precession command during the faster spin rate. Its spin rate profile does not match the actual gyro data well.

Rate table test 5, 15E look angle, 10E/sec rate, 90E roll position:

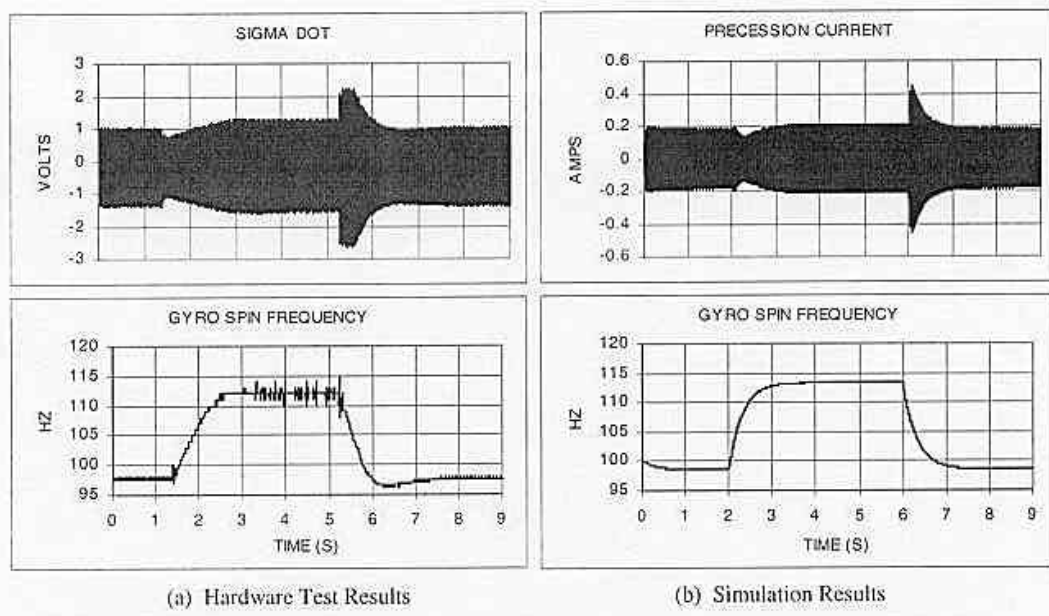


Figure 109 - Williams gyro data and model data for rate table test 5.

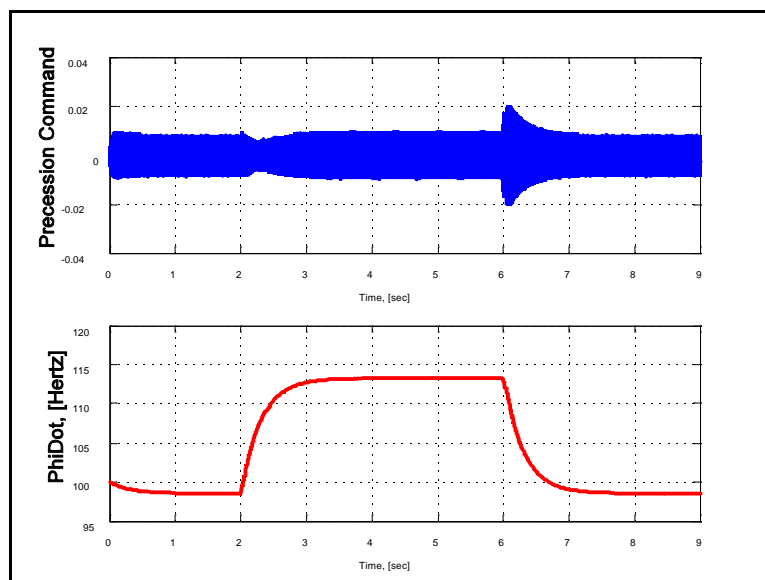


Figure 110 - BDWL response for rate table test 5.

The BDWL model matches the real gyro data well, showing a faster spin-up (due to the missile roll angle) and steady state spin rates less than 100 Hz and 115 Hz.

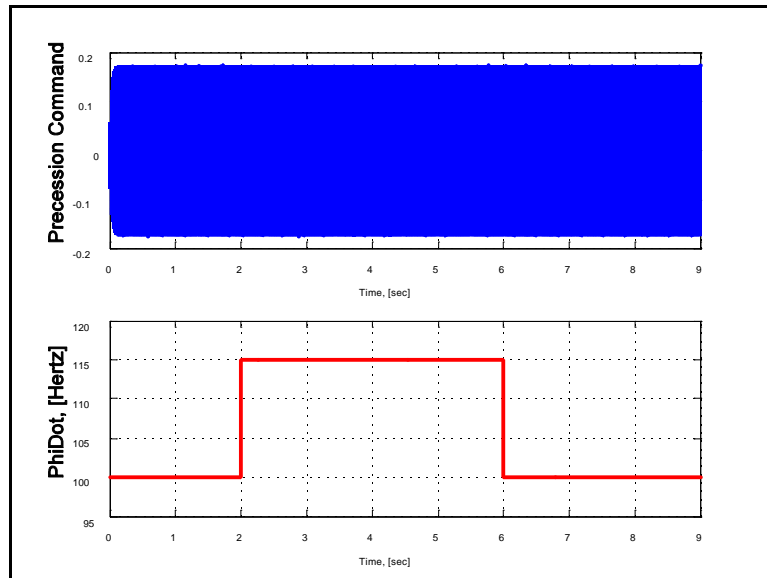


Figure 111 - Ideal response for rate table test 5.

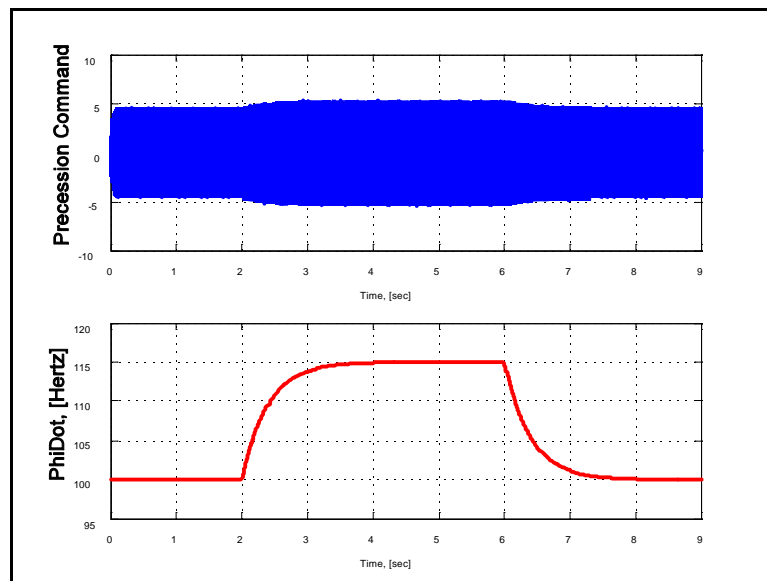


Figure 112 - Gallaspy response for rate table test 5.

As in previous tests, the Ideal and Gallaspy precession commands do not match the actual gyro sigma dot data well. The Ideal model spin rate has instantaneous response, while the Gallaspy spin rate is identical to all previous tests, with no response differences due to track rate, look angle, or missile roll position.

Rate table test 6, 30E look angle, 0E/sec rate, 90E roll position:

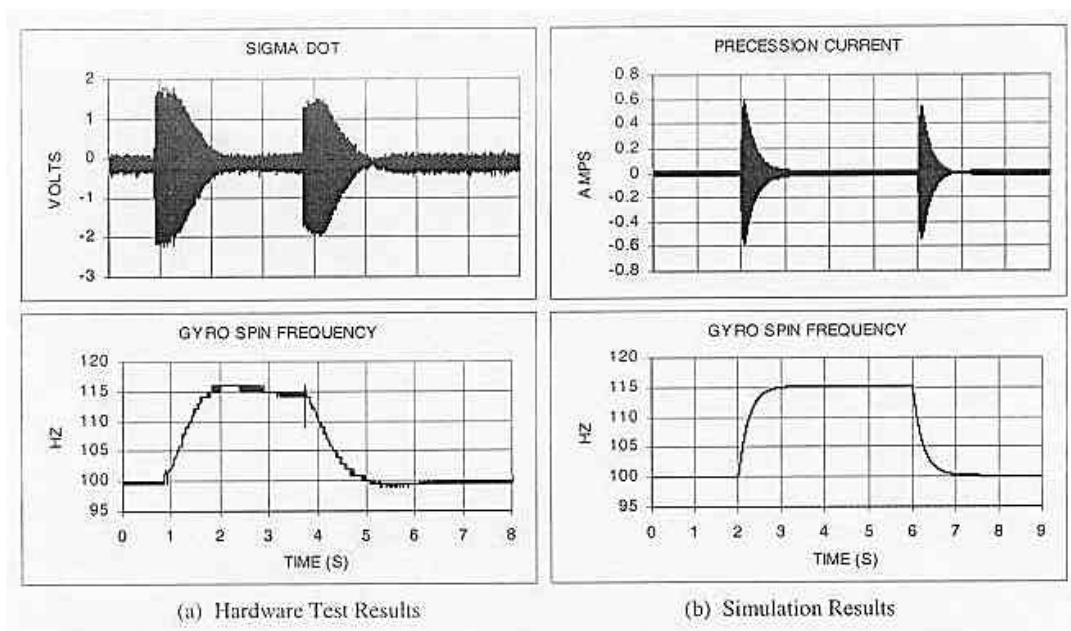


Figure 113 - Williams gyro data and model data for rate table test 6.

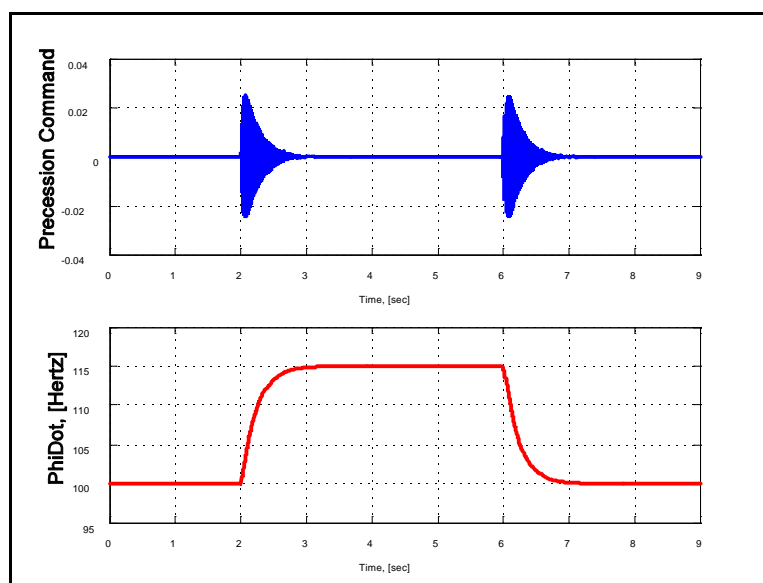


Figure 114 - BDWL response for rate table test 6.

The BDWL model again shows good correlation to the actual gyro data both in precession command and spin rate profile.

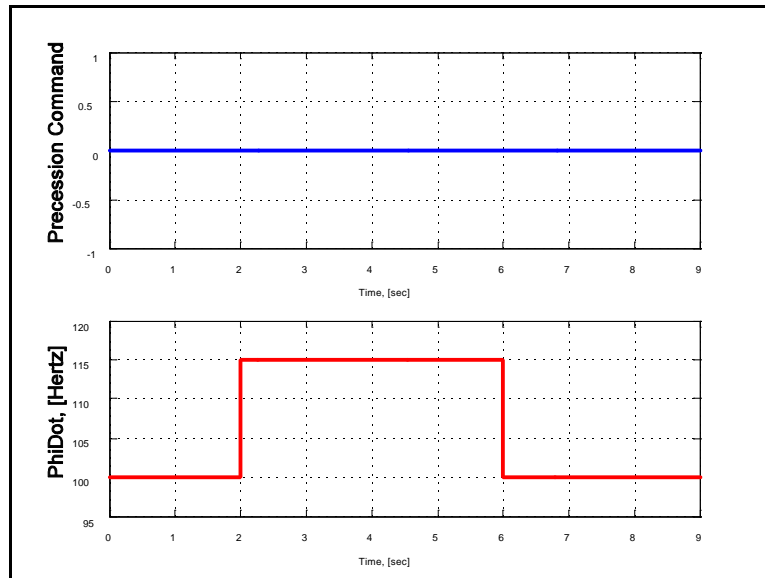


Figure 115 - Ideal response for rate table test 6.

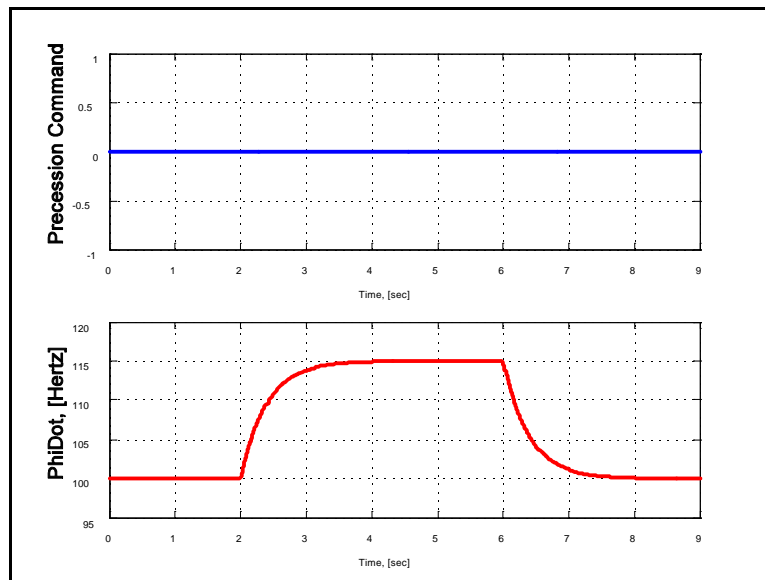


Figure 116 - Gallaspy response for rate table test 6.

The Ideal model and Gallaspy model show zero precession command for a zero rate target. The Ideal model spin profile is instantaneous, and the Gallaspy spin profile is identical to all previous tests.

Rate table test 7, 30E look angle, 5E/sec rate, 90E roll position:

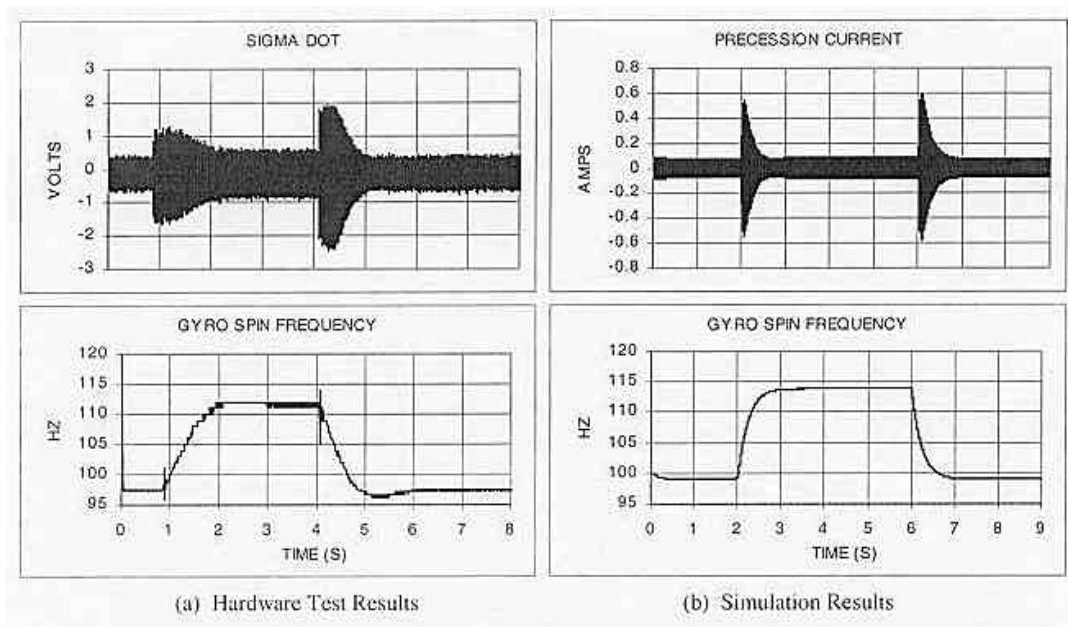


Figure 117 - Williams gyro data and model data for rate table test 7.

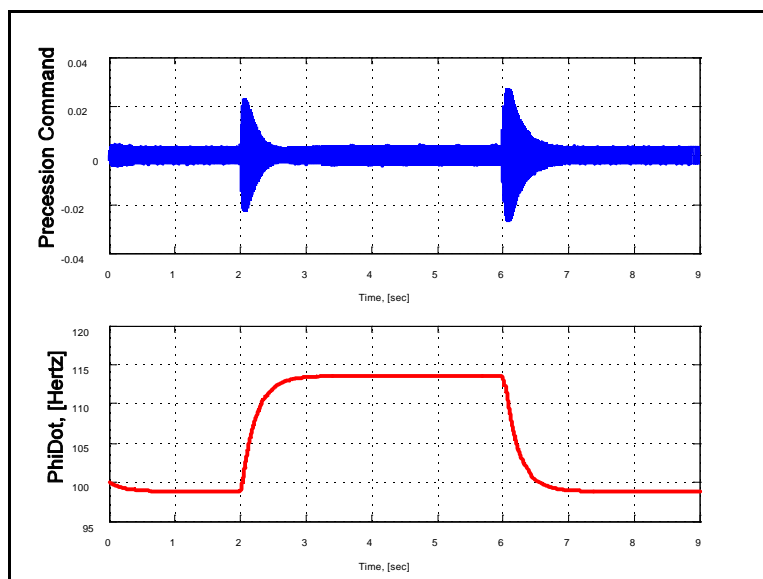


Figure 118 - BDWL response for rate table test 7.

The BDWL precession command matches the real gyro data well, even showing slightly less magnitude on spin-up. The spin profile also matches well, although the real gyro shows some overshoot on spin-down.

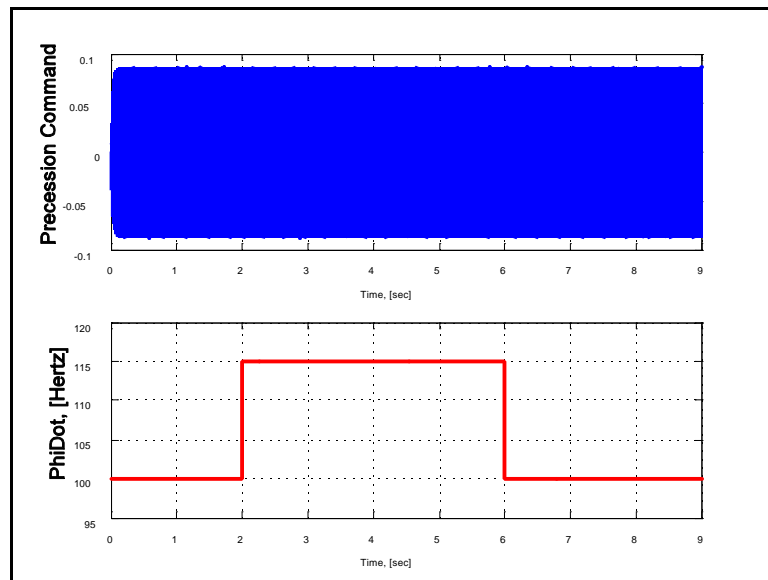


Figure 119 - Ideal response for rate table test 7.

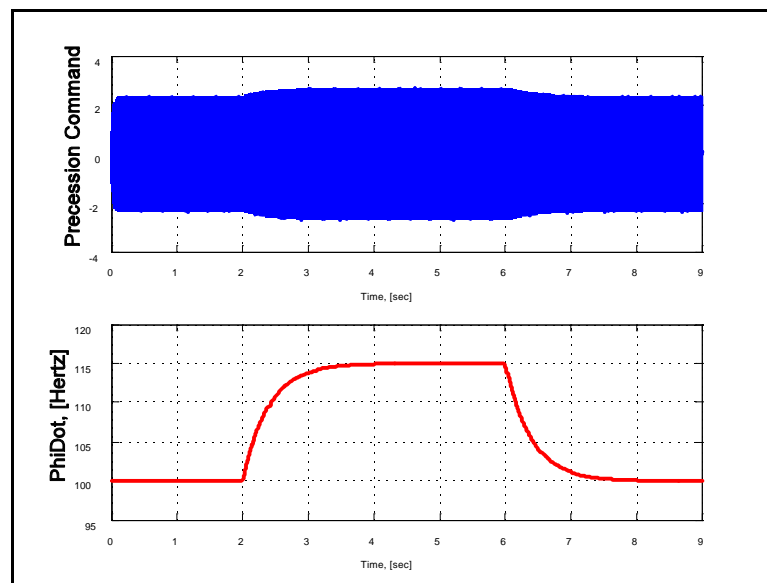


Figure 120 - Gallaspy response for rate table test 7.

The Ideal and Gallaspy models show no difference in gyro response for a different missile roll position.

In summary, the BDWL model showed the highest fidelity and matched the actual gyro rate table test data the best of the three candidate models. The

BDWL model showed precession and spin torque cross coupling, which increases with off-boresight angle. The BDWL gyro spin coils showed decreasing efficiency with increasing look angle, note that the combinations of gyro look angle and track rate in rate table tests 2, 4, 5, and 7 caused the actual gyro and the BDWL model to have steady state spin rates less than the commanded values of 100 Hz and 115 Hz. Look angle, track rate, and missile roll position showed the same types of affects on the BDWL model as the actual gyro.

The Ideal gyro model showed the least fidelity with no precession torque / spin torque coupling, no decrease in gyro control efficiency with increasing look angle, and unrealistic instantaneous spin responses.

The Gallaspy model's fidelity was higher than the Ideal model, but less than the BDWL model. The main difference between the Gallaspy model and the Ideal model was its spin response. The Gallaspy spin response could be tuned to a desired profile, but was constant regardless of missile conditions.

6.4 Gyro Signal Phase Comparison

Actual EO/IR missile gyro signals were recorded during testing in the NSWC Crane Missile Effectiveness Modeling and Simulation Laboratory. Four sets of tests were run, each with the gyro starting near missile body boresight tracking a target. The target was moved angularly off-axis at a constant rate, to a preset off-boresight angle. This test was repeated four times, with the target motion direction being rotated 90E between tests.

This results in gyro precession in four orthogonal directions (designated right, left, up and down), which should show the relative phase differences between the reference signal, cage coil (λ) signal, and sigma dot signal. Sigma dot is related to precession command and will be used here as a comparison to the gyro model precession command; some scaling may be necessary.

Recall that the reference signal does not change in phase or amplitude with gyro precession. The cage coil / λ signal increases in amplitude as a function of gyro off-boresight angle. Also, the relative phase of the λ signal, compared to the reference signal, gives the direction of gyro look-angle. The sigma dot / precession command amplitude is proportional to precession rate, its phase (relative to the reference signal) indicates precession direction.

In order to match lab signals with model signals, the amplitudes of the model signals were adjusted, and the proper missile roll position was found to best match the lab data (65E). This missile roll angle was used for all the model runs. The model signal time scale was also adjusted so that the model signals

best matched the actual lab test gyro data. Note that the relative timing/phasing of the three model signals was not changed, the time scale was adjusted identically for all three model signals in each case.

The Gallaspy gyro model has two reference signals, ref1 and ref2. In order to match lab test data, ref2 was used as the reference signal. Also, because of differences in the way the Gallaspy model handles gyro precession, a precession command signal was derived by transforming the model precession command from the non-rolling gyro with respect to inertial (NRGI) coordinate system to the gyro body-fixed coordinate system. It was found that the inverse of the \hat{y}_G component of the Gallaspy model precession command corresponded to the phase of the sigma dot signal from the lab gyro tests.

Table 1 shows the relative phase angles from the lab gyro testing for each precession direction. Note that the signals were all referenced to the “zero” phase position of the sigma dot signal. The lambda and sigma dot signals always have a phase difference of 180E. The actual gyro reference signals were not “clean” sinusoids. They had significant distortions. Also, the actual gyro sigma dot signals were very irregular due to the tracking algorithms used in the particular missile

being tested. This made measuring relative phase angles between

Table 1 - Gyro lab test signals relative phase angle data.

| Gyro Lab Test Data | Right | Down | Left | Up |
|--------------------|-------|------|------|-------|
| Sigma dot | 0E | 0E | 0E | 0E |
| Lambda | 180E | 180E | 180E | 180E |
| Reference | ~180E | ~90E | 0E | ~270E |

sigma dot and reference difficult. Hence, the “~” symbols in Table 1 denotes the best estimate of lab test signal relative phase measurements where the actual phase angle varied considerably.

Table 2 shows similar relative phase angle data for the gyro model

Table 2 - Gyro model signals relative phase angle data.

| Gyro Model Data | Right | Down | Left | Up |
|-----------------|-------|------|------|------|
| Prec cmd | 0E | 0E | 0E | 0E |
| Lambda | 180E | 180E | 180E | 180E |
| Reference | 180E | 90E | 0E | 270E |

signals. In this case, all three candidate gyro models (BDWL, Ideal, and Gallaspy) have identical relative phase relationships between their signals.

Note that the data in Table 2 represents signal values after the missile roll angle has been set to 65E to match the phase of the lab test data. As can be seen by comparing Table 1 and Table 2, the model data relative signal phase matches the lab data.

Table 3 shows the figure numbers for the various signal comparison charts. For each of the four precession directions, an “overall” signal chart is shown for the lab test data and each of the three models. Additionally, close-up

Table 3 - Signal comparison figure numbers.

| | Overall | | | | Signal Phase Comparison | | | |
|----------|---------|------|-----|------|-------------------------|------|-----|------|
| | Right | Left | Up | Down | Right | Left | Up | Down |
| Lab | 121 | 128 | 135 | 142 | - | - | - | - |
| BDWL | 122 | 129 | 136 | 143 | 125 | 132 | 139 | 146 |
| Ideal | 123 | 130 | 137 | 144 | 126 | 133 | 140 | 147 |
| Gallaspy | 124 | 131 | 138 | 145 | 127 | 134 | 141 | 148 |

signal comparison charts are shown with the lab test signals and signals from the models (one chart for each model comparison to lab test data). These figures show the relative phasing of the signals and show how well the model signals relative phase angles matched the lab test data.

The model signals in the overall and signal phase comparison plots were scaled in amplitude for comparison to the real gyro lab test signals. The lab test gyro reference signal changed in amplitude in some cases (see Figures 121, 128, 135, and 142). This was unexpected, as the reference signal was thought to remain at a constant amplitude. However, the reference signal did not change in amplitude in the case of horizontal left target motion (Figure 136). For the vertical down target motion (Figure 142), the reference signal positive peak changes in amplitude, while its negative peak remains constant. In any case, the reference signal's phase is its critical characteristic for gyro control.

It is possible that the apparent reference signal amplitude change was caused from measurement cross-talk from the lambda signal. All model reference signals remain at a constant amplitude.

The overall model lambda (cage coil) signals matched the lab test gyro signals well. The lab test lambda signals showed some amplitude before the target motion started. This is due to slight misalignment of the target/missile such that the target was slightly off of perfect missile boresight at the beginning of the test. In the model results, the lambda signal always started at zero amplitude, since the target was always started at perfect missile boresight.

The overall precession command signal plots for the three models were constant amplitude sinusoids whose phase (compared to reference) corresponds to the direction of target motion. The lab test sigma dot signal (comparable to model precession command) showed randomly varying amplitude and phase. This is due to differences in the track algorithms between the models and the actual missile/gyro used in the lab tests. Since the goal of this research was to develop gyro models, not tracker models, this difference is not considered significant to the results of this paper.

The signals from each of the three models were virtually identical, so they will be discussed here together (“model signals” in the rest of this section will refer to all three models). Examination of the signal phase comparison charts (Figures 125-127, 132-134, 139-141, and 146-148) shows that the model signals (particularly the phase angles) for the horizontal right and vertical down target motion match the lab test data very closely. The model signal phasing of the horizontal left and vertical up cases match the lab data well, but not as well as the “right” and “down” cases. This may be caused from slight misalignments of the missile body, or target motion direction.

The signal comparison charts also show that the reference signal is not a pure sinusoid. There are repeating irregularities in this signal. The cause of this is not known, the model reference signals were pure sinusoids. The irregular shape of the real gyro reference signal may be due to complex interactions between the magnetic flux of the gyro and the reference coils. This may be caused by the actual finite size of the reference coils. The reference coils are

represented in the models as singular point sized, which may explain this difference.

The irregular shape of the real gyro sigma dot signal matched the model precession command signals in some places, but did not match in others. This is due to differences between the actual missile and model track algorithms, as discussed above. Overall, the model signal phasing matched the actual missile data well.

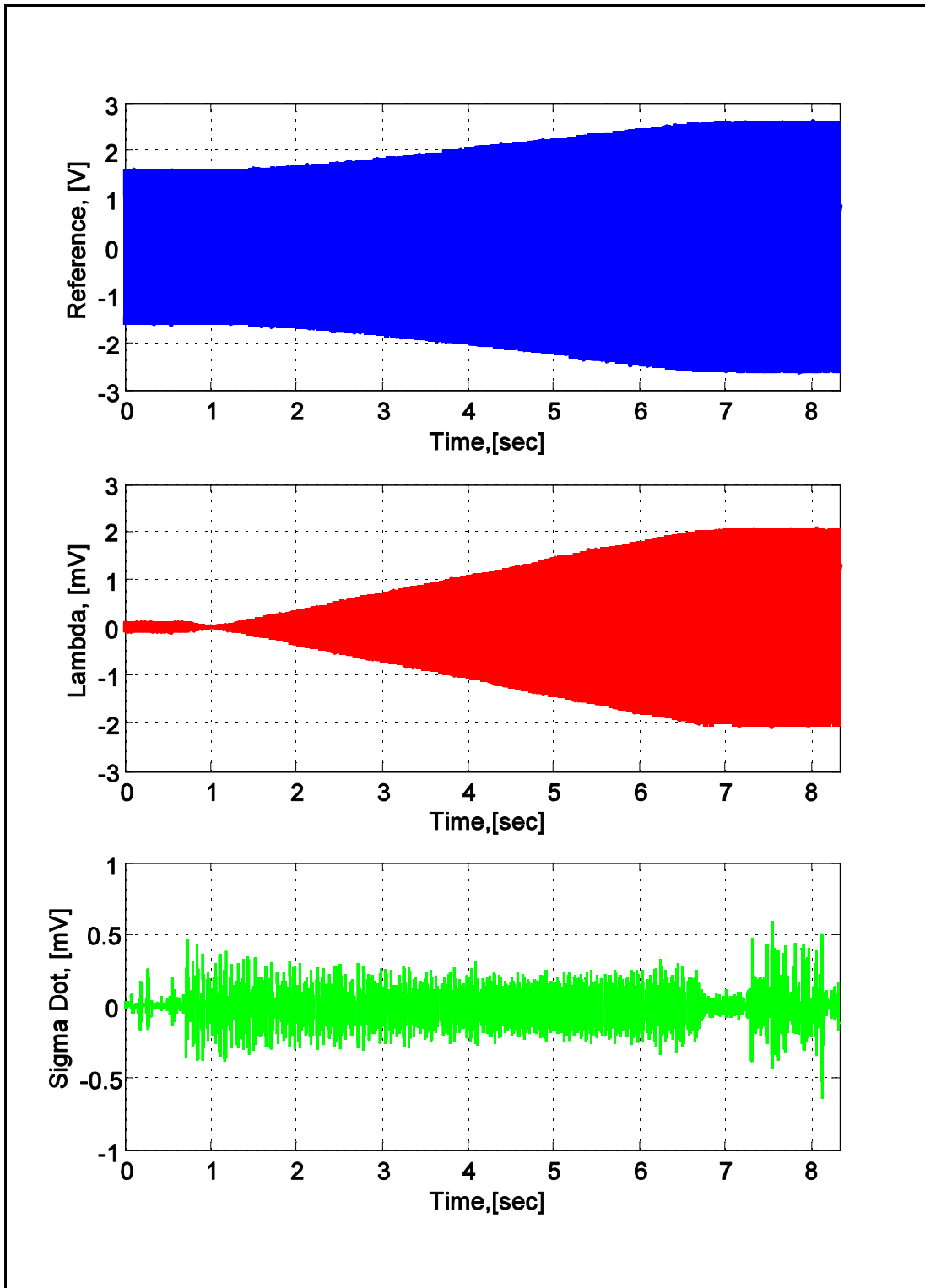


Figure 121 - Overall lab test gyro signals for horizontal right target motion.

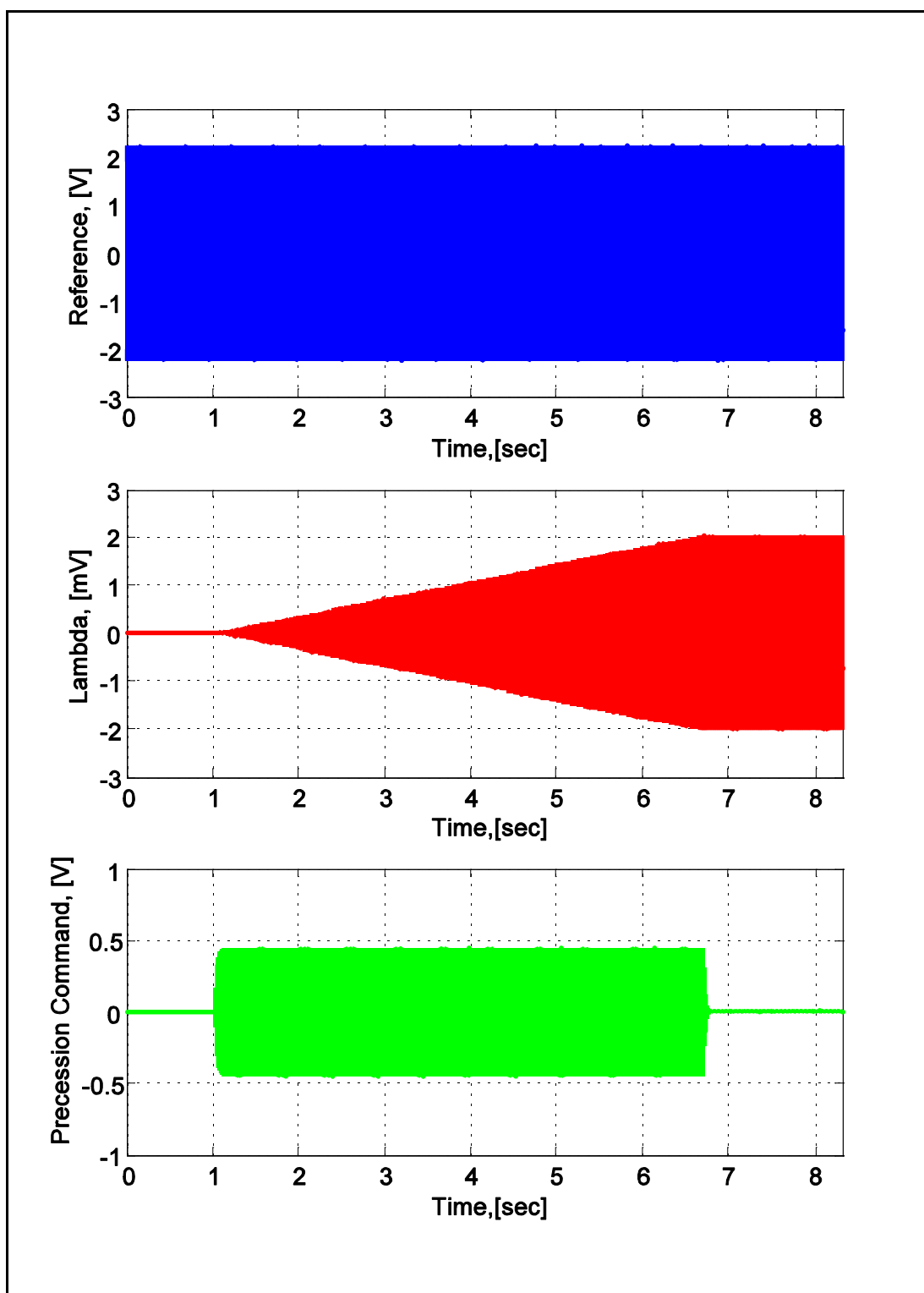


Figure 122 - BDWL overall signals for horizontal right target motion.

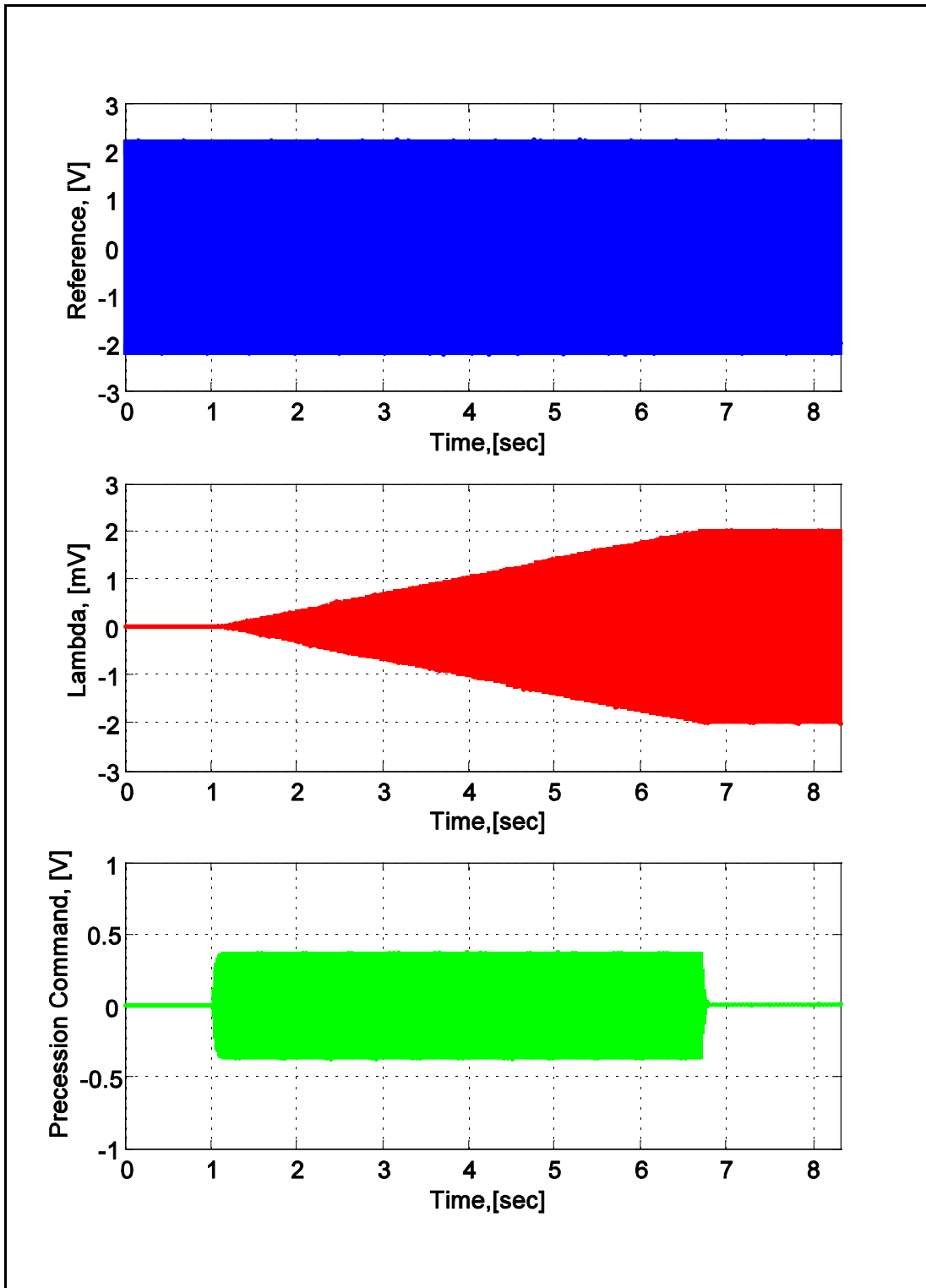


Figure 123 - Ideal overall signals for horizontal right target motion.

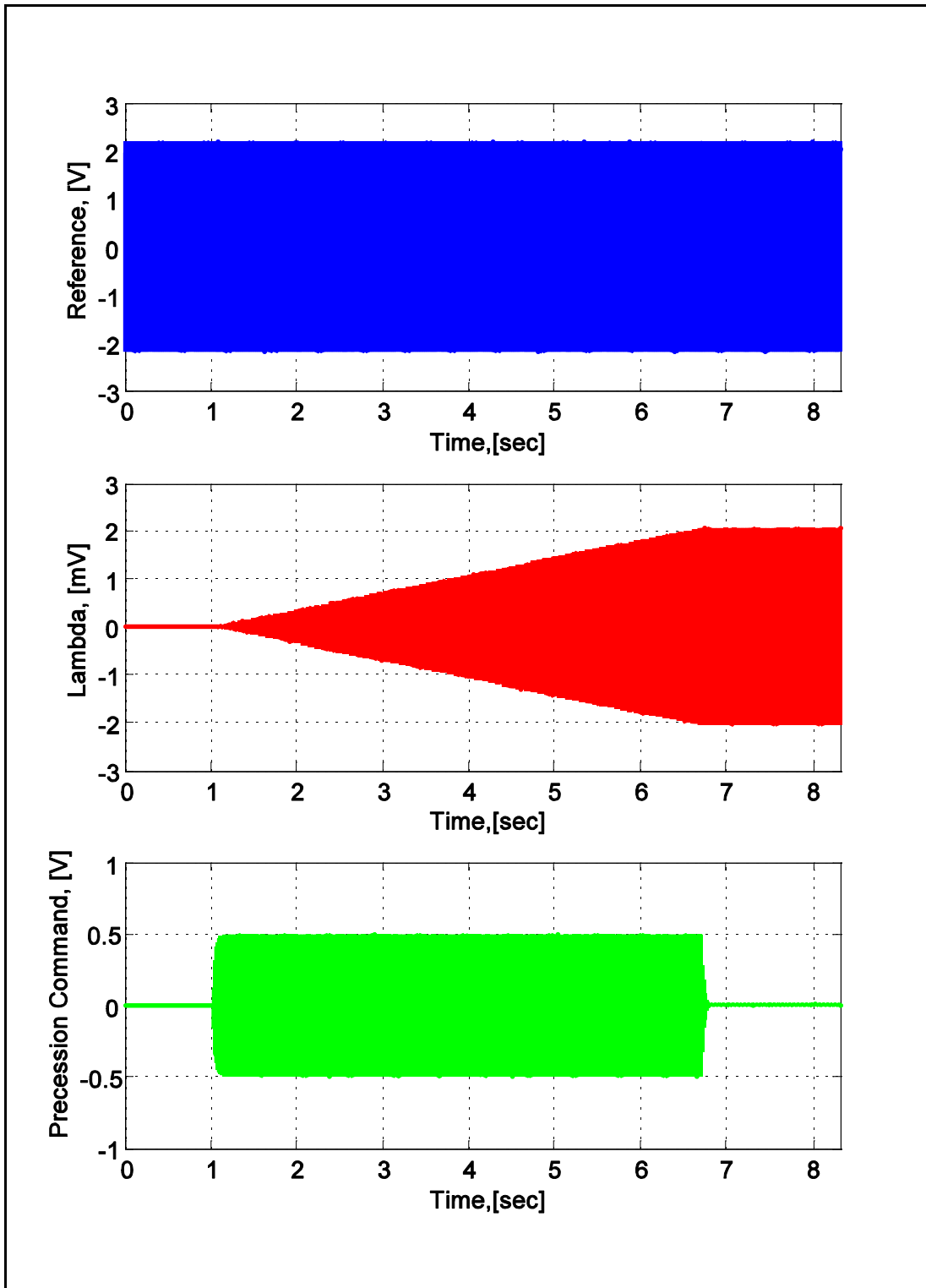


Figure 124 - Gallaspy overall signals for horizontal right target motion.

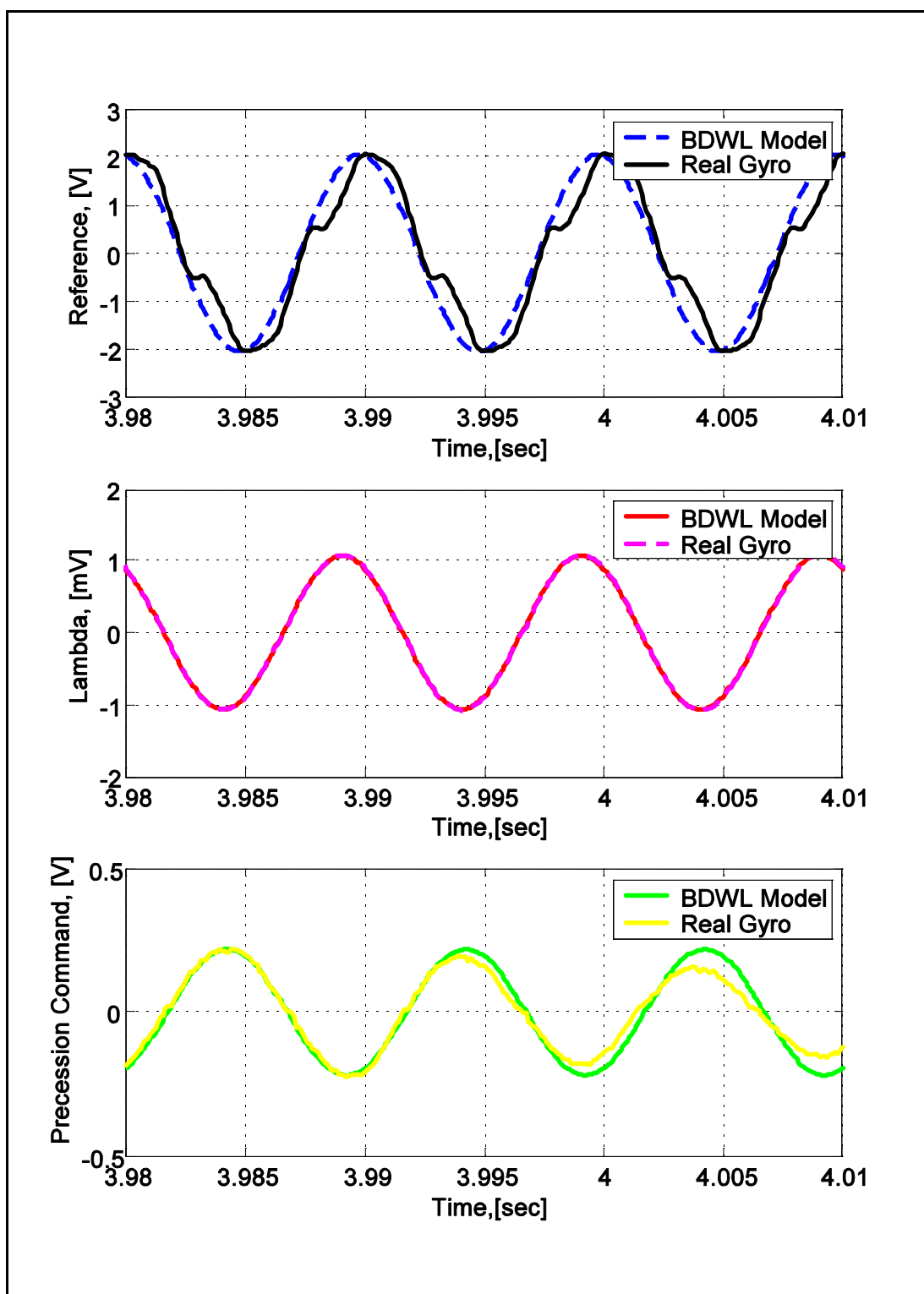


Figure 125 - BDWL comparison to lab test data for horizontal right target motion.

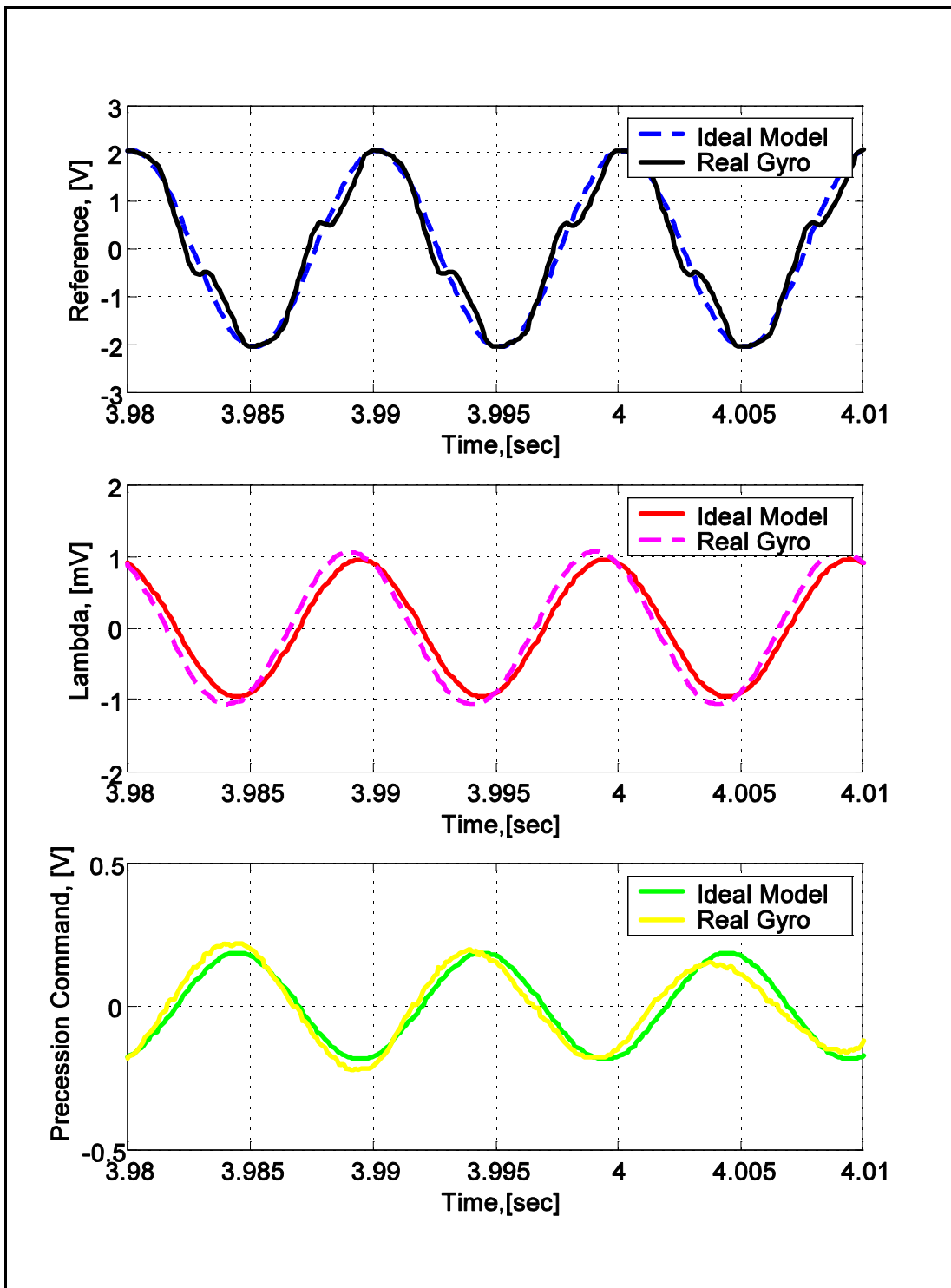


Figure 126 - Ideal gyro model comparison to lab test data for horizontal right target motion.

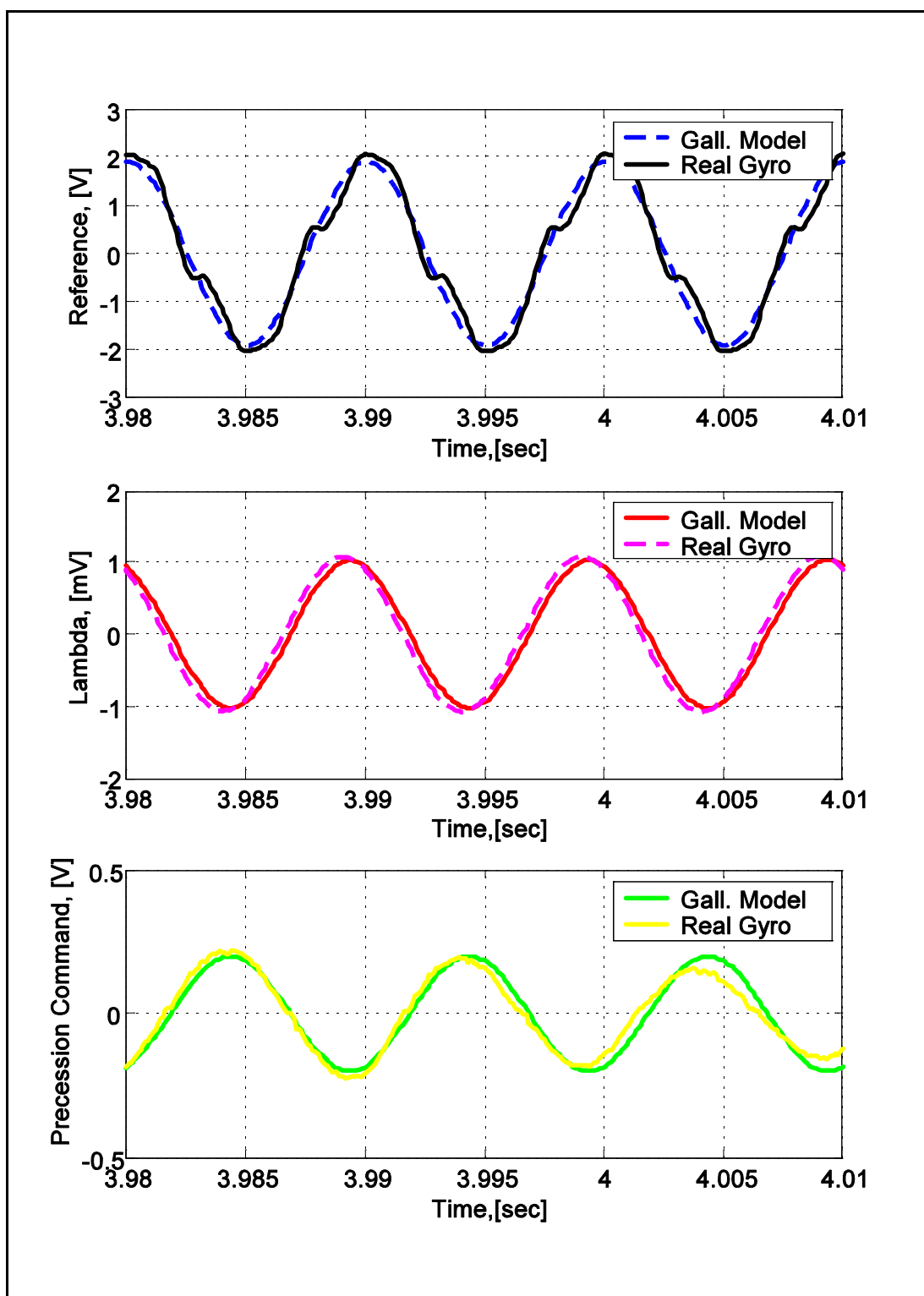


Figure 127 - Gallaspy comparison to lab test data for horizontal right target motion.

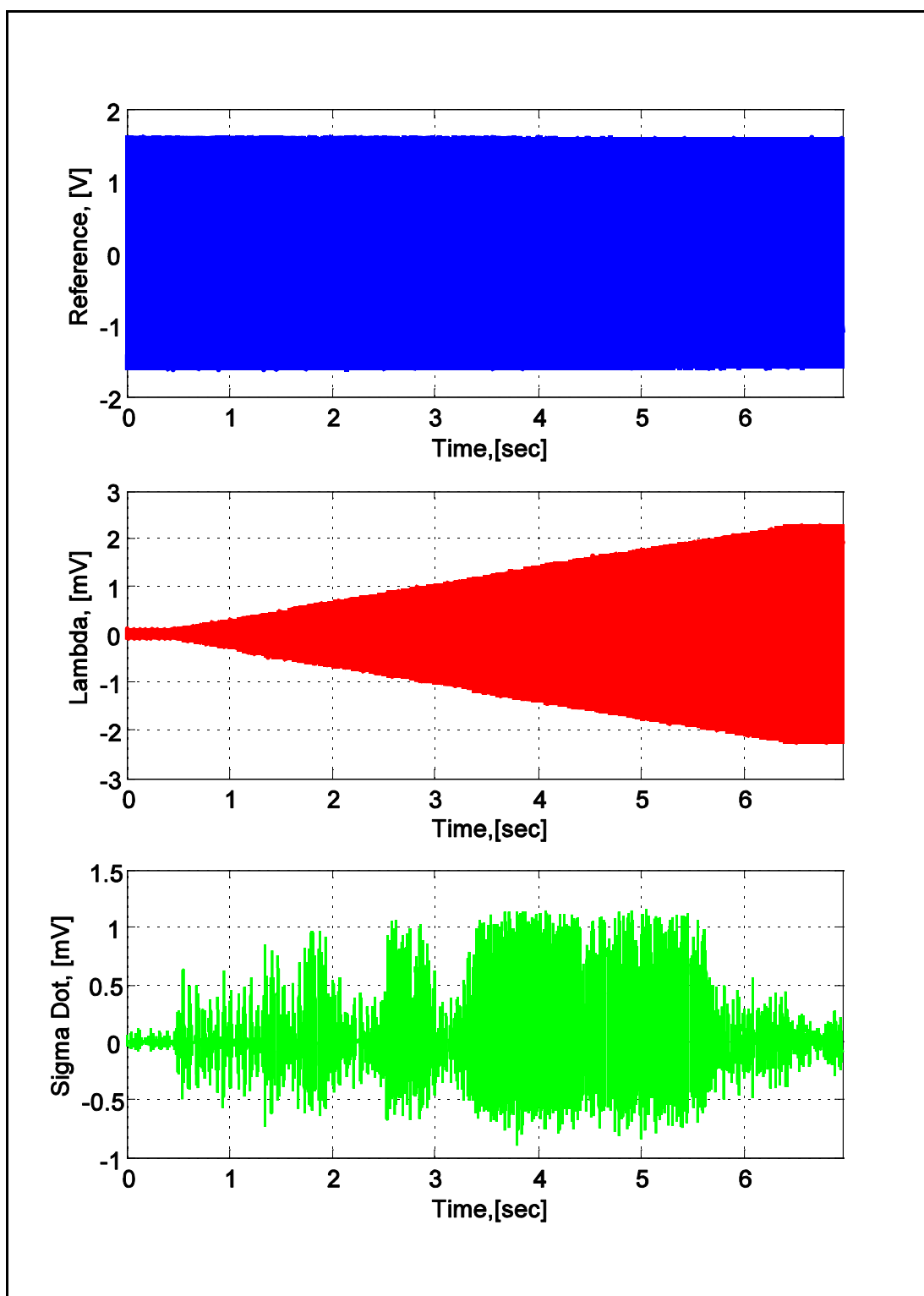


Figure 128 - Overall lab test signals for horizontal left target motion.

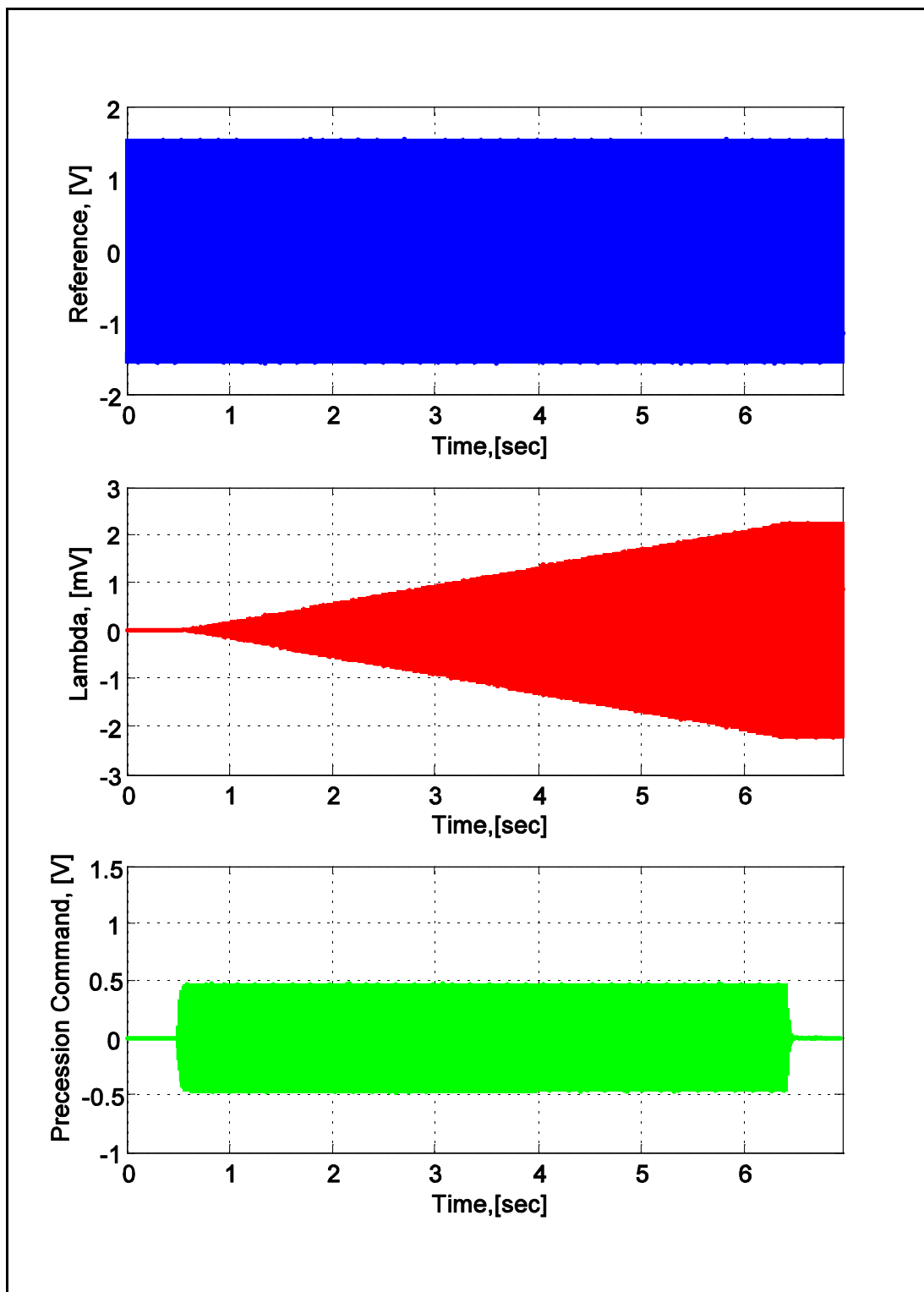


Figure 129 - BDWL overall signals for horizontal left target motion.

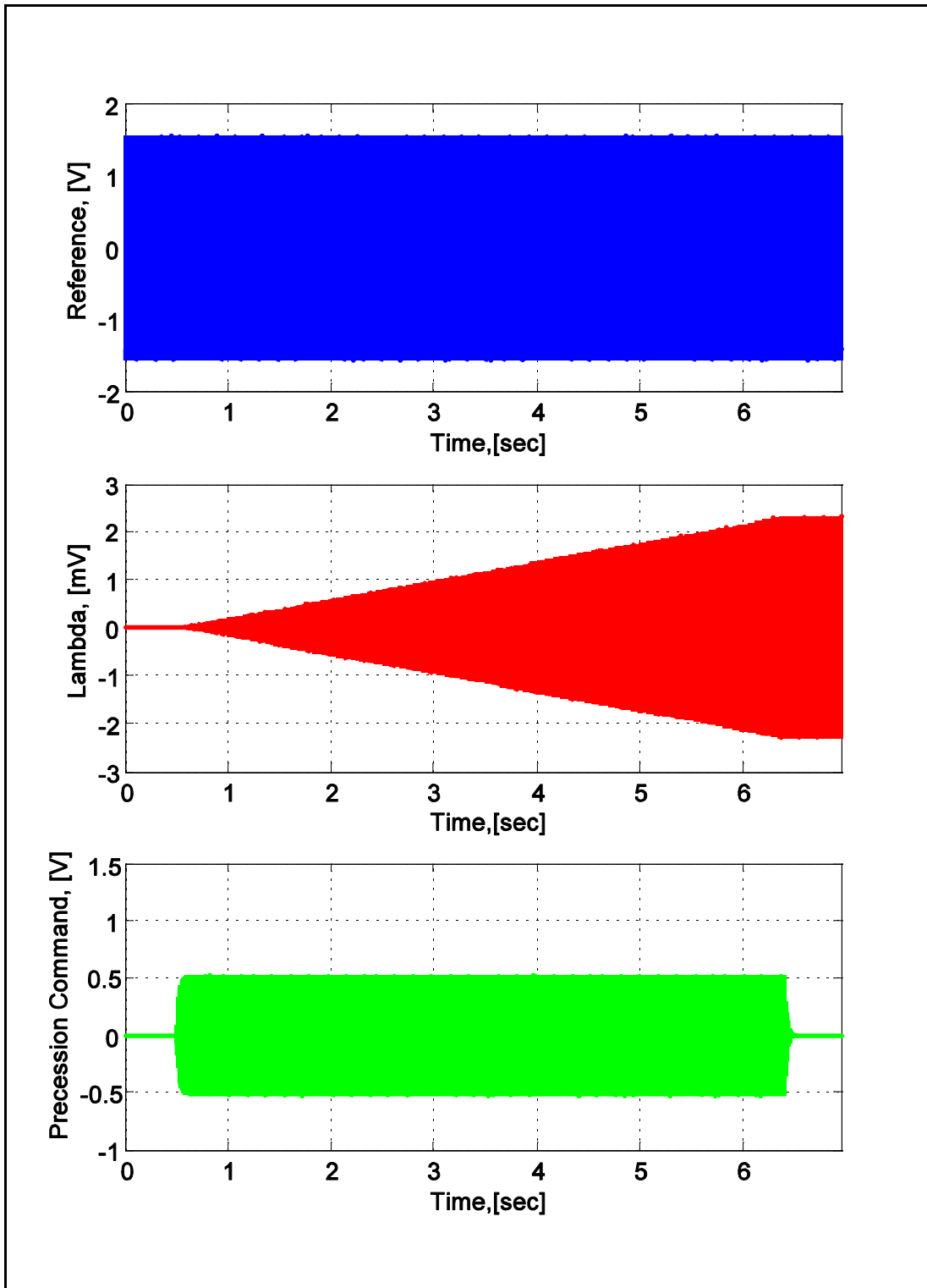


Figure 130 - Ideal overall signals for horizontal left target motion.

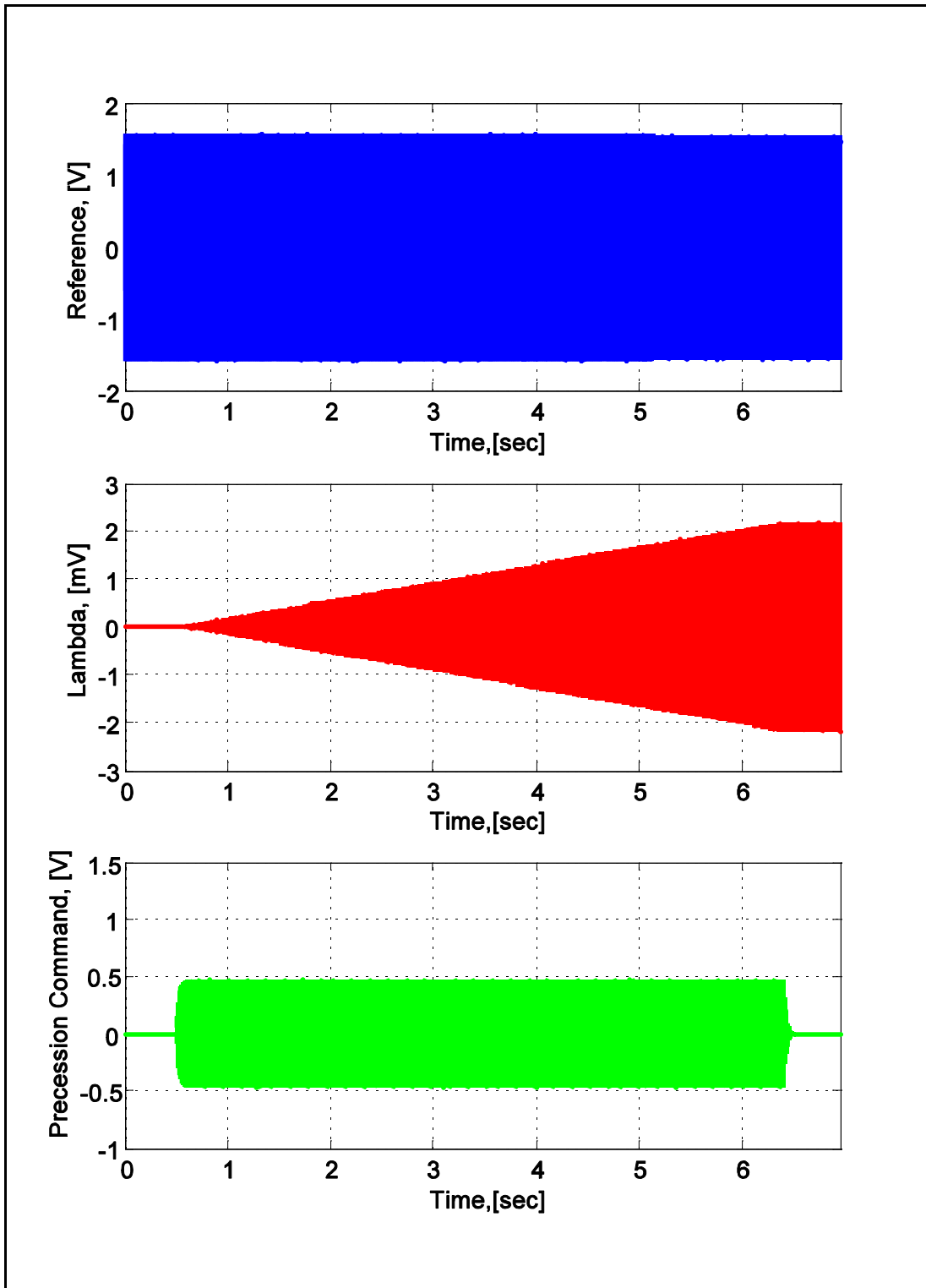


Figure 131 - Gallaspy overall signals for horizontal left target motion.

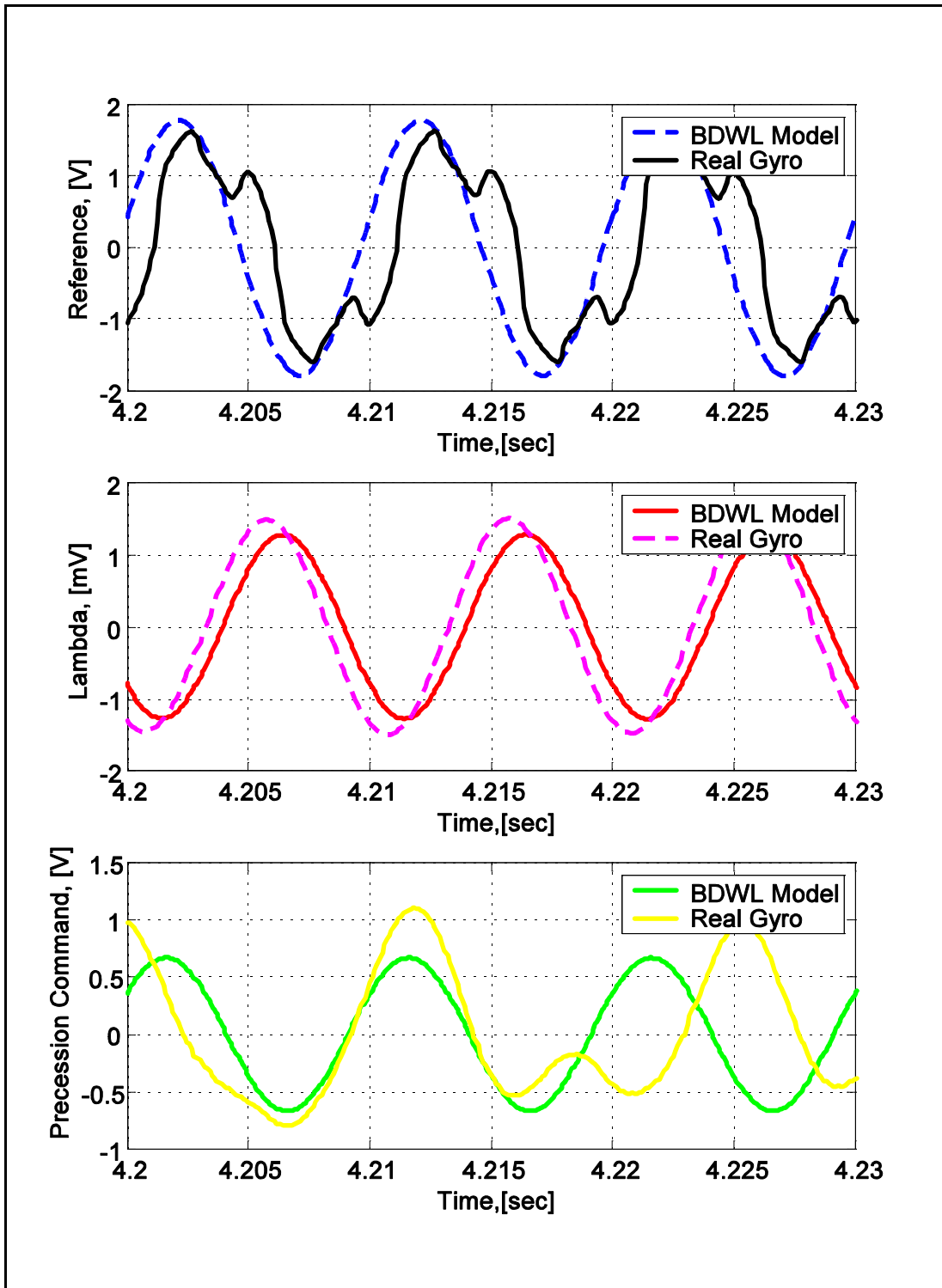


Figure 132 - BDWL comparison to lab test data for horizontal left target motion.

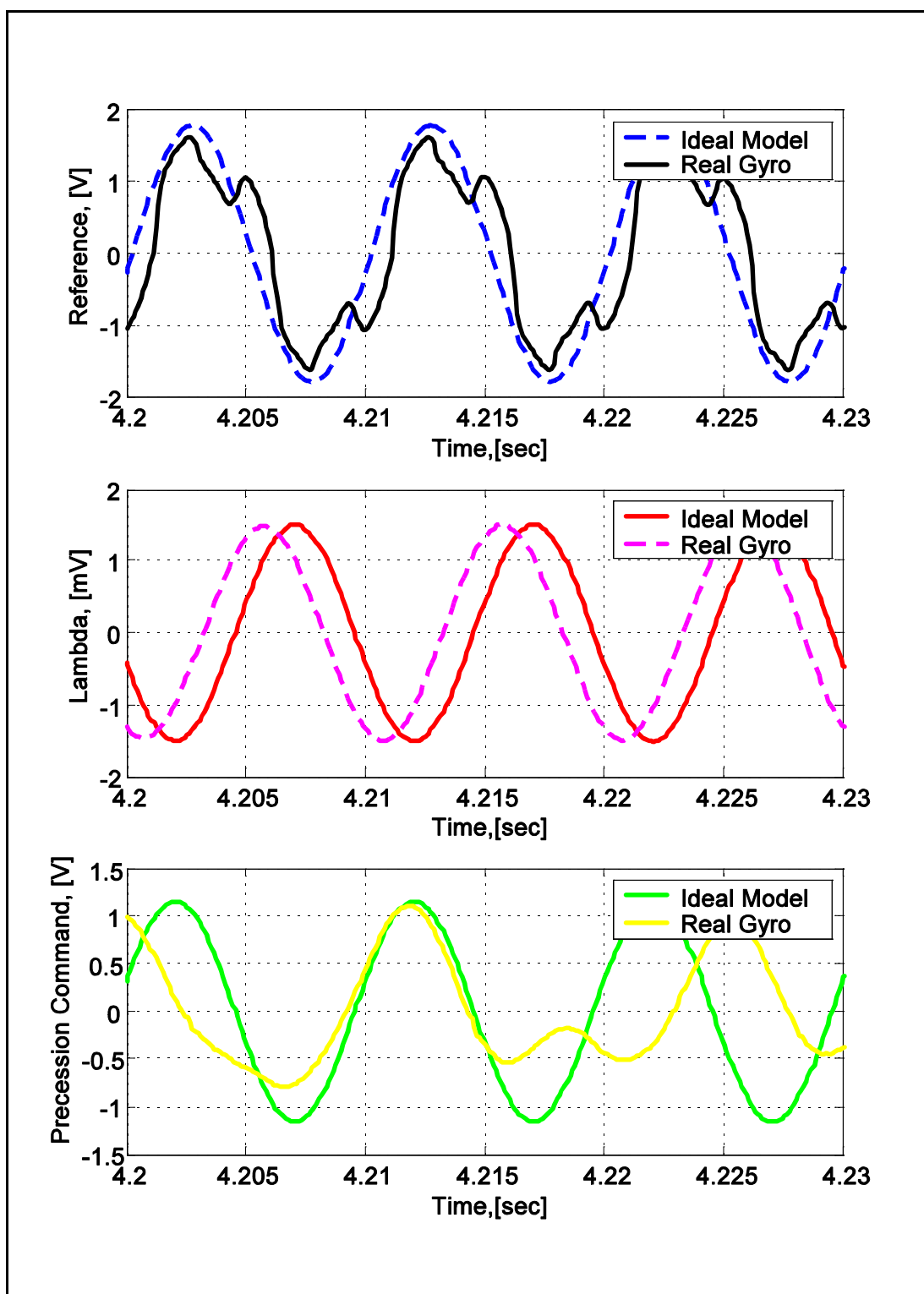


Figure 133 - Ideal gyro model comparison to lab test data for horizontal left target motion.

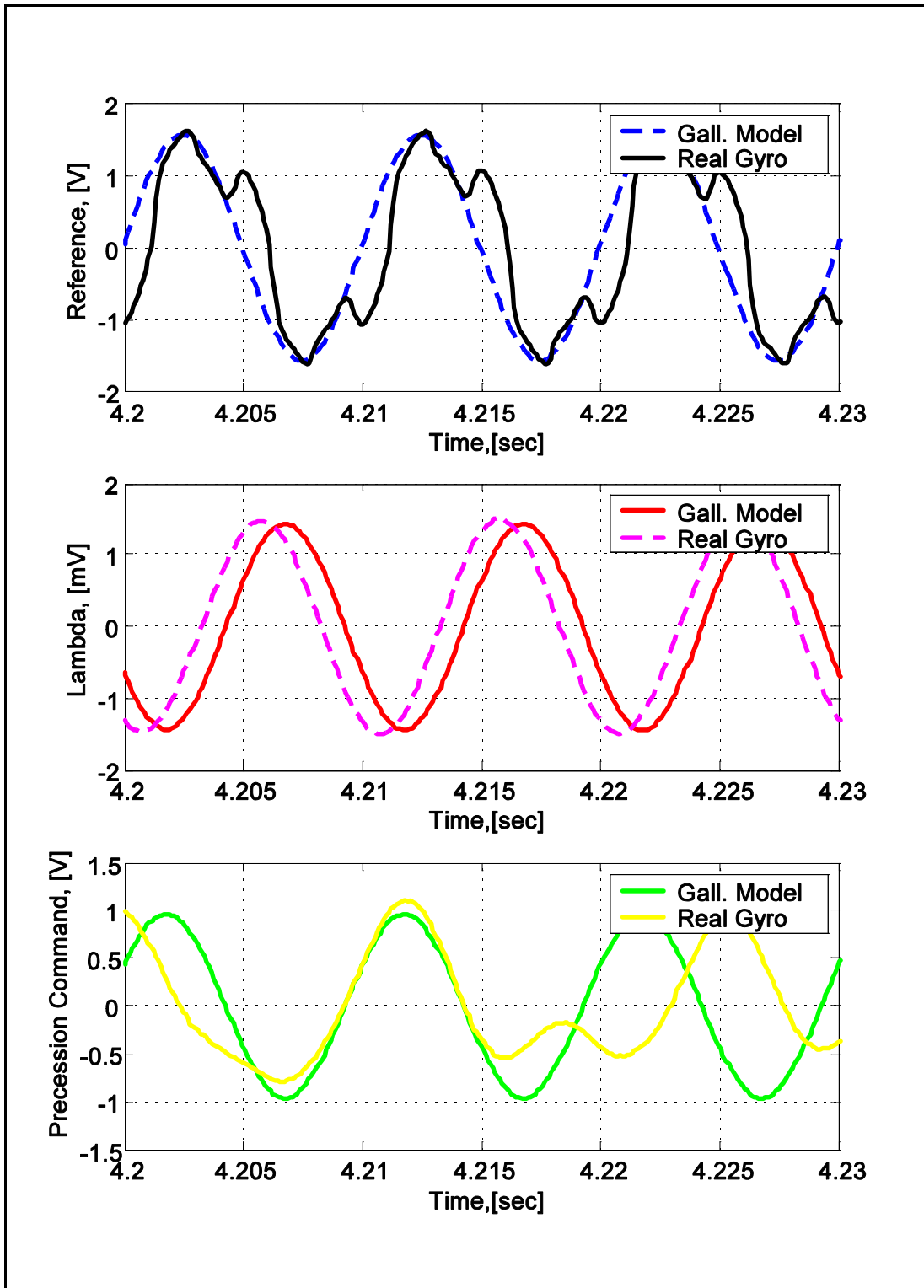


Figure 134 - Gallaspy comparison to lab test data for horizontal left target motion.

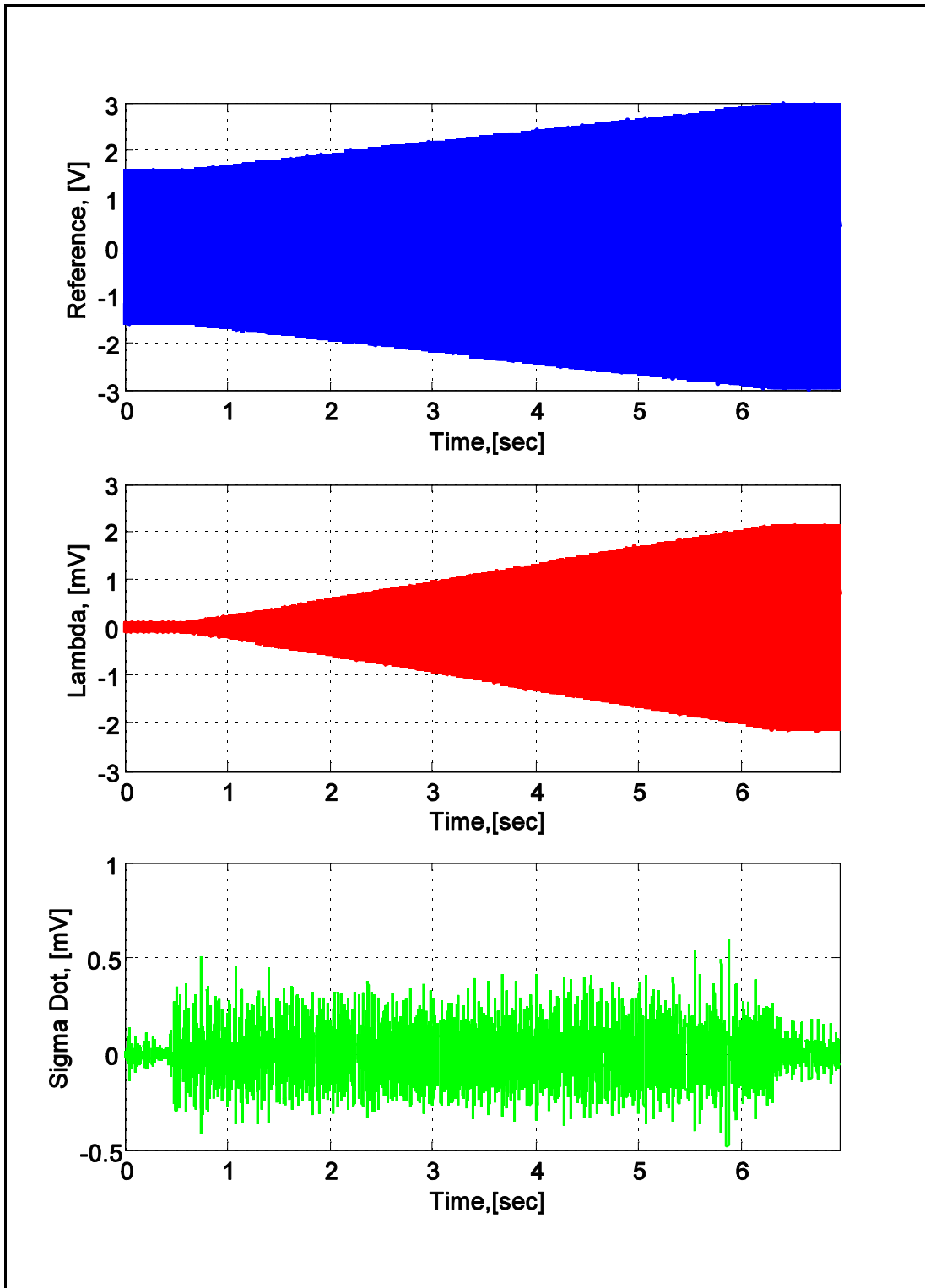


Figure 135 - Overall lab test signals for vertical up target motion.

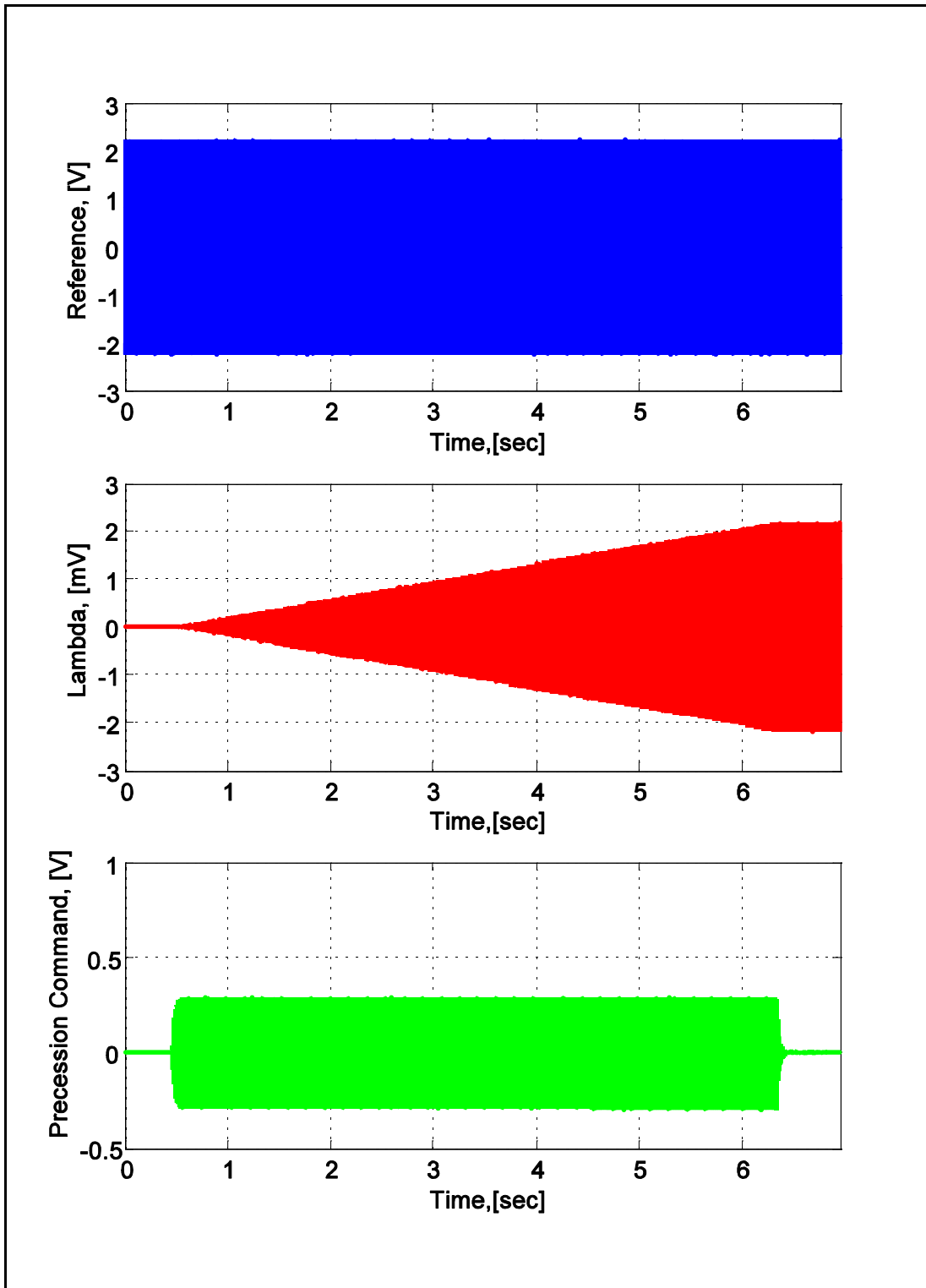


Figure 136 - BDWL overall signals for vertical up target motion.

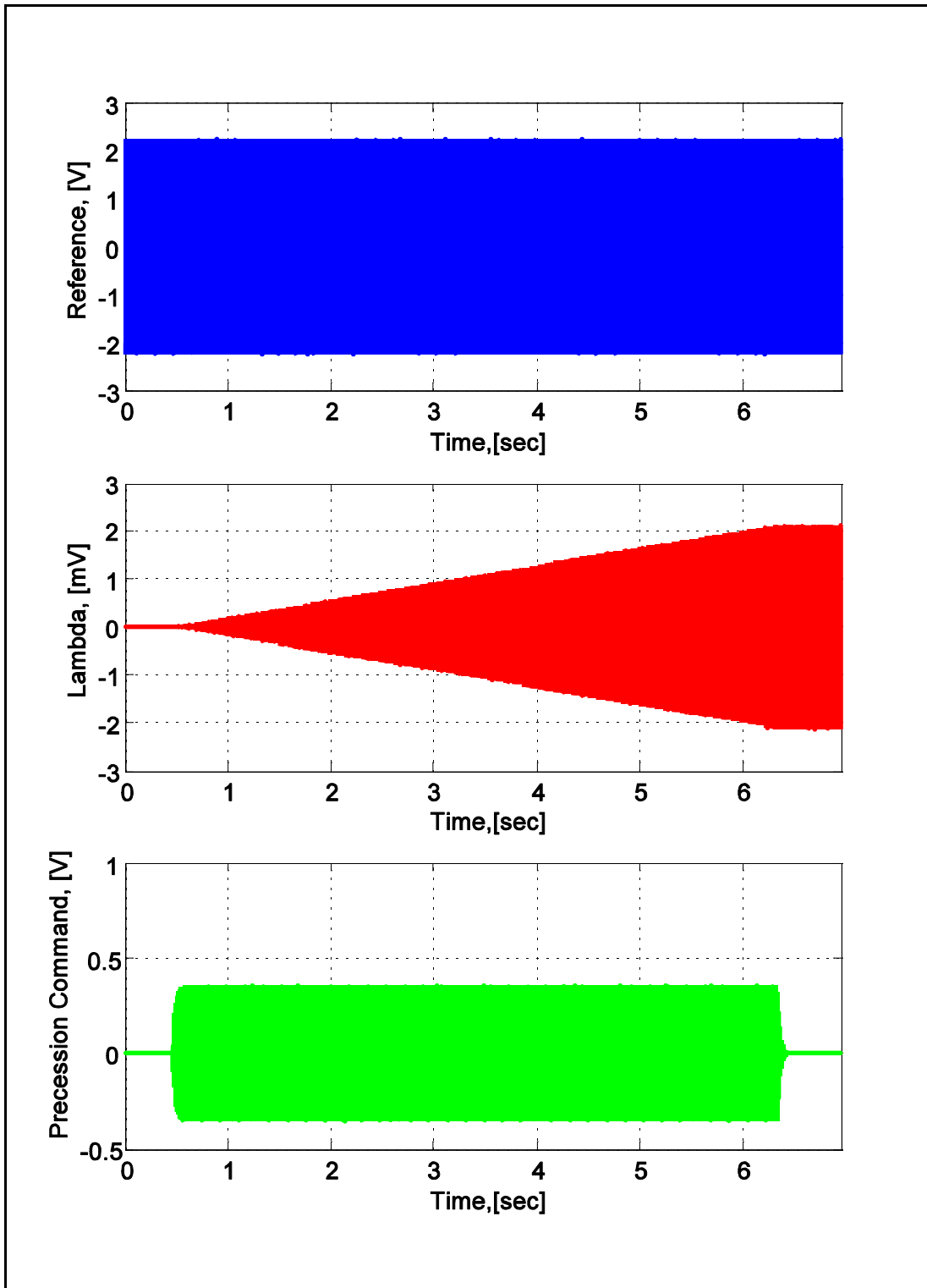


Figure 137 - Ideal overall signals for vertical up target motion.

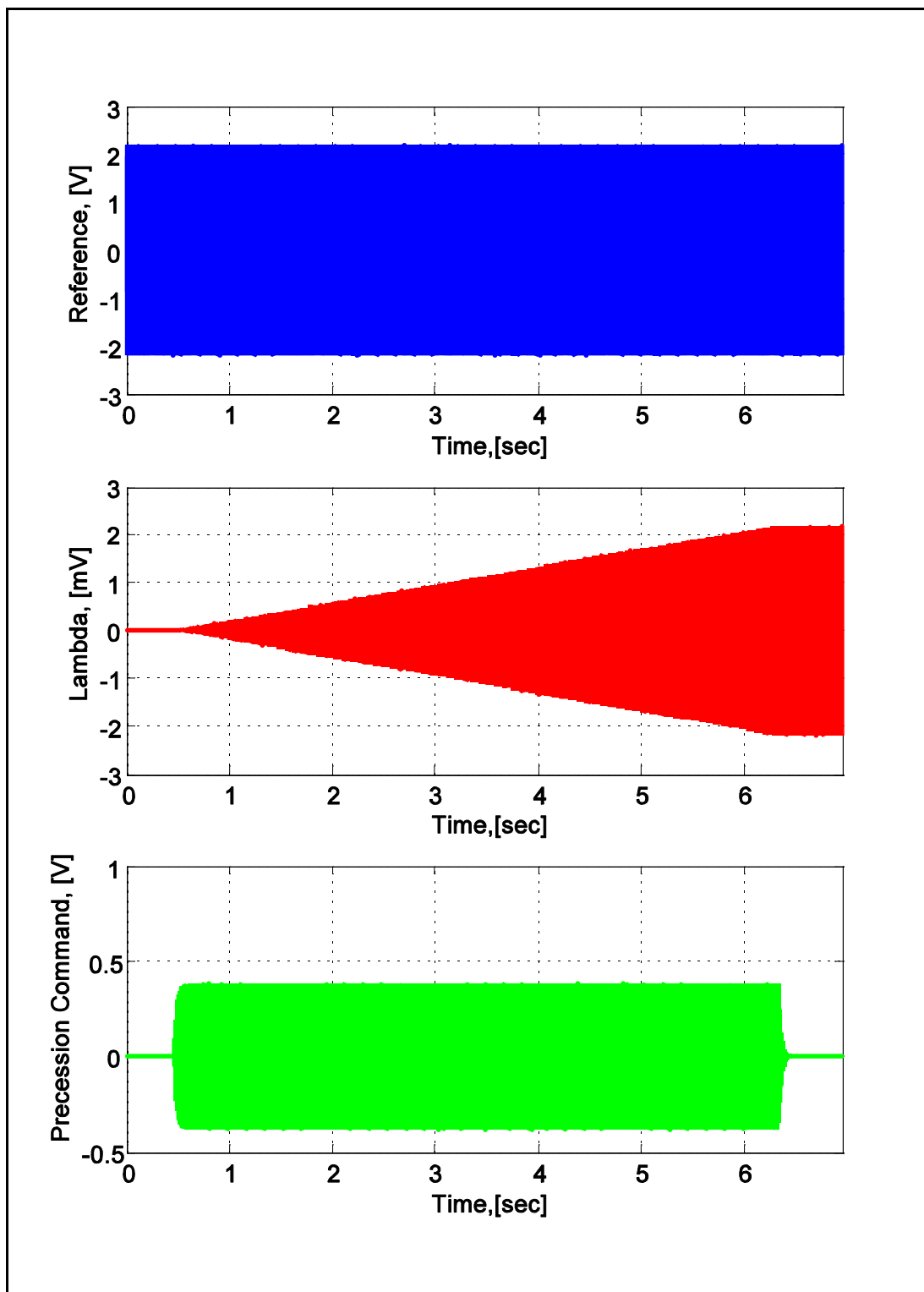


Figure 138 - Gallaspy overall signals for vertical up target motion.

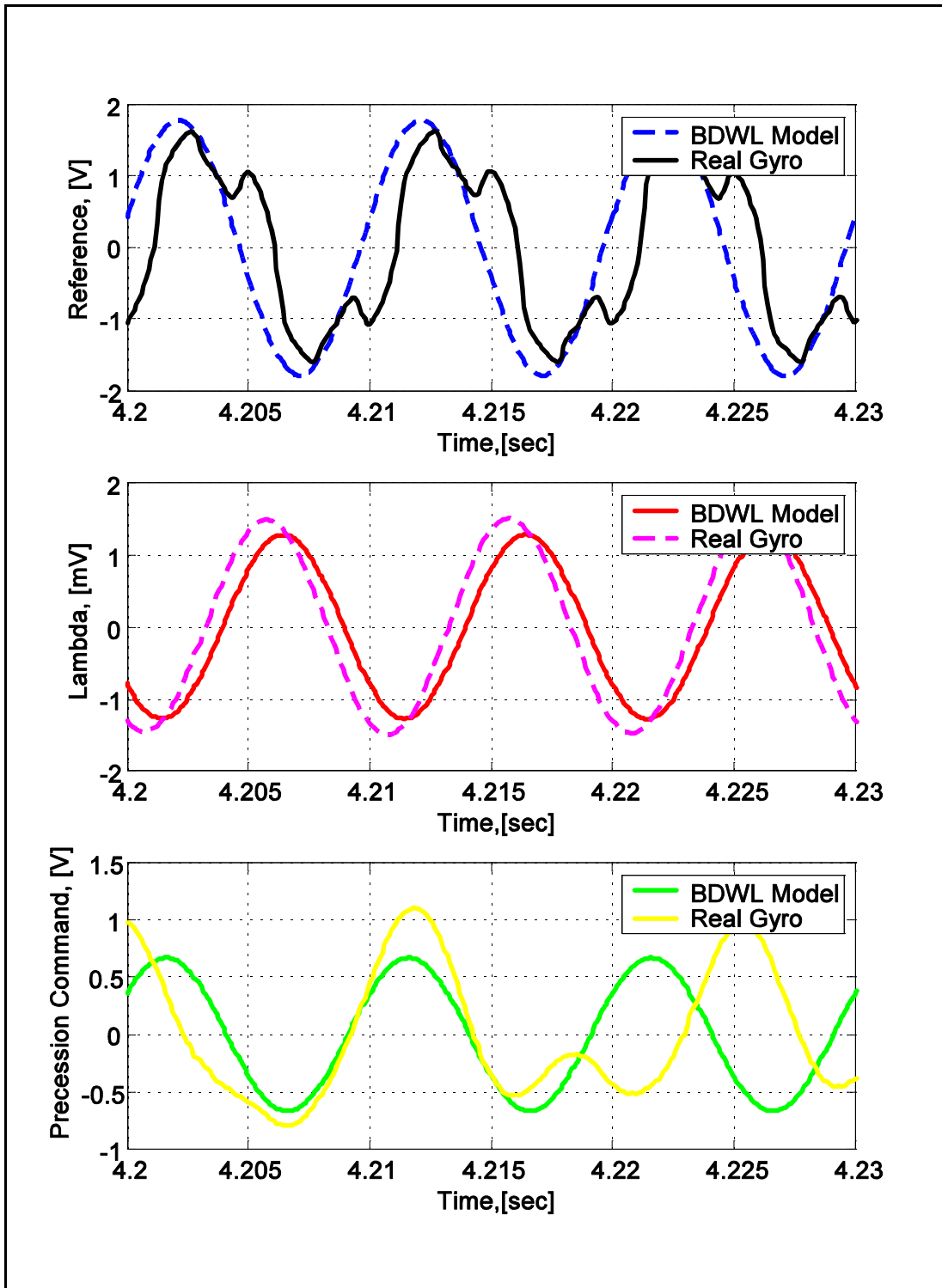


Figure 139 - BDWL comparison to lab test data for vertical up target motion.

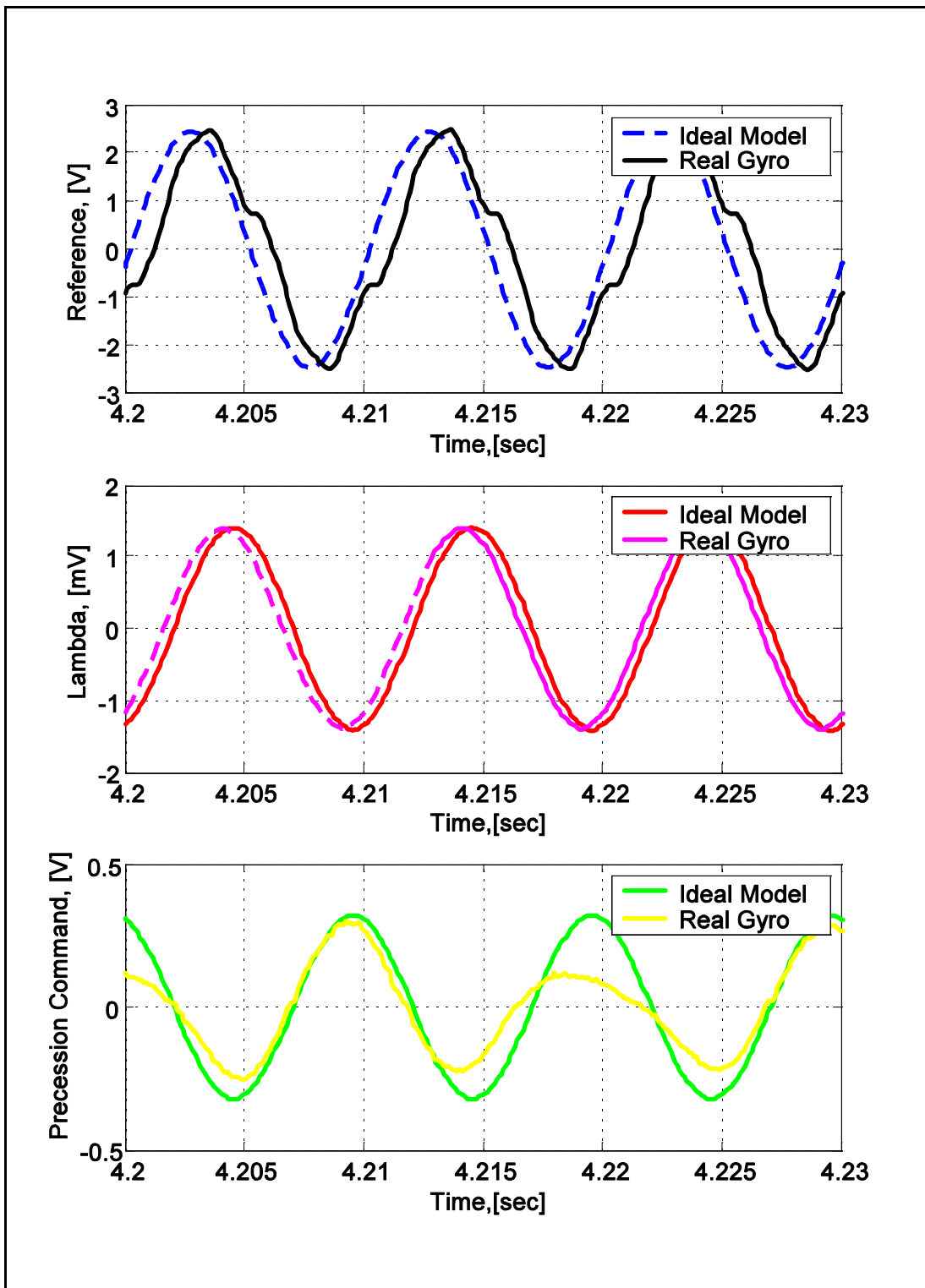


Figure 140 - Ideal gyro model comparison to lab test data for vertical up target motion.

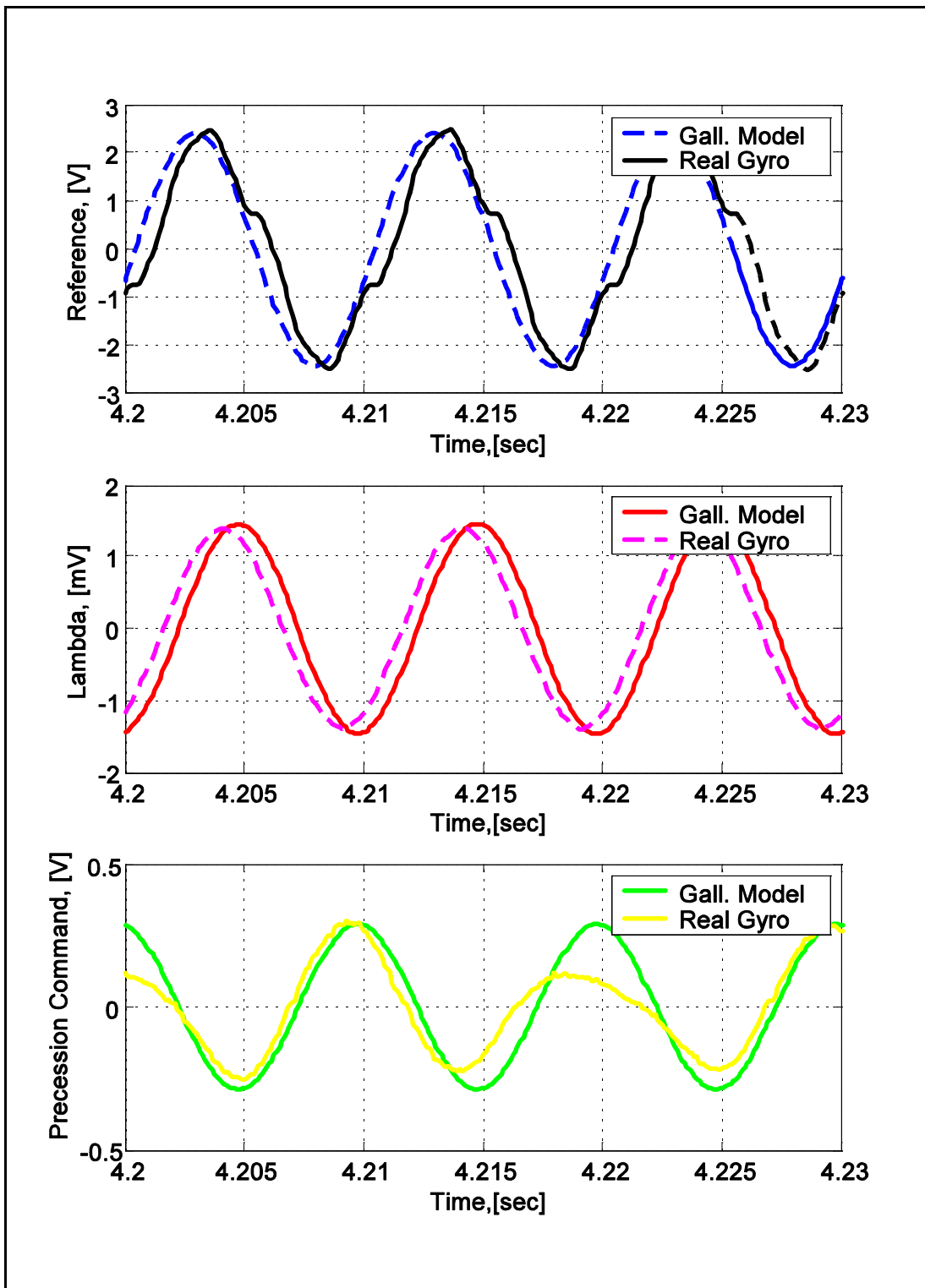


Figure 141 - Gallaspy comparison to lab test data for vertical up target motion.

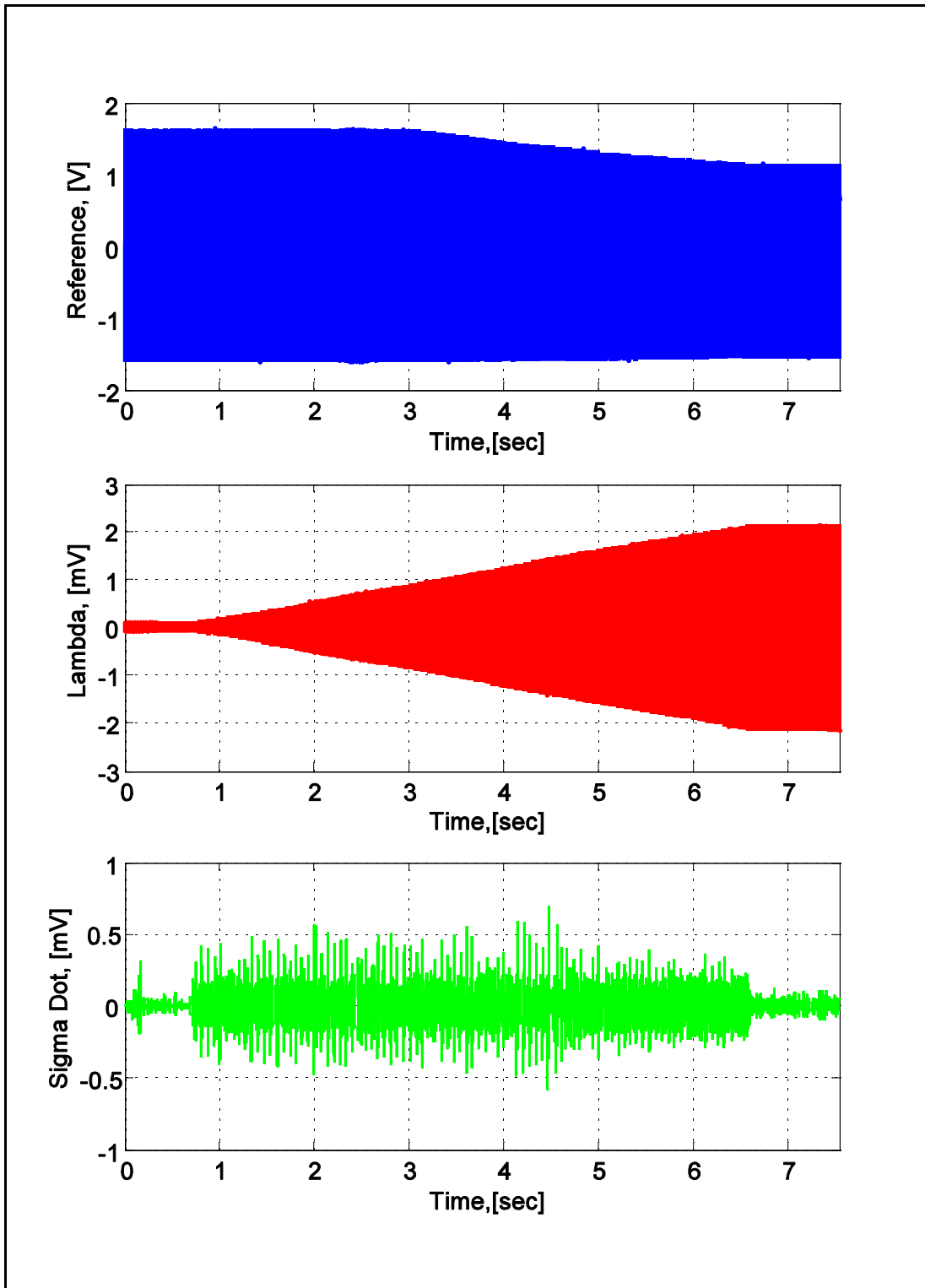


Figure 142 - Overall signals for lab test vertical down target motion.

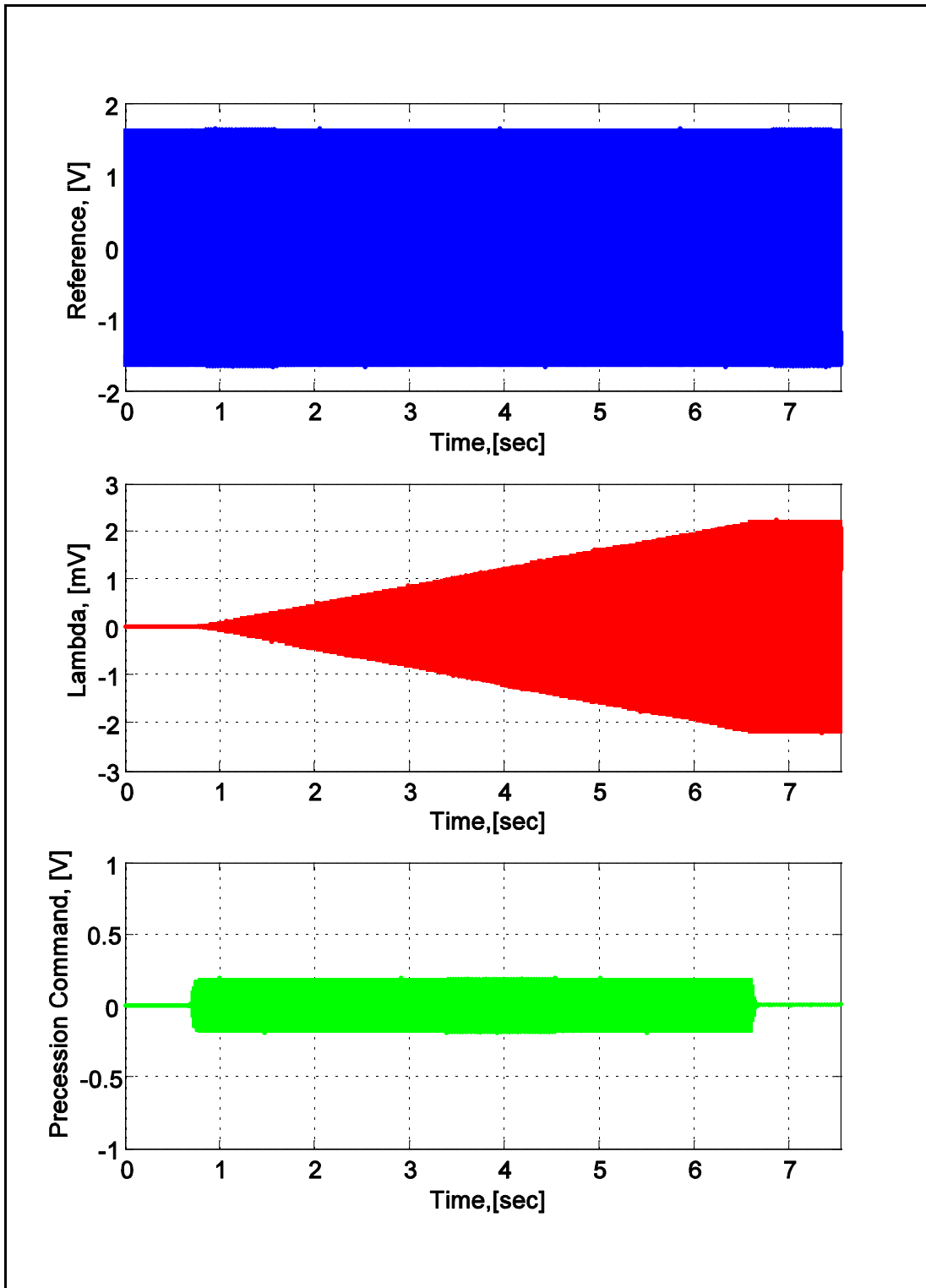


Figure 143 - BDWL overall signals for vertical down target motion.

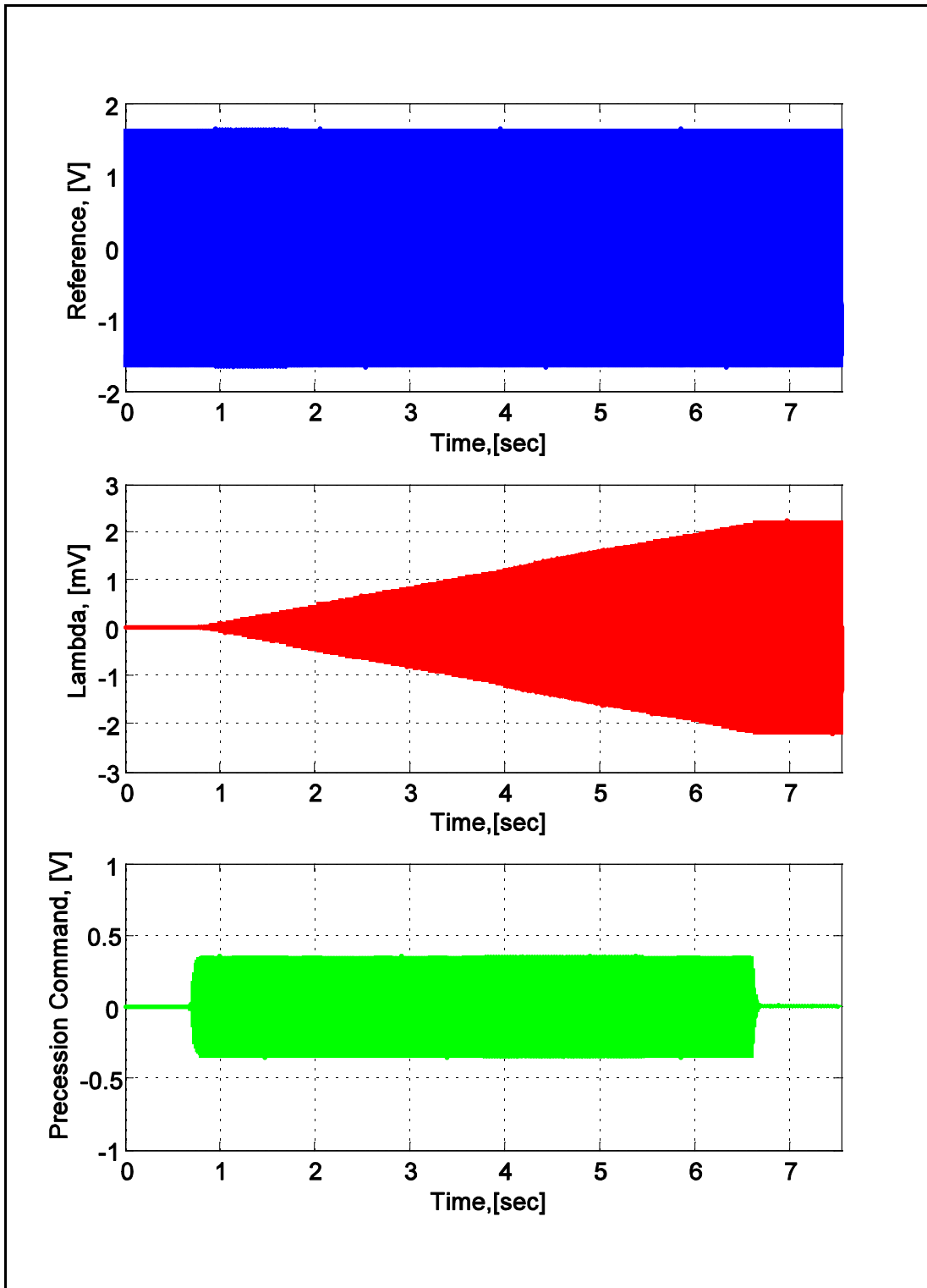


Figure 144 - Ideal overall signals for vertical down target motion.

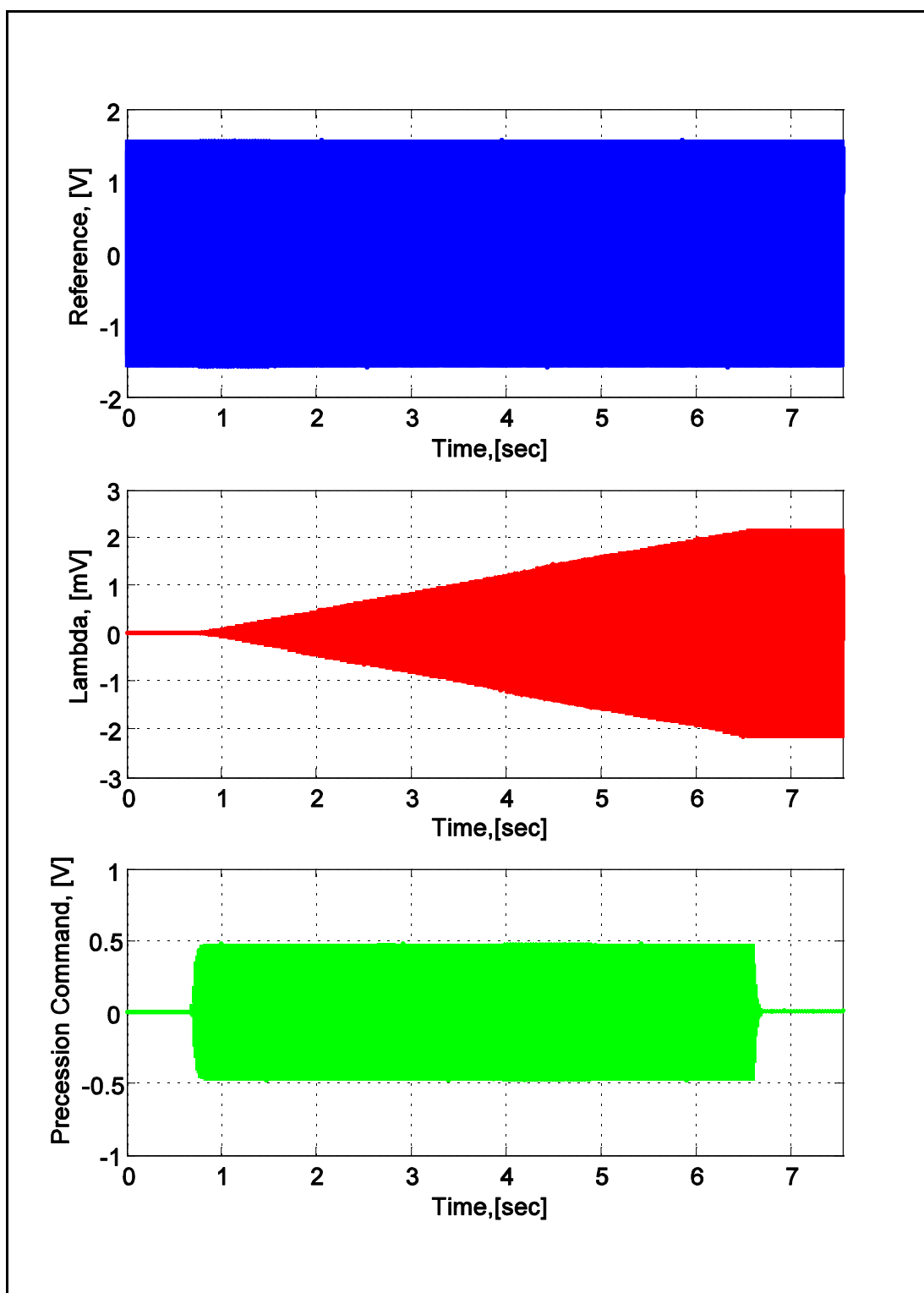


Figure 145 - Gallaspy overall signals for vertical down target motion.

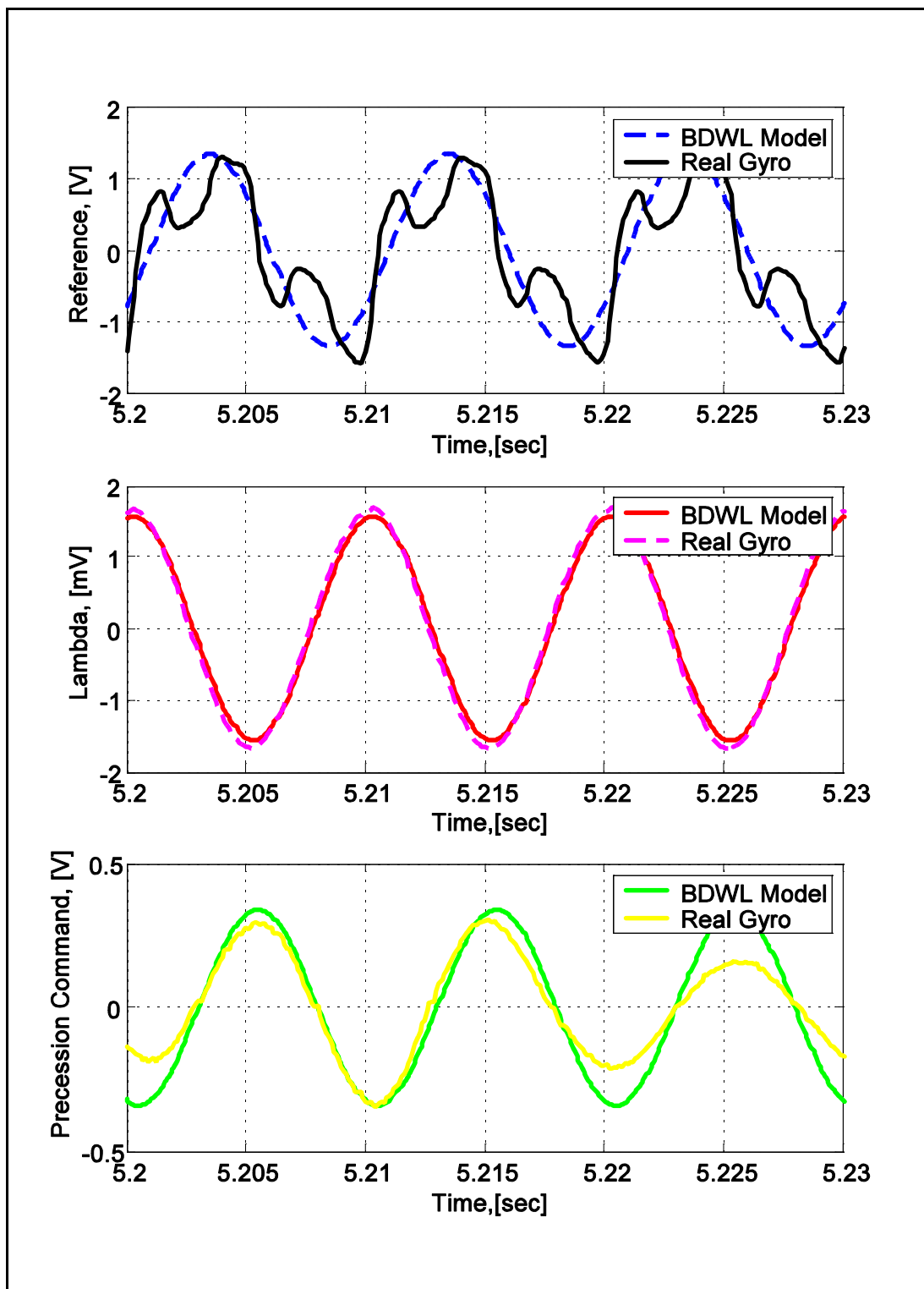


Figure 146 - BDWL comparison to lab test data for vertical down target motion.

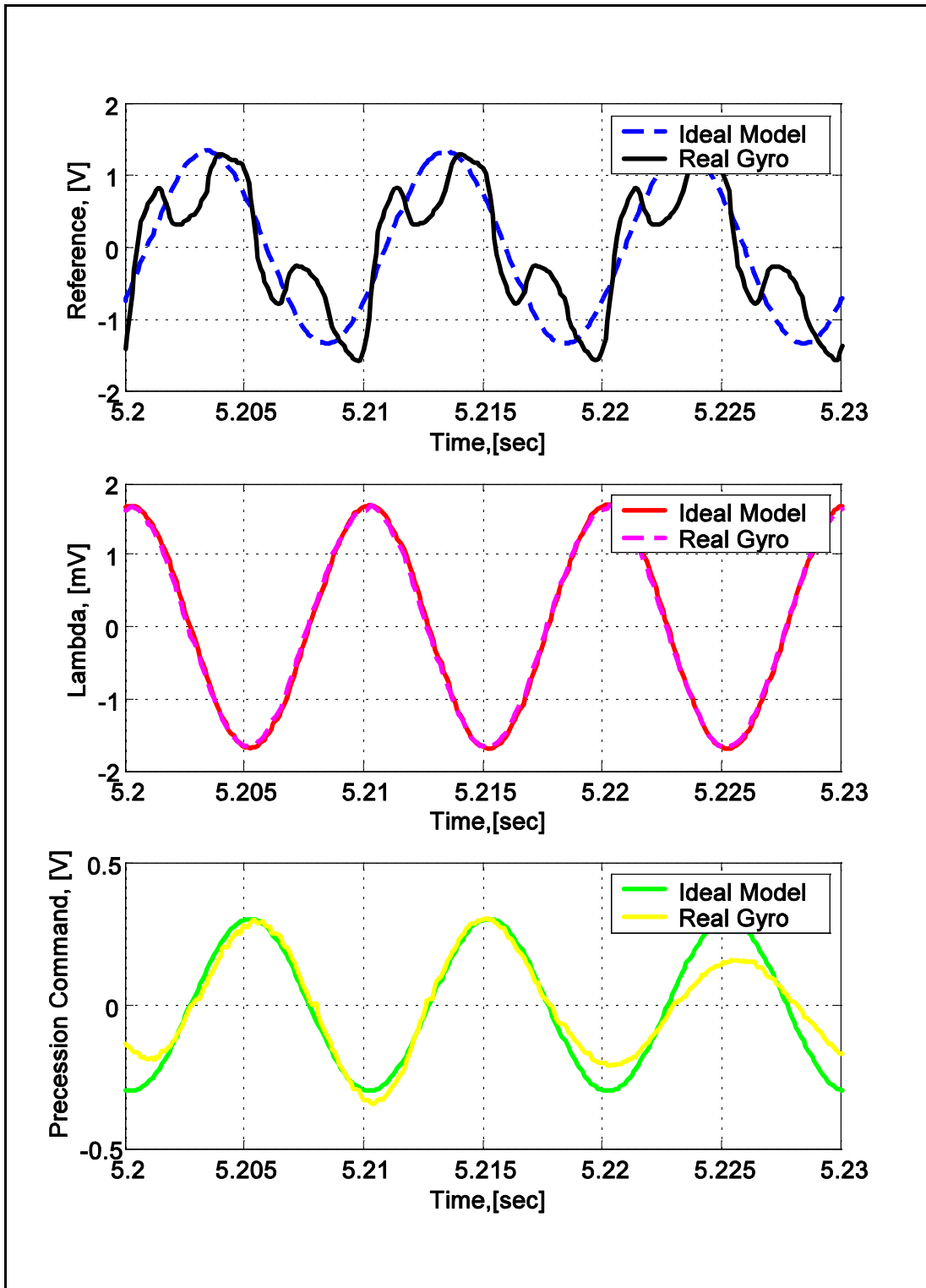


Figure 147 - Ideal gyro model comparison to lab test data for vertical down target motion.

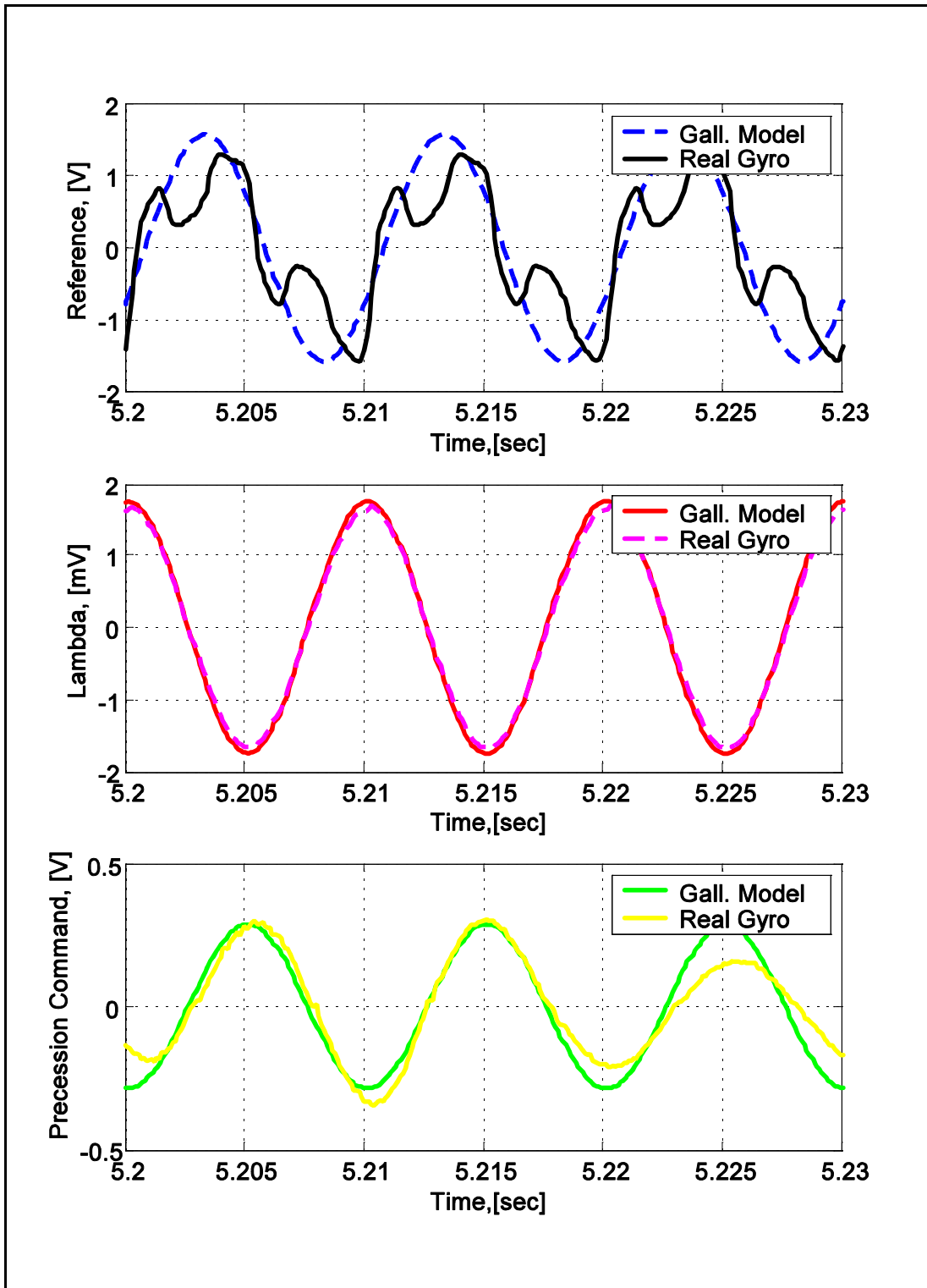


Figure 148 - Gallaspy comparison to lab test data for vertical down target motion.

7.0 Summary

Three gyro models were developed using the MATLAB/Simulink modeling tools produced by the MathWorks. The BDWL model was the most complex model. It featured gyro precession and spin torque models (including degradation with gyro look angle), gyro nutation and nutation damping, as well as the cross coupling effects of precession and spin for large off-boresight angles. The BDWL gyro models used equations of motion derived from Newtonian principles.

The Ideal gyro model was the least complex model, using simplistic idealized equations of motion. It included perfect gyro precession rates in the exact commanded direction, instantaneous spin-up and spin-down response, no coupling or degradation of spin and/or precession torques with gyro off-boresight angle, and no nutation or nutation damping.

The Gallaspy gyro model was a medium complexity model. It used gyro equations of motion derived from the Lagrange equations. The Gallaspy model featured precession and spin torque models, no spin or precession degradation effects from off-boresight angle, no precession / spin torque coupling, and no nutation or nutation damping.

Table 4 shows a comparison of the features of each gyro model. Also included in Table 4 is a measure of the computational efficiency of the models. Each of the open-loop gyro models was exercised using a 1 second simulation time. The total model run times were averaged using four repetitions for each model. Next, the average run times were normalized to the fastest model (the

Ideal model). These results are listed in Table 4 under “run time factor”. The larger the run time factor, the longer a model takes to run.

Table 4 - Model feature comparison.

| | BDWL | Ideal | Gallaspy |
|----------------------------------|--------|-------|----------|
| Equation of motion type | Newton | Ideal | Lagrange |
| Precession torque | Yes | No | Yes |
| Spin torque | Yes | No | Limited |
| Precession / spin coupling | Yes | No | No |
| Off-boresight torque degradation | Yes | No | No |
| Nutation / nutation damping | Yes | No | No |
| Run-time factor | 2.6 | 1.0 | 1.6 |

All three models were compared to actual gyro data in four areas: twice spin frequency nutation oscillations, open loop nutation damping misalignment, rate table tests with gyro spin-up and spin-down, and gyro signal phasing.

During the development of these gyro models, several utility Simulink blocks were developed which will be useful in many types of models. A Simulink block was developed which transforms a vector expressed in inertial (space) coordinates to body-fixed coordinates using Euler angles. A complementary block was developed which transforms a vector from body-fixed to inertial coordinates also using Euler angles. A Simulink block was developed to calculate a unit vector aligned with an input vector of any length. Also, a block was developed to calculate the gyro Euler angles with respect to a moving missile which uses the gyro inertial Euler angles and missile inertial Euler angles

as inputs. A formula was derived based on Lamm (13) to calculate the time derivative of a direction cosine matrix.

8.0 Conclusions

The BDWL model showed excellent agreement with the actual gyro data for the twice spin frequency nutation oscillations and the open-loop nutation damping. The Ideal and Gallaspy models did not match the actual gyro data in these cases, neither of these models includes any nutation effects.

The BDWL model had excellent correlation with the rate table spin-up and spin-down tests. The Gallaspy model showed good correlation in some cases and fair correlation in other cases. The Ideal model did not show good correlation to the rate table tests (see Figures 93 - 119).

All three models gave similar results, and showed good correlation to the actual gyro data in the signal phase angle tests.

Thus, the BDWL model showed the best correlation to real gyro data, but was the most computationally intensive. The Ideal gyro model had the worst correlation to actual gyro data, but was the least computationally intensive. The Gallaspy model gave performance somewhere between the BDWL and Ideal gyro models in both fidelity and computational requirements.

The performance of the Gallaspy model was controlled by the assumptions made in its development. The use of the Lagrange method to derive the equations of motion showed no benefits or disadvantages in comparison to the Newtonian equation of motion derivation.

The results of this thesis give the EO/IR missile simulation developer a good set of criteria for choosing features of a gyro model and balancing gyro model fidelity with model execution speed.

9.0 Recommendations for Further Study

This paper raised several issues for further study. The actual gyro lab data in Section 6.4 indicated that the reference signal may change in amplitude with gyro off-boresight angle. This should be investigated further so that this phenomenon can be added to high fidelity gyro models.

The real gyro reference signals in Section 6.4 also showed very irregular shapes. They were not simple sinusoids at the gyro spin frequency. These irregularities in the reference signal shape may be caused by complex interactions between the gyro magnetic flux and the reference coils. This is another area that should be examined further.

Various missiles use different tracking algorithms. The gyro models developed here used track loop algorithms derived from Williams (9). Thus, the results matched the Williams results well, but they did not match the NSWC Crane lab test data in Section 6.4. Much future work could be done characterizing different tracking algorithms and developing new track routines.

LIST OF REFERENCES

LIST OF REFERENCES

General References

1. Halliday, David and Robert Resnick. *Physics, Part 2*. New York: John Wiley and Sons, 1978.
2. Blakelock, John H. *Automatic Control of Aircraft and Missiles*. New York: John Wiley & Sons, 1965.
3. Ogata, Katsuhiko. *Modern Control Engineering*. 3rd ed, Upper Saddle River, N. J.: Prentice Hall, 1997.
4. Torby, Bruce J. *Advanced Dynamics for Engineers*. New York: CBS College Publishing, 1984.

Cited References

1. Dougherty, Terry. "Free Gyro Seeker Model for EO/IR Missile Systems," unpublished technical paper. China Lake, Calif.: Naval Air Warfare Center, August 1, 2000.
2. Greenwood, Donald T. *Principles of Dynamics*. 2nd ed. Englewood Cliffs, N. J.: Prentice-Hall, 1988.
3. Brown, James M. "Digital Model of a Generic Infrared Tracker." Master's thesis, Terre Haute, Indiana: Rose-Hulman Institute of Technology, May 1992.
4. Wu, Wei S. "Using Integral Coil to Drive a Two-Axis Gyroscope." *IEEE Transactions on Aerospace and Electronic Systems* **33** (1997): 322-328.
5. Kane, Thomas R., Peter W. Likins, David A. Levinson. *Spacecraft Dynamics*, New York: McGraw-Hill Book Company, 1983.
7. United Aircraft Corporation. *Gyro Primer, ... or "Selling Gyros for Fun and Profit."* Norwalk, Conn.: Norden Division of United Aircraft Corporation, 1958.
8. White, Stanley A. "Dynamics of a Solenoidal-Torqued Gyro-Stabilized Seeker Assembly for Guidance and Tracking." *IEEE Transactions on Aerospace and Electronic Systems* **10** (1974): 113:122.

9. Williams, David F. "Seeker Head Dynamics and Control," unpublished technical paper. Huntsville, Alabama: Dynetics Inc., 2000.
10. Williams, David F. "Two-Gimbal Gyro Dynamics Program for Analysis of the IRIS Seeker Dynamics," unpublished draft technical notes. Huntsville, Alabama: Dynetics Inc., 2000.
11. Williams, David F. "Gimbal Reaction Torque Model (Proposed)," unpublished technical notes. Huntsville, Alabama: Dynetics Inc., 2000.
12. Gallaspy, Jason M. "Gyro Model Prototyping in Simulink," unpublished technical report. Huntsville, Alabama: Dynetics, Inc., 2000.
13. Lamm, Darrell R. "Gyro Model Algorithms," unpublished technical report. Atlanta: Georgia Tech Research Institute, June 16, 2000.
14. General Dynamics. NWSC Crane Technical Training Course Notes, Rancho Cucamonga, Calif.: General Dynamics Valley System Division, 1989.
15. May, John J. and M. E. Van Zee. "Electro-Optic and Infrared Sensors," *Microwave Journal*, September 1983, reprint from author.
16. Heaston, R. J. and Smoots, C. W. "Introduction to Precision Guided Munitions," Chicago, IL: Guidance and Control Information Analysis Center, May 1983.
17. Faraone, J. N., Paaramann, L. D. and Smoots C. W. "Guidance Law Handbook for Classical Proportional Navigation," Chicago, IL: Guidance and Control Information Analysis Center, June 1978.
18. Lamm, Darrell R. "EO/IR JMASS Seeker Template: Reticle Processing Algorithms," unpublished technical report. Atlanta, GA: Georgia Tech Research Institute, December 8, 1999.
19. Brain, Marshall. "How Stinger Missiles Work." How Stuff Works. <http://www.HowStuffWorks.com> (20 July 2002).
20. AH-1W/AH-1Z Supercobra attack helicopter. USA army technology industry projects. <http://www.army-technology.com/projects/supcobra/supcobra6.html> (31 July 2002).
21. Eichblatt, E. J. and A. Pignataro. *Test and Evaluation of the Tactical Missile* Washington, DC: American Institute of Aeronautics and Astronautics, 1989.

22. White Sands Missile Range. Applied Sciences Division. Rate Table Laboratory. <http://www.mt.wsmr.army.mil/mtd-am-rate-table-lab.html> (11 October 2002).
23. Army Research Laboratory. Survivability and Lethality Analysis Directorate. Electronic Warfare. Modeling and Simulation. <http://www.arl.army.mil/slاد/services/elec-modeling.html> (11 October 2002).
24. Machover, Carl. *Basics of Gyroscopes*. New York: John F. Rider Publisher, 1960.
25. Larson, Roland E. and Robert P. Hostetler. *Calculus with Analytic Geometry*. 2nd ed, Lexington, Mass.: D. C. Heath and Company, 1982.